The Dissertation Committee for Hyun Seo Park Certifies that this is the approved version of the following dissertation:

Studies in the Photoelectrochemistry of Bismuth Vanadate Using Scanning Electrochemical Microscopy

Committee:

Allen J. Bard, Supervisor

Richard M. Crooks

Gyeong S. Hwang

Charles B. Mullins

Keith J. Stevenson

Studies in the Photoelectrochemistry of Bismuth Vanadate Using Scanning Electrochemical Microscopy

by

Hyun Seo Park, B.S.; M.S.

Dissertation

Presented to the Faculty of the Graduate School of

The University of Texas at Austin

in Partial Fulfillment

of the Requirements

for the Degree of

Doctor of Philosophy

The University of Texas at Austin

December, 2012

Dedication

To my biological & step mother.

To Professor Allen J. Bard.

Acknowledgements

I appreciate the discussions with Professor Gyeong S. Hwang, Professor Rodney S. Ruoff, Professor Charles B. Mullins, Professor Brian A. Korgel, Eunsu Paek, Bard group members, Dr. Hyung-Wook Ha, Dr. Kyoung Eun Kweon, and all my friends.

Studies in the Photoelectrochemistry of Bismuth Vanadate Using Scanning Electrochemical Microscopy

Publication No. _____

Hyun Seo Park, Ph. D.

The University of Texas at Austin, 2012

Supervisor: Allen J. Bard

Photoelectrochemical studies were performed on bismuth vanadate ($BiVO_4$) to understand chemical and physical properties of the photocatalysts, and to improve the photoactivity for water oxidation. Scanning electrochemical microscopy (SECM) was used to screen various dopants for $BiVO_4$, to calculate the photoconversion efficiencies to chemical energy at $BiVO_4$ electrodes, and to study the water oxidation intermediate radicals at the surface of $BiVO_4$. Tungsten and molybdenum doped $BiVO_4$ (W/Mo-$BiVO_4$) shows a photocurrent for water oxidation that is more than 10 times higher than undoped $BiVO_4$. Photoelectrochemical measurements and material analysis were done to discuss the factors that affect performance of $BiVO_4$. Finite elements analysis was also performed to explain the electron-hole transport and electrochemical reactions at W/Mo-$BiVO_4$ electrodes in solutions. Addition of conductive or electron accepting materials, e.g. reduced graphene oxide, into $BiVO_4$ was tried to study the electron-hole transport phenomena in the metal oxide electrodes. Surface adsorbed radicals produced during the water oxidation at W/Mo-$BiVO_4$ were interrogated by using SECM that the surface

coverage and decay kinetics of adsorbed hydroxyl radicals at W/Mo-$BiVO_4$ were measured. The quantum efficiencies of the injected photon conversion to chemical energy were obtained from the photoelectrochemical measurements by using SECM. SECM techniques and finite elements analysis were also used to measure the faradaic efficiency of water oxidation at W/Mo-$BiVO_4$ under irradiation. Finally, unbiased water splitting to generate hydrogen and oxygen from water splitting only using photon energy at W/Mo-$BiVO_4$ electrodes was demonstrated in a dual n-type semiconductor or Z-scheme device.

Table of Contents

List of Tables

List of Figures

Chapter 1. Introduction to Photoelectrochemistry and SECM

1.1 Photoelectrochemistry

Photoelectrochemistry studies electrochemical reactions occurred at semiconductor, i.e. photocatalyst, and solution interfaces under light irradiation.[1] Since the first photoelectrochemical experiment was performed by Becquerel in 1839,[2,3] fundamentals of photoelectrochemical reactions have been extensively studied.[4,5] Photon-conversion to chemical or electrical energy is initiated by electron excitation from a lower orbital level to a higher orbital level in the photocatalysts. For example, when bismuth vanadate ($BiVO_4$), which is an n-type metal oxide photocatalyst with a band gap size (E_g) of about 2.4 eV,[6] is irradiated, bonding electrons at O_{2p} orbitals are excited to V_{3d} orbitals leaving the holes at the valence band.[7] The excited electron-hole pairs are separated by the electric field developed at a semiconductor and solution junction[8] because of the electrochemical potential differences between the semiconductor and the solution phases.[9] Schematic presentations in Figure 1.1 show the electric filed developed at the semiconductor-solution junction. Consequently, the excited electron-hole pairs are used for oxidation reactions on the n-type semicondcutor-soluton interface in the presence of reducing species or for reduction reactions on the p-type semiconductor-solution junctions as shown in Figure 1.1(b). For example, photocurrent

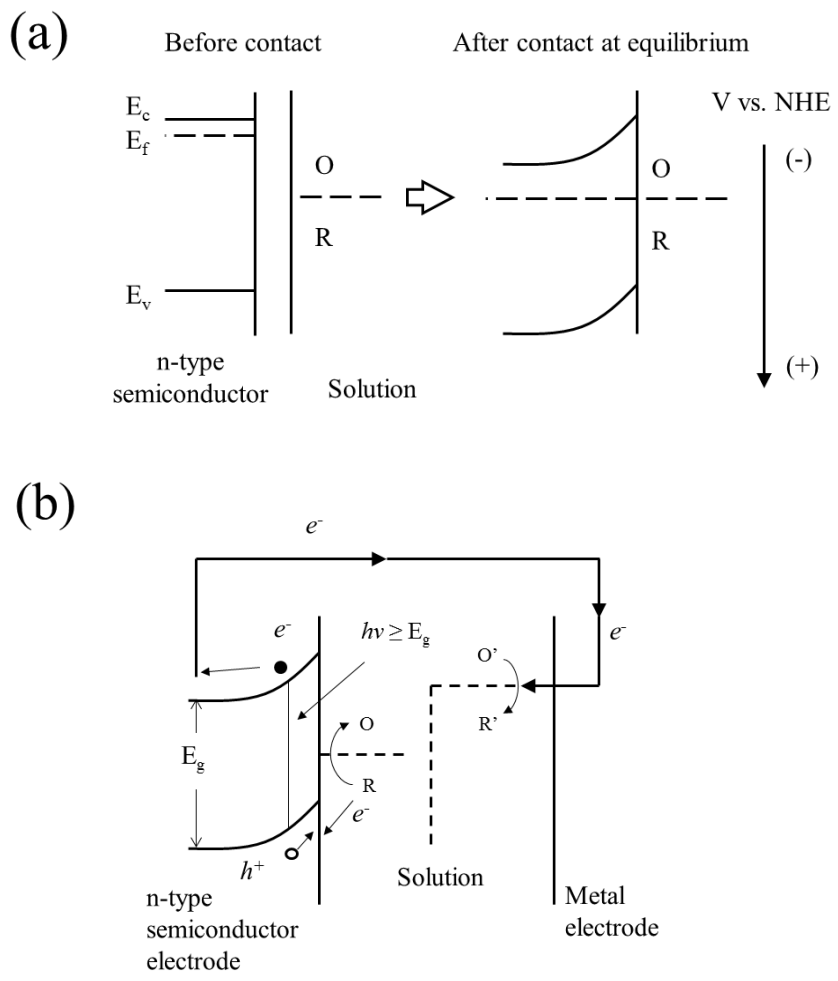

Figure 1.1. Schematic representations of (a) the foramtion of the semiconductor and solution junction under dark and (b) the electron flow and chemical reactions under irradiation in the photoelectrochemcial cell.[1]

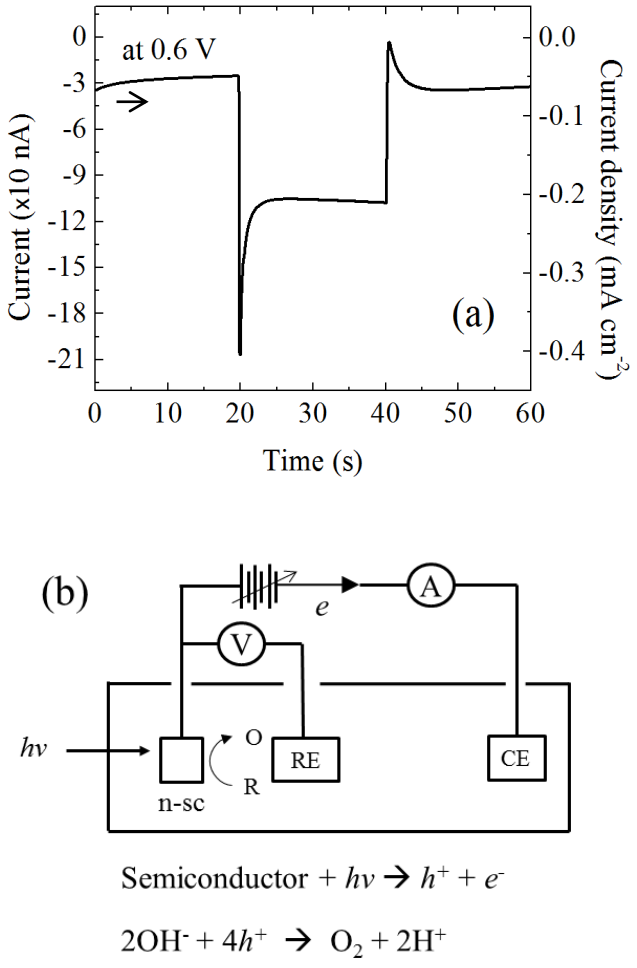

Figure 1.2. (a) Chronoamperogram of photocurrent for water oxidation at W and Mo doped-$BiVO_4$ electrode at 0.6 V (vs NHE) under UV-visible irradiation from 20 to 40 s. (b) Schematic representations of the electrochemical configurations to perform the photoelectrochemical experiments.

obtained for water oxidation at photoelectrode under irraidation and the electrochemical configurations are shown in Figure 1.2.

Efficiently and inexpensively converting radiant energy to chemical energy, and especially the water splitting reaction, has been a great challenge for many decades as the ultimate solution of a sustainable energy source.[5] After Fujishima and Honda suggested the possible photolysis of water using a TiO_2 photoanode,[4] tremendous efforts have been made to realize water splitting using solar energy. A major part of the research focused on finding a single useful material for this reaction, mostly based on large band gap metal oxide semiconductors like TiO_2, $SrTiO_3$, and others.[10,11,12] However, it is pretty clear that the needed driving force for water splitting requires a semiconductor band gap that can only absorb a small portion of the solar spectrum. To obtain a reasonable efficiency using smaller band gap materials, two or more photons must be absorbed to drive a single electron in the reaction. Other systems have been suggested, e.g., buried p-n junction electrodes,[13,14,15] tandem structures with dye-sensitized solar cells and a metal oxide,[16] and multiple bipolar photoelectrodes in a series connection,[17,18,19] where two or more semiconductors are combined to cover a wide solar wavelength window and create a sufficient potential to drive the water splitting reaction. Among the proposed systems, a dual n-type semiconductor device (or Z-scheme) was suggested by this group in 1979 to overcome the single photoelectrode problem.[9] Since that time, many efforts have been made to find a suitable combination of photoelectrodes and redox couples to demonstrate PEC water splitting by a Z-scheme.[20]

The semiconductor properties important in the design of photocatalysts required for a photosynthetic system, e.g. a photoelectrochemical cell to split water to hydrogen and oxygen, have largely been taken to be the band-gap energy, E_g, and the band-edge locations, E_c and E_v (usually with considerations of factors affecting stability).[5,21] These affect the amount of solar energy absorbed in the material and the energies of electrogenerated carriers (holes and electrons). However, many other factors affect the performance and efficiency of the photocatalyst, such as the depth of penetration of the incident radiation, the carrier mobility, the depth of the electric field at the surface, the rate of recombination of the photogenerated carriers in the bulk and on the surface, and the carrier transfer rate to solution species. Clearly both the photocatalyst composition and its structure are important.

Photoelectrochemical measurements of photocatalysts performed in the three electrode electrochemcial system show the chemical and physical properties of photocatalysts. Figure 1.3 shows the photooxidation current at W and Mo-doped $BiVO_4$ for sulfite oxidation under strong irradiation (400 mW cm^{-2}). The conduction band edge of n-type or the valence band edge of p-type photoelectrodes can be estimated from the onset potential of the linear sweep voltammogram. In addition, capacitance mesurements of photoelectrodes shows the flat band position and majority carrier density of the photocatalysts accodring to the Mott-Schottky relationship.[8]

$$1/ C_{sc}^2 = (2/q\varepsilon\varepsilon_0 N_D) (E-E_{fb}-kT/q) \qquad (1\text{-}1)$$

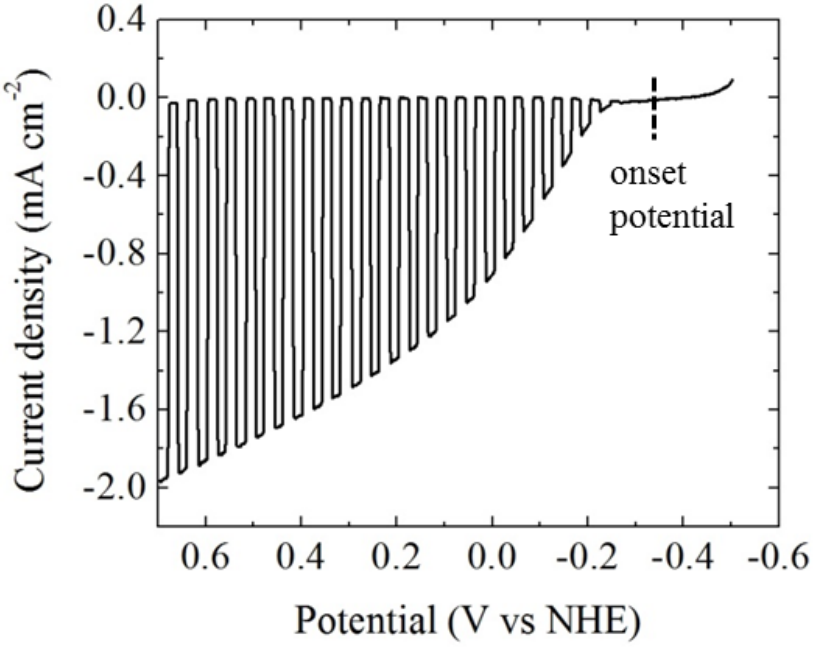

Figure 1.3. Linear sweep voltammogram of W and Mo doped-$BiVO_4$ for sulfite oxidation under strong UV-visible irradiation (400 mW cm^{-2}). The measurements was perfomed in 0.1 M Na_2SO_3 and 0.1 M Na_2SO_4 solution (pH 7, 0.2 M sodium phosphate buffer). Scan rate was 20 mV s^{-1}.

where C_{sc} is the space charge capacitance in F cm^{-2}, q is the electronic charge in C, ε is the dielectric constant of the semiconductor, ε_0 is the permittivity of free space, N_D is the majority carrier density in cm^{-3}, E is the applied potential in V, E_{fb} is the flat band potential in V, κ is the Boltzmann constant, and T represents the temperature in K. The flat band potential is obtained from the x-intercept of the tangent line of Mott-Schottky plot on potential axis (Figure 1.4).

The band-gap energy of photocatalysts can also be obtained from the incident photon to conversion efficiency (IPCE) measurements.

$$\text{IPCE (\%)} = (1240 / \lambda) \times i_{ph} / P_{in} \times 100 \qquad (1\text{-}2)$$

where λ is the wavelength of illuminated light in nm, i_{ph} is the measured photocurrent density in mA cm^{-2}, and P_{in} is the incident power density in mW cm^{-2}. IPCE is obtained from the photocurrent measurements as shown in Figure 1.5 under monochromatic irradiation. The onset wavelength of IPCE is the band-gap size of photocatalysts. For example, the band-gap of W and Mo-doped $BiVO_4$ obtained from IPCE measurements (Figure 1.5) is about 2.4 eV, i.e. 520 nm. In sum, the entire band structure of photocatalysts is measured by the electrochemical measurements, e.g. the conduction and valence band edges measured from LSV and Mott-Schottky plots, and the band-gap energy obtained from IPCE measurements. Also, the activity of photocatalysts is obtained from the photocurrent measured in the electrochemical experiments.

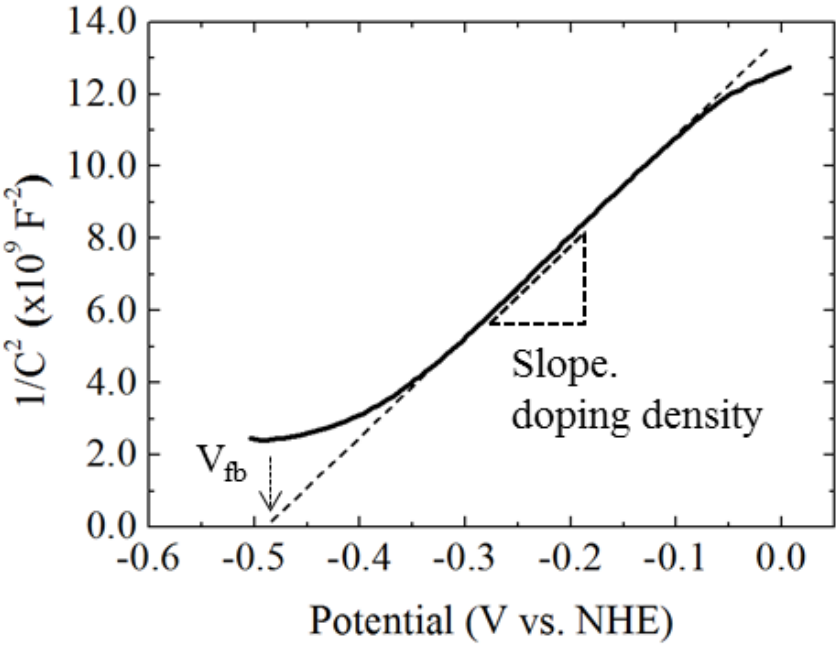

Figure 1.4. Mott-Schottky plots of W and Mo-doped $BiVO_4$ obtained from the capacitance measurements. AC amplitude of 10 mV was applied for each potential and AC frequency used for the measurements was 1000 Hz. Tangent lines of the M-S plots are drawn to obtain the flat band potential.

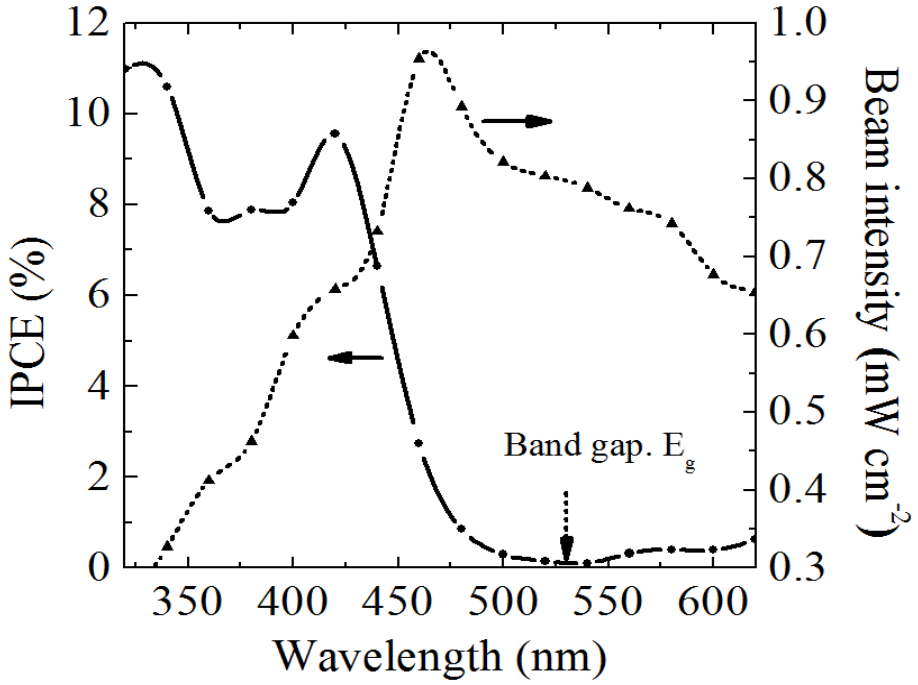

Figure 1.5. Incident photon to current conversion efficiency (IPCE) plots of W and Mo-doped $BiVO_4$ film electrodes with a thickness of about 200 nm for water oxidation (circle). The photocurrent was measured at 0.6 V in 0.1 M Na_2SO_4 aqueous solution under irradiation. The irradiation power at the corresponding illumination at the discrete wavelength used is indicated on the plot (triangle).

1.2 Scanning Electrochemcial Miscroscopy

Since its development in the late 1980's, scanning electrochemical microscopy (SECM) has proven to be a powerful tool for performing high resolution chemical characterizations on all types of surfaces (insulating, semiconducting and conducting) in solutions.[22,23] One area where SECM has been widely used is in studying mechanisms of heterogeneous inner-sphere reactions on catalytic surfaces. For example, the oxygen/hydrogen evolution reactions (OER and HER), oxygen reduction reactions (ORR), and hydrogen oxidation reactions (HOR), at Pt, Pd, Au, Hg, and other electrodes or nanoparticles have all been characterized using SECM.[24,25,26]

In addition, studying reactions at semiconducting electrodes is also possible using SECM. One example is the one-electron outer-sphere oxidation kinetics of $Ru(NH_3)_6^{2+}$ which was investigated using the feedback mode of SECM at WSe_2 and Si electrodes without photon injection to the semiconductor.[27] In addition, the modification, degradation, and photooxidation of semiconductors (e.g. etching of GaAs, GaP, or CdTe surface using Br^-/Br_2 redox couple or the photooxidation of Ta_3N_5) have also been studied using SECM.[28,29] Recently, SECM was also used to discover new electrocatalysts, photocatalysts, and photosensitizers by combinatorial rapid screening methods.[30,31,32,33] Combinatorial methods have been explored as a quick screening method to find suitable photoanodes for water oxidation which utilize metal oxides,[34] e.g. Fe_2O_3,[35,36,37,38] WO_3,[39,40] $BiVO_4$,[41,42] and chalcogenides, e.g., CdSe, $CuInSe_2$, and Cu_2ZnSnS-Se.[43,44,45] The setup of SECM equipment to prepare the photocatalysts arrays for rapid combinatorial screening is shown in Figure 1.6.

To perform these electrochemical characterizations, several techniques (or modes) of SECM have been developed which utilize an ultramicroelectrode (UME) tip with proper redox chemicals in solutions.[46,47,48,49,50,51] UME has smaller electrode diameter than the diffusion layer developed at the electrode surface so as to quickly achieve steady state current.[52] The steady state current of disk UME is[52]

$$i_{ss} = 4nFAD_0C_0^* / \pi r_0 = 4nFD_0C_0^* r_0 \quad (1\text{-}3)$$

where n is a stoichiometric number of electrons involved in an electrochemical reaction, F is the Faraday constant, A is the electrode area, D_0 is the diffusion coefficient of species in solution, C_0^* is the bulk concentration of species, and r_0 is a radius of UME. For example, typical cyclic voltammogram of Au UME with a diameter of 10 μm in 1 mM ferrocenemethanol (FcMeOH) and 0.1 M Na_2SO_4 aqueous solution is shown in Figure 1.7. The steady state current obtained from CV, i.e. 0.8 nA, is well agreed with that calculated from the equation (1-3).

The tip current of UME measured as a function of the distance between tip-substrate, i.e. d, is called an approach curve (Figure 1.7(b)).[53] When the tip is only several tip diameters away from the substrate, the approach curve provides information of the nature of the substrate. For example, Figure 1.7(b) shows the tip current of Au UME with a diameter of 10 μm as the tip moved toward the insulting substrate in 1 mM FcMeOH solution. When a diffusive flux of species towards the UME is limited by the short distance between the tip and the substrate, the steady state current measured at UME is reduced from that measured at bulk solution, i.e. negative feedback.

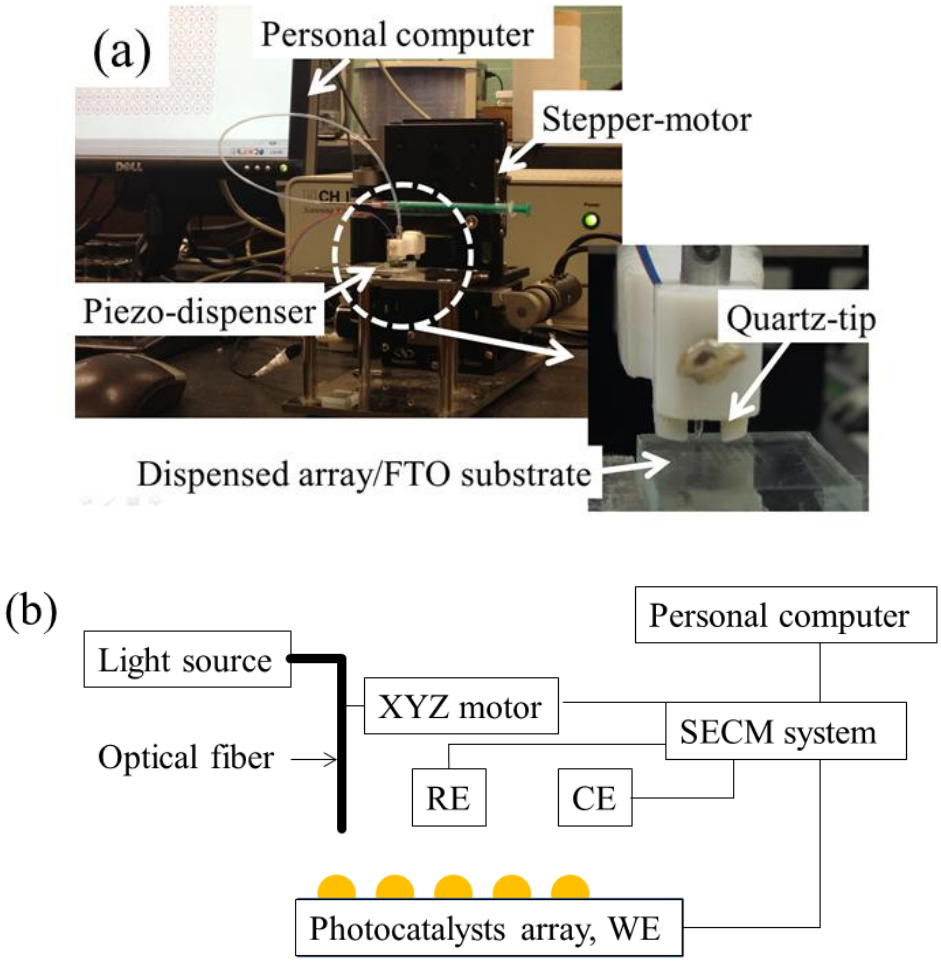

Figure 1.6. Photographic images and schematic representations of the SECM setup for (a) rapid sysnthesis of photocatalysts array, and (b) rapid screening PEC measurements under irradiation.

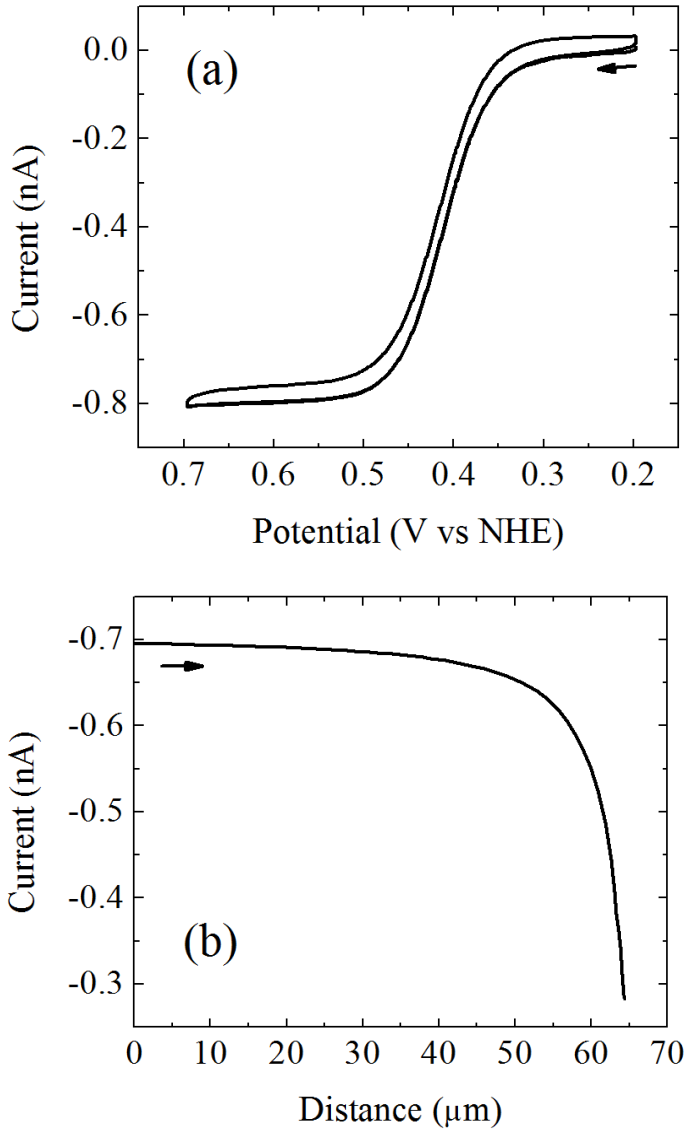

Figure 1.7. (a) Cyclicvoltammogram of Au UME with a diameter of 10 μm in 1 mM ferrocenemethanol and 0.1 M Na_2SO_4 aqueous solution. Scan rate is 20 mV s^{-1}. (b) Approach curve at an insulating substrate in the same solution in (a) as the Au tip approached to the substrate with the scan rate of 1 μm/0.1 s. Tip potential is held at 0.7 V vs NHE.

Approximate forms of the numerical results shown below describe the approach curve for an insulating substrate or negative feedback current.[53]

$$i(L) = (0.292 + 1.5151/L + 0.6553 \exp(-2.4035/L))^{-1} \quad (1\text{-}4)$$

where L is the normalized distance between the tip and the substate, d, with respect to the tip radius, a (L = d/a). For a conductive substrate, the reduced or oxided species at the tip is regenerated by the reverse reaction of the tip at the conductive substrate, and it increases the diffusive flux of reactive species towards the tip so as to increase the tip current, i.e. positive feedback. Then, the tip current at the conducting substrates is:[53]

$$i(L) = 0.68 + 0.78377/L + 0.3315 \exp(-1.0672/L) \quad (1\text{-}5)$$

The most popular modes of SECM include positive/negative feedback, tip generation/substrate collection (TG/SC), tip collection/substrate generation (TC/SG), and a redox competition mode of SECM.[54,55] For example, Figure 1.8 and Figure 1.9 show the schematic presentations of TC/SG mode of SECM and results of the SECM experiments using TC/SG mode of SECM. In Figure 1.8, photooxidation of chemical species, e.g. ferrocene, occurs at an n-type semiconductor electrode (SG) under irradiation, and the oxidized species diffuses back to the tip placed closely on the photoelectrode that to be reduced again (TC). As discussed above, SECM can provide information of the nature of chemical reactions at photoelectrodes and the nature of semiconductor surface by using various techniques of SECM in the electrochemistry and photochemistry.

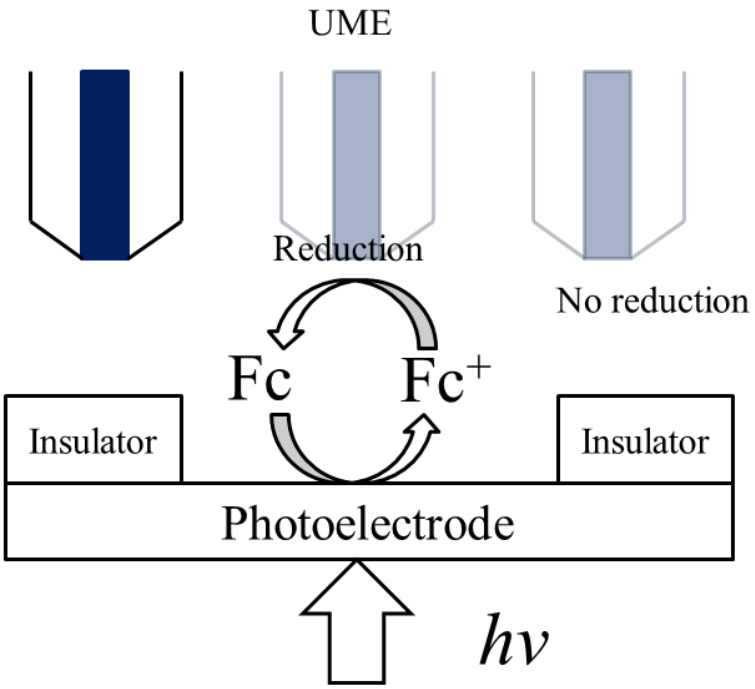

Figure 1.8. Schematic example of tip collection/substrate generation mode of SECM using photoelectrodes and ultramicroelectrode(UME). The redox couple, i.e. ferrocene, is photooxide to ferrocenium at a photoelectrode under irradiation (substrate generation), and the ferroceinum is diffused to UME and is reduced back to ferrocene (tip collection).

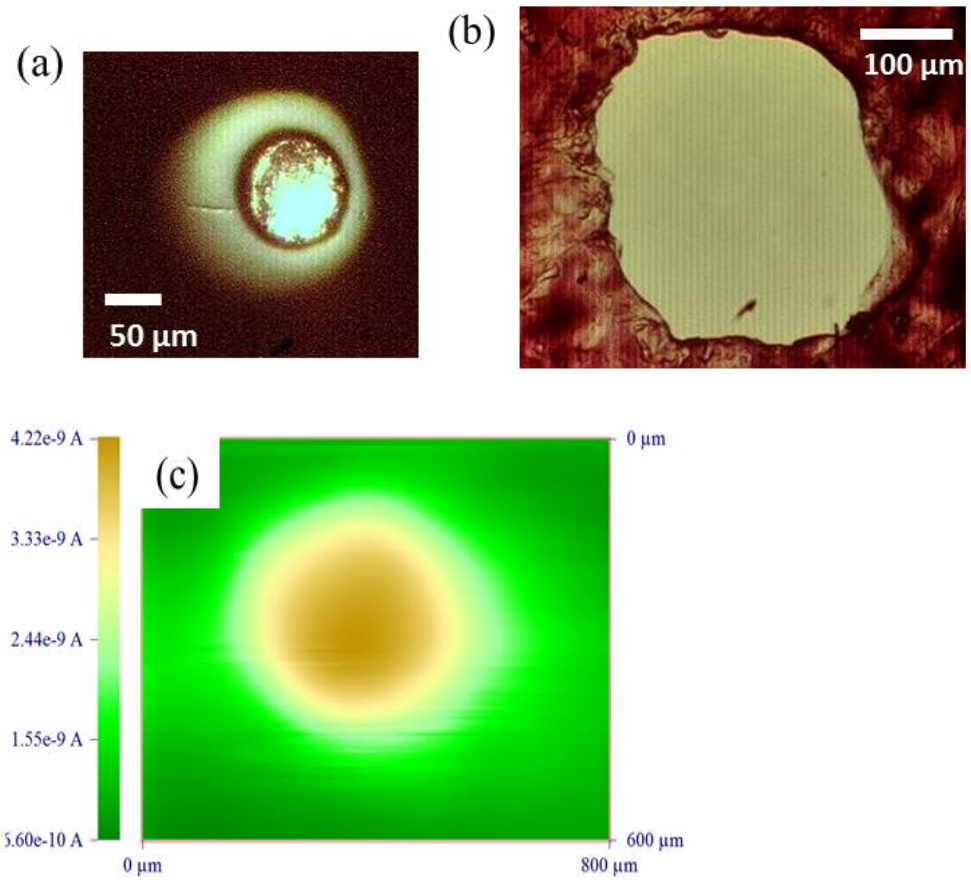

Figure 1.9. Optical microscope images of Au UME with a diameter of 100 µm (a), small photoelectrode covered by polytetrafluoroethylene tape (b), and SECM scanning image of the electrode shown in (b) from tip collection and substrate generation mode of SECM in 1 mM ferrocenemethanol and 0.1 M Na_2SO_4 solution (c).

The factors which affect the photoactivity of photocatalysts to have electrochemical reactions under irradiation are described from the rapid screening of photocatalysts using SECM in Chapter 2. Chapter 3 deals with the mechanistic processes and quntum efficiencies of excited electron-hole pairs and the reactions at a photocatalyst surface under irradiation investigated by SECM. The details of electron-hole transports in the electric field developed in the photocatalysts are explained in Chapter 4 using finite elements analysis. Chapter 5 finally describes the photoelectrochemical device for the unbiased photolysis of water using the photocatalysts developed herein.

1.3 References

[1] Bard, A. J. *Science* **1980,** *207,* 139-144.

[2] Brattain, W. H.; Garrett, C. G. B. *Bell Syst. Tech. J.* **1955,** 34, 129-176.

[3] Nozik, A. J. *Ann. Rev. Phys. Chem.* **1978,** *29,* 189-222.

[4] Fujishima, A.; Honda, K. *Nature,* **1972,** *238,* 37-38.

[5] Bard, A. J.; Fox, M. A. *Acc. Chem. Res.* **1995,** *28,* 141-145.

[6] Kudo, A.; Omori, K.; Kato, H. *J. Am. Chem. Soc.* **1999,** *121,* 11459-11467.

[7] Oshikiri, M.; Mauro, B. *J. Phys. Chem. B* **2006,** *110,* 9188-9194.

[8] Bard, A. J.; Faulkner, L. R. *Electrochemical Methods: Fundamentals and Applications; Wiley: New York,* **2001**; Chapter 18, pp 736-768.

[9] Bard, A. J. *J. Photochem.* **1979,** *10,* 59-75.

[10] Youngblood, W. J.; Lee, S.-H. A.; Maeda, K.; Mallouk, T. E. *Acc. Chem. Res.* **2009**, *42*, 1966-1973.

[11] Li, L.; Duan, L.; Xu, Y.; Gorlov, M.; Hagfeldt, A.; Sun, L. *Chem. Commun.* **2010**, *46*, 7307-7309.

[12] Brimblecombe, R.; Koo, A.; Dismukes, G. C.; Swiegers, G. F.; Spiccia, L. *J. Am. Chem. Soc.* **2010**, *132*, 2892-2894.

[13] Walter, M. G.; Warren, E. L.; McKone, J. R.; Boettcher, S. W.; Mi, Q.; Santori, E. A.; Lewis, N. S. *Chem. Rev.* **2010**, *110*, 6446-6473.

[14] Boettcher, S. W.; Warren, E. L.; Putnam, M. C.; Santori, E. A.; Turner-Evans, D.; Kelzenberg, M. D.; Walter, M. G.; McKone, J. R.; Brunschwig, B. S.; Atwater, H. A.; Lewis, N. S. *J. Am. Chem. Soc.* **2011**, *133*, 1216-1219.

[15] Rocheleau, R. E.; Miller, E. L.; Misra, A. *Energy & Fuels* **1998**, *12*, 3-10.

[16] Sivula, K.; Le Formal, F.; Gratzel, M. *ChemSusChem* **2011**, *4*, 432-449.

[17] Cervera-March, S.; Smotkin, E. S.; Bard, A. J.; Campion, A.; Fox, M. A.; Mallouk, T.; Webber, S. E.; White, J. M. *J. Electrochem. Soc.* **1988**, *135*, 567-573.

[18] Smotkin, E.; Bard, A. J.; Campion, A.; Fox, M. A.; Mallouk, T.; Webber, S. E.; White, J. M. *J. Phys. Chem*. **1986**, *90*, 4604-4607.

[19] Smotkin, E. S.; Cervera-March, S.; Bard, A. J.; Campion, A.; Fox, M. A.; Mallouk, T.; Webber, S. E.; White, J. M. *J. Phys. Chem.* **1987**, *91*, 6-8.

[20] Maeda, K.; Higashi, M.; Lu, D.; Abe, R.; Domen, K. *J. Am. Chem. Soc.* **2010**, *132*, 5858-5868.

[21] Bard, A. J. *J. Phys. Chem.* **1982**, *86*, 172-177.

[22] Bard, A. J.; Fan, F.-R.; Kwak, J.; Lev, O. *Anal. Chem.* **1989,** *61,* 132-138.

[23] Kwak, J.; Bard, A. J. *Anal. Chem.* **1989,** *61,* 1221-1227.

[24] Sanchez-Sanchez, C. M.; Rodriguez-Lopez, J.; Bard, A. J. *Anal. Chem.* **2008,** *80,* 3254-3260.

[25] Bertoncello, P. *Energy Environ. Sci.* **2010,** *3,* 1620-1633.

[26] Shah, B. C.; Hillier, A. C. *J. Electrochem. Soc.* **2000,** *147,* 3043-3048.

[27] Horrocks, B. R.; Mirkin, M. V.; Bard, A. J. *J. Phys. Chem.* **1994,** *98,* 9106-9114.

[28] Mandler, D.; Bard, A. J. *J. Electrochem. Soc.* **1990,** *137,* 2468-2472.

[29] Cong, Y.; Park, H. S.; Wang, S.; Dang, H. X.; Fan, F.-R. F.; Mullins, B.; Bard, A. J. *J. Phys. Chem. C* **2012,** *116,* 14541-14550.

[30] Fernandez, J. L.; Walsh, D. A.; Bard, A. J. *J. Am. Chem. Soc.* **2005,** *127,* 357-365.

[31] Kylberg, W.; Wain, A. J.; Castro, F. A. *J. Phys. Chem. C* **2012,** *116,* 17384-17392.

[32] Ye, H.; Park, H. S.; Bard, A. J. *J. Phys. Chem. C* **2011,** *115,* 12464-12470.

[33] Lee, J.; Ye, H.; Pan, S.; Bard, A. J. *Anal. Chem,* **2008,** *80,* 7445-7450.

[34] Katz, J. E.; Gingrich, T. R.; Santori, E. A.; Lewis, N. S. *Energy Environ. Sci.* **2009**, *2,* 103-112.

[35] Woodhouse, M.; Herman, G. S.; Parkinson, B. A. *Chem. Mater.* **2005**, *17,* 4318-4324.

[36] Jang, J. S.; Lee, J.; Ye, H.; Fan, F.-R. F.; Bard, A. J. *J. Phys. Chem. C.* **2009**, *113,* 6719-6724.

[37] He, J.; Parkinson, B. A. *ACS Comb. Sci.* **2011**, *13,* 399-404.

[38] Jang, J. S.; Yoon, K. Y.; Xiao, X.; Fan, F.-R. F.; Bard, A. J. *Chem. Mater.* **2009**, *21*, 4803-4810.

[39] Baeck, S. H.; Jaramillo, T. F.; Brandli, C.; McFarland, E. W. *J. Comb. Chem.* **2002**, *4*, 563-568.

[40] Liu, W.; Ye, H.; Bard, A. J. *J. Phys. Chem. C* **2010**, *114*, 1201-1207.

[41] Ye, H.; Lee, J.; Jang, J. S.; Bard, A. J. *J. Phys. Chem. C* **2010**, *114*, 13322-13328.

[42] Park, H. S.; Kweon, K. E.; Ye, H.; Paek, E.; Hwang, G. S.; Bard, A. J. *J. Phys. Chem. C* **2011**, *115*, 17870-17879.

[43] Liu, G.; Liu, C.; Bard, A. J. *J. Phys. Chem. C* **2010**, *114*, 20997-21002.

[44] Liu, G.; Bard, A. J. *J. Phys. Chem. C* **2010**, *114*, 17509-17513.

[45] Riha, S. C.; Parkinson, B. A.; Prieto, A. L. *J. Am. Chem. Soc.* **2011**, *133*, 15272-15275.

[46] Mirkin, M. V.; Nogala, W.; Velmurugan, J.; Wang, Y. *Phys. Chem. Chem. Phys.* **2011,** *13*, 21196-21212.

[47] Zaera, F. *Chem. Rev.* **2012,** *112*, 2920-2986.

[48] Snowden, M. E.; Guell, A. G.; Lai, S. C. S.; McKelvey, K.; Ebejer, N.; O'Connell, M. A.; Colburn, A. W.; Unwin, P. R. *Anal. Chem.* **2012,** *84*, 2483-2491.

[49] Lee, C.; Kwak, J.; Bard, A. J. *Proc. Natl. Acad. Sci. USA* **1990,** *87*, 1740-1743.

[50] Patten, H. V.; Lai, S. C. S.; Macpherson, J. V.; Unwin, P. R. *Anal. Chem.* **2012,** *84*, 5427-5432.

[51] Grisotto, F.; Ghorbal, A.; Goyer, C.; Charlier, J.; Palacin, S. *Chem. Mater.* **2011,** *23*, 1396-1405.

[52] Bard, A. J.; Faulkner, L. R. *Electrochemical Methods: Fundamentals and Applications; Wiley: New York,* **2001**; Chapter 5, pp 168-176.

[53] Bard, A. J.; Faulkner, L. R. *Electrochemical Methods: Fundamentals and Applications; Wiley: New York,* **2001**; Chapter 16, pp 669-675.

[54] Bard, A. J.; Mirkins, M. V.; Unwin, P. R.; Wipf, D. O. *J. Phys. Chem.* **1992,** *96,* 1861-1868.

[55] Eckhard, K.; Chen, X.; Turcu, F.; Schuhmann, W. *Phys. Chem. Chem. Phys.* **2006,** 8, 5359-5365.

Chapter 2. SECM for Photocatalyst Discovery and Improvement

2.1 Introduction

Combinatorial screening of the photocatalysts has been used to find a new photocatalysts including scanning electrochemical microscopy (SECM) based on scanning with a fiber optic and robotic fabrication of arrays; these have been useful in finding photocatalysts with the desired composition.[1,2,3-8] The rapid screening by SECM of metal oxide and metal sulfide semiconductors has been useful in finding highly active photocatalysts. For example, we recently developed W-doped $BiVO_4$, which has several times higher photoactivity for water oxidation than undoped $BiVO_4$.[7] Solid solutions of $Zn_xCd_{1-x}Se_yS_{1-y}$ were also developed using the SECM screening method to find the optimum values of *x* and *y* to tune the band-gap and photoelectrochemical activity for polysulfide oxidation.[8] Development of an excellent photocatalysts with high conversion efficiency for light, along with electrocatalysts to drive the desired reactions are essential in design of the overall photoelectrochemical system to achieve the photosynthetic production of a fuel, such as hydrogen from water. SECM as described above has been proven to be a very useful tool for discovering a complicated composition with optimal properties.

In the nearly 40 years since Fujishima and Honda suggested the possibility of water splitting in a photoelectrochemical cell,[9] there have been enormous efforts to find a photocatalyst and electrocatalysts for this reaction. However, to date none of these investigated photocatalysts has fulfilled all of the necessary design requirements for

practical photosynthetic water splitting.[10] $BiVO_4$ is a promising material that can adopt a wide range of dopants with doping levels of 10 atomic percent (at%) or more to tune its optical and chemical properties.[11,12] $BiVO_4$ has a band-gap of 2.4 - 2.5 eV which harvests visible light and it has been studied as a water oxidation photocatalyst.[13,14,15,16,17,18,19] Furthermore, the photocatalytic activity of $BiVO_4$ also depends on its crystal structure and the monoclinic scheelite-like $BiVO_4$ is a much more active structure than a tetragonal scheelite or tetragonal zircon structure.[13] To improve the photoactivity, chemical treatment of $BiVO_4$ has also been investigated. Soaking of $BiVO_4$ films in aqueous $AgNO_3$ solution is suggested as a material treatment to enhance its stability and photocatalytic activity for water oxidation.[14] As mentioned above, doping of a 4th material into the $BiVO_4$ has also been studied to increase the photoactivity and W is an excellent dopant for $BiVO_4$ using the SECM screening method.[7]

Herein, a further increase in the photoelectrocatalytic activity of W-doped $BiVO_4$ by additional doping with Mo was demonstrated by using SECM. A robotic dispensing system was used to prepare a photocatalyst array with different dopants based on W-doped $BiVO_4$. These arrays were screened by SECM.

2.2 Experimental

$Bi(NO_3)_3 \cdot 5H_2O$, (99.999%) and $(NH_4)_{10}H_2(W_2O_7)_6 \cdot xH_2O$ (99.99%) were obtained from Strem Chemicals (Newburyport, MA). Na_2HPO_4 (99.9%), NaH_2PO_4 (99.5%) and ethylene glycol were purchased from Fisher Scientific (Pittsburg, PA). VCl_3 (99%, Alfa-Aeser, Ward Hill, MA), $(NH_4)_6Mo_7O_{24} \cdot 4H_2O$ (99.98%, Sigma-Aldrich,

St. Louis, MO), Na_2SO_4 (99.0%, Sigma-Aldrich, St. Louis, MO), and Na_2SO_3 (99.6%, Mallinckrodt Baker, Phillipsburg, NJ) were used as received. Fluorine-doped tin oxide (FTO, TEC 15, Pilkington, Toledo, OH) was used as a substrate for dispensed arrays of metal oxide and as a substrate for the bulk film electrode. Deionized Milli-Q water was used as the solvent in electrochemical experiments.

Photocatalyst arrays were fabricated using a CH Instruments model 1550 dispenser (Austin, TX) consisting of a stepper-motor based XYZ positioner with a piezoelectric dispensing tip. The dispensing system was connected to a personal computer to control the position of piezoelectric jetting tip. The tip is robotically moved to a programmed position over the conducting substrate and jetting is performed from the tip by applying a potential of 80 V for 40 μs. The distance between two photocatalyst spots on the array was about 800 μm with a spot diameter of about 500 μm. Each spot had a total of 18 drops of the precursor solutions of Bi-V (5:5 in atomic ratio, total concentration of 0.1 M or 0.02 M), W (0.02 M), and the 5^{th} material (0.02 M). The relative number of dispensed drops from each solution was controlled to obtain the targeted spot composition. After completing the dispensing, the arrays were annealed in air at 500 °C for 3 h, ramped from room temperature to 500 °C at a ramp rate of 1 °C per minute.

The bulk metal oxide semiconductor thin film electrodes were prepared on FTO by drop casting using 100 μl precursor solution with total concentrations of 5 mM and the targeted atomic compositions. The bulk film was also annealed in air at 500 °C for 3 h.

A CH Instruments Model 990B SECM potentiostat (Austin, TX) was used to control the fiber optic position and collect the photocurrent from dispensed arrays on FTO. A CH Instruments Model 630D Electrochemical Analyzer was used as a potentiostat for the experiments with thin film electrodes. A platinum gauze counter electrode and a Ag/AgCl reference electrode in 3 M KCl solution were used to complete the three electrode configuration. However, the potential reported here is quoted with respect to the normal hydrogen electrode (NHE). Conductance measurements were performed using a Model 1286 electrochemical interface and Model 1250 frequency response analyzer (Solatron Analytical, Hampshire, England). Electrochemical impedance spectroscopy was conducted in 0.1 M Na_2SO_4 solution with an AC amplitude of 10 mV at each applied potential and measurements were conducted at three different frequencies: 200, 500, and 1000 Hz. For photoelectrochemical measurements, illumination was with a Xenon lamp (XBO 150 W, Osram, Munich, Germany) with full output for UV-visible irradiation or with a 420 nm cut-off filter (WBF-3, Oriel, Darmstadt, Germany) for visible irradiation. A monochromator (Photon Technology International, Birmingham, NJ), silicon photodetector (Model 818-UV, Newport, Irvine, CA), and optical power meter (Model 1830-C, Newport, Irvine, CA) were used to obtain the incident photon to current conversion efficiency (IPCE).

UV-visible absorption spectra were acquired with a Milton Roy Spectronic 3000 array spectrophotometer (New Rochelle, NY) for wavelengths from 320 nm to 900 nm. X-ray diffraction (XRD) measurements were performed using a Bruker-Nonius D8 advanced powder diffractometer (Madison, WI) operated at 40 kV and 40 mA with Cu

Kα radiation (λ=1.54 Å). Grazing incidence XRD (GIXRD) with incidence angle of 1° on detector scan mode was performed to obtain the diffractogram from the thin film electrodes on FTO. The scan rate was 12° per minute in 0.02° increments of 2θ from 10° to 90°. The obtained diffractogram was analyzed using the Material Analysis Using Diffraction (MAUD) program developed by Luca Lutterotti.[20] MAUD analysis is based on the Rietveld refinement method. Fitting of XRD patterns using MAUD was continued until a refinement reliability factor, such as R_w and σ, become less than 10 and 2. X-ray photoelectron spectroscopy (XPS) was performed on a Kratos Axis Ultra DLD instrument (Manchester, UK) with a monochromatic Al X-ray source with 180° hemispherical electron energy analyzer. For XPS, thin metal oxide films were prepared on FTO substrate. Scanning electron microscopy (SEM) images were obtained with a LEO1530 SEM at a working voltage of 10 kV with working distance of 5 mm.

2.3 Discovery of Metal Oxide Photocatalysts

Photoelectrocatalyst arrays based on $BiVO_4$ with different levels of W and Mo doping were prepared as the schematic shown in Figure 2.1. A pL robotic tip dispensed a different number of precursor solution drops on pre-programmed spots on the FTO substrate to control their atomic compositions. Several identical spots of undoped $BiVO_4$ were also prepared on the top and bottom rows of the arrays to ensure the reproducibility of the dispensing system. Undoped $BiVO_4$ is also used as an internal standard. From the second row of the array, the atomic concentration of W and Mo was controlled from 0 at% to 10 at%. For example, the spot at the far left top corner

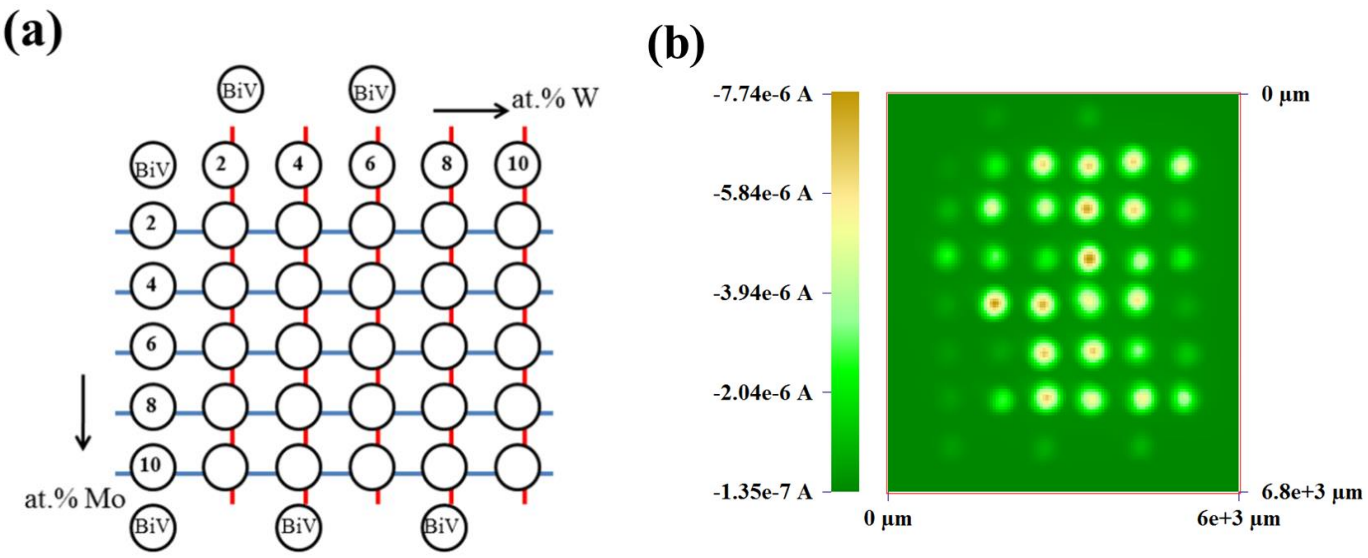

Figure 2.1. (a) Schematic diagram of the atomic composition of dispensed photoelectrocatalysts on FTO. Each spot has total of 18 drops of the precursor solutions of Bi/V (0.1 M or 0.02 M), W (0.02 M), and Mo (0.02 M) in ethylene glycol. (b) SECM image of Bi/V/W/Mo oxide photoelectrocatalysts dispensed on FTO with different doping levels of W and Mo as shown in (a). The photocurrent for sulfite oxidation was measured at 0.4 V vs. NHE in 0.1 M Na_2SO_3 and 0.1 M Na_2SO_4 solution under UV-visible irradiation. Scan rate of fiber optic was 500 µm s^{-1} (or 50 µm per 0.1 second as the setting condition of SECM) and the distance between the fiber optic and substrate was 150 µm.

contains 0 at% of W and Mo, and its content of W increased up to 10 at% moving from the left to the right columns. The doping levels of Mo also increase from 0 at% to 10 at% from the top to the bottom rows. Both W and Mo are added to $BiVO_4$ in the middle spots of the array. The spot at the far right bottom corner has both 10 at% of W and 10 at% of Mo in $BiVO_4$, i.e. $Bi_{0.4}V_{0.4}W_{0.1}Mo_{0.1}O_x$. Note that compositions are represented in terms of the amount of reactant used in the array preparation; analysis of the spots showed actual compositions were close to these.[7]

The arrays were first scanned observing the photocurrent from sulfite oxidation on the photocatalyst spots as shown in Figure 2.1(b). Those shown in Figure 2.1(b) yield the photocurrent measured at 0.4 V (vs. NHE). The average photocurrent from the spots of undoped $BiVO_4$ in Figure 2.1(b) was 0.7 ± 0.2 μA. However, the photocurrent from $BiVO_4$ doped with W from 4 at% to 8 at% was much higher (about 7 to 9 times) than that from undoped $BiVO_4$, confirming our earlier work.[7] The photooxidation currents from $BiVO_4$ doped with 4, 6, and 8 at% of W in the array were similar to each other with a current of 6.2 ± 0.1 μA.

Doping with Mo also improved the photocurrent, e.g. $BiVO_4$ doped with 4 at% Mo showed an oxidation current of 2.6 μA, three times higher than that of undoped $BiVO_4$. The improvement of photocurrent by W doping on $BiVO_4$ was larger than that from the Mo-doped $BiVO_4$. However photocatalyst spots, which were doped with both W and Mo showed even greater photoactivity than $BiVO_4$ doped with W alone. Among the doubly-doped photoelectrocatalysts, $BiVO_4$ doped with 2 at% W and 6 at% Mo (this particular composition is denoted as W/Mo-doped $BiVO_4$) shows the highest

photooxidation current among the prepared spots. The obtained photocurrent of W/Mo-doped $BiVO_4$ in this array was 7.7 μA, which is about 25% higher than the photocurrent from W-doped $BiVO_4$.

In addition, the normalized photocurrent of those dispensed spots compared with undoped $BiVO_4$ as an internal standard was considered from several identically-prepared samples with the same array configuration as that in Figure 2.1(a). While the photocurrent from the dispensed arrays can be affected by small changes of the incident Xe lamp beam intensity delivered through the fiber optic and by thickness variation of the dispensed spots, the relative photocurrents were quite reproducible. Thus for five reproduced samples, the relative photocurrents normalized with respect to undoped $BiVO_4$ were 6 (±2) for 6 at% W-doped $BiVO_4$ and 9 (±3) for W/Mo-doped $BiVO_4$ (Table 2.1). The photocurrent of 4 at% Mo-doped $BiVO_4$ was 3.5 (±0.7), which was also higher than the photocurrent from undoped $BiVO_4$. However, the enhanced photoelectrochemical activity of W/Mo-doped $BiVO_4$ did not increase with higher doping levels of W and Mo. In fact, the photocurrent from more heavily doped samples than W/Mo-doped $BiVO_4$ with either W or Mo shows a decreased photoactivity in SECM experiments compared with the optimally doped sample.

The photoelectrochemical behavior of W/Mo-doped $BiVO_4$ was further studied in 0.1 M Na_2SO_4 solution by SECM experiments to examine oxygen evolution (Figure 2.2). The pL-dispensing robotic tip was also used to prepare arrays as shown in the schematic in Figure 2.2(a). Spot arrays of W (2 at%)-doped $BiVO_4$ with different levels of Mo doping were prepared from pre-mixed W (2 at%)-Bi-V solution (0.1 M or 0.02 M) and

	$BiVO_4$	Bi/V/Mo(4%)	Bi/V/W(6%)	Bi/V/W(2%)/Mo(6%)
SECM spot photocurrent (μA)	0.7 (±0.3)	2.1 (±0.3)	4 (±1)	6 (±1)
Normalized current to $BiVO_4$	1	3.5 (±0.7)	6 (±2)	9 (±3)

Table 2.1. Summary of the photocurrent obtained from SECM experiments. $BiVO_4$ with various different doping levels of W and Mo were prepared as shown in Figure 2.1. The photooxidation current of the dispensed spots was measured using SECM. Scanning of dispensed spots was performed in 0.1 M Na_2SO_3 and 0.1 M Na_2SO_4 solution at 0.4 V vs. NHE under UV-visible irradiation.

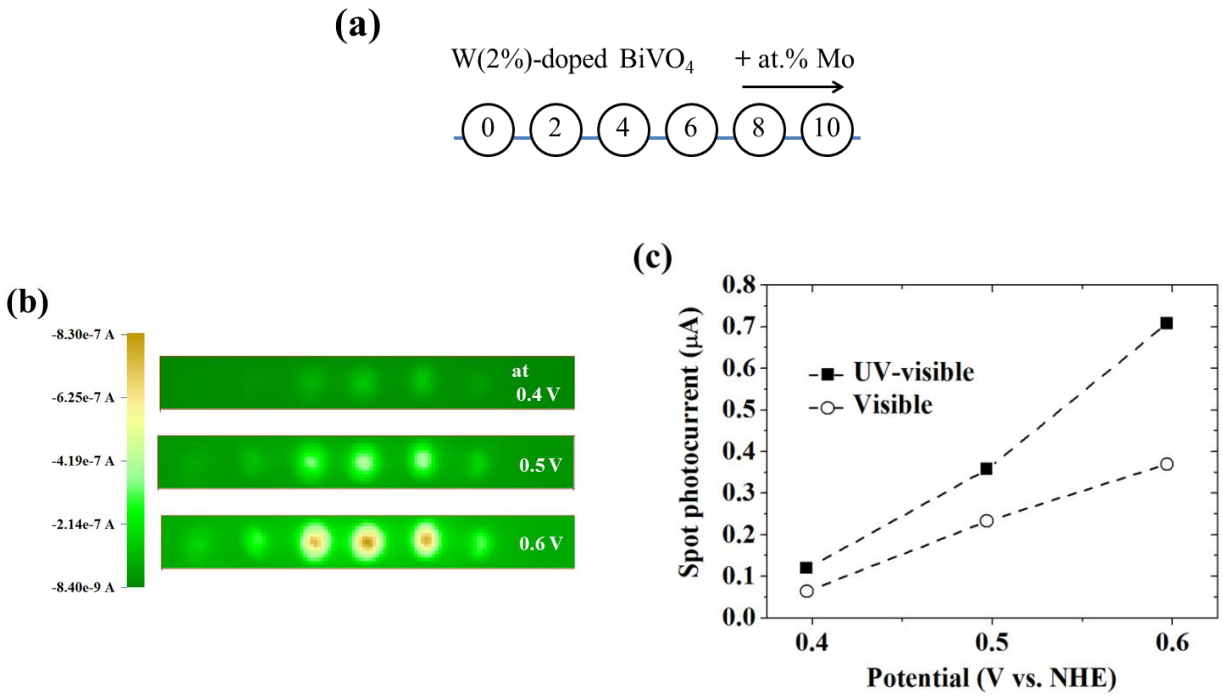

Figure 2.2. (a) Schematic diagram of the atomic composition of dispensed photocatalysts on FTO. Each spot has total of 18 drops of the pre-mixed precursor solutions of W(2 at%)-Bi/V (0.1 M or 0.02 M), and Mo (0.02 M) in ethylene glycol. (b) SECM images of spot arrays with different doping levels of Mo on W(2 at%)-$BiVO_4$ as shown in (a). The photocurrent for water oxidation was measured at 0.4, 0.5, and 0.6 V vs. NHE in 0.1 M Na_2SO_4 solution under UV-visible irradiation. Scan rate of fiber optic was 500 μm s^{-1} (or 50 μm per 0.1 second as the setting condition of SECM) and the distance between the fiber optic and substrate was 150 μm. (c) Summary of SECM scanning of W/Mo-doped $BiVO_4$ shown in (b) under UV-visible and visible irradiation.

0.02 M precursor solution of Mo. The current shown in Figure 2.2(b) measured the photocurrent for water oxidation at three different potentials: 0.2, 0.3, and 0.4 V under UV-visible irradiation. SECM scanning at different potentials can be used to estimate the linear sweep voltammogram of bulk film electrodes from the array spot response. The results shown in Figure 2.2(c) for spot scanning of W/Mo-doped $BiVO_4$ for water oxidation at different potentials agree with the film voltammograms in Figure 2.3 when the area is normalized (correction factor of about 400). The W/Mo-doped $BiVO_4$ still shows higher photoactivity than W(2 at%)-$BiVO_4$ for water oxidation.

In addition to Mo, a number of other metal components (M) were doped into $BiVO_4$ and the spot arrays examined by SECM with the same array configuration as that in Figure 2.1(a) (M instead of Mo in Figure 2.1(a)). The results of SECM scanning of BiV-W-M, summarized in Table 2.2, show that doping of Tl and Zn into $BiVO_4$ increases the photocurrent for sulfite oxidation on $BiVO_4$. For example, the photoactivity of $BiVO_4$ improved about two times by doping of Tl. However, no element among the examined metal components, except Mo, showed a positive doping effect on the photoactivity of BiV-W-O.

2.4 Factors in the Metal Doping for Metal Oxide Photocatalysts

To confirm the improved photoactivity of W/Mo-doped $BiVO_4$ compared with W-doped $BiVO_4$ or undoped $BiVO_4$, thin film electrodes on FTO substrate of a larger area (2.25 cm^2) were prepared. For W-doped $BiVO_4$, the atomic ratio in between Bi, V, and W was 4.5:5:0.5, as in our previous report, to achieve the maximum photocurrent in

Effect on BiV-O	Effect on BiV-W-O	Element	Precursor used for spot array preparation
Positive	Positive	Mo	$(NH_4)_6Mo_7O_{24}$
Positive	Negative	Tl, Zn	$TlNO_3$, $Zn(NO_3)_2$
Negative	Negative	K, Cr, Fe, Co, Sr, Ir, Pb, Eu, Ga, B	KNO_3, $Cr(NO_3)_3$, $Fe(NO_3)_2$, $Co(NO_3)_2$, $Sr(NO_3)_2$, K_3IrCl_6, $Pb(NO_3)_2$, $Eu(NO_3)_3$, $Ga(NO_3)_3$, H_3BO_3

Table 2.2. Summary of SECM scanning experiments of BiV-W-M. Several metal components with W were doped to $BiVO_4$ with the same array configurations as shown for Mo in Figure 2.1(a). Positive or negative effect of doping on the photoactivity of $BiVO_4$ and BiV-W-O were determined based on the photocurrent obtained from the scanning of dispensed spots. Scanning was performed in 0.1 M Na_2SO_3 and 0.1 M Na_2SO_4 solution at 0.4 V vs. NHE under UV-visible irradiation.

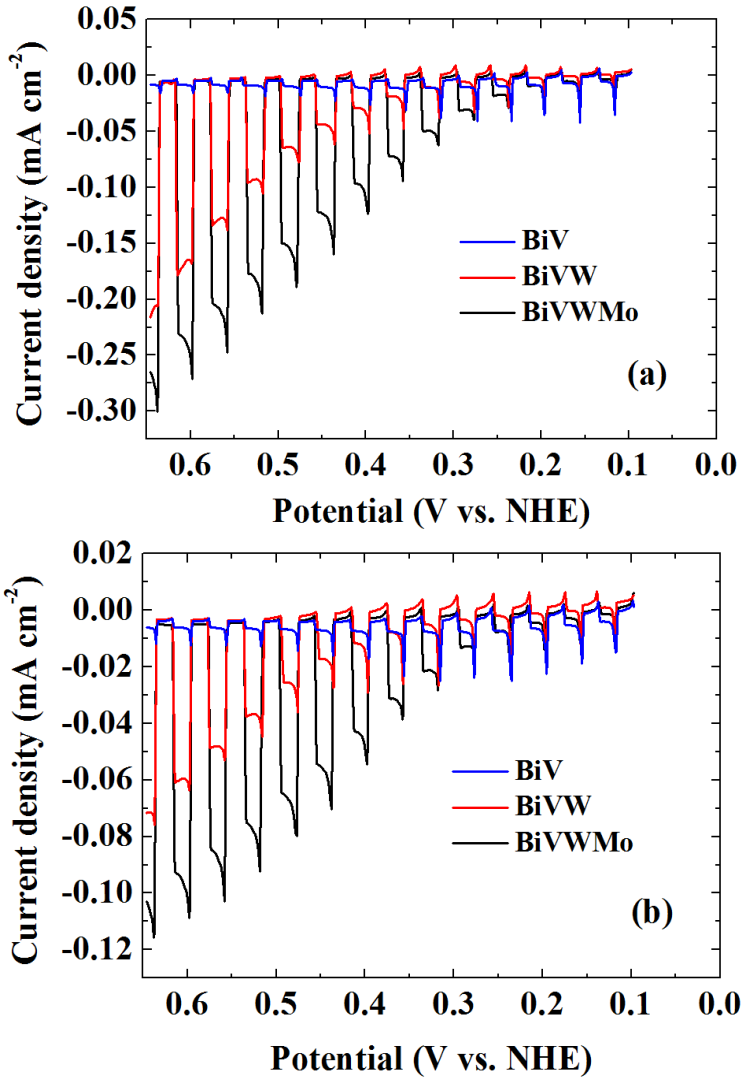

Figure 2.3. Linear sweep voltammograms of undoped $BiVO_4$ (blue), W-doped $BiVO_4$ (red), and W/Mo-doped $BiVO_4$ (black) with chopped light under (a) UV-visible irradiation and (b) visible irradiation in the 0.1 M Na_2SO_4 aqueous solution (pH 7, 0.2 M sodium phosphate buffered). Beam intensity was about 120 mW cm^{-2} from full xenon lamp and scan rate was 20 mV sec^{-1}.

the bulk film.[7] For W/Mo-doped $BiVO_4$, the atomic ratio in between Bi, V, W, and Mo was 4.6:4.6:0.2:0.6 according to the results from SECM experiments described above. The atomic composition of W/Mo-doped $BiVO_4$ thin film was confirmed by XPS measurement (Figure 2.4 and Table 2.3). In addition, the surface of the prepared W/Mo-doped $BiVO_4$ was observed by scanning electron microscopy (SEM, Figure 2.5). The crystal size in SEM images was usually less than 1 μm and the surface of the film was smooth with a few holes that expose the FTO substrate through the $BiVO_4$ film.

The photocurrent shown in Figure 2.3 was measured in 0.1 M Na_2SO_4 solution (pH 7, 0.2 M sodium phosphates buffered) for water oxidation on the bulk film electrodes. The dramatically increased photocurrent of W-doped $BiVO_4$ with respect to undoped $BiVO_4$ is shown in Figure 2.3, which also agrees with our previous report.[7] The photocurrent of $BiVO_4$ for water oxidation increased from 0.01 mA cm^{-2} to 0.17 mA cm^{-2} at 0.6 V by W doping under UV-visible irradiation. However, the photocurrent further improved with the consecutive doping of Mo on W-doped $BiVO_4$. The obtained photocurrent for water oxidation of W/Mo-doped $BiVO_4$ is 0.23 mA cm^{-2} at 0.6 V, which is about 40 % higher than that of W-doped $BiVO_4$ under UV-visible irradiation (Figure 2.3(a)). The improvement of W/Mo-doped $BiVO_4$ compared with W-doped $BiVO_4$ is also observed under visible irradiation in Figure 2.3(b). In summary, the results using thin film electrodes confirm the results of the SECM experiments using the dispensed arrays.

Fill factors of the obtained current-potential curves in Figure 2.3 were found to compare the current-potential characteristic of W/Mo-doped $BiVO_4$ with that of W-doped

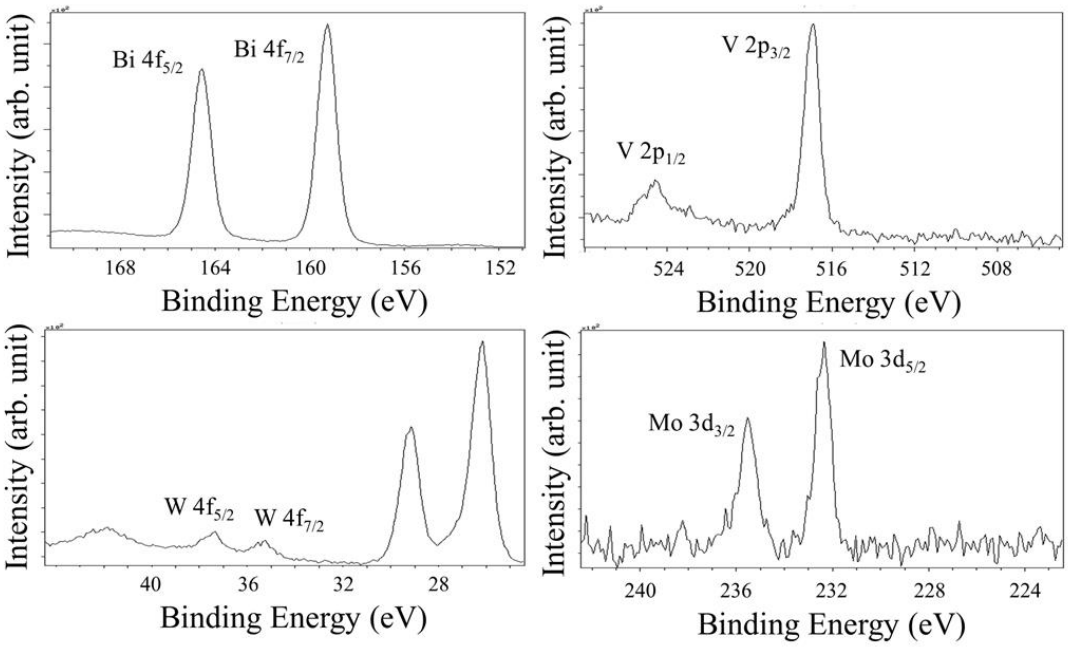

Figure 2.4. XPS of W/Mo-doped $BiVO_4$. The $BiVO_4$ film doped with 2 at% of W and 6 at% of Mo was prepared on the FTO substrate. The spectra were obtained from the film after about an hour of electrochemical experiment in 0.1 M Na_2SO_4 (pH 7, 0.2 M sodium phosphate buffered) and vigorously rinsed with D.I. water before XPS measurement.

Peak	Position BE (eV)	FWHM (eV)	Raw area (cps)	RSF	Atomic mass	Atomic conc.%	Mass conc.%
Bi 4f	159	0.932	37369	9.14	209	58	82
V 2p	517	0.875	5544	2.12	51	33	11
W 4f	37	0.863	493	3.52	184	2	3
Mo 3d	232	0.765	1548	3.32	96	6	4

Table 2.3. Atomic composition of W/Mo-doped $BiVO_4$ calculated based on XPS measurements.

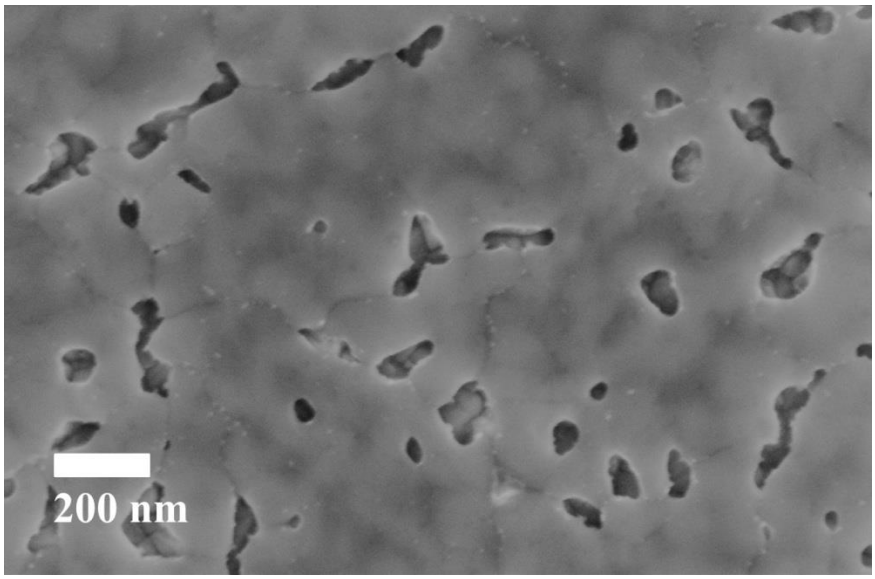

Figure 2.5. SEM image of W/Mo-doped $BiVO_4$ films which was drop casted on the FTO substrate.

$BiVO_4$. To calculate the fill factor, the power density measured from the bulk film, $P_{measured}$ in mW cm^{-2} at an electrode potential of E in V, and the optimum power density, $P_{optimum}$ in mW cm^{-2}, that is the theoretical maximum power density of the ideal electrode were defined by the following equations:

$$P_{measured} = (E\text{-}E_{open\ circuit})\ i_{photo} \quad (2\text{-}1)$$

$$P_{optimum} = (E_{short\ circuit}\text{-}E_{open\ circuit})\ i_{short\ circuit} \quad (2\text{-}2)$$

where $E_{open\ circuit}$ is the electrode potential where the photooxidation current starts to flow, i_{photo} in mA cm^{-2} is an anodic photocurrent at the electrode potential of E, $E_{short\ circuit}$ is the largest electrode potential which was applied in the experiment, and $i_{short\ circuit}$ in mA cm^{-2} is the photocurrent at $E_{short\ circuit}$. Then, the fill factor is calculated as:

$$\text{Fill factor} = P_{max} / P_{optimum} \quad (2\text{-}3)$$

where P_{max} is the maximum power density observed from the calculated $P_{measured}$. Then, the obtained fill factors are 0.17 for W/Mo-doped $BiVO_4$ and 0.12 for W-doped BiO_4 in Figure 2.3(a). In summary, the improved photoactivity of $BiVO_4$ by doping with W and Mo is shown as a better characteristic of the current-potential behavior. This indicates the facilitated photoelectrochemical reaction of the hole in the valence band with the species on the metal oxide electrode surface at the low overpotential region.

UV-visible absorption spectra of the thin film electrodes are shown in Figure 2.6. The thickness of the thin films used for the absorption measurements, measured by SEM from the cross-section images of the films on FTO substrate, was about 200 nm. The error bar shown in the absorption spectrum of W/Mo-doped $BiVO_4$ at a wavelength of 400 nm is the deviation of absorbance caused by thickness variations within the film

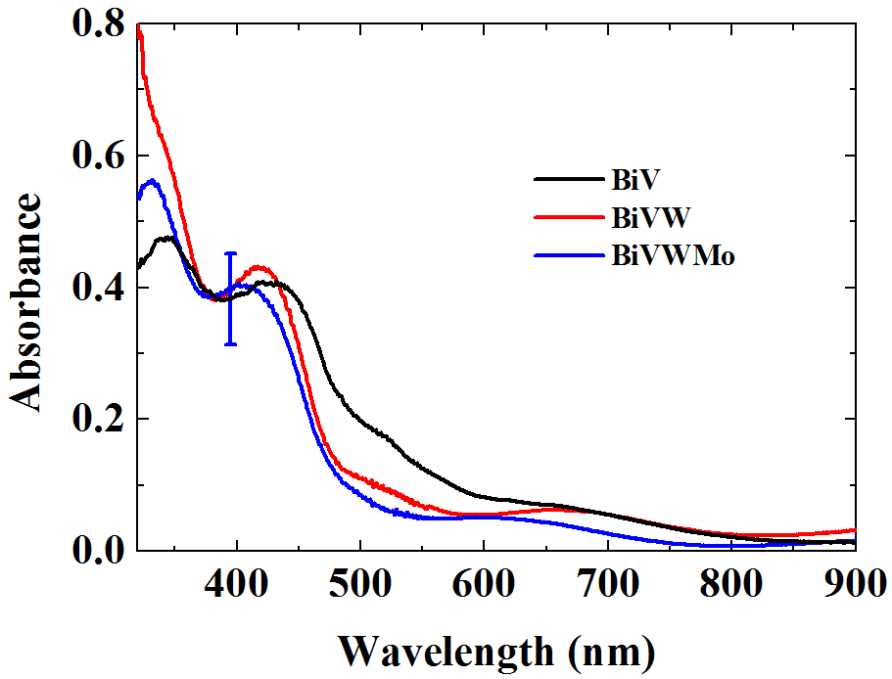

Figure 2.6. UV-visible absorption spectra obtained from undoped $BiVO_4$ (black), W-doped-$BiVO_4$ (red) and W/Mo doped-$BiVO_4$ (blue). The error bar noted at the wavelength of 400 nm for W/Mo-doped $BiVO_4$ was obtained from three different regions of the same sample to show the deviation of absorptivity by the non-uniformity of film thickness. The thickness of bulk films was around 200 nm for both electrode films.

prepared by drop casting on a FTO substrate. Within this variation, the absorption spectra of W-doped $BiVO_4$ and W/Mo-doped $BiVO_4$ do not show significant differences.

In addition, the ratio of the photocurrent under visible irradiation (> 420 nm) to that under UV-visible irradiation is similar for both W/Mo-doped $BiVO_4$ and W-doped BiO_4, ~ 0.4, (Figure 2.3). We thus conclude that the enhanced photoactivity of W/Mo-doped $BiVO_4$ compared with W-doped $BiVO_4$ does not originate from any difference in the light absorbance or optical properties, i.e. E_g.

IPCE measurements of W/Mo-doped $BiVO_4$ and W-doped $BiVO_4$ were also performed as shown in Figure 2.7. The photocurrents measured at 0.6 V under monochromatic irradiation were used to calculate the ratio of photogenerated power to the incidence irradiation power according to the following equation:

$$\text{IPCE (\%)} = (1240 / \lambda) \times i_{ph} / P_{in} \times 100 \qquad (2\text{-}4)$$

where λ is the wavelength of illuminated light in nm, i_{ph} is the measured photocurrent density in mA cm^{-2}, and P_{in} is the incident power density in mW cm^{-2}. To obtain the photooxidation current, linear sweep voltammetry (LSV) was performed with and without the light irradiation for each monochromatic wavelength and the current difference between two voltammograms at 0.6 V was taken as the photocurrent. The reported IPCE depends upon the nature of the reaction (i.e. water oxidation vs. sacrificial donor oxidation), the applied potential, the wavelength of the irradiation, and the thickness and absorbance of the photocatalyst film. In Figure 2.7 the potential used for the IPCE measurements is less than the thermodynamic potential for water oxidation, ~ 0.8 V, under the experimental conditions. The scan rate was 20 mV sec^{-1} and the

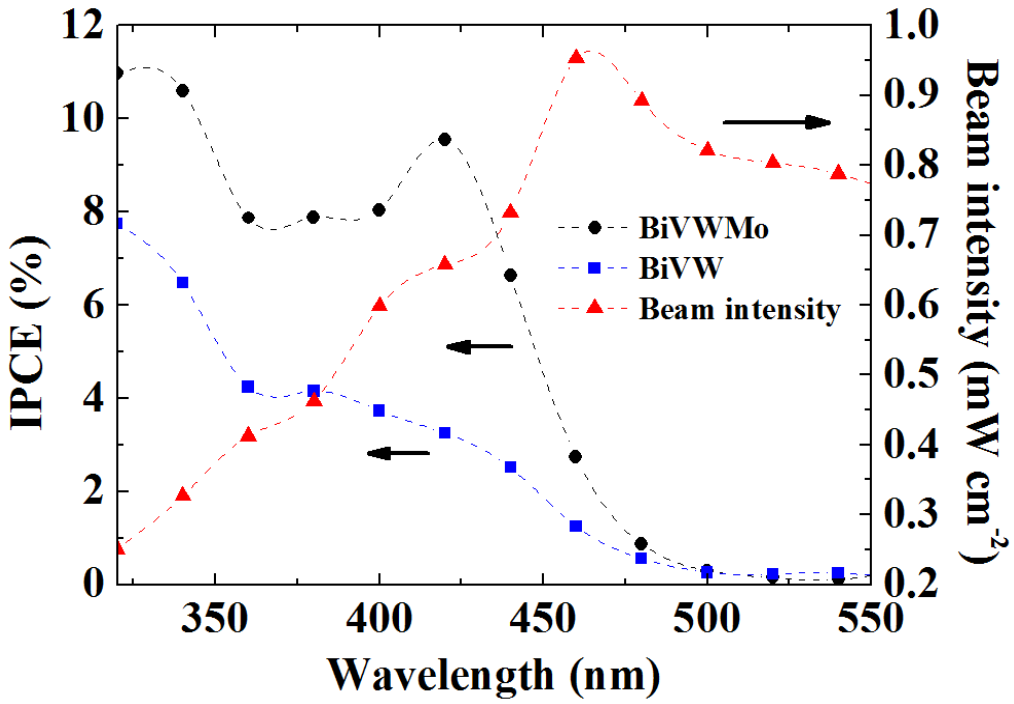

Figure 2.7. IPCE plots of W-doped $BiVO_4$ (blue) and W/Mo-doped $BiVO_4$ (black) film electrodes with a thickness of about 200 nm. The photocurrent measured at 0.6 V in 0.1 M Na_2SO_4 aqueous solution. The irradiation power at the corresponding illumination at the discrete wavelength used is indicated on the plot (red). The dashed lines are added for clarity.

potential was swept from 0.1 V to 0.65 V. In the IPCE spectrum, the photooxidation current starts to flow from about 500 nm, which indicates that both W/Mo-doped $BiVO_4$ and W-doped $BiVO_4$ have a band-gap size of 2.4 to 2.5 eV, which is similar to that of undoped $BiVO_4$. So, the enhanced photoactivity of W/Mo-doped $BiVO_4$ compared with W-doped $BiVO_4$ or undoped $BiVO_4$ is not raised from the modification of band-gap size. However, IPCE measurements still show the improved photoactivity of W/Mo-doped $BiVO_4$ over W-doped $BiVO_4$ under a low intensity monochromatic irradiation. In consideration of the similar absorbance and band-gap size, the enhanced water photooxidation of W/Mo-doped $BiVO_4$ electrode over W-doped $BiVO_4$ electrode is not from modified absorption properties by the consecutive doping of W and Mo in $BiVO_4$, but rather from a better separation of the excited hole and electron pair.

Capacitance measurements were conducted to obtain a Mott-Schottky plot (Figure 2.8). The flat band potential of semiconductor film in a liquid junction can be estimated from the Mott-Schottky equation:[21]

$$1/ C_{sc}^2 = (2/e\varepsilon\varepsilon_0 N_D) \quad (E\text{-}E_{fb}\text{-}kT/e) \qquad (2\text{-}5)$$

where C_{sc} is the space charge capacitance in F cm^{-2}, e is the electronic charge in C, ε is the dielectric constant of the semiconductor, ε_0 is the permittivity of free space, N_D is the carrier density in cm^{-3}, E is the applied potential in V, E_{fb} is the flat band potential in V, κ is the Boltzmann constant, and T represents the temperature in K. The temperature related term ($\kappa T/e$) in equation (2-5) is negligible, 0.0257, at room temperature. The flat band potential is obtained from the x-intercept of the tangent line of Mott-Schottky plot on potential axis.

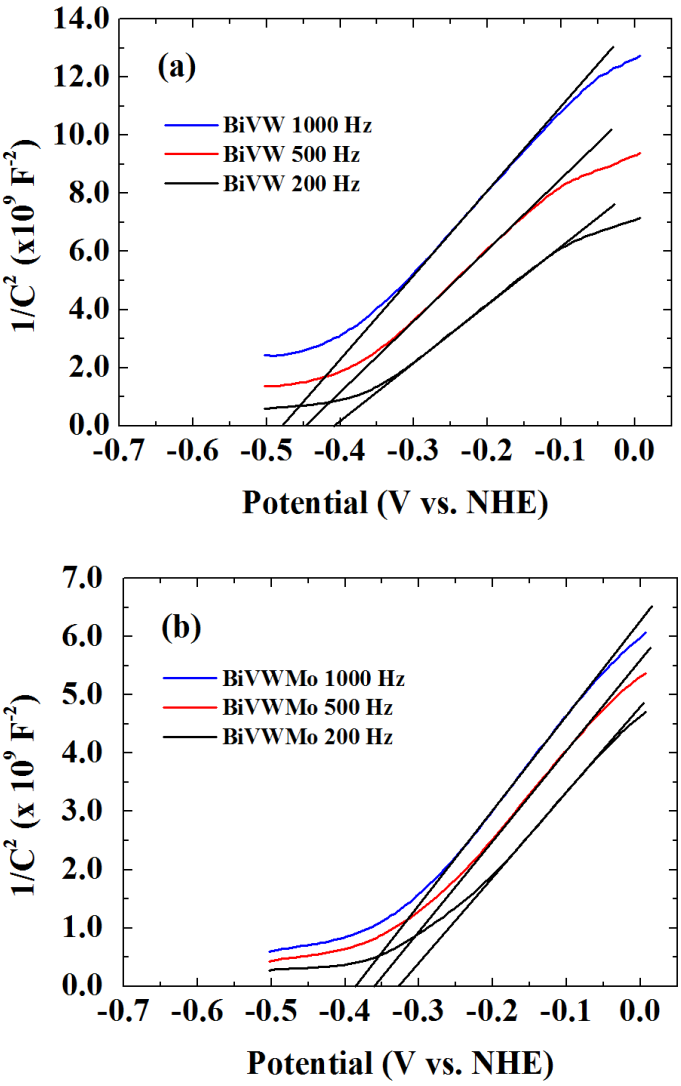

Figure 2.8. Mott-Schottky plots of (a) W-doped $BiVO_4$ and (b) W/Mo-doped $BiVO_4$ obtained from the capacitance measurements. AC amplitude of 10 mV was applied for each potential and three different AC frequencies were used for the measurements; 1000 Hz (blue), 500 Hz (red) and 200 Hz (black). Tangent lines of the M-S plots are drawn to obtain the flat band potential.

The flat band potential of W/Mo-doped $BiVO_4$ in 0.1 M Na_2SO_4 solution, from the results at a frequency of 1000 Hz, is about -0.4 V, which is about 0.1 V positive of that of W-doped $BiVO_4$. However, the flat band potential obtained from the Mott-Schottky plot shows a frequency dependency as shown in Figure 2.8. The non-converging frequency dependency of the Mott-Schottky plot might originate from nonideality of the surface of a drop cast semiconductor film on FTO for the capacitance measurement,[22] e.g. from the many grain boundaries of polycrystalline $BiVO_4$ and an inhomogeneous distribution of crystal sizes over the film surface. Although the carrier density (N_D) of the semiconductor can, in principle, also be calculated from the slope of Mott-Schottky plot, the quantitative analysis on the carrier density of the films was not performed because of the non-ideal behavior of Mott-Schottky plot as described above because of nonideality of the films, including different roughness factors between the samples and the effects of exposed FTO. However, the carrier density of W/Mo-doped $BiVO_4$ is about twice that of W-doped $BiVO_4$ as shown in the slope of the Mott-Schottky plots. In summary, W/Mo-doped $BiVO_4$ shows a positive shift of the flat band position of about 0.1 V compared with W-doped $BiVO_4$ and shows higher donor density than W-doped $BiVO_4$.

The photocatalytic activity of $BiVO_4$ is significantly affected by the crystal structure. For example, $BiVO_4$, with a monoclinic scheelite-like structure, shows several hundred times higher photocatalytic activity in aqueous $AgNO_3$ solution than the tetragonal scheelite structure $BiVO_4$. The band gap of tetragonal $BiVO_4$ is bigger than monoclinic $BiVO_4$, 2.9 eV vs. 2.5 eV, for the tetragonal and monoclinic $BiVO_4$,

respectively, but the reason for the significant differences in photoactivity for the different crystal structures has not been clearly elucidated. The structure of $BiVO_4$ is also deformed by adding W and Mo; this was studied using XRD analysis (Figure 2.9 and Figure 2.10). W-doped $BiVO_4$ and W/Mo-doped $BiVO_4$ show major peaks of the monoclinic scheelite-like $BiVO_4$ (PDF #14-0688) in Figure 2.9 and in a wider range of diffractograms in Figure 2.11. No noticeable peaks appeared from any secondary phases in the XRD patterns. Thus, the result from XRD measurements indicates that W and Mo can be dissolved at up to 8 at% as a solid solution in $BiVO_4$ without the formation of other secondary phases such as WO_x or MoO_x.

However, there is an observable shift of the XRD patterns by adding W and Mo to the monoclinic $BiVO_4$. The shift and merging of peaks are indicated by arrows at 34°, 47° and 59° in Figure 2.9. The peaks at 34.5° and 35.2° are indexed to the (2 0 0) and (0 0 2) lattices of the monoclinic scheelite-like $BiVO_4$ (Figure 2.9(iii)). By adding 5 at% W to $BiVO_4$, the two peaks closely shift towards each other and the two peaks finally merge into a single peak when 2 at% of W and 6 at% Mo are doped into $BiVO_4$. Similar behavior is also observed for the peaks at 46.7° and 47.9° which are indexed to the (2 4 0) and (0 4 2) lattices of the monoclinic scheelite-like $BiVO_4$. They first shift towards each other at low doping levels of W (Figure 2.9(ii)), then the peaks merge into a single peak with higher doping levels of W and Mo (Figure 2.9(i)). A small peak also appeared at 59.4° which is closely placed to the peak at 59.9° for undoped $BiVO_4$. The peak at 59.4° shifts towards and finally merges with the peak at 58.4° during consecutive doping of W and Mo into $BiVO_4$.

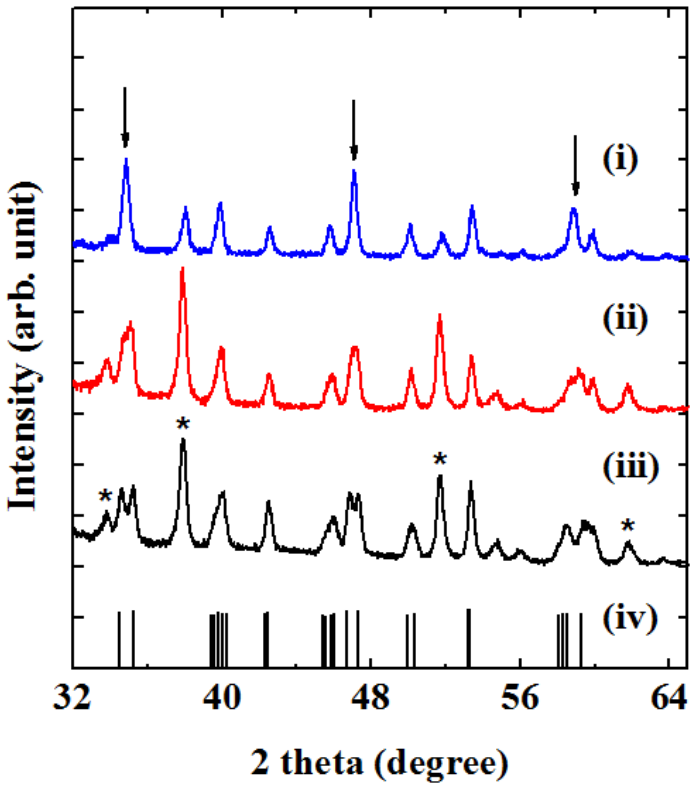

Figure 2.9. XRD patterns of (i) 2 at% W and 6 at% Mo-doped $BiVO_4$, (ii) 5 at% W-doped $BiVO_4$, and (iii) undoped $BiVO_4$. The reference patterns of the monoclinic scheelite-like $BiVO_4$ (iv, PDF #14-0688) and patterns from FTO substrate (*) are also indicated. Arrows indicate the shift of peaks as its atomic composition varied from pristine $BiVO_4$ to $BiVO_4$ doped by W and Mo.

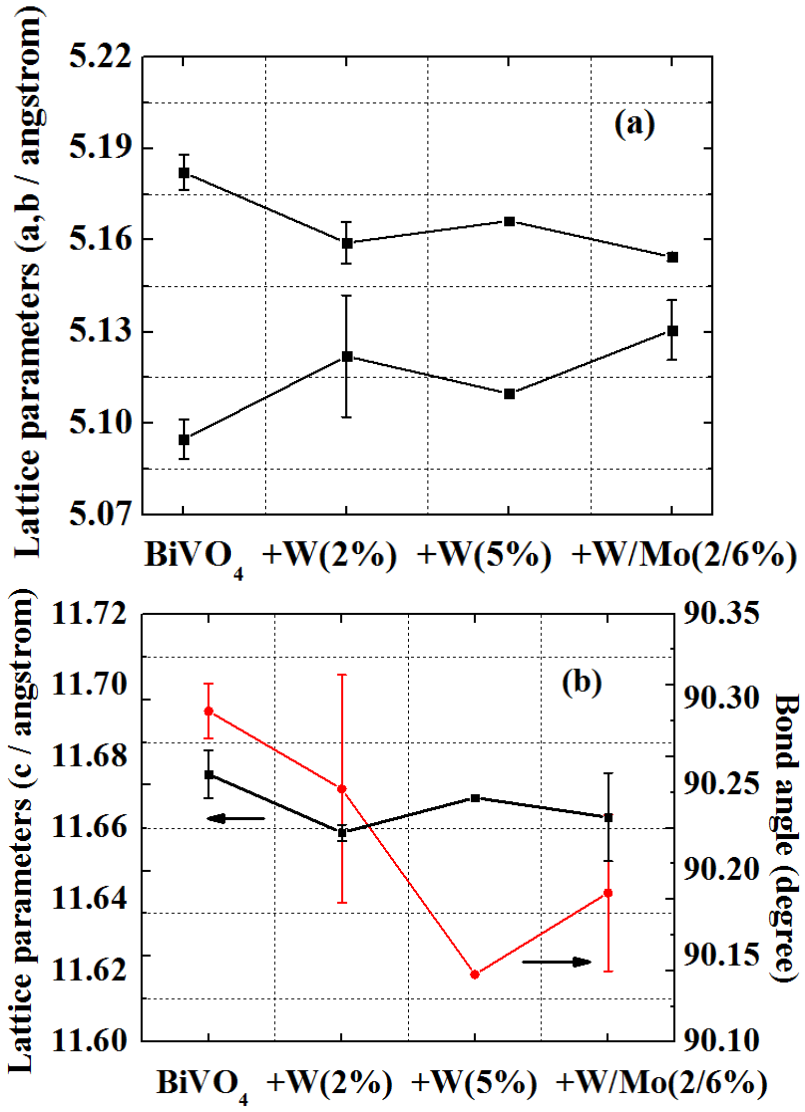

Figure 2.10. Lattice parameters estimated from Rietveld refinement of the XRD patterns which are shown in Figure 2.9. The refinement was performed by MAUD program for undoped $BiVO_4$, 2 at% W-doped $BiVO_4$, 5 at% W-doped $BiVO_4$, and 2 at% W and 6 at% Mo-doped $BiVO_4$.

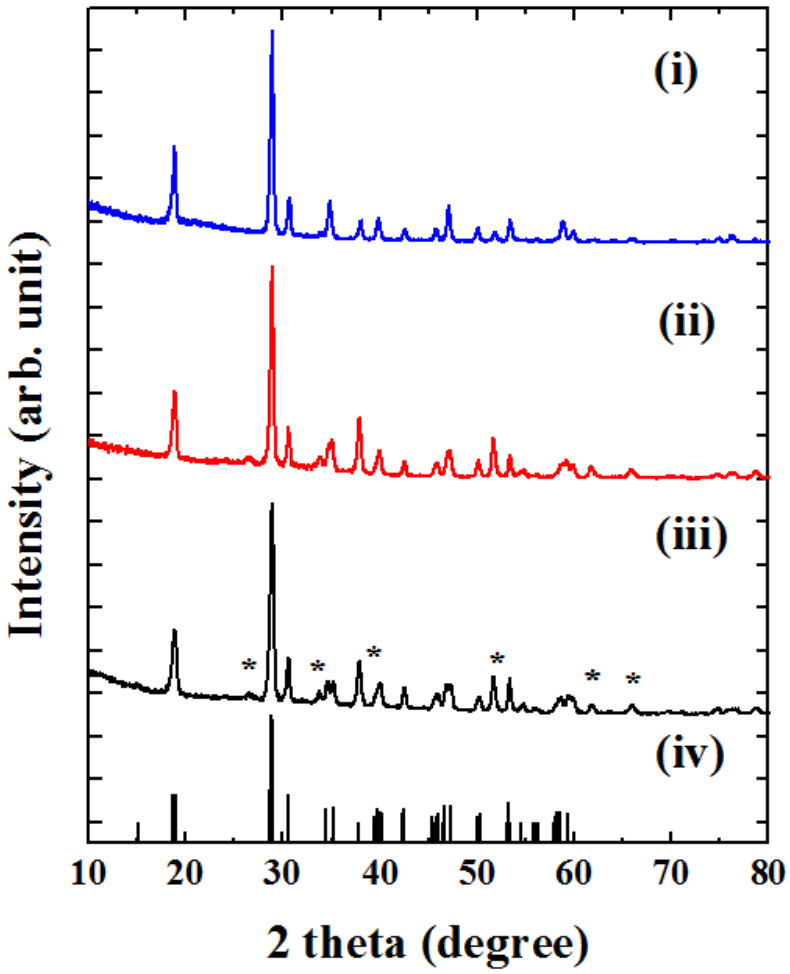

Figure 2.11. XRD patterns obtained from (i) W/Mo-doped $BiVO_4$, (ii) W-doped $BiVO_4$, and (iii) $BiVO_4$ without doping. The patterns shown here were obtained from more wide range of 2θ than that shown in Figure 2.9 to show the overall diffractograms of the bulk semiconductor films. The reference pattern of the monoclinic scheelite-like $BiVO_4$ (iv, PDF# 14-0688) and the peaks from FTO substrate (*) are also indicated in the diffractograms.

The Rietveld refinement of the XRD patterns reveals the deformation of the crystal structure of monoclinic scheelite-like $BiVO_4$ with doping of W and Mo (Figure 2.10). The results indicate that the cell dimensions and the crystal symmetry of $BiVO_4$ continuously change from monoclinic to tetragonal with doping of W and Mo. The structural deformation and the changes of crystal symmetry of $BiVO_4$ obtained in this study agree well with the results from Sleight et al. reported in 1975.[12] Sleight also suggested the formation of catalytically active defect vacancies on the crystal surface by doping of W or Mo into $BiVO_4$, but the analysis obtained here cannot determine the existence of vacancies on the surface of $BiVO_4$. The crystal deformation might be caused by a substitutional defect of V^{5+} ions being replaced by W^{6+} and Mo^{6+}, both of which have larger tetrahedral ionic radii than V^{5+} (tetrahedral ionic radii for V^{5+}, Mo^{6+} and W^{6+} are 0.35 Å, 0.41 Å, and 0.42 Å, respectively. [23] However, the relationship of the crystal deformation of $BiVO_4$ with the corresponding photoelectrochemical properties has not been clearly explained and further investigation is needed.

2.5 Conclusions

Metal doping of the metal oxide photoelectrocatalyst, $BiVO_4$, dramatically increases its activity for water oxidation. Scanning electrochemical microscopy (SECM) was used to screen various dopants for their photoelectrochemical performance and to optimize the used dopant material concentrations with this photocatalyst**.** For example adding Mo to W-doped $BiVO_4$ enhanced the performance. The photocatalytic activity was examined on larger electrodes by means of photoelectrochemical and

electrochemical measurements. The developed photoelectrocatalyst, W and Mo-doped $BiVO_4$, shows a photocurrent for water oxidation that is more than 10 times higher than undoped $BiVO_4$. XRD analysis confirms a solid solution of W/Mo-doped $BiVO_4$ without the formation of secondary phases. Distortion of the crystal structure of monoclinic scheelite-like $BiVO_4$ by addition of W and Mo is also revealed by X-ray diffraction and Rietveld refinement analysis. Capacitance measurements reveal a shift in the flat band position of W/Mo-doped $BiVO_4$ by Mo doping into W-doped $BiVO_4$. The results indicate that the consecutive doping of W and Mo into the metal oxide photocatalyst introduces improved electron-hole separation without a significant change of the band-gap or the materials optical properties. Also, the rapid screening method by SECM has been shown to be a tool to develop an active photocatalyst such as W/Mo-doped $BiVO_4$.

2.6 References

[1] Woodhouse, M.; Parkinson, B. A. *Chem. Soc. Rev.* **2009,** 38, 197-210.

[2] Baeck, S. H.; Jaramillo, T. F.; Brandli, C.; McFarland, E. W. *J. Comb. Chem.* **2002,** 4, 563-568.

[3] Lee, J.; Ye, H.; Pan, S.; Bard, A. J. *Anal. Chem.* **2008**, *80*, 7445-7450.

[4] Jang, J. S.; Lee, J.; Ye, H.; Fan, F.-R. F.; Bard, A. J. *J. Phys. Chem. C* **2009**, *113*, 6719-6724.

[5] Jang, J. S.; Yoon, K. Y.; Xiao, X.; Fan, F.-R. F.; Bard, A. J. *Chem. Mater.* **2009**, *21*, 4803-4810.

[6] Liu, W.; Ye, H.; Bard, A. J. *J. Phys. Chem. C* **2010**, *114*, 1201-1207.

[7] Ye, H.; Lee, J.; Jang, J. S.; Bard, A. J. *J. Phys. Chem. C* **2010**, *114*, 13322-13328.

[8] Liu, G.; Liu, C.; Bard, A. J. *J. Phys. Chem. C* **2010**, *114*, 20997-21002.

[9] Fujishima, A.; Honda, K. *Nature* **1972**, *238*, 37-38.

[10] Bard, A. J. *J. Am. Chem. Soc.* **2010**, *132*, 7559-7567.

[11] Yao, W.; Ye, J. *J. Phys. Chem. B* **2006**, *110*, 11188-11195.

[12] Sleight, A. W.; Aykan, K.; Rogers, D. B. *J. Solid State Chem.* **1975**, *13*, 231-236.

[13] Tokunaga, S.; Kato, H.; Kudo, A. *Chem. Mater.* **2001**, *13*, 4624-4628.

[14] Sayama, K.; Nomura, A.; Arai, T.; Sugita, T.; Abe, R.; Yanagida, M.; Oi, T.; Iwasaki, Y.; Abe, Y.; Sugihara, H. *J. Phys. Chem. B* **2006**, *110*, 11352-11360.

[15] Walsh, A.; Yan, Y.; Huda, M. N.; Al-Jassim, M. M.; Wei, S.-H. *Chem. Mater.* **2009**, *21*, 547-551.

[16] Myung, N.; Ham S.; Choi S.; Chae Y.; Kim, W.-G.; Jeon, Y. J.; Paeng, K.-J.; Chanmanee, W.; de Tacconi, N. R.; Rajeshwar K. *J. Phys. Chem. C* **2011,** 115, 7793-7800.

[17] Van de Krol, R.; Liang Y.; Schoonman J. *J. Mater. Chem.* **2008,** 18, 2311-2320.

[18] Kudo, A.; Omori, K.; Kato, H. *J. Am. Chem. Soc*. **1999**, *121*, 11459.

[19] Sayama, K.; Nomura, A.; Arai,T.; Sugita, T.; Abe, R.;Yanagida, M.; Oi, T.; Iwasaki, Y.; Abe, Y.; Sugihara, H. *J. Phys. Chem. B* **2006,** *110,* 11352-11360.

[20] Ferrari, M.; Lutterotti, L. *J. Appl. Phys.* **1994**, *76*, 7246-7255.

[21] Bard, A. J.; Faulkner, L. R. *Electrochemical Methods Fundamentals and Application*, 2nd ed.; John Wiley & Sons: New York, **2001**, pp 746-752.

[22] Cardon, F.; Gomes, W. P. *J. Phys. D: Appl. Phys.* **1978**, *11*, L63-L67.

[23] Corbel, G.; Laligant, Y.; Goutenoire, F.; Suard, E.; Lacorre, P. *Chem. Mater.* **2005**, *17*, 4678-4684.

Chapter 3. Interrogation of Reaction Intermediates at Photocatalyst Surface

3.1 Introduction

The oxygen evolution reactions (OER) in aqueous solution has been extensively studied at photo- or electro- catalysts.[1,2,3,4,5] The intermediate radicals produced during water oxidation, e.g. OH•, O•, or H_2O•, have been detected mostly at TiO_2 surfaces using spin trapping, electro spin resonance spectroscopy (ESR), fluorescence spectra, and infrared spectroscopy.[6,7,8] For example, the photogenerated OH• radicals at a Pt/TiO_2 surface were reported by the photocatalytic generation of salicylic acid from benzoic acid in acidic aqueous solution.[9] Other kinds of surface radicals, e.g. oxygen radical (O•) at a powdery TiO_2 surface, have also been investigated using multiple internal reflection infrared spectroscopy (MIR-IR)[10] and electron paramagnetic resonance spectroscopy (EPR)[11] during the OER under irradiation.

In photochemistry, the external quantum efficiency, EQE, (i.e. the ratio between the reaction products and the number of incident photons) and the internal quantum efficiency, IQE, (i.e. the ratio between the reaction products and the number of absorbed photons) are important figures to quantify the photoactivity and to analyze reaction mechanisms at the photocatalyst.[12,13] The quantum efficiency is a function of many different factors including illumination intensity, properties of the adsorbed species, the intrinsic properties of the semiconductor catalyst (e.g. electron/hole mobility, carrier lifetime, and doping density), and the reaction mechanisms of the redox couple in the solution.[14,15] For example, the EQE of OH• formation at powdery TiO_2 is less than 0.5

% as reported using spin trapping and EPR measurements.[16] Also, an IQE of approximately 30 % was obtained under very low intensity irradiation (~40 nW cm^{-2}) for organic decomposition through the formation of OH• at a TiO_2 film.[17] Recently, Zigah et al. reported the adsorbate coverage of OH• on TiO_2 nanotubes using the surface-interrogation mode of SECM (SI-SECM), but the quantum efficiencies were not calculated because the irradiated or absorbed number of photons at the electrode was not measured.[20] However, the amount of adsorbed OH• was reported to be 338 μC cm^{-2} for this nanostructured TiO_2.

Recently, SI-SECM has been introduced to study absorbed surface species on an electrode, e.g. a chemisorbed oxide layer on Au or Pt UME was titrated using $Ru(NH_3)_6^{2+/3+}$ and methylviologen redox couples.[18,19] Also, SI-SECM was able to interrogate hydroxyl radicals (OH•) adsorbed on an illuminated nanostructured TiO_2 film.[20] In that study, the adsorbed radicals were generated from the oxidation of chemisorbed hydroxide ions by photo-generated holes at the nanostructured TiO_2 surface. With varying the time for the decay reaction of the radicals, e.g. dimerization of OH• to hydrogen peroxide (H_2O_2), or its reaction with a radical scavenger (MeOH), a reversible $IrCl_6^{2-/3-}$ redox couple was then used to titrate the remaining OH• at the surface using the transient feedback mode of SECM, i.e. SI-SECM.

In this study, which builds on the SI-SECM mode demonstrated in the previous report,[20] we quantitatively study the water oxidation process at a W and Mo doped $BiVO_4$ (2 atomic % of W and 6 atomic % of Mo doped into $BiVO_4$, hereafter referred to as W/Mo-$BiVO_4$) electrode. $BiVO_4$ has been shown to be a promising n-type

photocatalyst since Kudo et al. reported its photocatalytic activities in 1999.[21] In addition, W and Mo have been found to be effective shallow donors of $BiVO_4$, and an increase in photocatalytic activity when $BiVO_4$ is doped with W or Mo has been reported for both water oxidation and organic degradation.[22,23,24,25,26] SECM was also used to find an optimal ratio of W/Mo-$BiVO_4$ by rapid combinatorial screening for photocatalytic water oxidation.[22,27]

As described above, most of the surface studies on photocatalysts have been performed on various TiO_2 systems, and to the best of our knowledge no studies have yet been reported for $BiVO_4$. Herein, we report the SI-SECM of the adsorbed radicals at W/Mo-$BiVO_4$ electrodes and provide quantitative figures for the water oxidation reactions. Consequently, the results show the analytic scheme of photon absorption and water oxidation processes at W/Mo-$BiVO_4$.

3.2 Experiments

$Bi(NO_3)_3 \cdot 5H_2O$ (99.999%), $(NH_4)_{10}H_2(W_2O_7)_6 \cdot xH_2O$ (99.99%) were purchased from Strem Chemicals (Newburyport, MA). VCl_3 (99%) and K_2IrCl_6 (99.95%) were purchased from Alfa-Aesar (Ward Hill, MA). $(NH_4)_6Mo_7O_{24} \cdot 4H_2O$ (99.98%), Na_2SO_4 (99.0 %), Na_2SO_3 (99.6 %), ferrocenemethanol (FcMeOH, 97%), PbO_2 (97%) were obtained from Sigma-Aldrich (St. Louis, MO). NaH_2PO_4 (99.5%), Na_2HPO_4 (99.9%), MeOH (99.9%) were purchased from Fisher Scientific (Pittsburg, PA). Deionized Milli-Q water (D.I. water, 18 MΩ-cm) was used as the solvent for electrochemical experiments.

Fluorine-doped tin oxide (FTO, TEC 15, Pilkington, Toledo, OH) was used as a photoanode substrate. The UME tip electrode consists of a Au wire (99.99 %, Goodfellow, Devon, PA) with a diameter of 50 μm coated by a borosilicate glass sheath. The tip was polished using alumina suspensions (0.3 and 0.05 μm diameter powder, Buehler, IL) on abrasive discs. W/Mo-$BiVO_4$ photoelectrodes were drop-casted onto the FTO substrate. Briefly, 2.2 mM $Bi(NO_3)_3{\cdot}5H_2O$, 2.5 mM VCl_3, 8 μM $(NH_4)_{10}H_2(W_2O_7)_6{\cdot}xH_2O$, and 43 μM $(NH_4)_6Mo_7O_{24}{\cdot}\ 4H_2O$ solutions in ethylene glycol were prepared. Then, 100 μL of the precursor solution was drop-casted on the FTO substrate (1.5 x 1.5 cm^2) and was annealed at 500 ℃ over 3h. Finally, expandable PTFE tape (maximum thickness of 88 μm, Fisher Scientific, Pittsburg, PA) was perforated using a needle (Easy touch, 31 gauge, 260 μm diameter) and the W/Mo-$BiVO_4$ electrode was covered by the perforated PTFE tape (Figure 3.3(c) and (d)). The depth and area of the exposed photoanode through the PTFE were measured using a Wyko NT9100 optical surface profiler (Veeco, New York). A Pt wire counter electrode and a saturated KCl Ag/AgCl reference electrode were used to complete the three electrode configuration. However, all potentials reported here are quoted versus the normal hydrogen electrode (NHE).

A scanning electrochemical microscope (SECM, Model 920C, CH Instruments, Austin, TX) was used as a potentiostat for the electrochemical experiments. For the SECM experiments, an ELH bulb (300 W, GE 38476, General Electric, Fairfield, CT) was used as a light source in the custom-built enclosure with a cooling fan. A custom-made electrochemical cell composed of Teflon was used to hold the three electrodes and

a light guide (3 mm diameter) underneath the photoelectrode. Schematic presentations of the experimental configuration are shown in Figure 3.1. A silicon photodetector (Model 818-UV) with an attenuator (OD3), and an optical power meter (Model 1830-C) purchased from Newport (Irvine, CA) were used to measure the irradiation intensities. A xenon lamp (XBO 150W, Osram, Munich, Germany) with full output was also used to provide the UV-Visible irradiation.

3.3 Calculation Methods

Electrochemical simulations were done using COMSOL Multiphysics v.3.5 software (Burlington, MA). The simulations domain and electrode configurations were set as shown in Figure 3.2. A constant flux of 1.75×10^{-5} mol/m^2·s of the product generated from the substrate was used to simulate the OER at the photoanode. The diffusion coefficient of oxygen, D_{O2}, was taken as 2×10^{-9} m^2/s in an aqueous solution. Fick's second law for axisymmetric diffusion was used to simulate the diffusion of oxygen generated at the photoanode in the solution.

$$dC(r,z,t)/dt = D_{O2} \times (d^2C(r,z,t)/dr^2 + 1/r \times dC(r,z,t)/dr + d^2C(r,z,t)/dz^2) \qquad (3\text{-}1)$$

The rate constant was assumed to be 0.1 m/s in the calculations. The tip potential bias was set at a potential negative of 0 V with the standard redox potential of 0.34 V. The large rate constant at a more negative potential at the tip was used to ensure the diffusion limited collection of oxygen at ring electrode. Simulations were done to study the TC/SG mode of SECM with various different distances between the tip and the substrate.

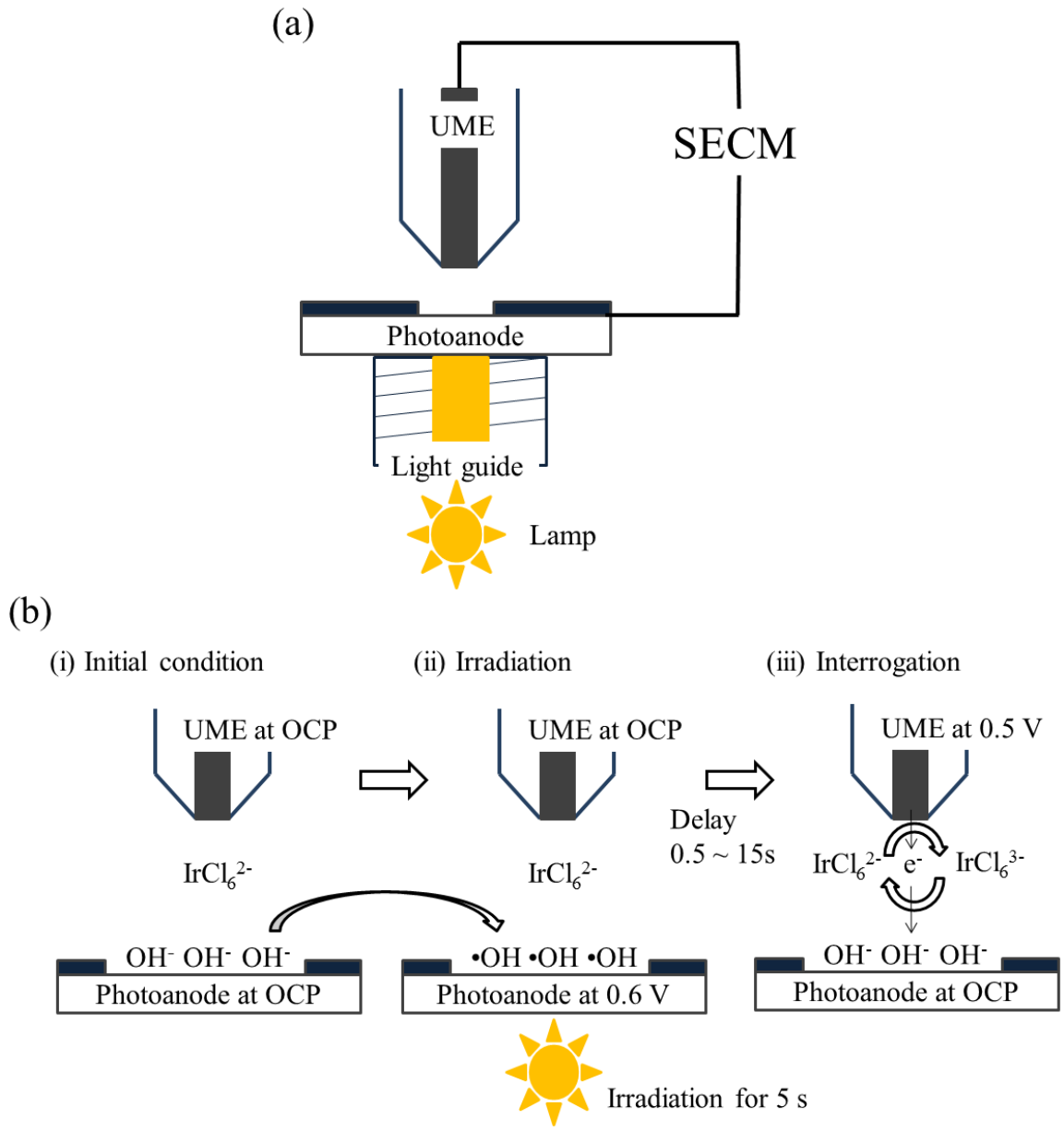

Figure 3.1. Schematic diagram of the experimental configurations of surface interrogation mode of SECM (a), and chemical reactions (b). The Au UME tip and W/Mo-$BiVO_4$ photoanode were allowed to rest at open circuit under dark at initial (b-i), then photon injection to generate hydroxyl radicals (OH•) at W/Mo-$BiVO_4$ (b-ii), followed by the titration using $IrCl_6^{2-/3-}$ couple under dark (b-iii).

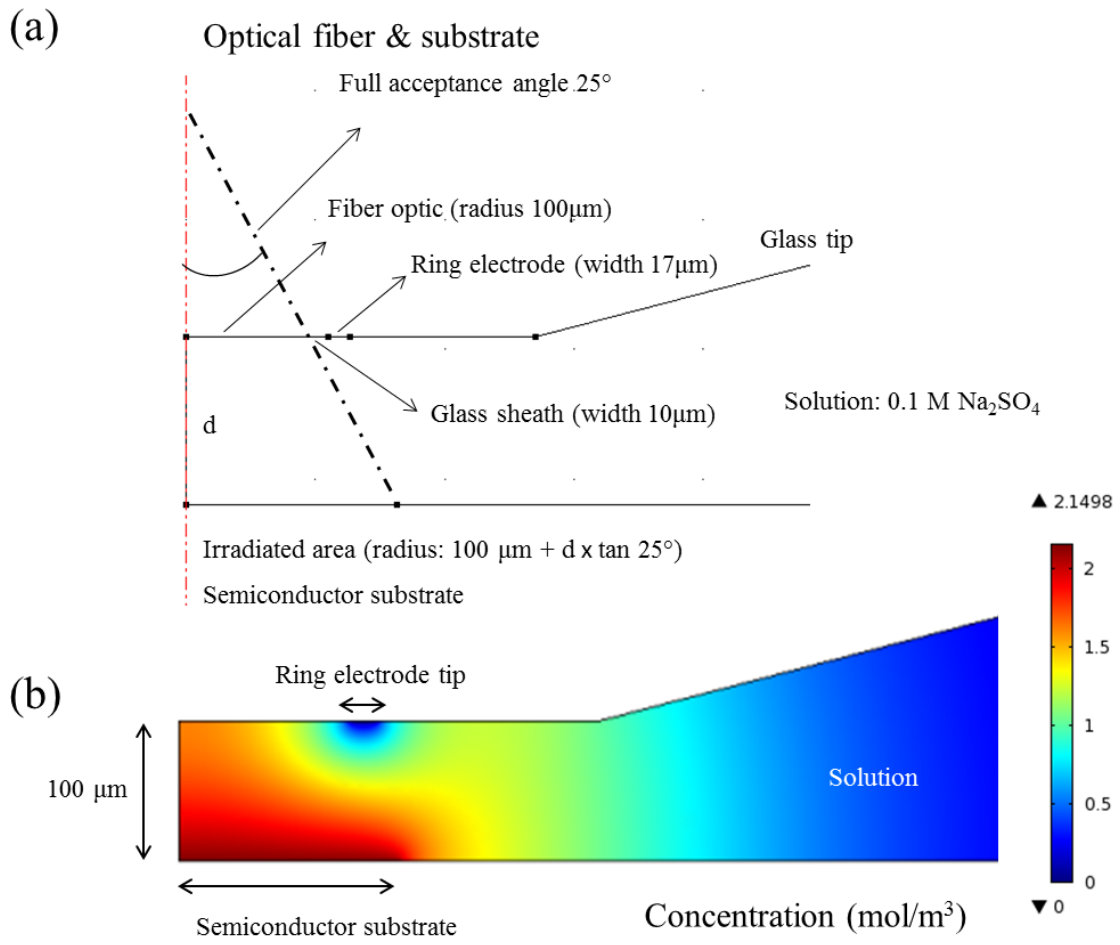

Figure 3.2. (a) Simulation domain of TC/SG mode of SECM for finite elements analysis and (b) the calculated concentration of solution species which are generated at the substrate (red) and are collected at the tip electrode (blue). The distance between the tip and the substrate was varied to calculate the collection efficiency of TC/SG mode of SECM.

The tip current was calculated from the concentration gradient of oxygen species at the tip surface.

$$di/dr = (2\pi nFD_{O2} \times r \times dc/dr) \quad (3\text{-}2)$$

where F is the Faraday constant, i is the tip current. Then, theoretical collection efficiency, η_{th}, i.e., the ratio of the tip (collection) current and the substrate (generation) current was calculated.

3.4 Quantification of Surface Radicals at W/Mo-$BiVO_4$

The exposed area of the W/Mo-$BiVO_4$ electrode and the thickness of the insulating layer around the W/Mo-$BiVO_4$ were measured before performing any electrochemical experiments to suitably place the tip UME above the photoanode and to quantify the results of the surface interrogation. Optical microscope images of the Au UME and the photoanode are shown in Figure 3.3. Also shown is an optical surface profile which was used to measure the exposed area of the photoanode, i.e. 3.9×10^{-4} cm^2, where the Teflon insulator covered most of the substrate (Figure 3.3(d)). The thickness of Teflon insulating tape around the exposed photoanode was measured to be about 20 μm.

Before performing the surface interrogation, the Au UME and the photoanode were aligned by measuring approach curves in 1 mM FcMeOH + 0.1 M KCl aqueous solution. Cyclic voltammograms (CV) of the Au UME in 1 mM FcMeOH showed typical steady state behavior for a 50 μm UME with fast outer-sphere reactions (Figure 3.4(a)). The diffusion limited oxidation current of FcMeOH was measured at the Au

UME, i_{Tip}, while the tip approached the insulating substrate using the stepper motor of the SECM (Figure 3.4(b), approach curve of SECM). In the approach mode of SECM, the Au UME was held at 0.7 V (vs NHE) as the tip moved toward the substrate with the increment distance of 1 μm per 0.2 s (or 5 μm s^{-1}). Because the flux of FcMeOH at the Au UME is limited by the very small tip-substrate distance, d, the oxidation current at the tip decreased as shown in Figure 3.4(b).[28] The approach curves were obtained at four different spots around the exposed W/Mo-$BiVO_4$ while the vertical level of the substrate was aligned on a level-adjustable SECM stage. Finally, the Au UME tip was placed close to the substrate where d was about 12μm with $i_{Tip}/i_{infinite} = 0.4$, where $i_{infinite}$ is the tip current measured far from the substrate.

After horizontally aligning the tip to the substrate, TC/SG-SECM was used to vertically place the UME above the exposed photoanode. To perform the TC/SG-SECM, the Au UME was placed at about 12 μm above the photoanode as discussed above. Then, the potential of the Au UME was set at 0.3 V in order to perform ferrocenium reduction (TC) and the potential of the W/Mo-$BiVO_4$ electrode was held at 0.4 V under the light irradiation to oxidize the ferrocene (SG). Figure 3.4(c) shows the scanning image obtained from TC/SG-SECM. The electrochemical image from SECM agrees well with the optical microscope image and the optical profile image as shown in Figure 3.3(c) and (d). Then, the Au UME was placed at the center of the W/Mo-$BiVO_4$ electrode as determined from the scanning image of TC/SG-SECM. The tip was moved down an additional 20 μm to compensate for the Teflon thickness which was measured

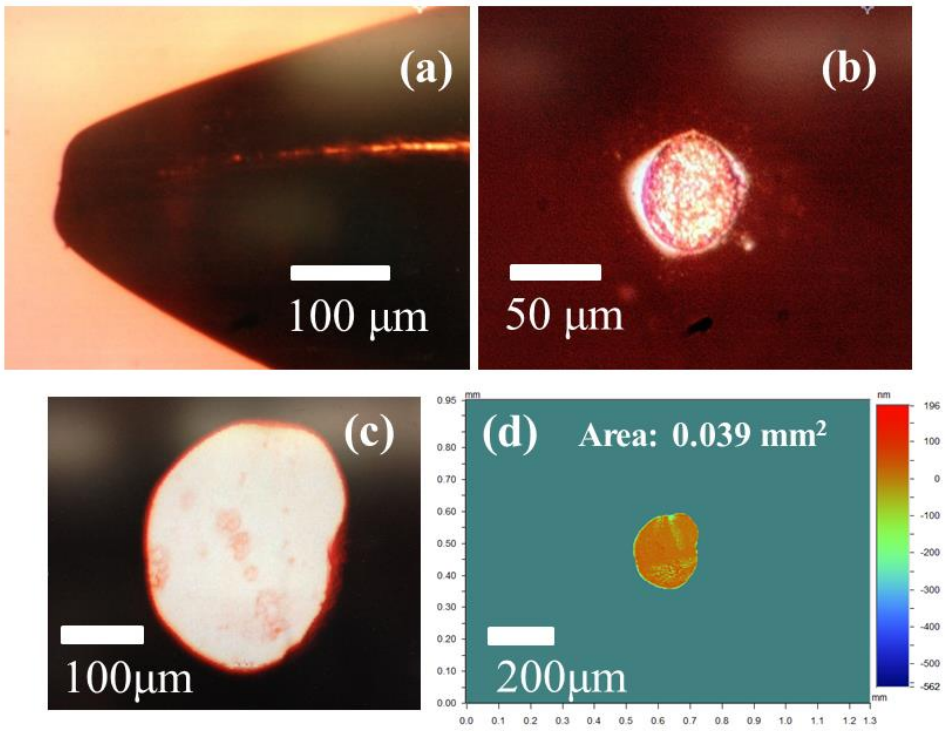

Figure 3.3. Optical microscopic images of Au UME from side (a) and top (b), and the image of the W/Mo-$BiVO_4$ photoanode covered by the insulating layer (c). Optical surface profiler images of the photoanode (d) that is identical W/Mo-$BiVO_4$ shown in (c). The optical profiler was used to measure the exposed area of the photoanode (0.039 mm^2) and to measure the thickness of the insulating Teflon layer on the photoanode (~ 20 μm).

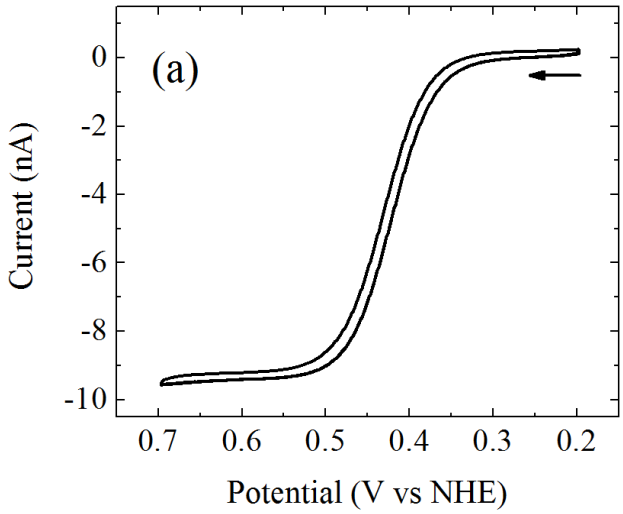
(a)
Current (nA)
0
-2
-4
-6
-8
-10
0.7
0.6
0.5
0.4
0.3
0.2
Potential (V vs NHE)

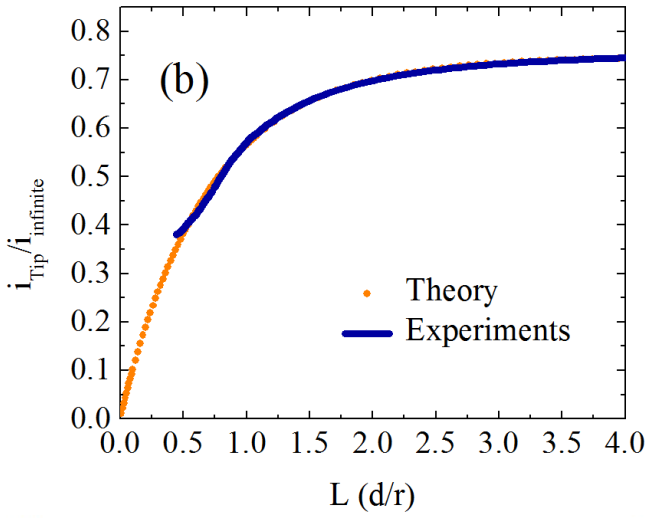
(b)
$i_{Tip}/i_{infinite}$
0.8
0.7
0.6
0.5
0.4
0.3
0.2
0.1
0.0
0.0
0.5
1.0
1.5
2.0
2.5
3.0
3.5
4.0
L (d/r)
Theory
Experiments

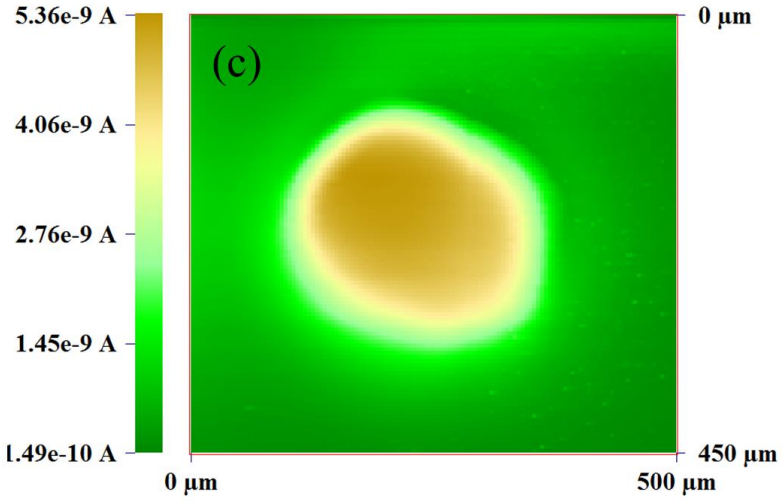
(c)
5.36e-9 A
4.06e-9 A
2.76e-9 A
1.45e-9 A
1.49e-10 A
0 µm
450 µm
0 µm
500 µm

Figure 3.4. Cyclic voltammogram (CV) (a), approach curve (b, blue solid line) of Au UME, and SECM image of tip collection-substrate generation (TC-SG) experiments on W/Mo-$BiVO_4$ (c) in a 1 mM ferrocenemethanol (FcMeOH) and 0.1 M KCl aqueous solution. CV was measured at bulk solution with scan rate of 20 mV s^{-1} in (a). For the approach curve in (b), Tip moved toward the insulating substrate with the increment distance of 1 μm per 0.2 s. The tip potential was 0.7 V (vs NHE). The theoretical curve (yellow dot) in (b) was obtained with R_g=2.[1] d is the distance between the tip and the substrate, and r is the radius of the tip, i.e. 25 μm. For TC/SG-SECM in (c), tip potential was held at 0.3 V and the substrate was at 0.4 V under UV-visible irradiation. Scan rate was 20 μm s^{-1} with the increment distance of 4 μm and the increment time was 0.2 s. The tip was placed about 12 μm above the substrate. ([1]Sun, P.; Laforge, F. O.; Mirkin, M. V. *Phys. Chem. Chem. Phys.* **2007,** *9,* 802–823.

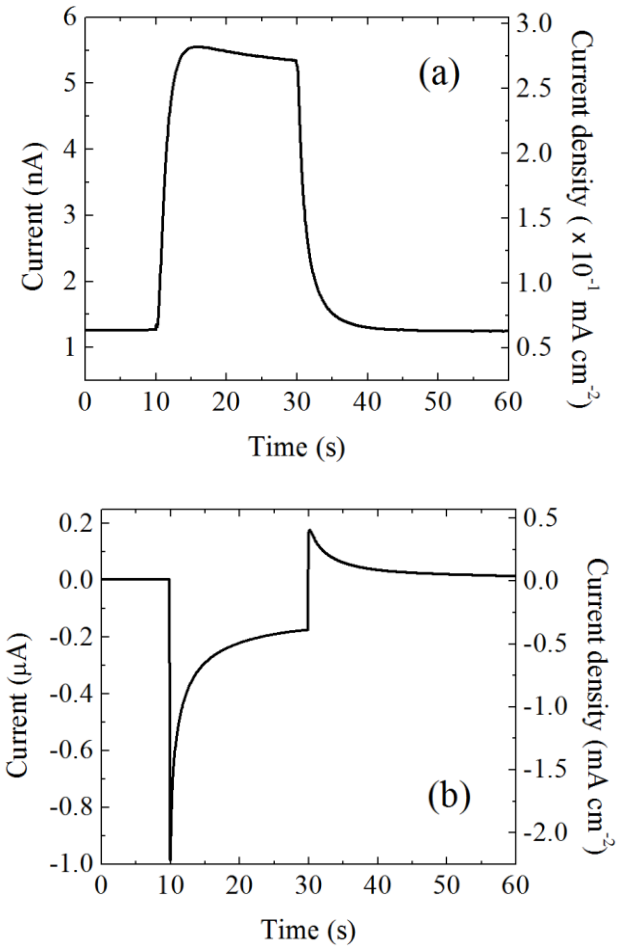

Figure 3.5. Tip collection current at Au UME (a) and substrate generation current at W/Mo-$BiVO_4$ (b) in a 1 mM FcMeOH and 0.1 M KCl aqueous solution. UV-visible irradiation was done from 10 to 30 s in the electrode configuration as shown in Figure 3.1(a). The potential of Au UME was 0.3 V (vs NHE) and W/Mo-$BiVO_4$ was held at 0.4 V. Au UME was placed about 12 μm above the substrate. Electrode area of the Au UME and the W/Mo-$BiVO_4$ electrode was 2.0 x 10^{-5} cm^2 and 4.6 x 10^{-4} cm^2, respectively.

by the optical profiler in Figure 3.3(d). Finally, the Au UME and W/Mo-$BiVO_4$ were properly aligned to perform the surface interrogation.

Before performing the surface interrogation experiment with the $IrCl_6^{2-/3-}$ redox couple, the collection efficiency, i.e. the ratio of the tip current and the substrate current, using the ferrocene/ferrocenium redox couple was measured for each electrode configuration. The current density for the ferrocenium reduction at the Au UME was 0.22 mA cm^{-2} and the photocurrent density for the ferrocene oxidation was 0.38 mA cm^{-2} at W/Mo-$BiVO_4$ under the irradiation at t=30 s (Figure 3.5(b)). Consequently, the measured collection efficiency was 57 %.

After the Au UME and the W/Mo-$BiVO_4$ electrodes were positioned as described above, the solution was changed to a 1 mM K_2IrCl_6 and 0.1 M Na_2SO_4 solution (pH 4.5) to perform the surface interrogation. Figure 3.1(b) shows a schematic of the experimental configurations with the corresponding chemical reactions for the SI-SECM used for these measurements. As stated above, the distance between Au UME and W/Mo-$BiVO_4$ was about 12 μm.

An $IrCl_6^{2-/3-}$ redox couple was used as the titrant because it has several favorable properties. First, the $IrCl_6^{2-/3-}$ redox couple has a fast reversible one-electron transfer reaction, thus its kinetics of undergoing oxidation and reduction are negligible. Second, it is stable in the chemical environments used in these experiments and does not react with O_2 (the byproduct at the photoanode). Finally, there are no side-reactions at the tip electrode, e.g. O_2 reduction, at the potential used for the interrogation (tip potential of 0.5 V, Figure 3.6).

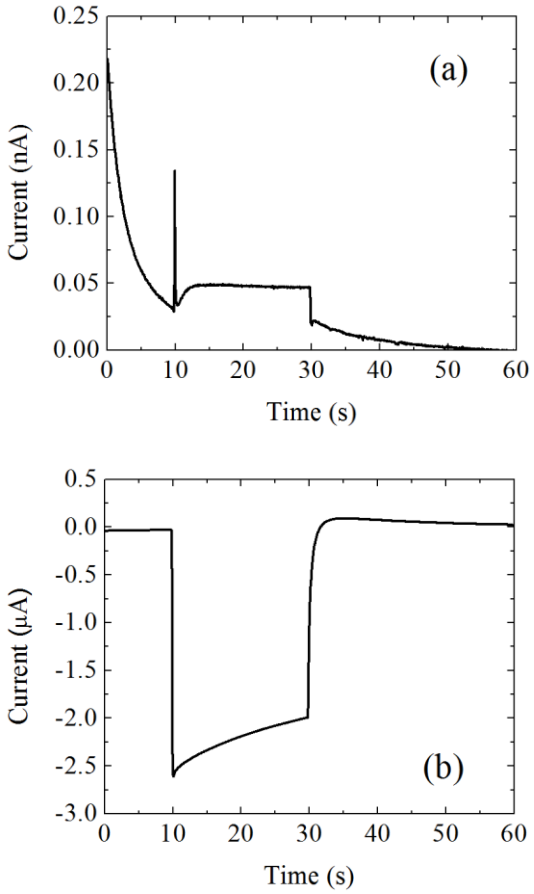

Figure 3.6. Tip collection for oxygen reduction at Au UME (a) and substrate generation for water oxidation at W/Mo-$BiVO_4$ (b) in 0.1 M Na_2SO_4 aqueous solution (0.2 M phosphate buffer, pH 7). The potential of tip was at 0.5 V (vs NHE) and W/Mo-$BiVO_4$ was held at 0.6 V. The irradiation was switched on from 10 to 30 s with an ELH lamp (300 W) through the light guide (diameter of 3 mm) in the experimental configurations shown in Figure 3.1. Au UME tip with a diameter of 50 μm was used and the area of W/Mo-doped $BiVO_4$ was larger than that used in Figure 3.5 to increase the generation current.

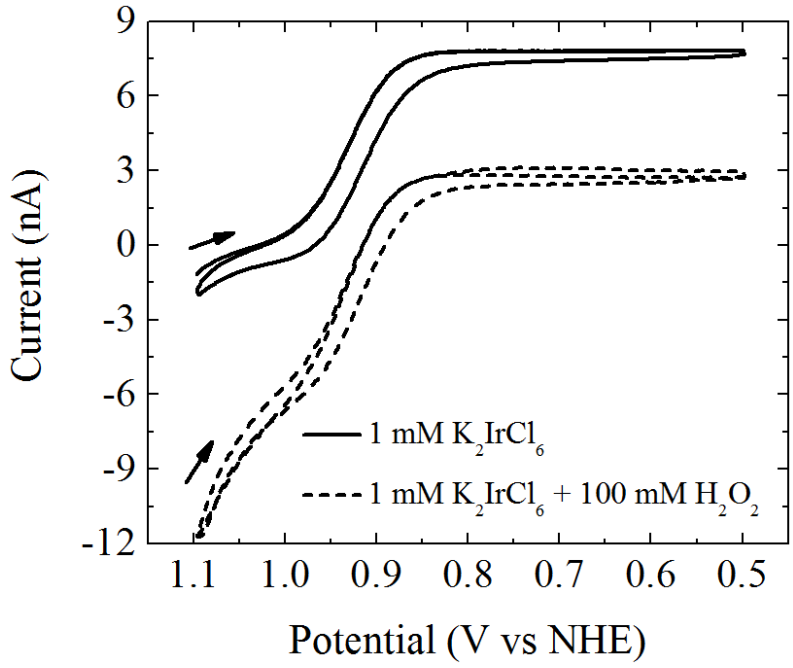

Figure 3.7. Cyclic voltammogram at Au UME tip in 1 mM K_2IrCl_6 and 0.1 M Na_2SO_4 aqueous solution (solid line) and that in the presence of 0.1 M H_2O_2 (dashed line). Scan rate was 20 mV s^{-1}.

A CV at the Au UME in the bulk solution away from the substrate shows a reduction current of $IrCl_6^{2-}$(reaction (3-3), Figure 3.7) and no other redox reactions were observed as stated above.

$$IrCl_6^{2-} + e \leftrightarrow IrCl_6^{3-} \qquad (E^0 = 0.87 \text{ V vs NHE}) \qquad (3\text{-}3)$$

For SI-SECM, OH• were generated by the photogenerated holes at W/Mo-$BiVO_4$ under irradiation.

$$W/Mo\text{-}BiVO_4 + h\nu \rightarrow e^- + h^+ \qquad (3\text{-}4)$$

$$OH^- + h^+ \rightarrow OH\bullet \qquad (E^0 = 1.8 \text{ V vs NHE, at pH 4.5}) \qquad (3\text{-}5)$$

Stable adsorbed OH^- have been previously studied using infrared spectroscopy at a photoanode, e.g. anatase TiO_2,[29,30] and the surface OH• produced from reaction (3-5) have been considered to be the primary intermediates for the photooxidation reactions in aqueous solutions at a TiO_2 surface.[31] For $BiVO_4$, non-dissociative adsorption of water molecules at a Bi-site of $BiVO_4$ has been suggested from first-principle calculations.[32] However, no experimental observations of surface adsorbed ions or water molecules in aqueous solutions at a $BiVO_4$ electrode have, to the best of our knowledge, been previously reported. Herein, the OH• is assumed to be the dominant intermediate of water oxidation from the photogenerated holes, but the nature of its surface reactions still needs to be examined.

Next, $IrCl_6^{3-}$ was electrochemically produced at the Au UME according to reaction (3-3) at a tip potential of 0.5 V. Consequently reactive OH• at W/Mo-$BiVO_4$ were titrated by the generated $IrCl_6^{3-}$ at the tip, which diffused from the tip to the substrate in a few tens of ms.

$IrCl_6^{3-} + OH\bullet \rightarrow IrCl_6^{2-} + OH^-$ (3-6)

In the presence of the OH• at W/Mo- $BiVO_4$, the chemically produced $IrCl_6^{2-}$ by reaction (3-6) at the substrate diffused back to the tip which increases the reduction current of electrochemical reaction (3-4) because of the increased diffusive flux of $IrCl_6^{2-}$ to the tip (positive feedback). As the OH• is consumed by reaction (3-6), the diffusive flux of $IrCl_6^{2-}$ to the tip is also reduced. Thus the tip current decreases because of the absence of the OH• at W/Mo-$BiVO_4$. For example, Figure 3.8 shows the chronoamperograms (CAs) of $IrCl_6^{2-}$ reduction at a Au UME with/without the adsorbed OH• on W/Mo-$BiVO_4$; the yellow line is the CA in the presence of the generated adsorbates, and the grey line is without the adsorbed OH•. Consequently the current difference between two CAs indicates the amount of adsorbed radicals at the photoanode. However, if time is allowed between the radical generation and the interrogation ("Delay" in Figure 3.1(b)), decay of the surface OH• can occur by (a) H_2O_2 generation from the dimerization of OH•, (b) free radical generation by desorption of the surface OH• to the bulk solution which can further react to form H_2O_2, and (c) if there are trapped electrons at the surface, reduction of the OH• back to OH^-, i.e. surface recombination..

$2OH\bullet \rightarrow H_2O_2$ (rate constant, k) (3-7)

OH• (adsorbed) → OH• (solution) (3-8)

$OH\bullet \text{ (adsorbed)} + e^- \rightarrow OH^-$ (3-9)

Small amounts of H_2O_2 can be produced at W/Mo-$BiVO_4$ during the OH• generation. However, if there is excess H_2O_2 in the solution, it may decrease the

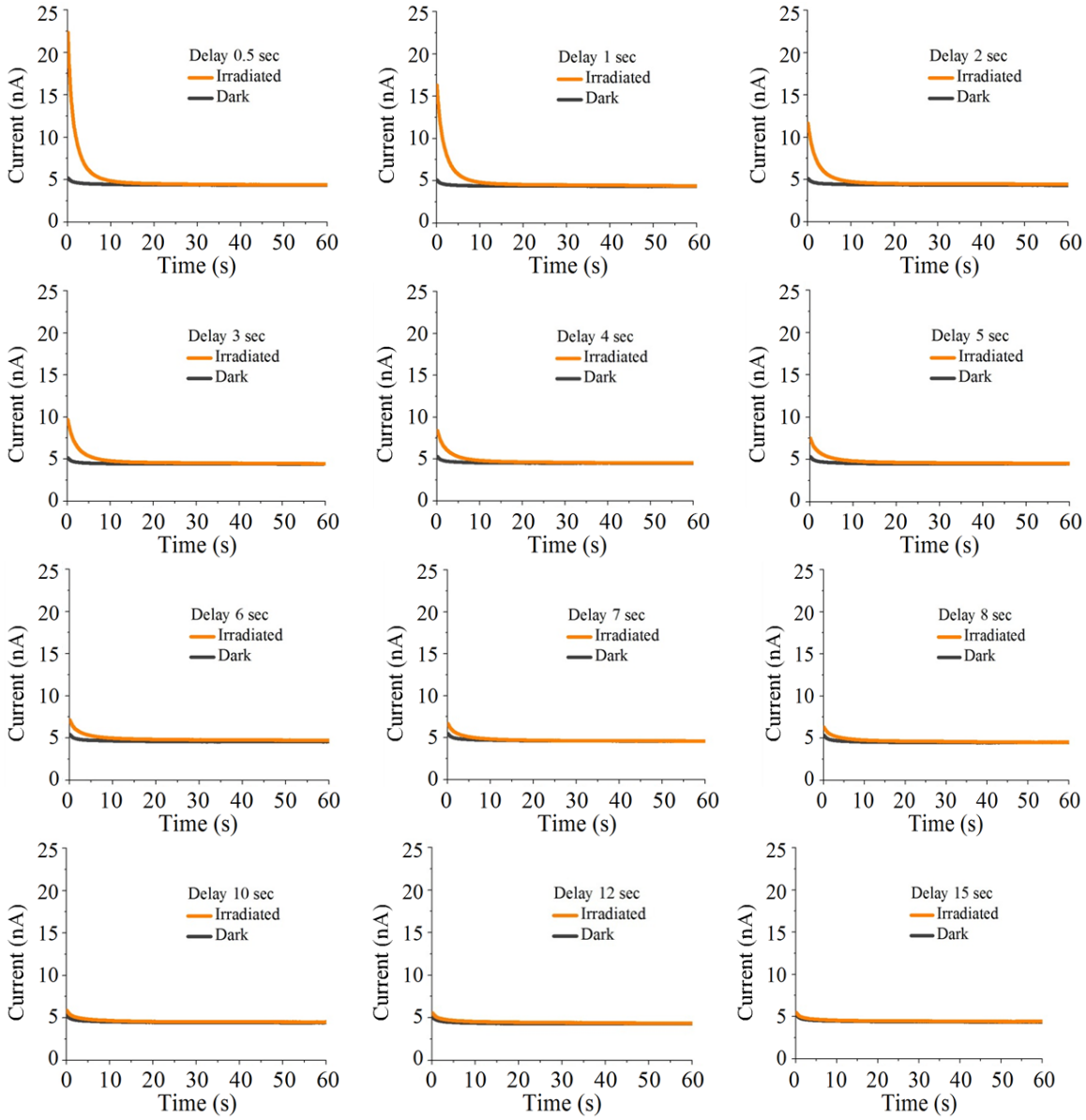

Figure 3.8. Chronoamperograms (CAs) of surface interrogation using Au UME on the W/Mo-$BiVO_4$ electrode with different decay time from 0.5 s to 15 s after UV-Visible irradiation for 5 s (yellow). CA of that without the irradiation is shown as grey solid line. The potential of Au UME was 0.5 V (vs NHE) and the W/Mo-$BiVO_4$ was held at 0.6 V during the irradiation. The potential and experimental configurations for the

measurements were set as shown in Figure 3.1. Measurements were done in 1 mM K_2IrCl_6 and 0.1 M Na_2SO_4 aqueous solution. Au UME was placed about 12 μm above W/Mo-$BiVO_4$.

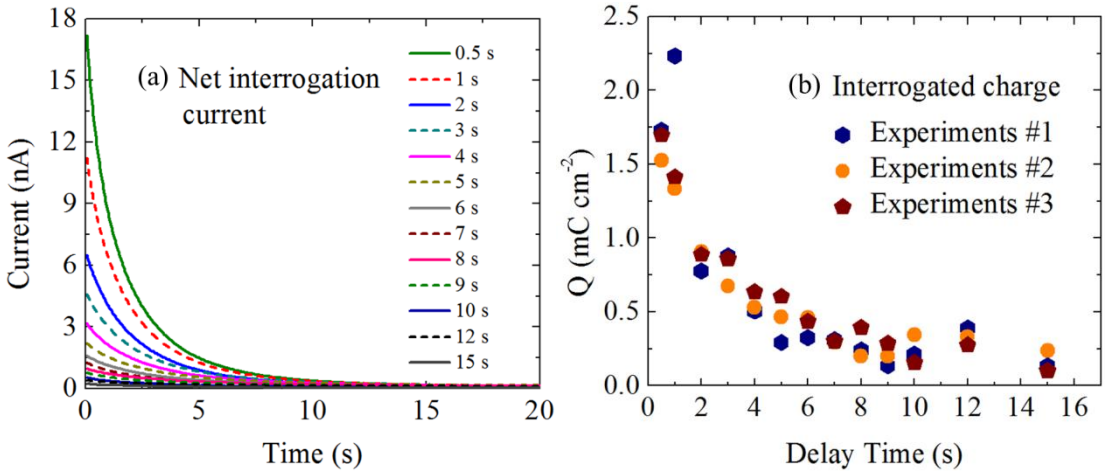

Figure 3.9. From the CAs, the net interrogation current, i.e. current difference of CAs with/without the irradiation, was calculated in (a) with various decay time from 0.5 to 15 s. Then, the charge densities from repeated interrogation measurements were calculated in (b). The potential of Au UME was 0.5 V (vs NHE) and the W/Mo-$BiVO_4$ was held at 0.6 V during the irradiation. The potential and experimental configurations for the measurements were set as shown in Figure 3.1. Measurements were done in 1 mM K_2IrCl_6 and 0.1 M Na_2SO_4 aqueous solution. Au UME was placed about 12 μm above W/Mo-$BiVO_4$.

interrogation current at the tip by chemical reaction (3-10) competing with electrochemical reduction reaction (3-3) at the tip.

$$H_2O_2 + 2IrCl_6^{2-} \rightarrow 2H^+ + O_2 + 2IrCl_6^{3-} \quad (3\text{-}10)$$

CV in the presence of excess H_2O_2 (100 mM) in the solution showed that homogeneous chemical reduction of $IrCl_6^{2-}$ to $IrCl_6^{3-}$ can occur in solution as shown in Figure 3.7 (dotted line). Also, if desorbed OH• exist between the tip and the photoanode, the interrogation current overestimates the amount of adsorbed OH• because reaction (3-6) can occur in solution.

However, homogeneous reaction (3-10) is slow in contrast to the fast oxidation of $IrCl_6^{3-}$ with the energetic OH• in reaction (3-6).[20] Also, the tip response changed in CV because reaction (3-10) was only observed in the presence of excess H_2O_2 (100 mM), and the possible H_2O_2 generation at W/Mo-$BiVO_4$ was only on the order of picomoles at the surface., The amount of desorbed OH• in solution was considered negligible compared to that of adsorbed OH• at TiO_2.[31] Herein, the degree of surface recombination was also minimized by applying a positive bias to W/Mo-$BiVO_4$, i.e. 0.6 V vs NHE which is about 0.8 eV of band bending based on the flat band potential of W/Mo-$BiVO_4$,[22] to have a facile removal of the excited-electron from the electrode surface and to minimize the electron-trapping at the surface. Then, surface reactions (3-6) and (3-7) can be assumed to be the dominant processes for the generation and consumption of OH•. Then, the amount of adsorbed OH• at the photoanode and the kinetic constant of OH• dimerization can be obtained as shown below.

$$dC_{OH\bullet}/dt = - k \times C_{\bullet OH}^2 \quad (3\text{-}11)$$

$$dC_{OH\bullet}/C_{\bullet OH}^{2} = - k \times dt \quad (3\text{-}12)$$

$$1/C_{OH\bullet} = kt + 1/C_0 \quad (3\text{-}13)$$

where k is the rate constant of dimerization reaction (3-7); t is the decay time allowed for the dimerization; $C_{OH\bullet}$ is the surface concentration of adsorbed OH• at the photoanode at t; and C_0 is the surface coverage of OH• at t=0. Therefore, if $C_{OH\bullet}$ is measured with different decay times using SI-SECM, k and C_0 can be obtained from the slope and y-intercept of equation (3-13).

In order to measure $C_{OH\bullet}$, SI-SECM was done with various decay times from 0.5 to 15 s (Figure 3.8). As longer decay time was allowed, the net interrogated current, i.e. the difference between CAs measured with/without the irradiation, decreased as expected since more adsorbates disappeared with increased time allowed. The resulting net interrogation currents are summarized in Figure 3.9(a). Then, the values of $C_{OH\bullet}$ at different times were obtained by integrating the net interrogation current as shown in Figure 3.9(b). The integration of the net current was calculated for experimental times of CAs ranging from 0 to 20 s in Figure 3.9(a).

In order to obtain k and C_0, a reciprocal plot of $C_{OH\bullet}$ with different decay times is shown in Figure 3.10 (equation (3-13)). The slope of the plot, i.e. the kinetic rate constant of OH• dimerization, was obtained as 0.4 mC^{-1} cm^2 s^{-1} or 4 x 10^3 mol^{-1} m^2 s^{-1} and the *y*-intercept of the plot was 3.3 mC cm^{-2}. When the collection efficiency of the TC/SG-SECM is considered, i.e. 57 % as calculated in Figure 3.5, the surface coverage of the adsorbed OH• was 5.8 mC cm^{-2} (or 60 nmol cm^{-2}) at W/Mo-$BiVO_4$. The obtained coverage is about 20 times larger than that previously obtained from the nanotube TiO_2,

i.e. 338 μC cm^{-2}, under low intensity irradiation by using SI-SECM.[20] Rather, the value obtained is within the range of that measured at TiO_2 thin films with adsorbed alcohols or dye.[33] More discussion on the surface OH• is shown below.

SI-SECM was further demonstrated to study the reaction of OH• with an electron donor, e.g. MeOH.[34]

$$OH\bullet + CH_3OH \rightarrow H_2O + CH_2\bullet OH \text{ (rate constant, } k_M) \quad (3\text{-}14)$$

$$2CH_2\bullet OH + O_2 \rightarrow CH_2O + CH_3OH + \text{Product} \quad (3\text{-}15)$$

As discussed above for the dimerization of OH•, the rate constant of reaction (3-14), k_M, and the surface coverage of OH• at W/Mo-$BiOV_4$ in the presence of a hole scavenger can be obtained using SI-SECM. Reaction (3-14) can be considered as a pseudo-first order reaction with excess MeOH. Then,

$$dC_{OH\bullet}/dt = - k_M \times C_{OH\bullet} \quad (3\text{-}16)$$

$$dC_{OH\bullet}/C_{OH\bullet} = - k_M \times dt \quad (3\text{-}17)$$

$$\ln C_{OH\bullet} = - k_M \times t + \ln C_0 \quad (3\text{-}18)$$

SI-SECM was performed identically as shown above using a Au UME tip and a W/Mo-$BiVO_4$ substrate in 1 mM K_2IrCl_6, 2 M MeOH, and 0.1 M Na_2SO_4 aqueous solution. Figure 3.11 shows the results of the interrogation of OH• in the presence of excess MeOH. The apparent rate constant of reaction (3-14) was 0.1 s^{-1} obtained from the slope of equation (3-18), and the surface coverage of OH• was 5.7 mC cm^{-2} after considering the collection efficiency of SI-SECM. As expected, the decay of OH• in the presence of the electron donor is fast and agrees with the previous report.[20] The

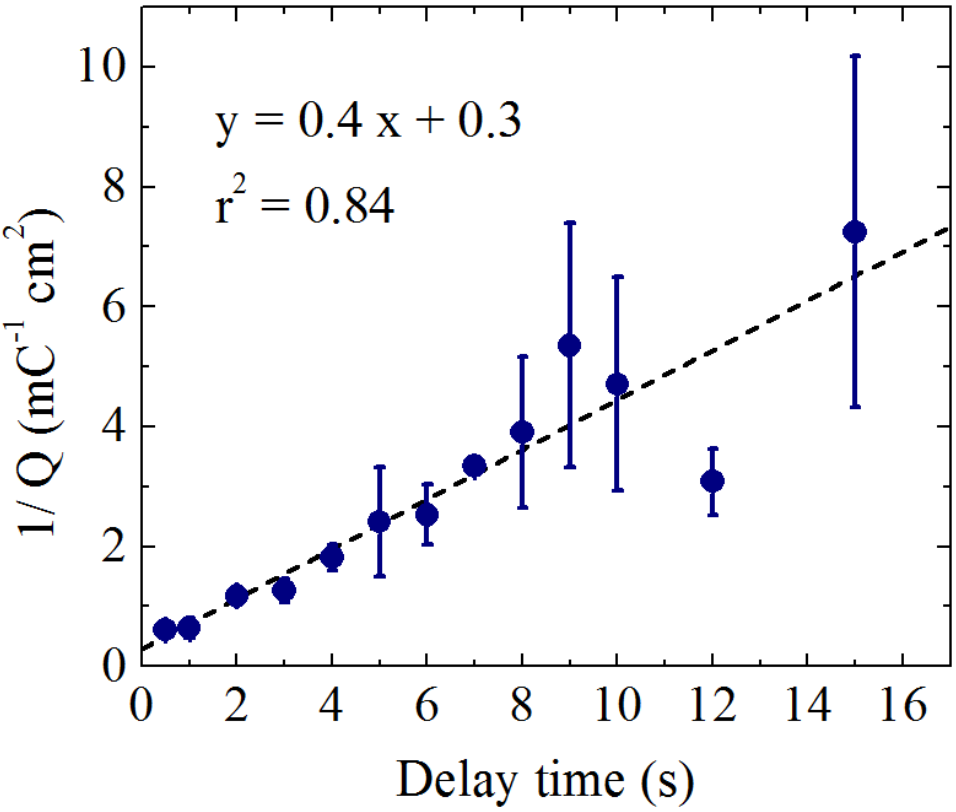

Figure 3.10. Reciprocal plot of the interrogation charges of OH• as a function of decay time. The interrogation charge was calculated in Figure 3.9(b) from the repeated interrogation measurements.

obtained surface coverage of OH• also agreed well with that obtained without the scavenger as shown in Figure 3.10.

3.5 Quantum Efficiencies of Photoreactions

Surface coverage of the adsorbed OH• obtained from SI-SECM provides quantitative values for the reaction processes of water oxidation at the photoanode. Herein, strong irradiation was done and the incident power through the light guide was about 980 mW cm^{-2}. Then, about 60 mW cm^{-2} was absorbed by the W/Mo-$BiVO_4$ film with a thickness of about 200 nm. If the average energy of absorbed photons is assumed to be 3 eV, taking into account the band gap energy and the absorbance of W/Mo-$BiVO_4$,[22] the rate of photon absorption was about 1.2×10^{17} cm^{-2} s^{-1}.

Rate of absorbed photon = 60 mJ cm^{-2} s^{-1}/ (3 eV x 1.6×10^{-19} J eV^{-1})

$$= 1.2 \times 10^{17} \text{ cm}^{-2} \text{ s}^{-1} \qquad (3\text{-}19)$$

The density of W/Mo-$BiVO_4$ molecules in the electrode was about 1.3×10^{17} cm^{-2} based on the materials properties of $BiVO_4$ and properties of the film applied on the electrode, i.e. 0.22 μmol cm^{-2} with about 200 nm of film thickness. Consequently the excitation frequency of W/Mo-$BiVO_4$ was about 1 s^{-1} under the irradiation conditions used. Then, 6 % of the absorbed photons were used to produce the surface OH• of 5.8 mC cm^{-2} or 3.6×10^{16} cm^{-2} as obtained above after 5 s of the irradiation.

% OH• to absorbed photon = 3.6×10^{16} cm^{-2} / (1.2×10^{17} cm^{-2} s^{-1} x 5 s) x 100

$$= 6\ \% \qquad (3\text{-}20)$$

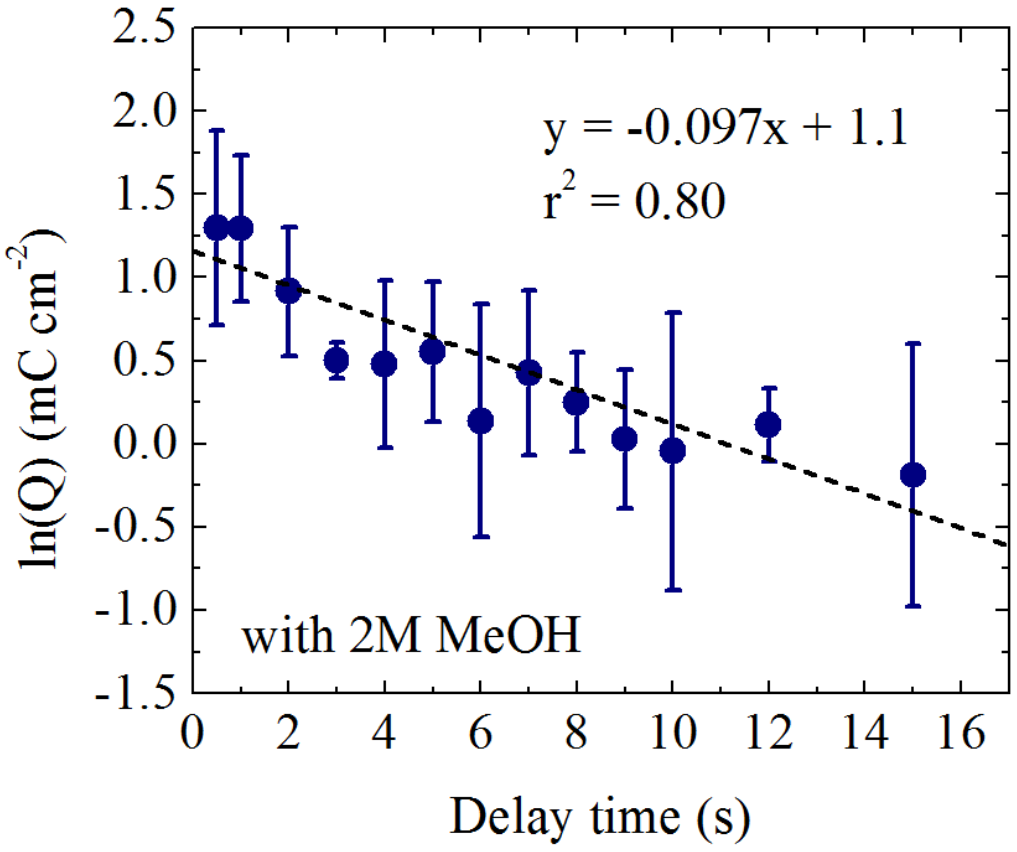

Figure 3.11. Plot of the interrogation charges of OH• as a function of decay time in the presence of excess MeOH in the solution. SI-SECM was done in 1 mM K_2IrCl_6, 2 M MeOH, and 0.1 M Na_2SO_4 aqueous solution with the experimental details as stated in Figure 3.9.

The results from SI-SECM indicate that 94 % of the excited electron-hole pairs produced by the injected photons during the 5 s recombined either in the bulk or at the surface of W/Mo-$BiVO_4$.

As mentioned above, the percent of generated holes which react with the chemisorbed OH^- at the electrode surface is a function of the total flux of photons absorbed in the photocatalysts. In this work, the amount of surface OH• was also a function of the illumination time (Figure 3.12), and the surface coverage showed asymptotic growth as the illumination time increased. The coverage of radicals may reach saturation with illumination times longer than 5 s at W/Mo-$BiVO_4$ under the irradiation intensity used here, but irradiation times longer than 5 s were not used so as to avoid bubble generation at the substrate. However, even with 1 s of irradiation, the interrogated charge was more than 50 % of that obtained after 5 s of irradiation. The results indicate that more than 15 % of the absorbed photons were initially used to produce the adsorbed radicals, and the efficiency decreased to 6 % after 5 s of irradiation. In other words, the quantum efficiency of the absorbed photon conversion to the adsorbed OH• decreased asymptotically as shown in Figure 3.12.

The minority carrier flux, which reached the electrode surface without surface recombination, was estimated using fast irreversible reactions, e.g. sulfite oxidation, at W/Mo-$BiVO_4$.[35] Figure 3.13 shows the photocurrent for sulfite oxidation at large W/Mo-$BiVO_4$ electrodes with film thickness of 200 nm under various irradiation intensities. Although the light intensities used in Figure 3.13 were about half of that

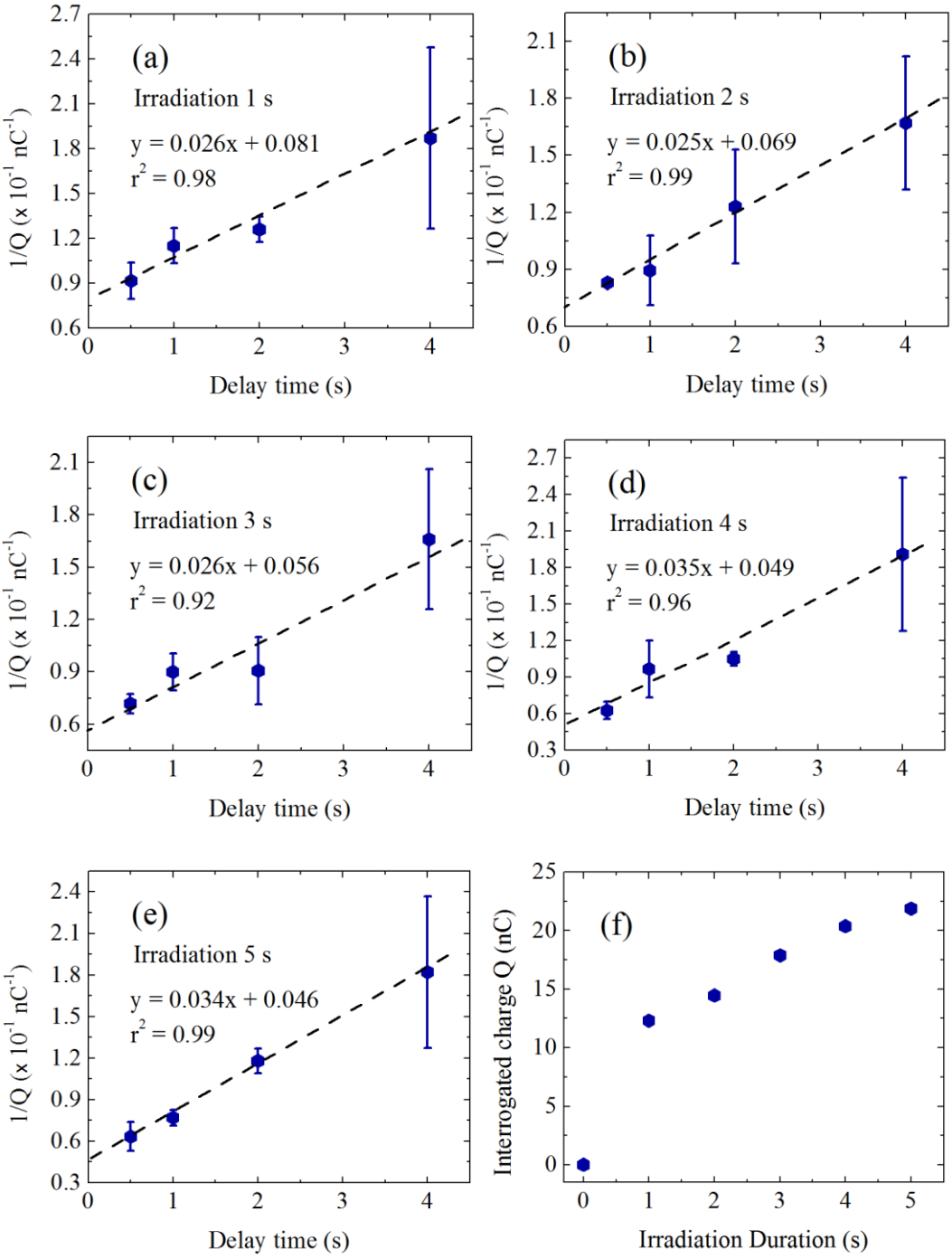

Figure 3.12. Interrogated charges of OH• at W/Mo-$BiVO_4$ with various irradiation durations of (a) 1, (b) 2, (c) 3, (d)4, and (e) 5 s. For each measurement, four different

decay times were allowed from 0.5 to 4 s. Experimental configurations were identical with that shown in Figure 3.1 and Figure 3.8 except the duration of UV-Visible irradiation. The interrogated charge of the OH• was summarized in (f) for the different irradiation time. Electrode area of W/Mo-$BiVO_4$ or the collection factor of the interrogation experiments were not considered in the results shown in (f).

used for SI-SECM, i.e. ~400 mW cm^{-2}, the sulfite oxidation current in Figure 3.13 approached the saturated values with increased irradiation intensity and the excited-hole flux at the electrode surface was calculated from the photocurrent. The excited-hole flux at 0.6 V was:

Hole flux at electrode surface = 1.8×10^{-3} C s^{-1} cm^{-2} / (96485 C mol^{-1}) x 6.02×10^{23} mol

$$= 1.1 \times 10^{16} \text{ cm}^{-2} \text{ s}^{-1} \quad (3\text{-}21)$$

So, the hole-flux at the surface without surface recombination corresponded to about 9 % of the absorbed photon flux, i.e. 1.2×10^{17} cm^{-2} s^{-1}. It indicates that about 91 % of excited electron-hole pairs were bulk-recombined before they reached the surface.

Further, the water oxidation current was measured to calculate the quantum efficiency of the photon-conversion to oxygen evolution. Figure 3.14 shows the water oxidation current at W/Mo-$BiVO_4$ under chopped irradiation. The measured current for water oxidation was about 0.2 mA cm^{-2} at 0.6 V (pH 7), which corresponds to a hole flux of 1.2×10^{15} cm^{-2} s^{-1}, i.e., 1 % of the absorbed photons. The obtained IQE was smaller than the previously reported value, e.g. 5~10 %,[22] mainly because of the strong irradiation used here. Also, the obtained current was measured in a more basic solution (pH 7) than that used in SI-SECM (pH 4.5), and the water oxidation efficiency will be lower in acidic medium. However, the obtained hole flux for water oxidation corresponded to 11 % of the holes that reached the surface without surface recombination (1.1×10^{16} cm^{-2} s^{-1}). In other words, 89 % of the hole flux at the electrode surface (9.8×10^{15} cm^{-2} s^{-1}) was consumed by surface recombination with excited electrons produced

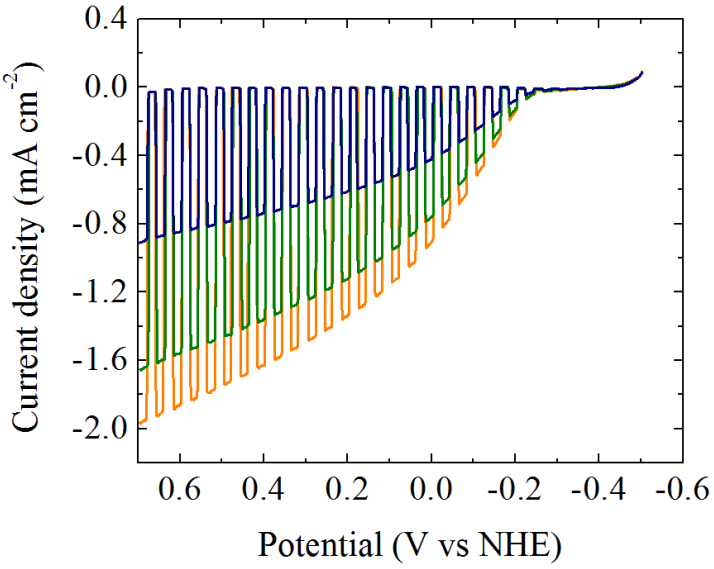

Figure 3.13. Linear sweep voltammogram of W/Mo-$BiVO_4$ with chopped light under UV-Visible irradiation in 0.1 M Na_2SO_4 and 0.1 M Na_2SO_4 aqueous solution (pH 7). Beam intensity was gradually increased from 100 (blue), 300 (green) to 400 mW cm^{-2} (yellow) with full output from a xenon lamp. Scan rate was 20 mV s^{-1}.

near the surface. The extent of surface recombination for 1 s corresponds to about 30 % of the surface adsorbed OH• (3.6×10^{16} cm^{-2}). If we assume reaction (3-9) is the major process of the surface recombination, then about 30 % of surface OH• was reduced and re-generated by excited electron-hole pairs for every second at steady state. The calculations are summarized in Figure 3.15 and Table 3.1.

The quantitative analysis from SI-SECM measurements indicates that the most significant loss of photon energy conversion to chemical energy at W/Mo-$BiVO_4$ is from the bulk recombination, i.e. 91 % of the absorbed photons. The surface recombination loss is also significant, i.e. about 8 % of the absorbed photons, or about 30 % of the surface OH• underwent recombination every second. The recombination loss should be addressed to further increase the photoactivity of W/Mo-$BiVO_4$. It has been widely reported that the surface recombination can largely be reduced by using electrocatalysts, e.g. IrO_x, Co_3O_4, Pt, and cobalt oxide deposited from a phosphate medium (Co-Pi) for water oxidation.[25,36] Also, bulk recombination of $BiVO_4$ has been reduced by doping the W, Mo, or P, [22,27,37] or adopting heterojunctions, e.g. WO_3 or SnO_2, to $BiVO_4$.[38,39,40,41] The techniques mentioned above will be investigated to improve the quantum efficiencies of W/Mo-$BiVO_4$, and SI-SECM will be used as a versatile tool to elucidate the effects of the modification of the photoelectrodes.

3.6 Quantification of Faradaic Efficiency

SECM was used to detect the oxygen generated from W/Mo-$BiVO_4$ electrodes under light irradiation. A Au ring electrode coated around the fiber optic was

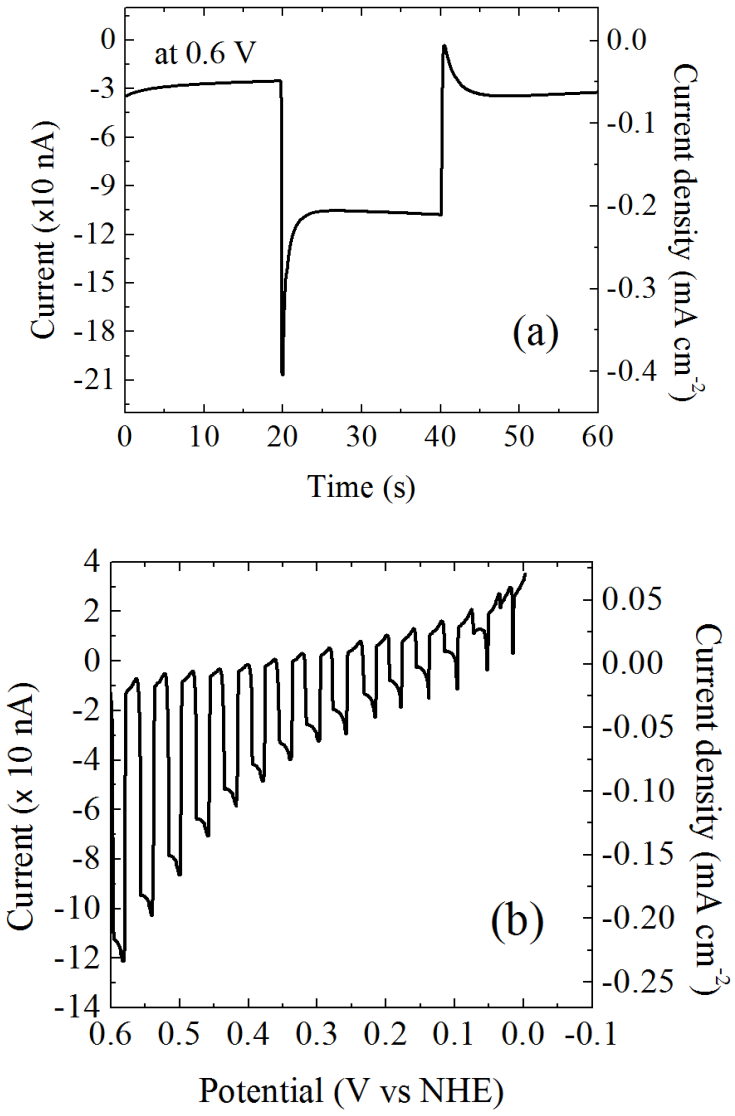

Figure 3.14. Chronoamperogram of photocurrent for water oxidation at W/Mo-$BiVO_4$ electrode at 0.6 V (vs NHE) (a) and its linear sweep voltammogram (b) in 0.1 M Na_2SO_4 aqueous solution (pH 7). UV-Visible irradiation was switched on from 20 to 40 s in (a). Scan rate was 20 mV s^{-1} in (b). Electrode area was 5.1 x 10^{-4} cm^{-2} and the experimental conditions were as shown in Figure 3.1.

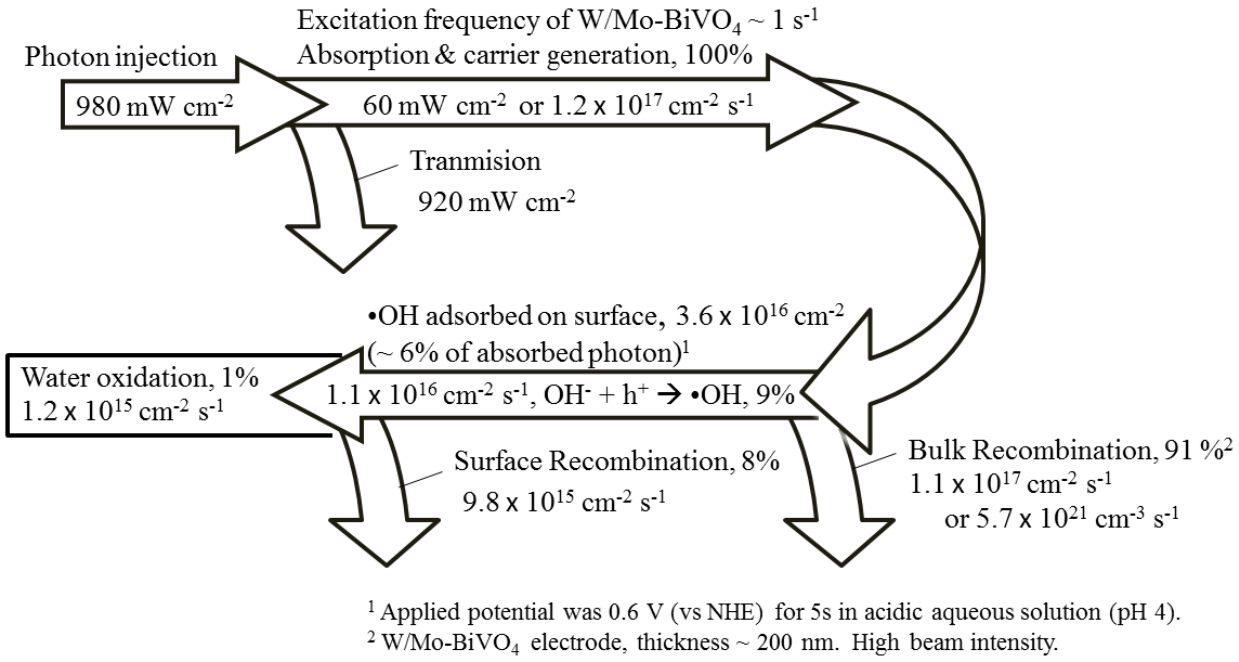

[1] Applied potential was 0.6 V (vs NHE) for 5s in acidic aqueous solution (pH 4).
[2] W/Mo-$BiVO_4$ electrode, thickness ~ 200 nm. High beam intensity.

Figure 3.15. Schematic representations of the photon and minority carrier reaction processes of the W/Mo-$BiVO_4$ for water oxidation. Quantitative values were calculated from the results in Figure 3.10, Figure 3.13, and Figure 3.14 with the experimental conditions stated therein.

	Surface coverage of OH• (mC cm^{-2})	Decay of OH•	
		Reaction	Rate constant
w/o scavenger	5.8	$2•OH \rightarrow H_2O_2$	4 x 10^3 mol^{-1} m^2 s^{-1}
with 2M MeOH	5.7	•OH + MeOH → Product	0.1 s^{-1}

Table 3.1. Results summary of SI-SECM measurements. The surface coverage and rate constant of radical reactions were obtained from Figure 3.10 and 3.11.

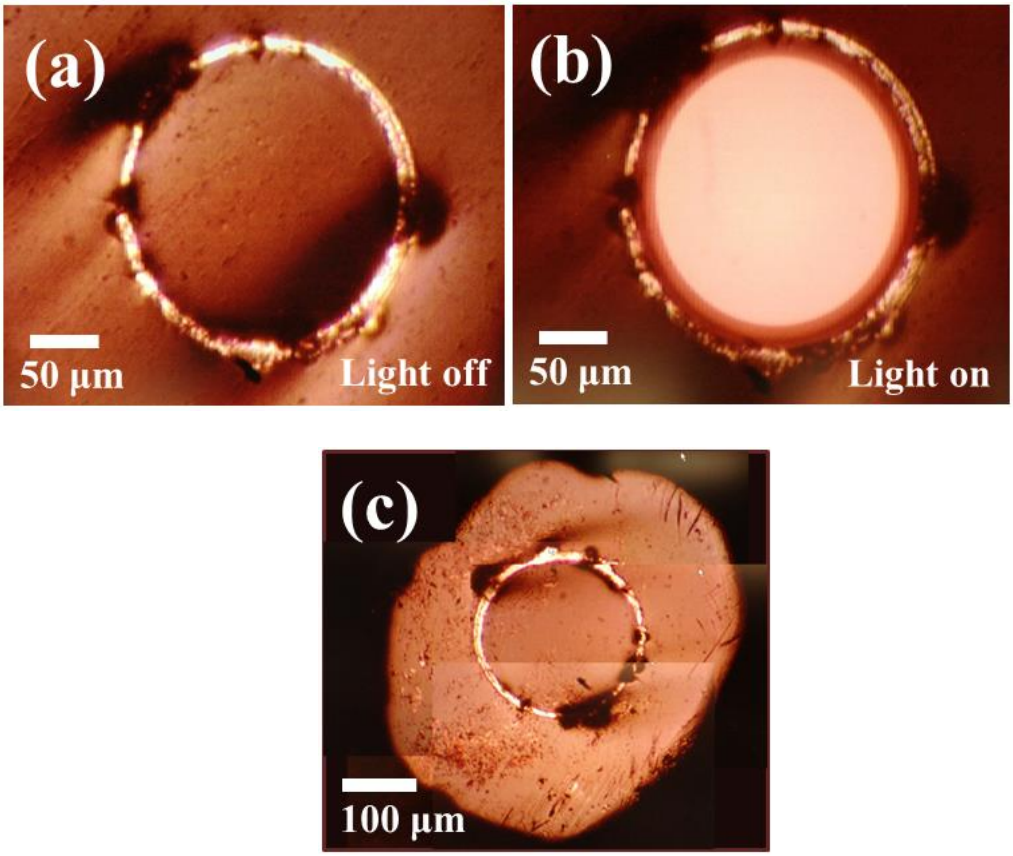

Figure 3.16. Optical microscopic images of a Au ring electrode coated on an optical fiber disk. The diameter of the fiber optic is 200 µm and Au ring electrode has a width of 17 µm. Microscopic images were taken (a) without fiber optic light illumination and (b) with the illumination through the fiber optic. The flat end of the tip including a glass sheath surrounding the fiber optic and the ring electrode has an overall diameter of about 500 µm (c).

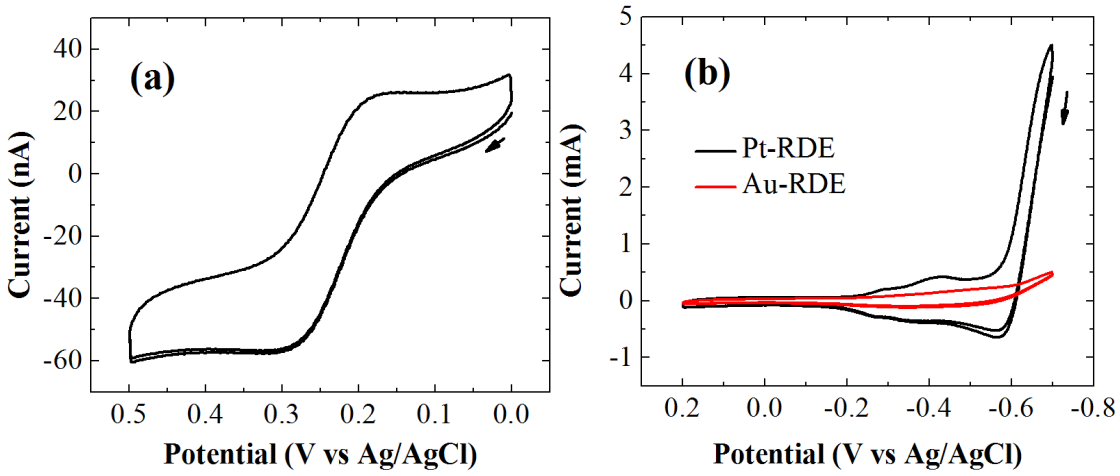

Figure 3.17. (a) Cyclic voltammogram (CV) of Au ring electrode in a 1 mM ferrocenemethanol (FcMeOH) and 0.1 M KCl aqueous solution. The geometry of the tip electrode is described in Figure 3.16. Scan rate: 20 mV/s. (b) CV of Au ring electrode (red) and Pt ring electrode (black) in a 0.1 M Na_2SO_4 aqueous solution (pH 7, 0.2 M sodium phosphate buffer). Pt was electrodeposited on Au ring electrode with a 10 mM H_2PtCl_6 and 0.1 M Na_2SO_4 solution by conducting three consecutive CVs from -0.7 V to 0.2 V at 20 mV/s.

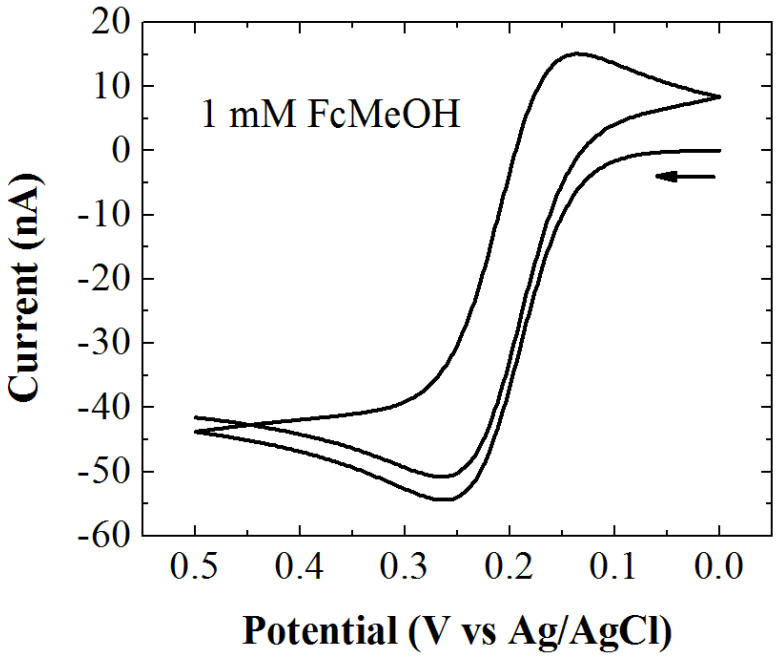

Figure 3.18. Simulated CV on Au ring electrode in a 1 mM ferrocenemethanol (FcMeOH) and 0.1 M KCl aqueous solution. The geometry of the tip electrode is described in Figure 3.16. Scan rate: 20 mV/s.

used as the tip electrode as shown in Figure 3.16. The optical fiber has a diameter of 200 μm and a doped SiO_2 clad surrounding the optical fiber with a thickness of 10 μm. Au was coated around the SiO_2 with a thickness of about 20 μm, then a borosilicate glass sheath finally coated around the Au RE. The outer diameter of the ring electrode/fiber optic tip was about 500 μm (as shown in Figure 3.16(c)).

Figure 3.17(a) shows a cyclic voltammogram (CV) of the Au electrode in a 1 mM ferrocenemethanol (FcMeOH) and 0.1 M KCl solution. The current obtained from the ring electrode in the SECM configuration is a function of (a) the outer ring radius, (b) the ratio of inner and outer ring electrode radii, and (c) the ratio of outer glass sheath and the outer ring electrode radii (Rg).[42] Here, the ratio of inner and outer ring radii was about 0.92 (or 220 μm/240 μm) and Rg was about 2.1 (or 500 μm/240 μm). The current measured from ring electrode at long distance from the substrate was a little larger than that obtained from the numerical simulation (Figure 3.18) which may imply a small deviation of the electrode area from that defined in the simulation. However, the ring electrode coated around the fiber optic was successfully prepared and no severe leakage current was observed that can impede the TC/SG measurements.

To detect oxygen by the oxygen reduction reaction (ORR), the ring electrode was modified and Pt was deposited on a Au electrode to promote the ORR, since this reaction is slow on a Au electrode and a fast reaction is required for diffusion limited TC in SECM. Pt was deposited from a 10 mM H_2PtCl_6 and 0.1 M Na_2SO_4 aqueous solution by repeated cyclic voltammetry from 0.4 V to -0.5 V (vs NHE) for three scans at a rate of 20 mV s^{-1}.

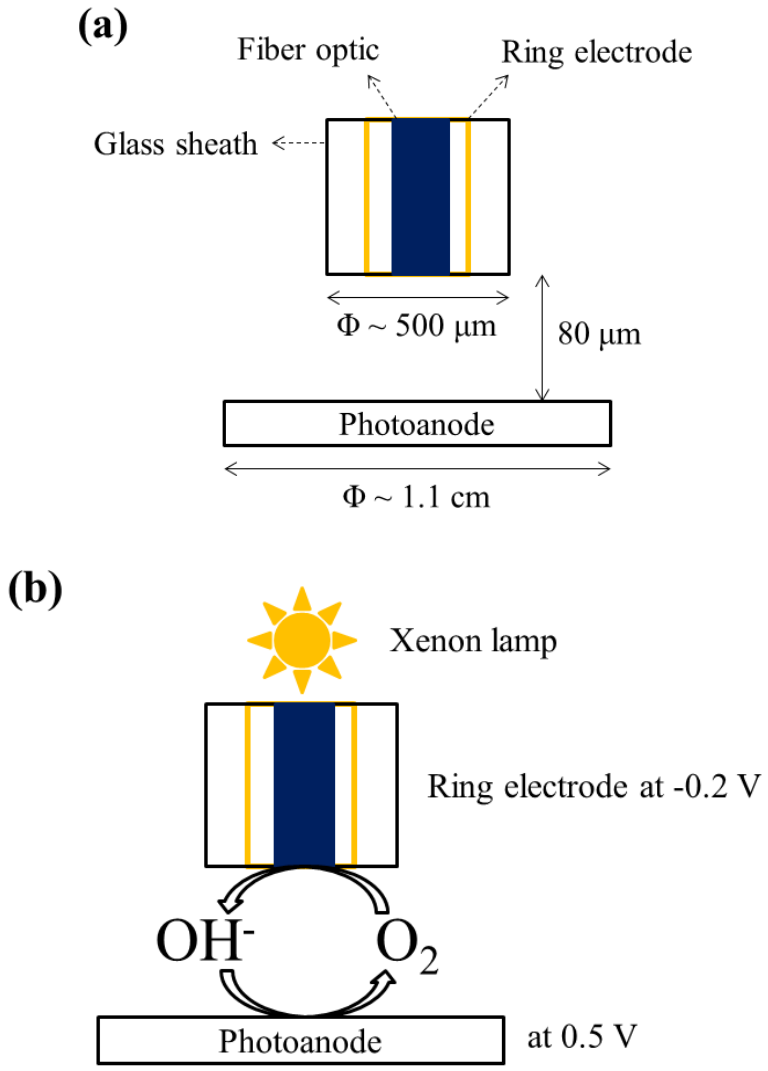

Figure 3.19. Schematic diagram of the TC/SG mode of SECM for (a) the electrode configuration and (b) showing the electrochemical reactions in which water oxidation occurs at a photoanode under irradiation, i.e., substrate generation with oxygen reduction at the Pt ring electrode.

The Pt electrode shows distinctive proton reduction peaks which is not observed at a Au electrode as shown in Figure 3.17(b).

The schematic diagram shown in Figure 3.19 illustrates the electrode configuration of the TC/SG mode of SECM. The Pt electrode/fiber optic was placed a few tens of μm above the photoanode substrate. A positive potential was applied to the photoanode to promote the OER and a negative potential was applied to the Pt electrode for the ORR. Then, the photoanode was irradiated with a xenon lamp and the current of both the tip and the substrate was measured to calculate the collection efficiency, i.e., the ratio of the tip (collection) current and the substrate (generation) current.

The collection efficiency is a function of the electrode geometry and the distance between the tip and substrate, *d*. In general, a higher collection efficiency is expected with a smaller *d*, because less species produced at the substrate is lost to the bulk solution through diffusion. As shown in Figure 3.20, the results from the numerical calculation show that a theoretical collection efficiency (η_{th}) of 0.68 is obtained at d= 80 μm and about 0.90 at d= 20 μm. In addition to the higher η_{th}, a short diffusion time, i.e., time required for the produced species at the substrate to reach the tip to be collected, can be achieved with a small *d* as the equation described below.

$$d^2 = 2Dt \qquad (3\text{-}22)$$

where *d* is the tip-substrate distance in cm, *D* is the diffusion coefficient in cm^2/s, and *t* is the diffusion time in s. When d= 20 μm, the diffusion time is about 100 ms with an oxygen diffusion coefficient of 2×10^{-5} cm^2/s.[43]

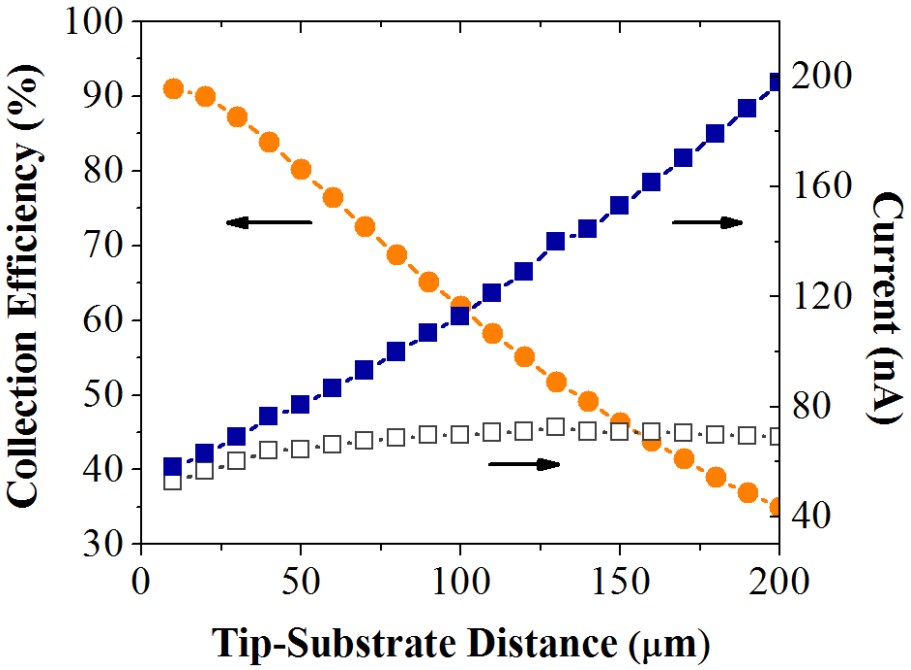

Figure 3.20. Calculated collection efficiency (solid circles), generated substrate current (solid squares), and collected tip current (empty squares) obtained from numerical simulations.

When an n-type semiconductor is used as the substrate, it is considered as a conductive electrode under strong light irradiation as the photooxidation occurs. However, the conductive area of the photoanode is only confined to the irradiated region and the rest of the semiconductor is still insulating. Consequently, when the ring electrode is used as the tip, the irradiated area under the fiber optic is changed when the tip-substrate distance changes, i.e. the area of the light distribution increases with *d*. The light distribution area can be calculated using the acceptance angle of the fiber optic, i.e., the angle in the fiber optic below which the light is spread. The acceptance angle of ring electrode/fiber optic used was 25°.

As discussed above, the theoretical collection efficiency (η_{th}) approaches 0.90 as the distance between the tip and the substrate decreases. Although the assumption on diffusion-limited substrate generation current is not fully satisfied due to the slow OER kinetics on the electrocatalyst at a pH less than 13,[44] it should not affect the constant flux assumption of the product generated from the substrate in the theoretical simulation of the OER at the photoanode. The generation current also decreases for the decreased area. Note that the illumination intensity was assumed to be strong enough that the simulated photocurrent from the substrate depended only on the irradiated area. In the TC/SG mode of SECM, a ring electrode/fiber optic was placed at 80 μm above the photoanode using a linear actuator (T-LA28A, Zaber Technologies Inc., Vancouver, Canada) to achieve both the large generation/collection current and reasonable collection efficiency (Figure 3.19(a)). Then, W/Mo-doped $BiVO_4$ was used as a photoanode to examine the TC/SG mode SECM. W/Mo-doped $BiVO_4$ has been reported to be a highly active and stable

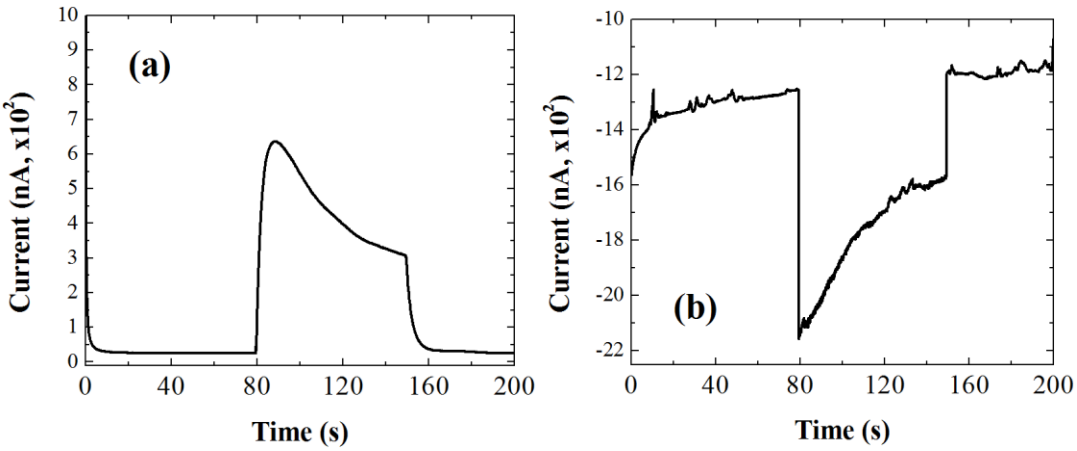

Figure 3.21. Chronoamperograms of tip collection (a) and substrate generation (b) for water oxidation on a W/Mo-doped $BiVO_4$ film in a 0.1 M Na_2SO_4 (pH 7, 0.2 M sodium phosphate buffer) aqueous solution. The measurements began under dark conditions and the UV-visible irradiation was the full output of the xenon lamp from 80 s to 150 s. As the radiation started, oxygen evolution current begins and the generation current at the W/Mo-$BiVO_4$ electrode is about 290 nA at 150 s. The generated oxygen diffuses and reaches to the Pt ring electrode where the oxygen reduction reaction occurs. The collected tip current from oxygen reduction is about 180 nA at 150 s. Absolute collection efficiency, which is the ratio of the collection current and the generation current, is about 0.60. The potential of the W/Mo-$BiVO_4$ electrode was held at 0.5 V and that of Pt electrode was -0.2 V.

photoanode for water oxidation.[22] W/Mo-doped $BiVO_4$ was placed in a 0.1 M Na_2SO_4 aqueous solution (pH 7, 0.2 M sodium phosphate buffer). Then, the ring electrode/fiber optic was placed 80 μm above the substrate as discussed above. The potential applied to the ring electrode was -0.2 V and to the photoanode 0.5 V to promote the ORR and OER, respectively. Chronoamperograms of the ring electrode/photoanode are shown in Figure 3.21. When the light was turned on at 80 s, the oxidation current at the W/Mo-doped $BiVO_4$ increased rapidly for the water oxidation. The generated oxygen diffused to the tip and was reduced at the Pt electrode. The collected current also rapidly increased as shown in Figure 3.21(a). The measured collection efficiency was about 0.60 which agrees well with the numerical simulation as discussed above with about a d= 80 μm. In summary, the TC/SG mode of SECM was demonstrated with a W/Mo-$BiVO_4$ substrate and Pt electrode/fiber optic to detect the oxygen generated at the photoanode.

3.7 Conclusions

SI-SECM has been used to study photogenerated surface OH• during water oxidation at W/Mo-$BiVO_4$. The OH• produced under strong irradiation at the W/Mo-$BiVO_4$ surface were interrogated using an $IrCl_6^{2-/3-}$ redox couple as the titrant of the radicals. The surface coverage of OH• obtained was 5.8 mC cm^{-2} after 5 s of UV-visible irradiation at W/Mo-$BiVO_4$. The kinetic rate constant of OH• dimerization to produce H_2O_2 was measured as 4×10^3 mol^{-1} m^2 s^{-1}. In a solution having excess hole scavengers, i.e. 2M MeOH, OH• experienced fast decay with a kinetic rate constant of 0.1 s^{-1}. Quantitative measurements showed that about 6 % of the absorbed photons

contribute to the production of adsorbed OH• at W/Mo-$BiVO_4$. However, more than 90 % of the excited electron-hole pairs were bulk-recombined before they reached the electrode surface. Also, about 30 % of the adsorbed OH•, which corresponds to 8 % of the absorbed photon flux, was reduced by the surface recombination every second. Finally, only 1 % of the absorbed photons were used for water oxidation at W/Mo-$BiVO_4$ under strong irradiation.

3.8 References

[1] Barber, J. *Chem. Soc. Rev.* **2009,** *38,* 185-196.

[2] Nakamura, R.; Okamura, T.; Ohashi, N.; Imanishi, A.; Nakato, Y. *J. Am. Chem. Soc.* **2005,** *127,* 12975-12983.

[3] Subbaraman, R.; Tripkovic, D.; Chang, K.-C.; Strmcnik, D.; Paulikas, A. P.; Hirunsit, P.; Chan, M.; Greeley, J.; Stamenkovic, V.; Markovic, N. M. *Nature Mater.* **2012**, *11,* 550-557.

[4] Zong, R.; Thummel, R. P. *J. Am. Chem. Soc.* **2005,** *127,* 12802-12803.

[5] Clausen, J.; Junge, W. *Nature* **2004,** *430,* 480-483.

[6] Jaeger, C. D.; Bard, A. J. *J. Phys. Chem.* **1979**, *83,* 3146-3152.

[7] Ahmed, A. Y.; Kandiel, T. A.; Oekermann, T.; Bahnemann, D. *J. Phys. Chem. Lett.* **2011,** *2,* 2461-2465.

[8] Schwarz, P. F.; Turro, N. J.; Bossmann, S. H.; Braun, A. M.; Wahab, A.-M. A. A.; Durr, H. *J. Phys. Chem. B* **1997,** *101,* 7127-7134.

[9] Izumi, I.; Fan, Fan, F.-R. F.; Bard, A. J. *J. Phys. Chem.* **1981,** *85,* 218-223.

[10] Nakamura, R.; Nakato, Y. *J. Am. Chem. Soc.* **2004,** *126,* 1290-1298.

[11] Micic, O. I.; Zhang, Y.; Cromack, K. R.; Trifunac, A. D.; Thurnauer, M. C. *J. Phys. Chem.* **1993,** *97,* 7277-7283.

[12] Park, S. H.; Roy, A.; Beaupre, S.; Cho, S.; Coates, N.; Moon, J. S.; Moses, D.; Leclerc, M.; Lee, K.; Heeger, A. J. *Nature Photon.* **2009,** *3,* 297-303.

[13] Nozik, A. J. *Inorg. Chem.* **2005,** *44,* 6893-6899.

[14] Nosaka, Y.; Fox, M. A. *J. Phys. Chem.* **1986,** *90,* 6521-6522.

[15] Ishibashi, K.; Fujishima, A.; Watanabe, T.; Hashimoto, K. *J. Phys. Chem. B* **2000,** *104,* 4934-4938.

[16] Nosaka, Y.; Komori, S.; Yawata, K.; Hirakawa, T.; Nosaka, A. Y. *Phys. Chem. Chem. Phys.* **2003,** *5,* 4731-4735.

[17] Ohko, Y.; Hashimoto, K.; Fujishima, A. *J. Phys. Chem. A* **1997,** *101,* 8057-8062.

[18] Rodriguez-Lopez, J.; Alpuche-Aviles, M. A.; Bard, A. J. *J. Am. Chem. Soc.* **2008,** *130,* 16985-16995.

[19] Rodriguez-Lopez, J.; Minguzzi, A.; Bard, A. J. *J. Phys. Chem. C* **2010,** *114,* 18645-18655.

[20] Zigah, D.; Rodriguez-Lopez, J.; Bard, A. J. *Phys. Chem. Chem. Phys.* **2012,** *14,* 12764-12772.

[21] Kudo, A.; Omori, K.; Kato, H. *J. Am. Chem. Soc.* **1999**, *121*, 11459-11467.

[22] Park, H. S.; Kweon, K. E.; Ye, H.; Paek, E.; Hwang, G. S.; Bard, A. J. *J. Phys. Chem. C* **2011**, *115*, 17870-17879.

[23] Berglund, S. P.; Rettie, A. J. E.; Hoang, S.; Mullins, C. B. *Phys. Chem. Chem. Phys.* **2012**, 14, 7065-7075.

[24] Pilli, S. K.; Furtak, T. E.; Brown, L. D.; Deutsch, T. G.; Turner, J. A.; Herring, A. M. *Energy Environ. Sci.* **2011,** *4*, 5028-5034.

[25] Zhong, D. K.; Choi, S.; Gamelin, D. R. *J. Am. Chem. Soc.* **2011,** *133*, 18370-18377.

[26] Kontic, R.; Patzke, G. R. *J. Solid State Chem.* **2012**, *189*, 38-48.

[27] Ye, H.; Lee, J.; Jang, J. S.; Bard, A. J. *J. Phys. Chem. C* **2010**, *114*, 13322-13328.

[28] Sun, P.; Laforge, F. O.; Mirkin, M. V. *Phys. Chem. Chem. Phys.* **2007**, *9*, 802-823.

[29] Tanaka, K.; White, J. M. *J. Phys. Chem.* **1982,** *86*, 4708-4714.

[30] Primet, M.; Pichat, P.; Mathieu, M.-V. *J. Phys. Chem.* **1971,** *75*, 1216-1220.

[31] Lawless, D.; Serpone, N.; Meisel, D. *J. Phys. Chem.* **1991,** *95*, 5166-5170.

[32] Ohikiri, M.; Boero, M. *J. Phys. Chem. B.* **2006,** *110*, 9188-9194.

[33] Shankar, K.; Basham, J. I.; Allam, N. K.; Varghese, O. K.; Mor, G. K.; Feng, X.; Paulose, M.; Seabold, J. A.; Choi, K.-S.; Grimes, C. A. *J. Phys. Chem. C* **2009,** *113*, 6327-6359.

[34] Ulanski, P.; Von Sonntag, C. *J. Chem. Soc., Perkin Trans.* **1999,** *2*, 165-168.

[35] Zhong, D. K.; Choi, S.; Gamelin, D. R. *J. Am. Chem. Soc.* **2011**, *133*, 18370-18377.

[36] Spray, R. L.; McDonald, K. J.; Choi, K.-S. *J. Phys. Chem. C* **2011**, *115*, 3497-3506.

[37] Jo, W. J.; Jang, J.-W.; Kong, K.-J.; Kang, H. J.; Kim, J. Y.; Jun, H.; Parmar, K. P. S.; Lee J. S. *Angew. Chem. Int. Ed.* **2012,** *51*, 1-6.

[38] Hong, S. J.; Lee, S.; Jang, J. S.; Lee, J. S. *Energy Environ. Sci.* **2011,** *4*, 1781-1787.

[39] Su, J.; Guo, L.; Bao, N.; Grimes, C. A. *Nano Lett.* **2011,** *11*, 1928-1933.

[40] Saito, R.; Maiseki, Y.; Sayama, K. *Chem. Commun.* **2012,** *48*, 3833-3835.

[41] Liang, Y.; Tsubota, T.; Mooij, L. P. A.; Van de Krol, R. *J. Phys. Chem. C* **2011,** *115*, 17594-17598.

[42] Lee, Y.; Amemiya, S.; Bard, A. J. *Anal. Chem.* **2001**, *73*, 2261-2267.

[43] Ferrell, R. T.; Himmelblau, D. M. *J. Chem. Eng. Data*, **1967,** *12*, 111-115.

[44] Minguzzi, A.; Fan, F.-R. F.; Vertova, A.; Rondininia, S.; Bard, A. J. *Chem. Sci.*, **2012**, *3*, 217-229.

Chapter 4. Composite Photoelectrodes and Finite Elements Analysis

4.1 Introduction

Metal oxide semiconductors, e.g., TiO_2, Fe_2O_3, WO_3 and $BiVO_4$, have been extensively studied as the water oxidation photocatalysts for the possible photolysis of water.[1] Metal oxide semiconductors are chemically stable, cheap and abundant, and their semiconducting properties, such as the size of band-gap, the band-edge locations, the carrier mobility, can be largely modified by the addition of dopant, e.g., Si-doped Fe_2O_3,[2] N-doped WO_3,[3] and W-doped $BiVO_4$.[4,5] However, the significant electron-hole recombination including the short minority carrier-lifetime and short carrier-diffusion length of metal oxide semiconductors are still considered as a major barrier to achieve a high conversion efficiency from the sunlight to the chemical energy, i.e., hydrogen from the water splitting.[6,7,8] Addition of conductive or electron accepting materials into the metal oxide semiconductor has been recently tried to address the rapid electron-hole recombination of the photocatalysts. For example, conductive $TiSi_2$ was incorporated to TiO_2,[9,10] WO_3,[11] and α-Fe_2O_3[12] to improve the electron transfer through the electrodes. Also, composite photocatalysts with carbon based conducting materials, such as carbon nanotube and reduced graphene oxide (RG-O), has been suggested for TiO_2[13,14,15] and $BiVO_4$[16] to overcome the rapid recombination of excited electron-hole pairs; the addition of conductive materials into semiconductors increases the conductivity of electrodes and the separations of excited electron-hole pairs. However, it also has the

possibility of acting as the interfacial traps, i.e., recombination centers of the electron-hole pairs.[17]

The chemistry of graphite oxide (GO) (or graphene oxide (G-O)) has been extensively studied for its properties and synthesis since Brodie's observation of GO in 1859.[18] G-O is intrinsically an insulator, but it is highlighted as a precursor for the graphene-like material, i.e., reduced graphene oxide (RG-O). G-O is a possible source of mass production of RG-O, and the chemical derivatives of G-O and RG-O are very promising for applications including polymer nano-composites, ultracapacitors, rechargeable batteries, sensors, and thin films.[19,20,21,22,23] Among the various applications, RG-O (or G-O) composites with photocatalysts have been reported to enhance photoactivity by adding RG-O as a conductive additive to facilitate the electron-hole separations in photocatalysts as described above.[14,15,16] Herein, we report the facile preparation and its photoelectrochemical behavior of RG-O/metal oxide composite photocatalysts based on $BiVO_4$ and W-Mo-doped $BiVO_4$ and its finite elements analysis to study the photoelectrodes properties.[24,25,26] $BiVO_4$, with a band gap of 2.4 eV, has been reported as a water oxidation photocatalyst to harvest visible light. Also, W-doped $BiVO_4$ or W-Mo-doped $BiVO_4$ has been recently shown by our group to yield a photocurrent for water oxidation that is more than 10 times higher than un-doped $BiVO_4$.[4,5] Using the $BiVO_4$ and W-Mo-doped $BiVO_4$, a simple two-step process was adopted to fabricate the composite electrodes in which G-O is exfoliated and homogenously dispersed in ethylene glycol solution by ultrasonication and then thermally reduced during the metal oxide formation by thermal annealing of drop-casted electrodes

in air. In addition, a Pt electrocatalyst was photodeposited onto the composite electrodes to remove kinetic limitations of water oxidation reactions on the composite electrodes; the effect of reduced electron-hole recombination by incorporation of RG-O clearly results in an increased photocurrent after the surface treatment.

4.2 Experimental

$Bi(NO_3)_3 \cdot 5H_2O$ (99.999%) and $(NH_4)_{10}H_2(W_2O_7)_6 \cdot xH_2O$ (99.99%) were obtained from Strem Chemicals (Newburyport, MA). H_2SO_4 (98%), HCl (Technical grade), $KMnO_4$ (99.6%), Na_2HPO_4 (99.9%), NaH_2PO_4 (99.5%), MeOH (99.8 %), and ethylene glycol were purchased from Fisher Scientific (Pittsburg, PA). H_2O_2 (30 wt% in water), $H_2PtCl_6 \cdot xH_2O$ (99.9%), $(NH_4)_6Mo_7O_{24} \cdot 4H_2O$ (99.98%), and Na_2SO_4 (99.0%) were purchased from Sigma-Aldrich (St. Louis, MO). VCl_3 (99%, Alfa-Aeser, Ward Hill, MA) and Na_2SO_3 (99.6%, Mallinckrodt Baker, Phillipsburg, NJ) were used as received. Fluorine-doped tin oxide (FTO, TEC 15, Pilkington, Toledo, OH) was used as a substrate of the electrodes. Deionized (DI) Milli-Q water was used as the solvent in electrochemical experiments.

Graphite oxide (GO) was synthesized by a modified Hummer's method.[27] Briefly, 100 mg of natural graphite (SP-1, Bay Carbon, Bay City, MI) was mixed with 50 ml concentrated H_2SO_4 in a flask, followed by the addition of 500 mg of $KMnO_4$. After addition of $KMnO_4$, the mixture was heated at 35 $^{\circ}$C and stirred for 2 h. Excess DI water (50 mL) was added to the flask (placed in an ice bath), and then more water (100 mL) was added followed by stirring in the ice bath for 1 h. H_2O_2 (30 wt% in water) was

then added to the mixture until no further gas evolution was observed, followed by stirring for 2 h. The final suspension was filtered and washed with HCl (10% in water) and dried in air. Suspensions of G-O platelets were prepared using an ultrasonic bath (2510R-MT, Bransonic, Danbury, CT) by sonication of GO in DI water or ethylene glycol for 1 h.

Thin film electrodes of the $BiVO_4$ (or $BiVO_4$ with 2 atomic% (at%) of W and 6 at% of Mo, W-Mo-doped $BiVO_4$) and RG-O/$BiVO_4$ (or RG-O/W-Mo-doped $BiVO_4$) composites were prepared on FTO substrate by drop casting the precursor solution. The metal oxide films were cast using 100 μl of a precursor solution with a total concentration of 20 mM in ethylene glycol. For RG-O/metal oxide composite electrodes, the targeted amount of GO powder was suspended in the metal oxide precursor solution and the solution was ultrasonicated for 1 h before the drop casting. Then, the film was annealed in air for 3 h at the temperatures from 400 ℃ to 550 ℃ ramped from room temperature at a ramp rate of 1 ℃ per minute.

Photodeposition of Pt on photoelectrodes was conducted in aqueous solution of 10 mM H_2PtCl_6 and 0.2 M MeOH. $BiVO_4$ (and W-Mo-doped $BiVO_4$) and its RG-O composite electrodes on FTO were placed in the Pt precursor solution in a borosilicate glass cell. UV-visible irradiation was then performed at full output with a Xenon lamp (XBO 150 W, Osram, Munich, Germany) for 30 min. Beam intensity was about 200 mW cm^{-2}. During the irradiation, photoreduction of Pt occurred on the thin film electrodes while MeOH was oxidized by the photoexcited electron and hole.[28]

A CH Instruments Model 630D Electrochemical Analyzer (Austin, TX) was used as a potentiostat for the experiments with the thin film electrodes. Illumination was with a Xenon lamp (XBO 150 W, Osram) at full output for UV-visible irradiation or using a 420 nm cut-off filter (WBF-3, Oriel, Darmstadt, Germany) for visible irradiation. A Pt gauze counter electrode and Ag/AgCl reference electrode in a saturated KCl solution were used to complete the three electrode configuration. However, all potentials reported here are with respect to the normal hydrogen electrode (NHE). X-ray diffraction (XRD) measurements were performed using a Bruker-Nonius D8 advanced powder diffractometer (Madison, WI) operated at 40 kV and 40 mA with Cu Kα radiation (λ=1.54 Å). Grazing incidence XRD (GIXRD) with incidence angle of 1° on detector scan mode was performed to obtain the diffractogram from the thin film electrodes on FTO. The scan rate was 12° per minute in 0.02° increments of 2θ from 15° to 80°. Scanning electron microscopy (SEM) images were obtained with a LEO 1530 SEM at a working voltage of 10 kV and working distance of 5 mm. Thermogravimetric analysis (TGA) was conducted from room temperature to 800 ℃ with a Perkin-Elmer TGA 4000 with a ramp rate of 1 ℃ per minute under dry air flow. X-ray photoelectron spectroscopy (XPS) was performed on a Kratos Axis Ultra DLD instrument (Manchester, UK) with a monochromatic Al X-ray source with 180° hemispherical electron energy analyzer.

4.3 Calculation Methods

Finite elements analysis was performed using COMSOL Multiphysics v.3.5 software (Burlington, MA) to study properties of the photoanode. Steady state Poisson's equation (equation (4-1)) and Nernst-Planck equations (equation (4-3) and (4-4)) were used to calculate the potential distribution and the electron-hole transports in the semiconductor electrodes. The physics and reactions used in the simulations are schematically summarized in Figure 4.1.

$$d\left(-\varepsilon_0\varepsilon_r \times d\psi/dx\right)/dx = \rho \qquad (4\text{-}1)$$

where ε_0 is the vacuum permittivity, ε_r is the relative permittivity, ψ is the potential (of Fermi level vs vacuum level), and ρ is the excess charge density. The simulations domain and constants were set as shown in Figure 4.2 and Table 4.1. ρ was defined as

$$\rho = (C_p + C_n - N_d) \times q \qquad (4\text{-}2)$$

where q is the element charge, N_d is the fixed electron doping density at thermal equilibrium, and C_n/C_p is the local carrier density of electron/hole, respectively. C_n/C_p was determined using the Nernst-Planck equations as shown below.

$$d(-D_n \times dC_n/dx + \mu_n \times C_n \times d\psi/dx) = -R + G \qquad \text{for } C_n \qquad (4\text{-}3)$$

$$d(-D_p \times dC_p/dx - \mu_p \times C_p \times d\psi/dx) = -R + G \qquad \text{for } C_p \qquad (4\text{-}4)$$

where D_n/D_p is the diffusion coefficient of electron/hole, and μ_n/μ_p is the mobility for electron/hole. The diffusion coefficient and mobility are related by the Einstein relation.

$$D_{n/p} = \mu_{n/p} \times kT/q \qquad (4\text{-}5)$$

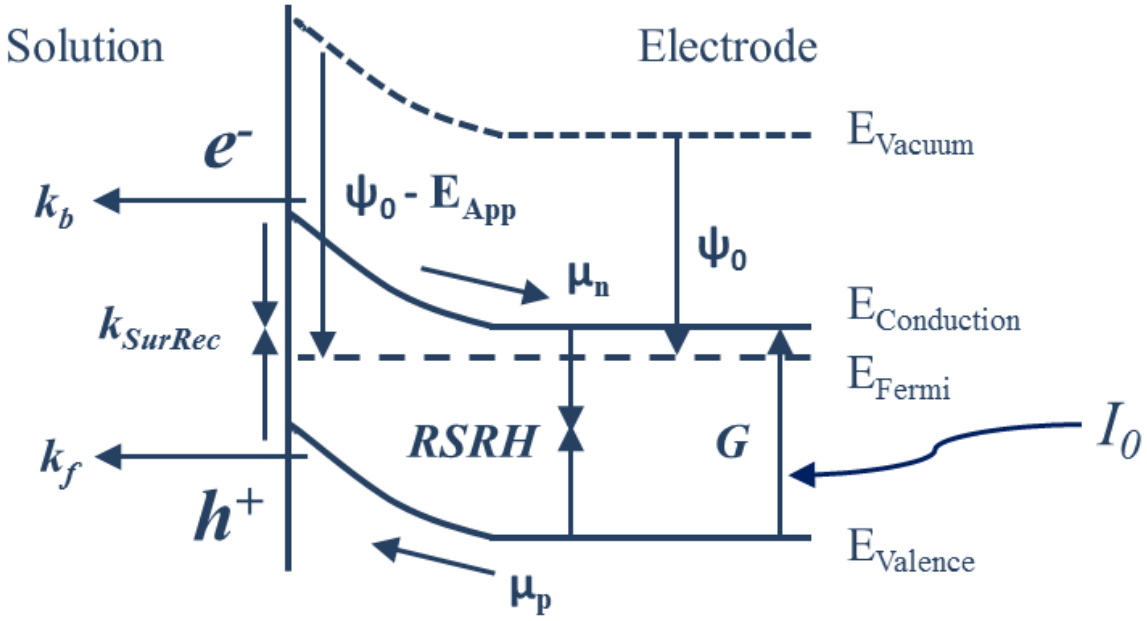

Figure 4.1. Schematic diagram of reaction processes of excited electron and hole in the photoelectrodes.

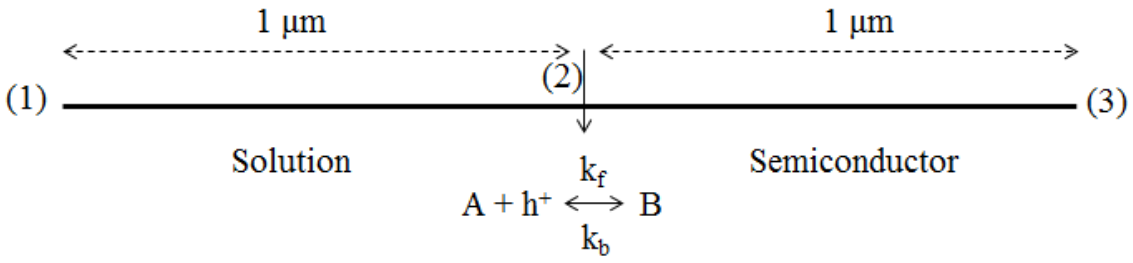

Figure 4.2. Simulation domain of the 1-dimentional finite elements analysis of photoelectrodes.

Parameter	Value	Units	Description
q	1.602×10^{-19}	C	Element charge
T	300	K	Temperature
k	1.38×10^{-23}	$J\ K^{-1}$	Boltzmann constant
ε_r	68		Relative permittivity of $BiVO_4$
ε_0	8.854×10^{-12}	$F\ m^{-1}$	Vacuum permittivity
χ_semi	4.5	eV	Electron affinity of $BiVO_4$
χ_solution	6	eV	Standard potential of chemical species in solution
E_g_semi	2.4	eV	Band gap size of $BiVO_4$
Vt	k x T / q	V	Thermal voltage
NA	6.02×10^{23}	mol^{-1}	Avogadro's number
Abs	2×10^4	cm^{-1}	Absorption coefficient of $BiVO_4$ at 400 nm
Ns	1×10^{18}	cm^{-3}	Available states of $BiVO_4$
n_i	Ns x exp(-Eg/(2kT))	cm^{-3}	Intrinsic doping density of $BiVO_4$
I_0	8×10^{16}	$cm^{-2}\ s^{-1}$	Number of irradiated photon at 400 nm
Thickness	1	µm	Thickness of $BiVO_4$ electrode
Da	1×10^{-5}	$cm^2\ s^{-1}$	Diffusion coefficient of chemical species A in solution
Db	2×10^{-5}	$cm^2\ s^{-1}$	Diffusion coefficient of chemical species B in solution
Ca_bulk	1×10^{-4} x NA	cm^{-3}	Number of chemical molecule A in solution (0.1 M)
Cb_bulk	1.3×10^{-6} x NA	cm^{-3}	Number of chemical molecule B in solution (1.3 mM)

Table 4.1. Constants used in the finite elements analysis simulations.

where k is the Boltzmann constant and T is the temperature. R is the electron-hole recombination rate in the bulk semiconductor and the trap-assisted Shockley-Read-Hall recombination equation was used in the simulations.[29]

$$R = (C_n+C_p - n_i^2) / (\tau_n(C_p + n_i) + \tau_p(C_n+n_i)) \quad (4\text{-}6)$$

where n_i is the intrinsic doping density and τ_n/τ_p is the recombination lifetime of electron/hole. Also, the surface recombination of electron and hole was considered as

$$dC_n/dt = dC_p/dt = - k_{SurRec} \times C_n \times C_p \quad \text{(at the electrode surface)} \quad (4\text{-}7)$$

where k_{SurRec} is the rate constant of the surface trap recombination. G in equation (4-3) and (4-4) is a generation rate of the charge carriers by the absorbed photon energy.

$$G = I_0 \times \alpha \times \exp(-\alpha x) \quad (4\text{-}8)$$

where α is the absorption coefficient of the photoanode, and I_0 is the incidence rate of photon. x is the penetration depth of the photon into the electrode. Initial conditions for ψ, C_n, and C_p were

$$\Psi_0 = kT/q \times (\ln(Cn_0/n_i) - \chi_{semi} - 0.5 \times E_g) \quad (4\text{-}9)$$

$$C_{n0} = n_d/2 + (n_d^2/4 + n_i^2)^{0.5} \quad (4\text{-}10)$$

$$C_{p0} = n_i^2/C_{n0} \quad (4\text{-}11)$$

where χ_{semi} is the electron affinity of semiconductor electrode, and E_g is the band gap size of the semiconductor. The density of available states (n_s) was set to obtain the intrinsic doping density (n_i) of photoelectrodes (equation (4-12)). The donor density (n_d) of $BiVO_4$ was determined from the previously reported experimental values.[5]

$$n_i = n_s \times \exp(-q \times E_g/2kT) \quad (4\text{-}12)$$

Boundary conditions for ψ, C_n, and C_p at the solution/electrode interface and at the electrode/metal contact were

$$\Psi_{solution} = \Psi_0 - E_{app} \quad (4\text{-}13)$$

$$dC_{n\_solution}/dx = - k_b \times C_n \times C_B - k_{SurRec} \times C_n \times C_p \quad (4\text{-}14)$$

$$dC_{p\_solution}/dx = - k_f \times C_p \times C_A - k_{SurRec} \times C_n \times C_p \quad (4\text{-}15)$$

$$\Psi_{metal} = \Psi_0 \quad (4\text{-}16)$$

$$C_{n\_metal} = C_{n0} \quad (4\text{-}17)$$

$$C_{p\_metal} = C_{p0} \quad (4\text{-}18)$$

where E_{app} is the applied potential, and k_f/k_b is the transfer rate constant of hole/electron of the reaction (4-19) and (4-20). C_A/C_B is the molecular concentration of A/B in the solution.

$$A + h^+ \rightarrow C\ (k_f) \quad (4\text{-}19)$$

$$B + e^- \rightarrow D\ (k_b) \quad (4\text{-}20)$$

The chemical species, i.e., A and B, were treated as the sulfite and the dissolved oxygen in the solution. C_A and C_B were assumed as a constant and the reaction rates of (4-19) and (4-20) were limited by the electron and hole fluxes at the electrode surface. Finally, linear sweep voltamograms (LSVs) of the photoelectrode were simulated as the E_{app} was changed from 0 to 1 V. The photocurrent (i) was calculated from the electron/hole flux at the electrode/metal interface.

$$i = q \times (dC_p/dx - dC_n/dx) \quad (4\text{-}21)$$

4.4 Effects of Electron Accepting Materials in Photocatalysts

The photoactivity of $BiVO_4$ and RG-O/$BiVO_4$ composite electrodes was first observed from sulfite oxidation in Figure 4.3. For the RG-O/$BiVO_4$ electrode, 5 wt% of G-O was added to the precursor solution of $BiVO_4$ during electrode preparation. The optimum concentration of RG-O in the composite electrode was determined by varying the amount of G-O in the precursor solution and the results are shown in Figure 4.4(a). 5 wt% G-O in the precursor solution corresponds to 14 $\mu g\ cm^{-2}$ of G-O on the prepared $BiVO_4$ electrode. As shown in Figure 4.4, the photoactivity of the resulting RG-O/$BiVO_4$ was greatly affected by small changes of G-O concentrations in the precursor solution. Note that the weight ratio of G-O is based on the amount of G-O prepared in the precursor solution of the metal salts, and is the ratio of G-O to the total amount of G-O and resulting metal oxide from the metal salts. The amount of RG-O in the resulting electrode is reduced after the thermal process used for electrode fabrication (see TGA results in Figure 4.5). However, the RG-O/$BiVO_4$ electrode prepared from 5 wt% G-O precursor solution showed several times higher photocurrent for sulfite oxidation both under UV-visible and visible light irradiation than that of $BiVO_4$ (see Figure 4.6 for response to visible light irradiation). As shown below in the finite elements analysis, thermally reduced G-O facilitates the transfer of photoexcited electrons to the back contact, i.e., conductive FTO, so the incorporation of RG-O into the photocatalyst results in an improved separation of the excited electron-hole pairs.[15]

The annealing temperature used for the preparation of RG-O/$BiVO_4$ composite electrodes was also varied (from 400 ℃ to 550 ℃) to observe the effect on the

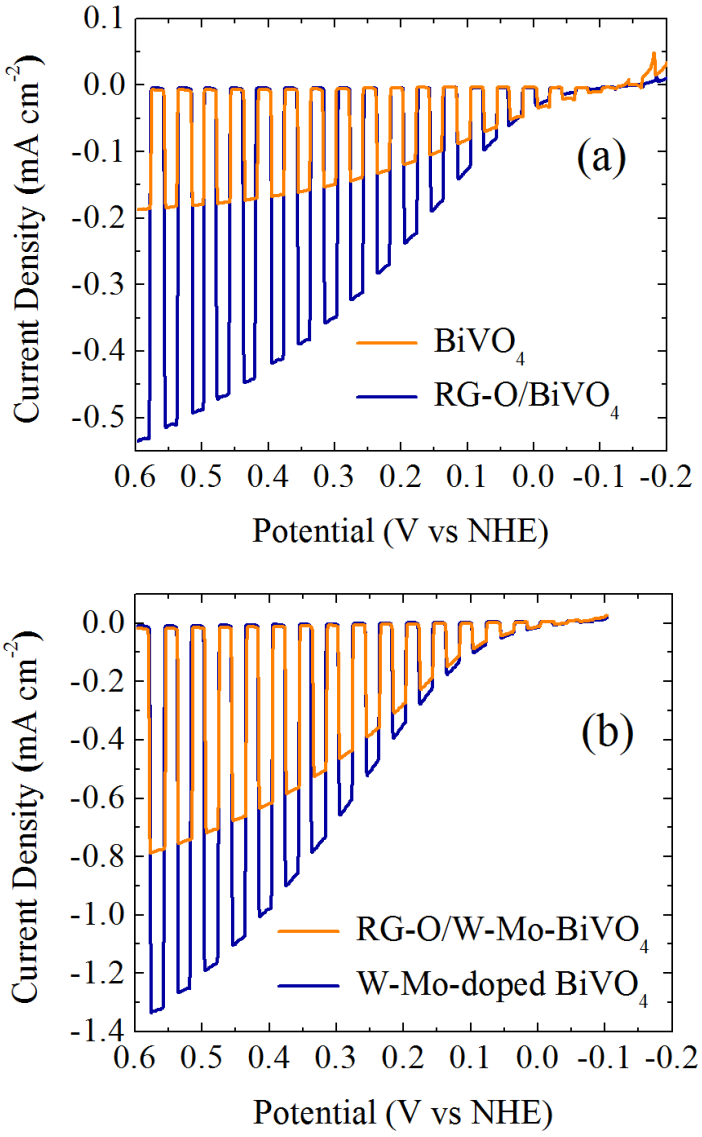

Figure 4.3. Linear sweep voltammograms of (a) $BiVO_4$ (yellow) and RG-O/$BiVO_4$ (blue) and (b) W-Mo-doped $BiVO_4$ (blue) and RG-O/W-Mo-doped $BiVO_4$ (yellow) for sulfite oxidation in 0.1 M Na_2SO_3 and 0.1 M Na_2SO_4 aqueous solution (pH 7, 0.2 M sodium phosphate buffered). Scan rate was 20 mV sec^{-1} and photocurrent was measured under chopped UV-visible irradiation. Beam intensity was about 120 mW cm^{-2}.

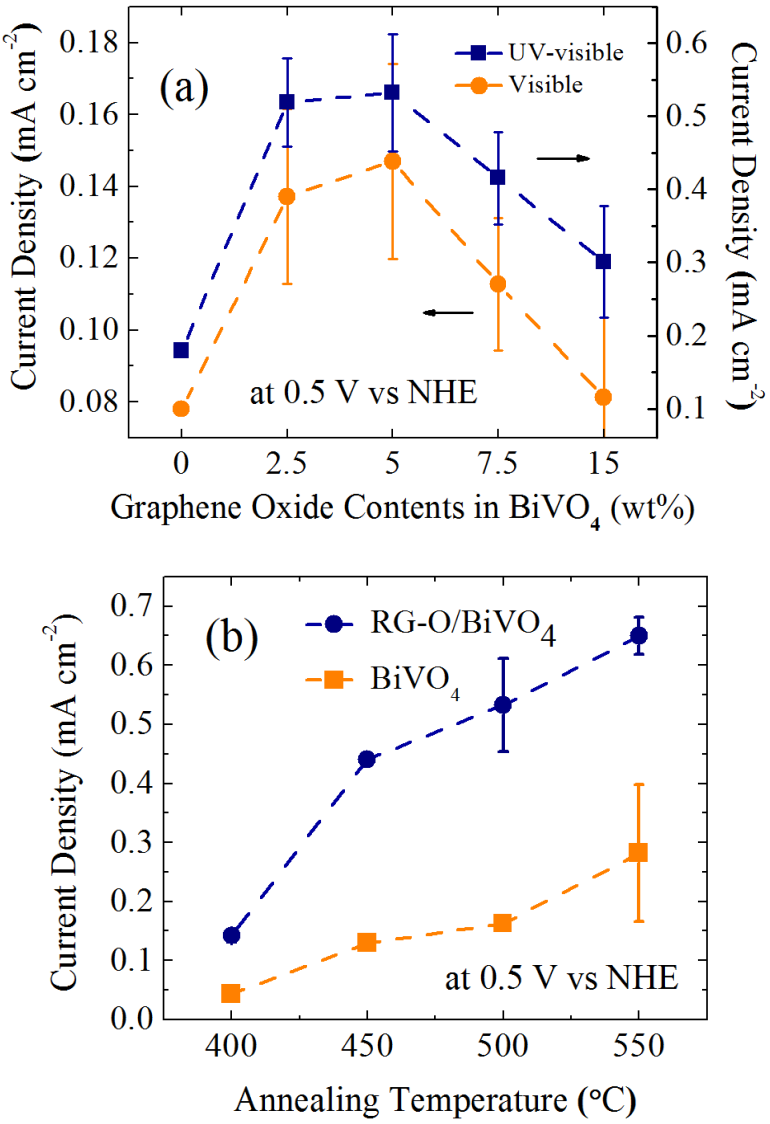

Figure 4.4. Photocurrent dependence of RG-O/$BiVO_4$ composite electrode on the weight ratio of G-O to $BiVO_4$ for sulfite oxidation (a) and on the annealing temperature on photocurrent of RG-O/$BiVO_4$ composite electrode for sulfite oxidation (b). RG-O/$BiVO_4$ composite electrodes were drop-casted on FTO and annealed at 500 ℃ for 3 hr

in air in (a). The amount of G-O in the precursor solution was 5 wt% of the resulting $BiVO_4$ in (b) and RG-O/$BiVO_4$ composite electrodes were annealed at various temperatures for 3 hr in air. The photocurrent was measured at 0.5 V (vs NHE) in 0.1 M Na_2SO_3 and 0.1 M Na_2SO_4 aqueous solution under UV-visible irradiation. Note that the weight ratio of G-O is based on the G-O prepared in the precursor solution of metal oxide, and the weight ratio of RG-O in the resulting electrode is likely changed during the thermal process used for fabricating the electrodes.

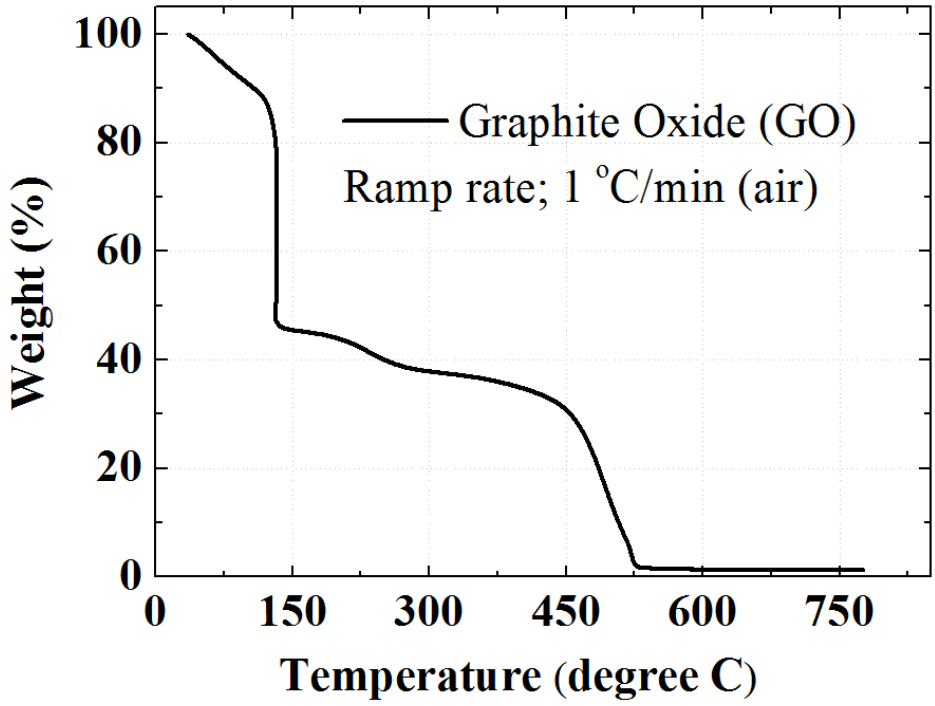

Figure 4.5. Thermogravimetric analysis (TGA) of graphite oxide (GO) in air. Temperature was ramped from room temperature to 800 ℃ at a ramp rate of 1 ℃ per minute.

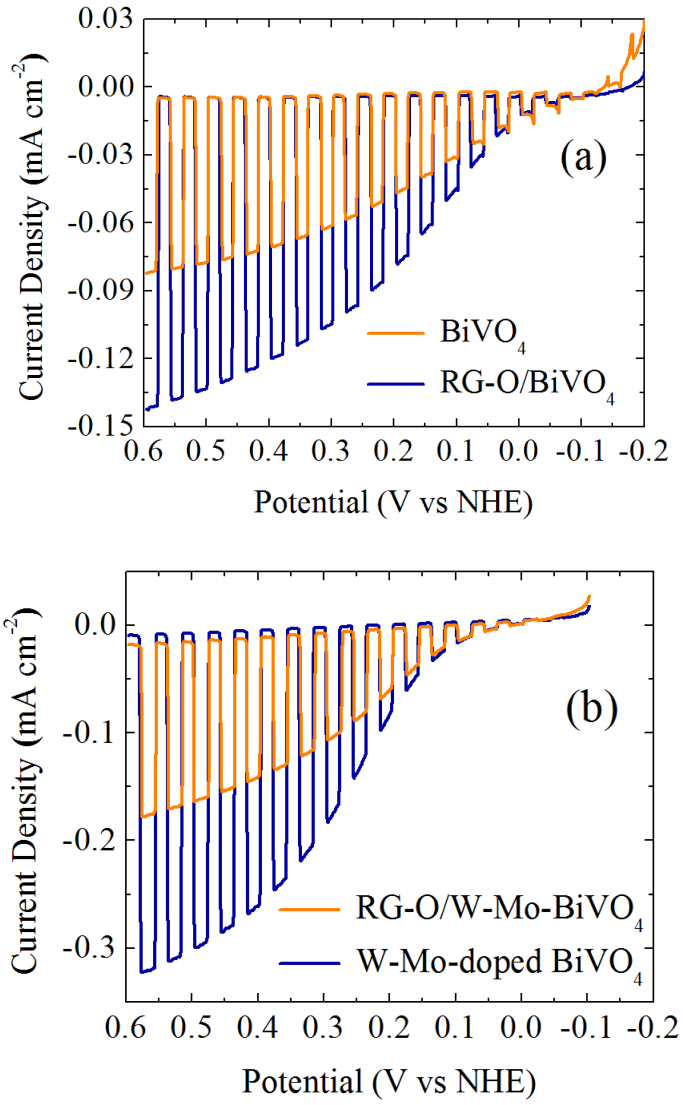

Figure 4.6. Linear sweep voltammograms of (a) $BiVO_4$ (yellow) and RG-O/$BiVO_4$ (blue) (b) W-Mo-doped $BiVO_4$ (blue) and RG-O/W-Mo-doped $BiVO_4$ (yellow) in 0.1 M Na_2SO_3 and 0.1 M Na_2SO_4 aqueous solution (pH 7, 0.2 M sodium phosphate buffered) under chopped visible irradiation. Scan rate was 20 mV sec^{-1}.

photoactivity of RG-O/$BiVO_4$ for sulfite oxidation (Figure 4.4(b)). The results show that RG-O/$BiVO_4$ or $BiVO_4$ fabricated at 400 ℃ has a far lower photoactivity, i.e., three times lower photocurrent at 0.5 V than those annealed at temperatures above 450 ℃.

The lower photocurrent of the composite electrodes prepared at 400 ℃ originated from the low photoactivity of tetragonal scheelite-like $BiVO_4$. The XRD pattern, shown in Figure 4.7, indicates that tetragonal scheelite-like $BiVO_4$ is formed in RG-O/$BiVO_4$ for the annealing temperature of 400 ℃, but the peaks from this tetragonal phase are not observed in RG-O/$BiVO_4$ at annealing temperatures above 450 ℃ as shown in Figure 4.8. Monoclinic scheelite-like $BiVO_4$, with a smaller bandgap of 2.4 eV, is much more photoactive than the tetragonal scheelite-like $BiVO_4$ (bandgap of 2.9 eV).[30] In addition, TGA analysis in Figure 4.5 shows that G-O is thermally reduced at temperatures of about 150 ℃ and both 400 ℃ and 450 ℃ are well above the temperature required for thermal reduction of G-O. XPS spectra for C1s of RG-O/$BiVO_4$ shown in Figure 4.9 indicate that the G-O in the precursor solution is being reduced at the elevated temperatures(see Figure 4.10 for survey scan).[31] However, further work is needed to study the chemistry of thermal reduction of G-O in air atmosphere and chemical environments used here, i.e., ethylene glycol.

In summary, the photoactivity of RG-O/$BiVO_4$ composite is greatly affected by the properties of the host $BiVO_4$. Also, XRD measurements show that RG-O does not disrupt the formation of the $BiVO_4$ crystal structure for the simple drop-casting method. With properly prepared $BiVO_4$, the increased photoactivity of the RG-O composite

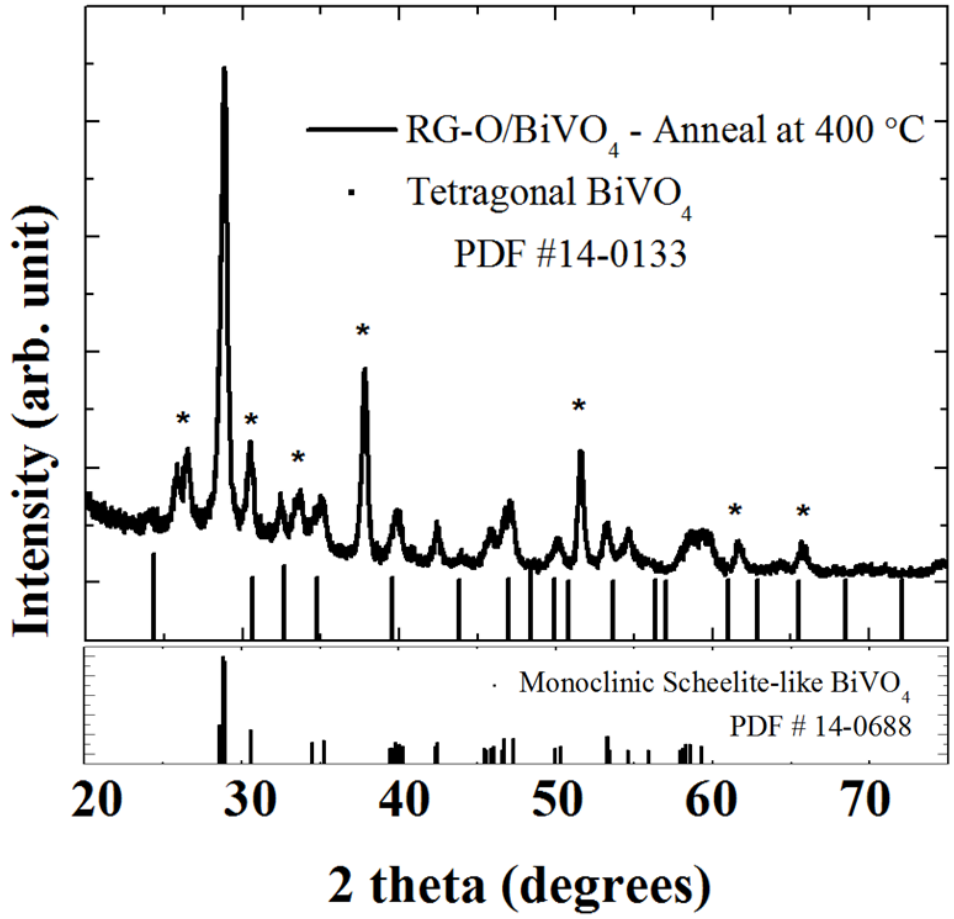

Figure 4.7. XRD pattern of RG-O/$BiVO_4$ annealed at 400 ℃. The reference patterns of the tetragonal scheelite $BiVO_4$ (PDF #14-0133), monoclinic scheelite-like $BiVO_4$ (PDF #14-0688), and patterns from FTO substrate (*) are also indicated.

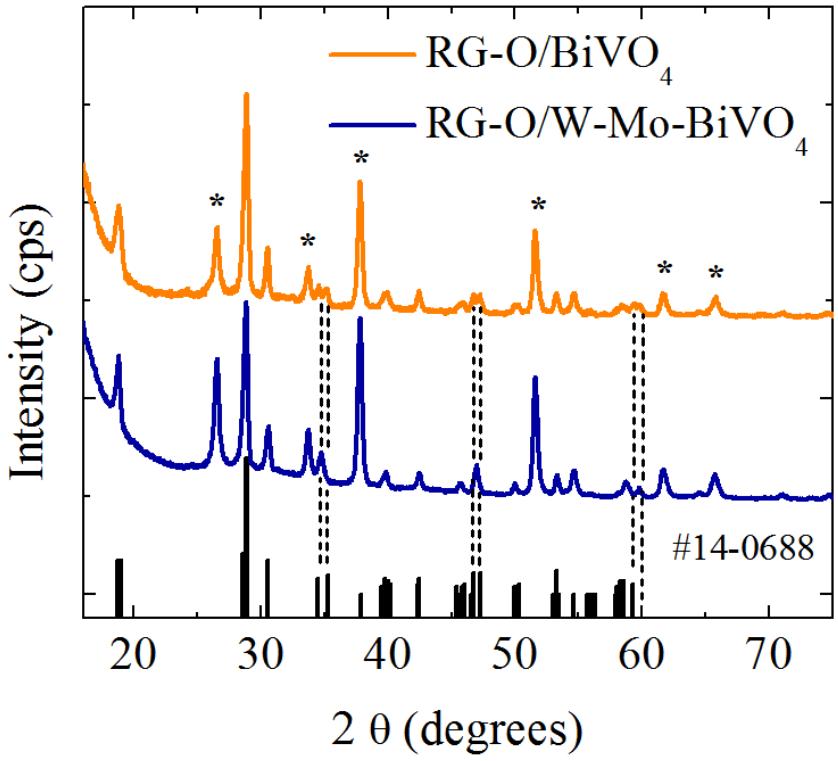

Figure 4.8. XRD patterns of RG-O/$BiVO_4$ (yellow) and RG-O/W-Mo-doped $BiVO_4$ (blue) annealed at 500 ℃. The reference patterns of the monoclinic scheelite-like $BiVO_4$ (PDF #14-0688, bottom line) and patterns from FTO substrate (*) are also indicated. Dotted lines indicate the characteristic shift of peaks from undoped $BiVO_4$ to the W-Mo-doped $BiVO_4$.

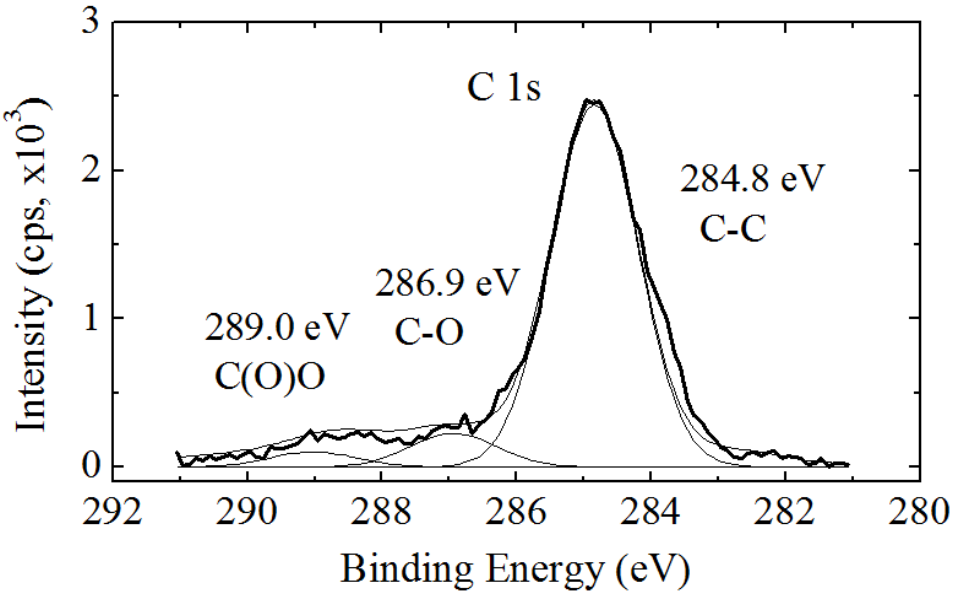

Figure 4.9. XPS spectra for C1s of RG-O/$BiVO_4$ composite electrodes. The RG-O/$BiVO_4$ was prepared from 5 wt% G-O precursor solution on the FTO substrate. The drop-casted film was annealed at 500 ℃ for 3 hr in air. Note that peaks are shifted (+1 eV) to compensate the sample charging effect in the XPS.

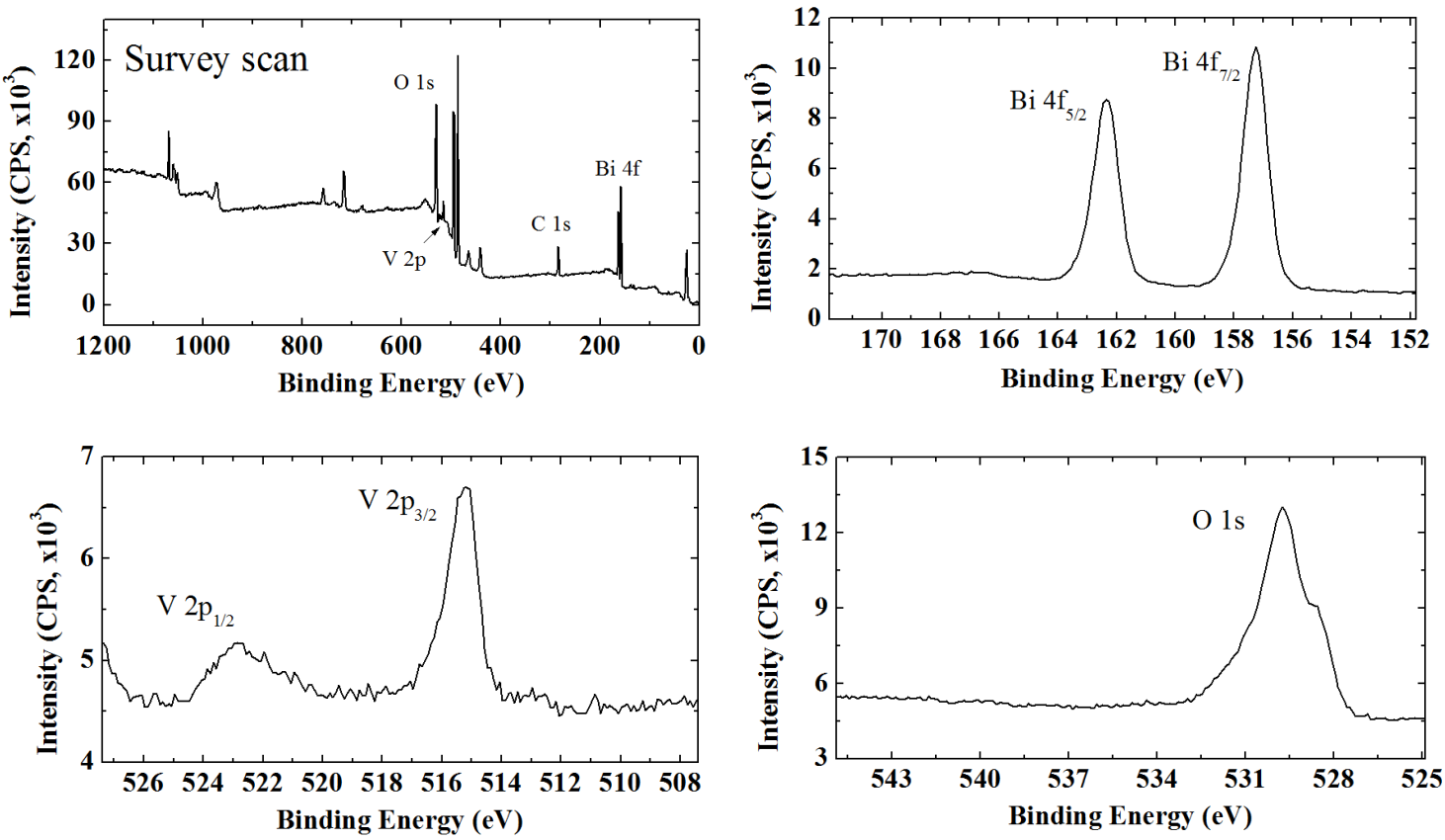

Figure 4.10. XPS spectra for RG-O/$BiVO_4$ composite electrodes. The RG-O/$BiVO_4$ was prepared from 5 wt% G-O precursor solution on the FTO substrate. The drop-casted film was annealed at 500 ℃ for 3 hr in air. Note that peaks are shifted (+1 eV) to compensate the sample charging effect in the XPS.

electrodes indicates that RG-O is an excellent additive for the drop-casted $BiVO_4$ to improve the photocatalytic activity.

RG-O composite electrodes with W-Mo-doped $BiVO_4$ were also prepared. W-Mo-doped $BiVO_4$ is a photocatalyst with several times greater photoactivity for water oxidation than undoped $BiVO_4$.[5] Enhanced separation of excited electron-hole pairs has been suggested as a reason for the improved photoactivity of W-Mo-doped $BiVO_4$. Briefly, the modified electronic structure of $BiVO_4$ by doping W and Mo with a small shift of the flat band potential increases the electron (or hole) transfer in $BiVO_4$.[5]

To determine if a further improvement of photoactivity of the W-Mo-doped $BiVO_4$ could be realized an RG-O composite electrode of W-Mo-doped $BiVO_4$ (RG-O/W-Mo-doped $BiVO_4$) was prepared from a solution of 5 wt% G-O and metal salts in ethylene glycol. Again note, RG-O does not affect the crystal formation of drop-casted W-Mo-doped $BiVO_4$ as shown by the XRD (Figure 4.8). In other words, XRD patterns of RG-O/W-Mo-doped $BiVO_4$ have the peaks from monoclinic scheelite-like $BiVO_4$ along with characteristic peak shifts caused by the tetragonal deformation of the monoclinic scheelite-like $BiVO_4$ by the doping of W and Mo at 35, 47, and 59 ^{o} in Figure 4.8. However, the observed photoactivity of RG-O/W-Mo-doped $BiVO_4$ was smaller than that of W/Mo-doped $BiVO_4$ without RG-O (Figure 4.3(b)). Photocurrent for sulfite oxidation measured at 0.5 V decreased about 40 % from 1.7 mA cm^{-2} to 1.0 mA cm^{-2} by the addition of RG-O to W-Mo-doped $BiVO_4$ under UV-visible irradiation (see Figure 4.6 for visible response). Effects of the annealing temperature on the photoactivity were

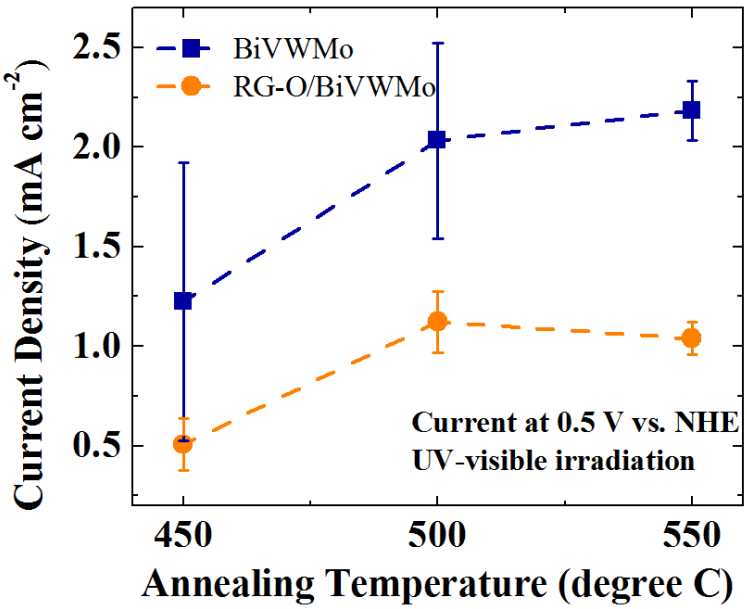

Figure 4.11. Effects of annealing temperature on photocurrent of RG-O/W-Mo-doped $BiVO_4$ composite electrodes for sulfite oxidation. RG-O/W-Mo-doped $BiVO_4$ composite electrodes were drop-casted on FTO and annealed at various temperature for 3 hr in air. Amount of G-O in the precursor solution was 5 wt% of the resulting W-Mo-doped $BiVO_4$. Photocurrent was measured at 0.5 V (vs. NHE) in 0.1 M Na_2SO_3 and 0.1 M Na_2SO_4 aqueous solution under UV-visible irradiation. Beam intensity from full Xenon lamp was about 120 mW cm^{-2}.

also studied for the RG-O/W-Mo-doped $BiVO_4$ at temperatures ranging from 450 ℃ to 550 ℃ (Figure 4.11) and RG-O/W-Mo-doped $BiVO_4$ shows lower photocurrent than W-Mo-doped $BiVO_4$ at all temperatures. The decrease of photoactivity of RG-O/W-Mo-doped $BiVO_4$ may imply that RG-O generates a recombination center or electron trap in W-Mo-doped $BiVO_4$. Also, the results indicate that the increased photocurrent of RG-O/$BiVO_4$ from $BiVO_4$ is not due to the increased electrode area or morphological changes of the photoelectrode; if the enhanced photoactivity of RG-O/$BiVO_4$ was due to the increased surface area of $BiVO_4$ as shown in the SEM images (Figure 4.12), a similar effect would also be seen for RG-O/W-Mo-doped $BiVO_4$.

It is established in sulfite oxidation that the incorporation of RG-O into $BiVO_4$ improves the photoactivity of undoped $BiVO_4$ as described above. There has also been a report of the improved photoelectrochemical water oxidation on RG-O/$BiVO_4$ composite electrodes.[16] However, the photocurrent measured for water oxidation showed that the increase of photocurrent by the RG-O addition to $BiVO_4$ is less marked for water oxidation than that for sulfite oxidation (Figure 4.13(a)). The enhancement of photocurrent for water oxidation by RG-O addition to $BiVO_4$ was only about 30 % at the potential of 0.6 V from 30 μA cm^{-2} to 40 μA cm^{-2}. Although there is a report of very large increases in photocurrent by addition of RG-O to $BiVO_4$ from a few μA cm^{-2} to tens of μA cm^{-2} for water oxidation,[16] in this study the effect of RG-O on $BiVO_4$, i.e., reduced electron-hole recombination in the thin film, is apparently smaller for the water oxidation than that for the sulfite oxidation. The smaller improvement of photocurrent with RG-O addition to $BiVO_4$ can be caused by the slower kinetics of inner-sphere reactions of water

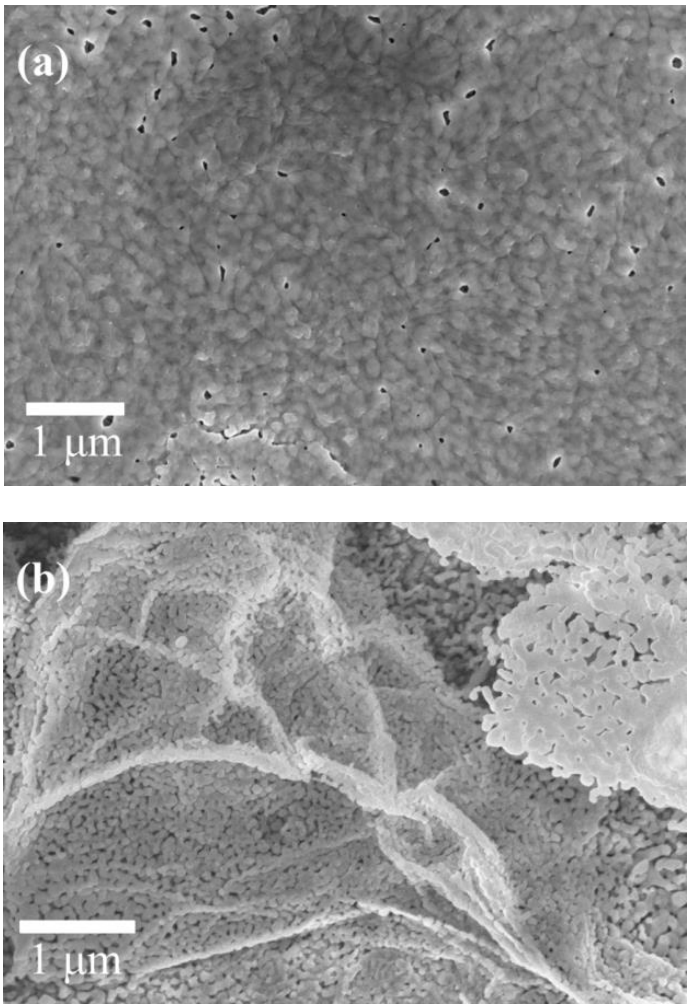

Figure 4.12. SEM images of (a) $BiVO_4$ and (b) RG-O/$BiVO_4$ which was drop-casted on FTO. RG-O/$BiVO_4$ was prepared with 5 wt% G-O and annealed at 500 ℃ in air for 3hr.

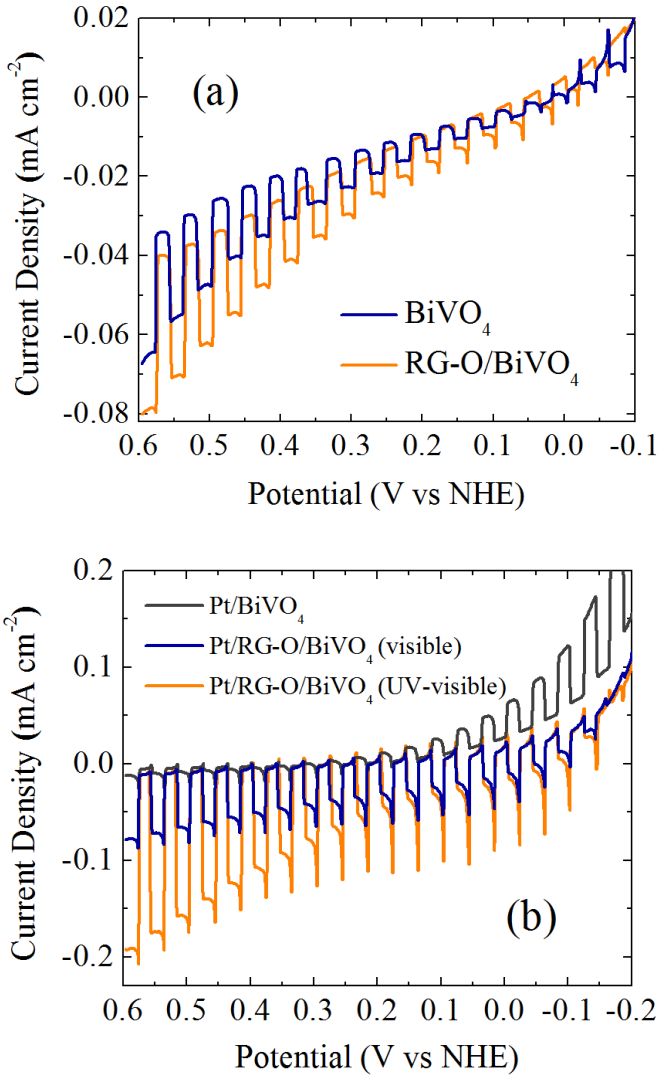

Figure 4.13. Linear sweep voltammograms of (a) $BiVO_4$ (blue) and RG-O/$BiVO_4$ (yellow) and (b) Pt/W-Mo-doped $BiVO_4$ (yellow for UV-Visible, blue for visible) and Pt/ $BiVO_4$ (black) for water oxidation in 0.1 M Na_2SO_4 aqueous solution (pH 7, 0.2 M sodium phosphate buffered). Scan rate was 20 mV sec^{-1}. Photocurrent was measured under chopped UV-visible irradiation. Beam intensity was about 120 mW cm^{-2}.

oxidation compared with the fast and irreversible sulfite oxidation. In other words, slow charge transfer from the photocatalyst to the adsorbate is the rate-determining step of photo-induced water oxidation. As a result, the effective separation of electron-hole pairs of RG-O/$BiVO_4$ is not apparently achieved for water oxidation yet is obvious for the fast sulfite oxidation. In addition, for W-Mo-doped $BiVO_4$ the negative effect of RG-O on the photoactivity of W-Mo-doped $BiVO_4$ was also confirmed in water oxidation (not shown here).

To increase the kinetics of water oxidation on $BiVO_4$ and RG-O/$BiVO_4$, a Pt electrocatalyst was photodeposited onto the electrodes.[32] The results in Figure 4.13(b) show that for water oxidation the photooxidation current of RG-O/$BiVO_4$ increased about five times by the addition of Pt catalyst from 40 μA cm^{-2} to 200 μA cm^{-2} at 0.6 V. In contrast to RG-O/$BiVO_4$, $BiVO_4$ without RG-O exhibited no improvement from the catalyst. Pt/$BiVO_4$ actually showed slightly lower currents than the film without the electrocatalyst. It indicates that $BiVO_4$ without G-O still suffers from the severe electron-hole recombination which limits the overall rate of reactions. However, it is also possible the Pt electrocatalysts were not properly photodeposited on $BiVO_4$ without G-O as the $BiVO_4$ shows poor photoactivity than RG-O/$BiVO_4$ in the given experimental conditions.

Finite elements analysis was performed to study the effects of addition of RG-O to $BiVO_4$. Experimental results shown in Figure 4.3 for sulfite oxidation were used to fit the simulation parameters, i.e., the hole/electron transfer rate constants (k_f/k_b in the equation (4-17) and (4-18)), the surface recombination rate constants (k_{SurRec}), the

electron/hole mobility (μ_n/μ_p), and the electron/hole recombination lifetime (τ_n/τ_p) of $BiVO_4$.

The simulated LSVs of $BiVO_4$, R-GO/$BiVO_4$ and W-Mo-doped $BiVO_4$ electrodes are shown in Figure 4.14 with the experimental results. The fitting parameters used for simulations are summarized in Table 4.2 and Table 4.3. The electron/hole diffusion length ($L_{n/p}$) calculated from diffusion coefficients and recombination lifetime was 2.8/1.1 nm for the electron/hole, respectively.

$$L_{n/p} = (D_{n/p} \times \tau_{n/p})^{0.5} \quad (4\text{-}22)$$

The recombination lifetime (~1 ps) and diffusion length (~2 nm) of $BiVO_4$ are similar to that reported for α-Fe_2O_3 which results in a poor photoactivity.[33] However, as the RG-O was added to $BiVO_4$, it provides a facile channel for electron transfer that increases the electron/hole mobility and the diffusion length. The electron/hole diffusion length increases about three times from 2.8/1.1 nm to 7.3/3.5 nm with the addition of RG-O to $BiVO_4$ (Table 4.3). The electron/hole diffusion length of W-Mo-doped $BiVO_4$ was even longer than that of RG-O/$BiVO_4$ as it is expected from the measured photocurrent in Figure 4.3 (16/9.3 nm). However, the obtained electron/hole recombination lifetime of photoelectrodes was extremely short as 0.1~0.3 ps. The electron/hole diffusion length of $BiVO_4$, RG-O/$BiVO_4$, and W-Mo-doped $BiVO_4$ are still much smaller than, for example, that of TiO_2 (~10 μm). So, W-Mo-doped $BiVO_4$ showed low fill factors in the current-potential behavior compared with the TiO_2.[34] However, the digital simulations show that improved electron/hole mobility and lifetime by addition of RG-O or W/Mo into $BiVO_4$ that results in a less electron/hole recombination

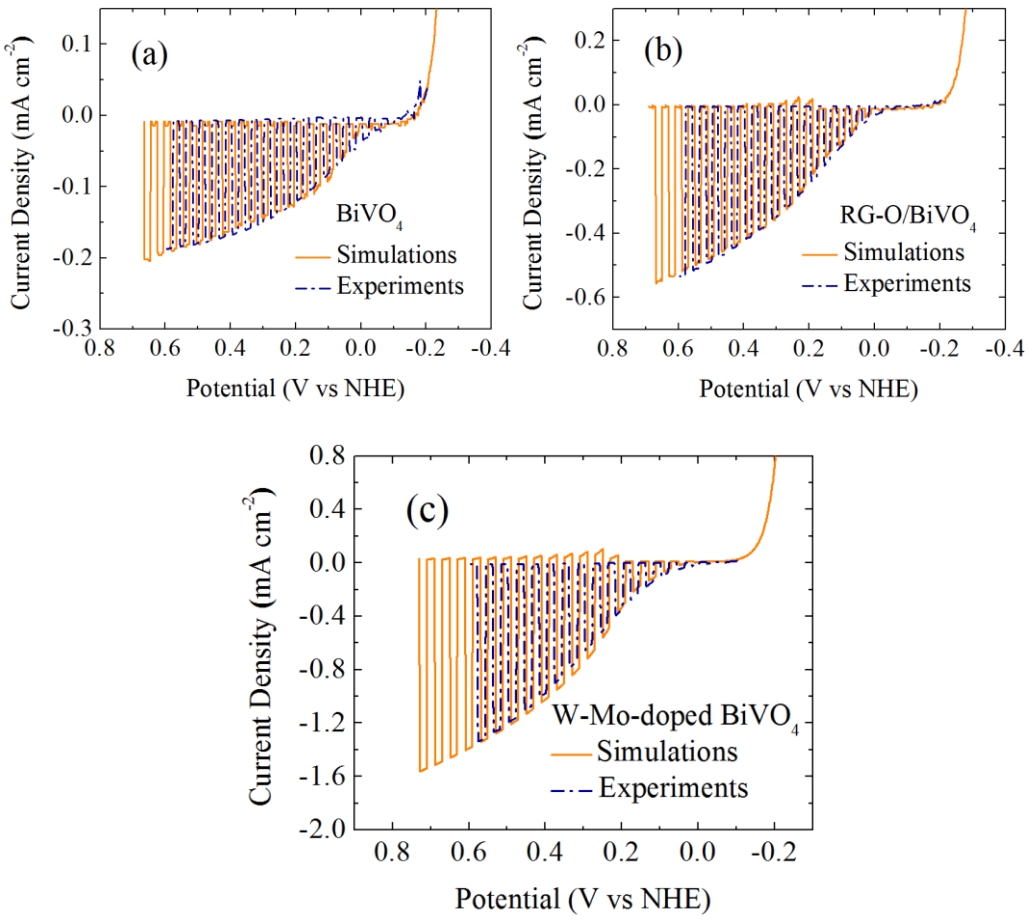

Figure 4.14. Comparison of simulated LSVs (yellow solid) to experimental results (blue dash) of (a) $BiVO_4$, (b) RG-O/$BiVO_4$, and (c) W-Mo-doped $BiVO_4$. The experimental results were taken from Figure 4.3 for sulfite oxidation under UV-visible irradiation. Scan rate was 20 mV s^{-1}. Parameters used for simulation fitting are summarized in Table 4.1 and Table 4.2.

Parameter	Value			Units	Description
	$BiVO_4$	RG-O/$BiVO_4$	W-Mo-$BiVO_4$		
μ_n	12	150	300	$cm^2\ V^{-1}\ s^{-1}$	Electron mobility
μ_p	2	35	100	$cm^2\ V^{-1}\ s^{-1}$	Hole mobility
τ_n	0.25	0.14	0.33	ps	Electron lifetime
τ_p	0.25	0.14	0.33	ps	Hole lifetime
n_d*	4×10^{19}	4×10^{18}	1×10^{17}	cm^{-3}	Donor doping density
k_f	8×10^{-17}	8×10^{-17}	1.2×10^{-16}	$cm^3\ s^{-1}$	Rate constant of reaction(19)
k_b	4×10^{-20}	1×10^{-21}	4×10^{-20}	$cm^3\ s^{-1}$	Rate constant of reaction(20)
k_{SurRec}	1×10^{-4}	2×10^{-5}	1×10^{-4}	$cm^4\ s^{-1}$	Rate constant of reaction(7)
$E_{FlatBand}$	-0.53	-0.41	-0.31	V	Flat band potential vs NHE at pH 7

Table 4.2. Simulation input parameters for $BiVO_4$, R-GO/$BiVO_4$, and W-Mo-doped $BiVO_4$ electrodes shown in Figure 4.14. *The donor doping density (n_d) of W-Mo-$BiVO_4$ that is larger than $BiVO_4$ has been reported and the W-Mo-$BiVO_4$ may also have larger intrinsic doping density (n_i) than $BiVO_4$ with the higher doping level of W and Mo into $BiVO_4$. However, n_i was fixed as a constant for the simulations in Figure 4.14 for all the electrodes that resulted in the lower n_d for W/Mo-doped $BiVO_4$ than $BiVO_4$. (Park, H. S.; Kweon, K. E.; Ye, H.; Paek, E.; Hwang, G. S.; Bard, A. J., *J. Phys. Chem. C*, **2011,** *115*, 17870-17879.)

Parameter	Value			Units	Description
	$BiVO_4$	RG-O/$BiVO_4$	W-Mo-$BiVO_4$		
D_n	3.1×10^{-1}	3.8	7.8	$cm^2\ s^{-1}$	Electron diffusion coefficient
D_p	5.2×10^{-2}	9.0×10^{-1}	2.6	$cm^2\ s^{-1}$	Hole diffusion coefficient
L_n	2.8	7.3	16	nm	Electron diffusion length
L_p	1.1	3.5	9.3	nm	Hole diffusion length

Table 4.3. Values calculated from input parameters shown in Table 4.2.

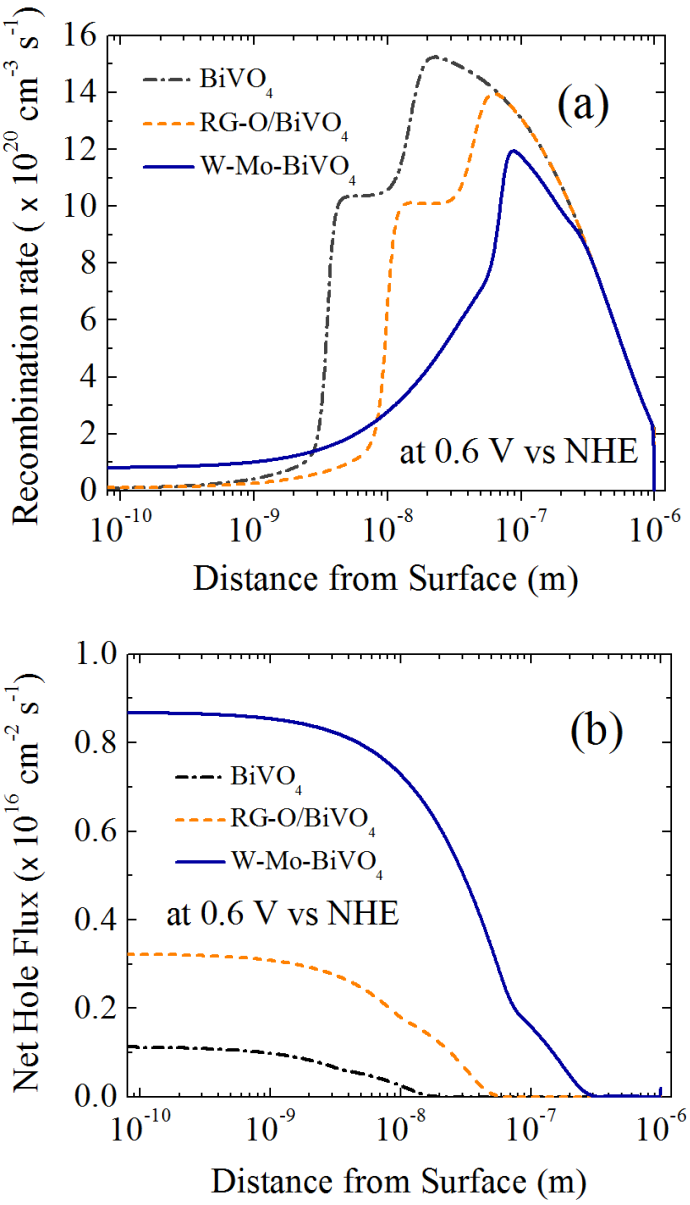

Figure 4.15. (a) Recombination rate of the excited electron-hole and (b) net hole flux in $BiVO_4$ (black dash-dot), RG-O/$BiVO_4$ (yellow dash), and W-Mo-doped $BiVO_4$ (blue solid) electrodes from the calculation shown in Figure 4.14.

rates in the bulk semiconductor (Figure 4.15(a)). The peak trap recombination rate of $BiVO_4$ electrode at 0.6 V (vs NHE) is 1.5 x 10^{21} cm^{-3} s^{-1}, and it decreases to 1.4 x 10^{21} cm^{-3} s^{-1} or to 1.2 x 10^{21} cm^{-3} s^{-1} for RG-O/$BiVO_4$ and W-Mo-doped $BiVO_4$ electrodes, respectively. As the recombination rate decreases, the net flux of the minority carrier at the electrode surface increases from 1 x 10^{15} cm^{-2} s^{-1} ($BiVO_4$) to 3 x 10^{16} (RG-O/$BiVO_4$) and to 9 x 10^{15} cm^{-2} s^{-1} (W/Mo-doped $BiVO_4$) as shown in Figure 4.15(b). The increased minority carrier flux and reduced recombination rates results in the improved photoactivity of RG-O/$BiVO_4$ and W-Mo-doped $BiVO_4$.

In summary, RG-O/$BiVO_4$ exhibited significantly improved photoactivity from $BiVO_4$ by the addition of the RG-O. The results indicate that RG-O efficiently facilitates the electron-hole separation of $BiVO_4$ or reduced electron-hole recombination rates in the bulk electrodes. Also, the metal doping of W/Mo into $BiVO_4$ shows positive effect on the photoactivity of $BiVO_4$. The quantitative semiconductor properties were estimated using finite elements analysis. In addition, the electrocatalyst, i.e., Pt, is required to release the kinetic limitations of water oxidation to realize the effect of reduced electron-hole recombination of the RG-O/$BiVO_4$ composite photocatalyst.

4.5 Conclusions

Addition of RG-O to the photocatalyst, $BiVO_4$, improved its photoactivity by about 3 times as studied in sulfite oxidation. It is believed that RG-O as a conductive channel of excited electrons reduces the electron-hole recombination rate, which is the main factor limiting high photoactivity of metal oxide photocatalysts. The improved

carrier diffusion length, carrier mobility and reduced recombination rate by the addition of RG-O and W/Mo dopants into $BiVO_4$ were studied by digital simulations. As results of the addition of RG-O and metal dopants into $BiVO_4$, the obtained electron/hole diffusion length increased from 2.8/1.1 nm ($BiVO_4$) to 7.3/3.5 nm (RG-O/$BiVO_4$) and to 16/9.3 nm (W/Mo-doped $BiVO_4$). However, improved electron-hole separation was not significant for water oxidation on RG-O/$BiVO_4$ because of the kinetic limitations of the inner-sphere water oxidation reaction; Pt as a catalyst was thus photodeposited onto RG-O/$BiVO_4$ to release the kinetic limitations. The resulting Pt/RG-O/$BiVO_4$ electrode showed several times higher photocurrent for water oxidation than Pt/$BiVO_4$ or $BiVO_4$.

4.6 References

[1] Alexander B. D.; Kulesza P. J.; Rutkowska I.; Solarska R.; Augustynski J. *J. Mater. Chem.* **2008,** 18, 2298-2303.

[2] Cesar I.; Kay A.; Martinez J. A. G.; Gratzel M. *J. Am. Chem. Soc.* **2006,** 128, 4582-4583.

[3] Cole B.; Marsen B.; Miller E.; Yan Y.; To B.; Jones K.; Al-Jassim M. *J. Phys. Chem. C* **2008,** 112, 5213-5220.

[4] Ye H.; Lee, J.; Jang, J. S.; Bard, A. J. *J. Phys. Chem. C* **2010**, *114*, 13322-13328.

[5] Park H. S.; Kweon K. E.; Ye H.; Paek E.; Hwang G. S.; Bard A. J. *J. Phys. Chem. C* **2011**, *115*, 17870-17879.

[6] Glasscock J. A.; Barnes P. R. F.; Plumb I. C.; Savvides N. *J. Phys. Chem. C.* **2007,** 111, 16477-16488.

[7] Kennedy J. H.; Frese Jr. K. W. *J. Electrochem. Soc.* **1978,** 125, 709-714.

[8] Butler M. A. *J. Appl. Phys.* **1977,** 48, 1914-1920.

[9] Lin Y.; Liu X.; Sheehan S.; Wang D. *J. Am. Chem. Soc.* **2009,** 131, 2772-2773.

[10] Banerjee S.; Mohapatra S. K.; Misra M. *J. Phys. Chem. C* **2011**, 115, 12643-12649.

[11] Liu R.; Lin Y.; Chou L.-Y.; Sheehan S. W.; He W.; Zhang F.; Hou H. J. M.; Wang D. *Angew. Chem. Int. Ed.* **2011,** 50, 499-502.

[12] Lin Y.; Zhou S.; Sheehan S. W.; Wang D. *J. Am. Chem. Soc.* **2011,** 133, 2398-2401.

[13] Mohapatra S. K.; Raja K. S.; Mahajan V. K.; Misra M. *J. Phys. Chem. C* **2008,** 112, 11007-11012.

[14] Ng Y. H.; Linghtcap I. V.; Goodwin K.; Matsumura M.; Kamat P. V. *J. Phys. Chem. Lett.* **2010**, 1, 2222-2227.

[15] Williams, G.; Seger B.; Kamat P. V. *Acs Nano* **2008**, 2, 1487-1491.

[16] Ng Y. H.; Iwase A.; Kudo A.; Amal R. *J. Phys. Chem. Lett.* **2010**, 1, 2607-2612.

[17] Fleetwood D. M.; Winokur P. S.; Reber Jr. R. A.; Meisenheimer T. L.; Schwank J. R.; Shaneyfelt M. R.; Riewe L. C. *J. Appl. Phys.* **1993,** 73, 5058-5074.

[18] Brodie B. C. *Philos. Trans. R. Soc. London*, **1859**, 149, 249-259.

[19] Dreyer D. R.; Park S.; Bielawski C. W.; Ruoff R. S. *Chem. Soc. Rev.* **2010**, 39, 228-240.

[20] Loh K. P.; Bao Q.; Eda G.; Chhowalla M. *Nat. Chem.* **2010,** 2, 1015-1024.

[21] Potts J. R.; Dreyer D. R.; Bielawski C. W.; Ruoff R. S. *Polymer* **2011,** 52, 5-25.

[22] Lee D. H.; Kim J. E.; Han T. H.; Hwang J. W.; Jeon S.; Choi S.-Y.; Hong S. H.; Lee W. J.; Ruoff R. S.; Kim S. O. *Adv. Mater.* **2010,** 22, 1247-1252.

[23] Stoller M. D.; Park S.; Zhu Y.; An J.; Ruoff R. S. *Nano Lett*. **2008**, *8*, 3498-3502.

[24] Laser, D.; Bard, A. J. *J. Electrochem. Soc.* **1976,** *123,* 1828-1832.

[25] Orazem, M. E.; Newman, J. *J. Elctrochem. Soc.* **1984,** *131,* 2574-2582.

[26] Anz, S. J.; Lewis, N. S. *J. Phys. Chem. B* **1999,** *103,* 3908-3915.

[27] Hummers W. S.; Offeman R. E. *J. Am. Chem. Soc.* **1958**, *80*, 1339.

[28] Kraeutler B.; Bard A. J. *J. Am. Chem. Soc.* **1978**, *100*, 4317-4318.

[29] Foley, J. M.; Price, M. J.; Feldblyum, J. I.; Maldonado, S. *Energy Environ. Sci.* **2012,** *5,* 5203-5220.

[30] Tokunaga S.; Kato H.; Kudo A. *Chem Mater.* **2001**, *13*, 4624-4628.

[31] Yang D.; Velamakanni A.; Bozoklu G.; Park S.; Stoller M.; Piner R. D.; Stankovich S.; Jung I.; Field D. A.; Ventrice Jr. C. A.; Ruoff R. S. *Carbon* **2009**, *47*, 145-152.

[32] Ye H.; Park H. S.; Bard A. J. *J. Phys. Chem. C.* **2011**, *115*, 12464-12470.

[33] Wheeler, D. A.; Wang, G.; Ling, Y.; Li, Y.; Zhang, J. Z. *Energy Environ. Sci.* **2012**, *5*, 6682-6702.

[34] Leng, W. H.; Barnes, P. R. F.; Juozapavicius, M.; O'Regan, B. C.; Durrant, J. R. *J. Phys. Chem. Lett.* **2010**, *1*, 967-972.

Chapter 5. Photoelectrochemical Water Splitting Device

5.1 Introduction

We show solar-fuel, i.e., H_2, generation, from true splitting of water (H_2 and O_2 formation) without external bias or sacrificial donors in a photoelectrochemical (PEC) device. PEC reactions, the hydrogen evolution reaction (HER) and oxygen evolution reaction (OER), occur on the interface between a semiconductor electrode, usually with an electrocatalyst, and a solution with a suitable counter electrode. The semiconductor electrode absorbs photons with a higher energy than its band gap and the absorbed energy excites a bonding electron of the semiconductor to the conduction band with a hole left in the valence band. The excited electron and hole are separated by the electric field created near the interface between the semiconductor and solution. Through the reactions on the semiconductor, the absorbed radiant energy is converted and stored as chemical energy, e.g., H_2 and O_2 from the photolysis of water.[1,2]

Efficiently and inexpensively converting radiant energy to chemical energy, and especially the water splitting reaction, has been a great challenge for many decades as the ultimate solution of a sustainable energy source.[3] To attain the practical photolysis of water in an economical way, (a) the semiconductor must be stable and not experience decomposition from the strong reductive and oxidative power of the excited electron and hole, (b) the band gap of the semiconductor must be small enough to utilize most of the solar energy spectrum but large enough to drive the desired chemical reaction, and (c) the semiconductor must have suitable positions of band-edges for the chemical reactions of

interest. In addition to those chemical and electrochemical criteria, the material should be abundant and inexpensive, so the total system of water photolysis can compete with other energy conversion systems, e.g., H_2 production by electrolysis using photovoltaic solar cells, steam reforming from fossil fuels, or pyrolysis of biomass.[4] Typical rough benchmarks generally quoted are 10 % solar efficiency, 10-year lifetime and installed power of $1/watt.[3]

After Fujishima and Honda suggested the possible photolysis of water using a TiO_2 photoanode,[5] tremendous efforts have been made to realize water splitting using solar energy. A major part of the research focused on finding a single useful material for this reaction, mostly based on large band gap metal oxide semiconductors like TiO_2, $SrTiO_3$, and others.[6,7,8] However, it is pretty clear that the needed driving force for water splitting (probably in the vicinity of 2 V which is in fact significantly larger than the often-quoted thermodynamic value of 1.23 V) requires a semiconductor band gap that can only absorb a small portion of the solar spectrum. To obtain a reasonable efficiency using smaller band gap materials, two or more photons must be absorbed to drive a single electron in the reaction. Other systems have been suggested, e.g., buried p-n junction electrodes,[9,10,11] tandem structures with dye-sensitized solar cells and a metal oxide,[12] and multiple bipolar photoelectrodes in a series connection,[13,14,15] where two or more semiconductors are combined to cover a wide solar wavelength window and create a sufficient potential to drive the water splitting reaction.

Among the proposed systems, a dual n-type semiconductor device (or Z-scheme) was suggested by this group in 1979 to overcome the single photoelectrode problem.[16]

Since that time, many efforts have been made to find a suitable combination of photoelectrodes and redox couples to demonstrate PEC water splitting by a Z-scheme.[17] Combinatorial methods have been explored as a quick screening method to find suitable photoanodes for water oxidation which utilize metal oxides,[18] e.g. Fe_2O_3,[19,20,21,22] WO_3,[23,24] $BiVO_4$,[25,26] and chalcogenides, e.g., CdSe, $CuInSe_2$, and Cu_2ZnSnS-Se.[27,28,29]

The photocatalytic activity of $BiVO_4$ was first reported by Kudo and co-workers in 1999,[30] and has been studied as a promising material for photo-oxidation of water because it has good chemical stability and the ability to harvest visible radiation.[31,32] $BiVO_4$ is a yellow pigment and was first reported as a naturally existing mineral in 1974.[33] Moreover, as described above, the photoactivity of $BiVO_4$ has been improved significantly by the combinatorial method employed by our group. Scanning electrochemical microscopy (SECM) has been used to screen metal dopants for $BiVO_4$, e.g., W and Mo,[25,26] that significantly improve the photoactivity of $BiVO_4$. In addition, our group has determined that Pt and cobalt oxides are good water oxidation electrocatalysts for W-doped $BiVO_4$.[35] As a result, W and Mo-doped $BiVO_4$ treated with $AgNO_3$[34] to passivate surface recombination and photodeposited with Pt, i.e., Pt-W/Mo-$BiVO_4$, shows more than 20 times enhanced photocurrent for the OER compared to that of untreated $BiVO_4$ (Figure 5.1(a)).

In this chapter, unbiased water splitting using a Z-scheme system is demonstrated using two Pt-W/Mo-$BiVO_4$ photoelectrodes or using a combination of $Zn_{0.2}Cd_{0.8}Se$ and Pt-W/Mo-$BiVO_4$. Redox couples in the Z-scheme configuration were I^-/IO_3^- for Pt-W/Mo-$BiVO_4$ electrodes or S_n^{2-}/S^{2-} for $Zn_{0.2}Cd_{0.8}Se$ electrodes.

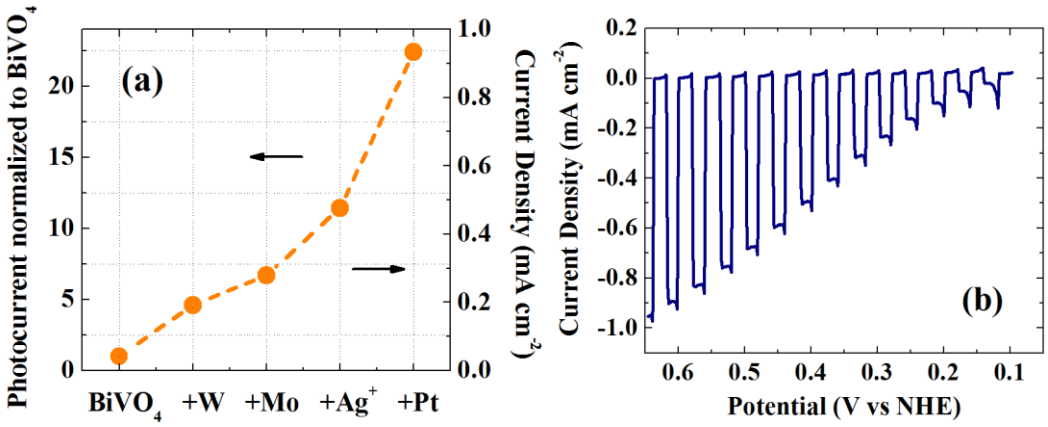

Figure 5.1. (a) Summary of photoactivity development of $BiVO_4$ and (b) linear sweep voltammogram of Pt-W/Mo-$BiVO_4$ for water oxidation under chopped UV-visible irradiation. Photocurrent was measured for water oxidation in neutral aqueous solution (pH 7, 0.2 M phosphate buffered, 0.1 M Na_2SO_4) under 120 mW cm^{-2} UV-visible irradiation. The photocurrent shown in (a) was chosen from the linear sweep voltammograms at 0.6 V (vs NHE) for different electrodes. Scan rate was 20 mV s^{-1}. Thin film electrodes of $BiVO_4$ or doped $BiVO_4$ were prepared by drop-casting precursor solution and the thickness of the resulting films was about 0.5 μm. W-doped $BiVO_4$ has a 5 atomic % W to (Bi+V) ratio and W/Mo-doped $BiVO_4$ has a 2 atomic % W and 6 % Mo to (Bi+V) ratio. For $AgNO_3$ treatment, W/Mo-$BiVO_4$ film was soaked in 10 mM $AgNO_3$ aqueous solution for 1 hr in the dark. Pt electrocatalyst was photodeposited under UV-visible irradiation for 30 min in 10 mM H_2PtCl_4 in the presence of 0.2 M MeOH.

5.2 Experimental

$Bi(NO_3)_3 \cdot 5H_2O$ (99.999%), $(NH_4)_{10}H_2(W_2O_7)_6 \cdot xH_2O$ (99.99%), and $Na_2S \cdot 9H_2O$ (98%) were obtained from Strem Chemicals (Newburyport, MA). $H_2PtCl_6 \cdot 6H_2O$ (99.9%), VCl_3 (99%), $Cd(NO_3)_2 \cdot 4H_2O$ (99.999%), and Ti foil (2.0 mm thick, 99.2 %) were purchased from Alfa-Aesar (Ward Hill, MA). $(CH_3)_2NC(Se)NH_2$ (97%), Se (100 mesh, 99.5%), $(NH_4)_6Mo_7O_{24} \cdot 4H_2O$ (99.98%), Na_2SO_4 (99.0%), $Ag(NO_3)$ (99%), $CoCl_2$ (98%), and Nafion perfluorinated resin solution (5 wt.% in lower aliphatic alcohols and water) were purchased from Sigma-Aldrich (St. Louis, MO). $ZnCl_2$ (98.55%), S (99.5%), and $NaIO_3$ (99.9%) were obtained from Mallinckrodt Baker (Phillipsburg, NJ). Na_2HPO_4 (99.9%), NaH_2PO_4 (99.5%), methanol (99.9%), isopropanol (99.5%), and ethylene glycol (99%) were purchased from Fisher Scientific (Pittsburg, PA). NaI (99%, EM Science, Gibbstown, NJ) were used as received. Fluorine-doped tin oxide (FTO, TEC 15, Pilkington, Toledo, OH) was used as the substrate for the film electrodes. Deionized Milli-Q water (D.I. water, 18 MΩ-cm) was used as the solvent in electrochemical experiments. Pt electrocatalyst supported on carbon (40 wt %, Pt/C, Johnson Matthey, London, UK) and a sulfonated tetrafluoroethylene membrane (51 μm thick, Nafion112, Dupont, Wilmington, DE) were used as received to prepare the membrane electrode assemblies.

Pt-W/Mo-doped $BiVO_4$ electrodes were prepared as previously described.[26,35] Briefly, a 20 μM $(NH_4)_{10}H_2(W_2O_7)_6 \cdot xH_2O$, 80 μM $(NH_4)_6Mo_7O_{24} \cdot 4H_2O$, 4.2 mM $Bi(NO_3)_3 \cdot 5H_2O$, and 5mM VCl_3 in ethylene glycol solution was prepared. Then, 100 μl of the precursor solution was applied onto an FTO substrate and it was annealed at 500

ºC for 3 h. The temperature was slowly ramped from room temperature to 500 ºC over 9 h. Then, the W/Mo-$BiVO_4$ film was treated in a 10 mM $Ag(NO_3)_3$ aqueous solution in the dark for 1 h.[34] The Pt electrocatalyst was photodeposited as previously reported.[35] The metal oxide film was placed in a 0.2 M MeOH and 10 mM H_2PtCl_6 aqueous solution and, while submerged, it was irradiated with a xenon lamp (XBO 150 W, Osram, Munich, Germany) for 30 min with full output. The irradiation power was about 150 mW cm^{-2}.

$Zn_{0.2}Cd_{0.8}Se$ electrodes were prepared using a drop casting technique.[27] A 70 mM $ZnCl_2$, 0.5 M $Cd(NO_3)_2$, and 0.5 M $N(CH_3)_2NH_2CSe$ (dimethylselenourea) ethylene glycol solution was prepared and 0.1 M hydrazine was added to this solution to prevent the oxidation of dimethylselenourea by dissolved O_2 in the ethylene glycol. In addition to preventing oxidation, hydrazine provides a possible chemical combustion during low temperature selenization of $Zn_{0.2}Cd_{0.8}Se$.[36] To form a uniform film of chalcogenide, multiple drop-casted coats (usually three) were applied. For each coat, 50 μL of the precursor solution was applied to the surface of the FTO (1 cm^2) substrate. Then, the film was placed into the pre-heated oven to evaporate the solvent at 140 °C for about 30 min in ambient air. Finally, the film was annealed at 350 °C for 30 min under Ar flow with a flow rate of about 10 mL / min in a tube furnace. The ramping rate of the furnace temperature was 20 °C / min beginning from room temperature. To prevent excess loss of Se from the film, around 0.2 g of selenium powder was placed beside the film and it was usually completely evaporated during the selenization. By selenization, the color of the $Zn_{0.2}Cd_{0.8}Se$ film was changed from dark red to dark grey.

CoS electrodes were prepared on polished Ti foil (1.5 cm^2). The Ti foil was alternately dipped into the 0.5 M $CoCl_2$ and 0.5 M Na_2S aqueous solutions to form a powdery CoS film. After multiple coats of CoS, the film was annealed at 100 °C for 12 h with a ramp rate of 1 °C/min beginning from room temperature. The heat treatment was conducted under Ar flow with a flow rate of 10 mL/min.

The membrane electrode assembly used for H_2 detection consisted of Pt/C electrocatalyst and a proton conductive membrane as a solid electrolyte. The membrane was sulfonated by soaking the membrane in a 0.1 M aqueous sulfuric acid solution at the boiling temperature for 1 h. After washing the sulfonated membrane with D.I. water, the membrane was firmly secured between two glass plates where 1 cm x 2 cm windows were allowed to dry the membrane. Then, Pt/C electrocatalyst suspended in isopropanol with Nafion resin (30 wt % of Nafion resin to Pt/C) was sprayed onto the dried Nafion membrane using a spray gun (GP-1, Fuso Seiki Co., Tokyo, Japan). N_2 gas was used as the carrier medium for the deposition and both sides of the membrane were sprayed at room temperature.

A CH Instruments Model 630D Electrochemical Analyzer (Austin, TX) was used as a potentiostat for the electrochemical experiments. A platinum gauze counter electrode and a Ag/AgCl reference electrode in saturated KCl solution were used to complete the three electrode configuration. It should be noted that all reported potentials in the three electrode configuration are quoted with respect to the normal hydrogen electrode (NHE). For the PEC measurements, illumination was done with a xenon lamp (XBO 150 W, Osram, Munich, Germany) with full output for the UV-visible irradiation,

or with a 420 nm cut-off filter (WBF-3, Oriel, Darmstadt, Germany) for the visible irradiation. A silicon photodetector (Model 818-UV, Newport, Irvine, CA) with an attenuator (OD3, Newport) and an optical power meter (Model 1815-C and Model 1830-C, Newport) were used to obtain light intensities. A gas chromatography-mass spectroscopy analyzer (GC-2014, Shimadzu Scientific Instruments, Columbia, MD) was used to analyze the gases produced from the PEC device. The electrochemical cells for water splitting were home-built with borosilicate glass (Figure 5.3 and Figure 5.4).

5.3 Unbiased Z-scheme Water Splitting

A linear sweep voltammogram (LSV) of Pt-W/Mo-$BiVO_4$ is shown in Figure 5.1(b) for the OER. LSV measured under chopped UV-visible irradiation with an intensity of 120 mW cm^{-2} shows rapid photoresponses. A current density of about 1 mA cm^{-2} was obtained at 0.6 V beyond the photo-onset potential of the OER for Pt-W/Mo-$BiVO_4$ in neutral aqueous solution (0.1 M Na_2SO_4, pH 7, 0.2 M sodium phosphate buffered) at 120 mW cm^{-2}. Figure 5.2(a-yellow) also shows the photocurrent for the OER under stronger irradiation (440 mW cm^{-2}) than that in Figure 5.1(b) for the identical Pt-W/Mo-$BiVO_4$ electrode. The photocurrent increases about 4 times as the light intensity increased from 120 mW cm^{-2} to 440 mW cm^{-2} in Figure 5.2(a). Some of the results shown utilize this stronger illumination intensity to shorten the experimental time necessary to detect the generated gases on the electrodes. The irradiation power as measured by the optical power meter varied slightly and is noted in each experiment.

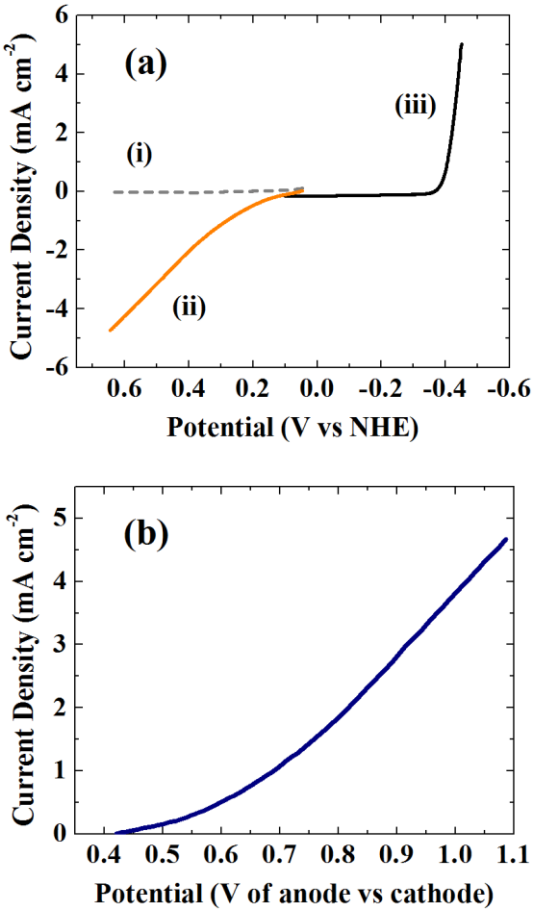

Figure 5.2. (a) Linear sweep voltammograms of Pt-W/Mo-$BiVO_4$ for water oxidation under dark (i) and under UV-visible irradiation with strong intensity of about 440 mW cm^{-2} (ii). Current for proton reduction was measured on a Pt mesh electrode (iii). The current was measured in 0.1 M Na_2SO_4 aqueous solution (pH 7, 0.2 M sodium phosphate buffered). Scan rate was 20 mV s^{-1}. (b) Current density and potential relationship is calculated from the data shown in (a) and it shows the water splitting current density for both proton reduction and water oxidation in a two electrode system as a function of potential difference between Pt-W/Mo-$BiVO_4$ and Pt electrodes in neutral aqueous solution.

The LSV in Figure 5.2(a) indicates that photocurrent for the OER on Pt-W/Mo-$BiVO_4$ begins around 50 mV vs NHE (line ii) demonstrating that the onset potential for the OER is largely shifted to the negative (by about 0.7 V) compared with the thermodynamic potential of O_2 evolution from water.

In Figure 5.2(a), proton reduction current begins at -0.4 V on platinum (Pt) electrodes (black line, iii) which is very close to the thermodynamic potential for proton reduction (5-1) in the neutral aqueous solution.

$$2H^+ + 2e \rightarrow H_2 \qquad (E^0 = -0.41 \text{ V at pH 7}) \qquad (5\text{-}1)$$

From the respective LSVs for the half reactions of water splitting, i.e. O_2 evolution (ii) and H_2 evolution (iii) as shown in Figure 5.2(a), the current density for water electrolysis under UV-visible irradiation using Pt-W/Mo-$BiVO_4$ and Pt is calculated as a function of the potential difference between the photoanode and the cathode in Figure 5.2(b). For example, to obtain a current density of 4 mA cm^{-2} in a two electrode configuration, H_2 generation occurs at -0.44 V (vs NHE), and the same current must flow through the anode for oxygen evolution at 0.58 V (vs NHE) as shown in Figure 5.2(a). This indicates that an electrochemical potential difference of 1 V (or 0.58 V – (-0.44 V)) needs to be applied between the anode and cathode to balance the electrochemical reactions in this two electrode system and generate a 4 mA current (Figure 5.2(b)). Then the minimum potential difference that must be applied between the Pt-W/Mo-$BiVO_4$ and the Pt electrodes to initiate water splitting under irradiation is about 0.4 V.

The additional potential needed in a PEC system not connected to an external power source can be supplied by a buried junction (e.g. one or more p-n junction semiconductor devices) or by another PEC cell, operating with a mediator (O,R). As shown in Figure 5.3(a), a pair of n-type semiconductors (semiconductor I (SCI) and semiconductor II (SCII)) can thus accomplish the photolysis of water in a Z-scheme.[16] Briefly, SCII and the metal electrode I (MI) are used for water splitting with the OER on SCII and the HER on MI in an aqueous solution. The other electrodes (SCI and MII) are used to absorb and convert additional photon energy to electrochemical energy by carrying out reduction and oxidation reactions in a separate cell containing an appropriate redox couple. For the system described here, Pt-W/Mo-$BiVO_4$ and Pt electrodes are used as SCII and MI as described above.

The redox couple O/R used was I^-/IO_3^-; this has been studied for photocatalytic water splitting by Abe et al. utilizing $SrTiO_2$, TiO_2, WO_3, and $BiVO_4$ powder.[37] They reported this redox couple was stable for prolonged experimental times. Thus the cell involved photooxidation of I^- on SCI (Pt-W/Mo-$BiVO_4$) and reduction of IO_3^- on MII (Pt).

LSVs for was I^-/IO_3^- redox reactions in aqueous solution (25 mM / 25 mM, pH 8.5) are shown in Figure 5.5(a). Reduction of IO_3^- occurs on Pt electrodes and the reduction current starts at 0.6 V with possible reactions occurred as listed below. The thermodynamic potentials below are calculated from Nernst equation for pH 8.5.[38]

$$2IO_3^- + 12H^+ + 10\ e^- \rightarrow I_2 + 6H_2O \qquad (E^0 = 0.59\ V \text{ at pH } 8.5) \qquad (5\text{-}2)$$

$$IO_3^- + 6H^+ + 6e^- \rightarrow I^- + 3H_2O \qquad (E^0 = 0.58\ V \text{ at pH } 8.5) \qquad (5\text{-}3)$$

$$I_2 + 2e^- \rightarrow 2I^- \qquad (E^0 = 0.54\ V \text{ at pH } 8.5) \qquad (5\text{-}4)$$

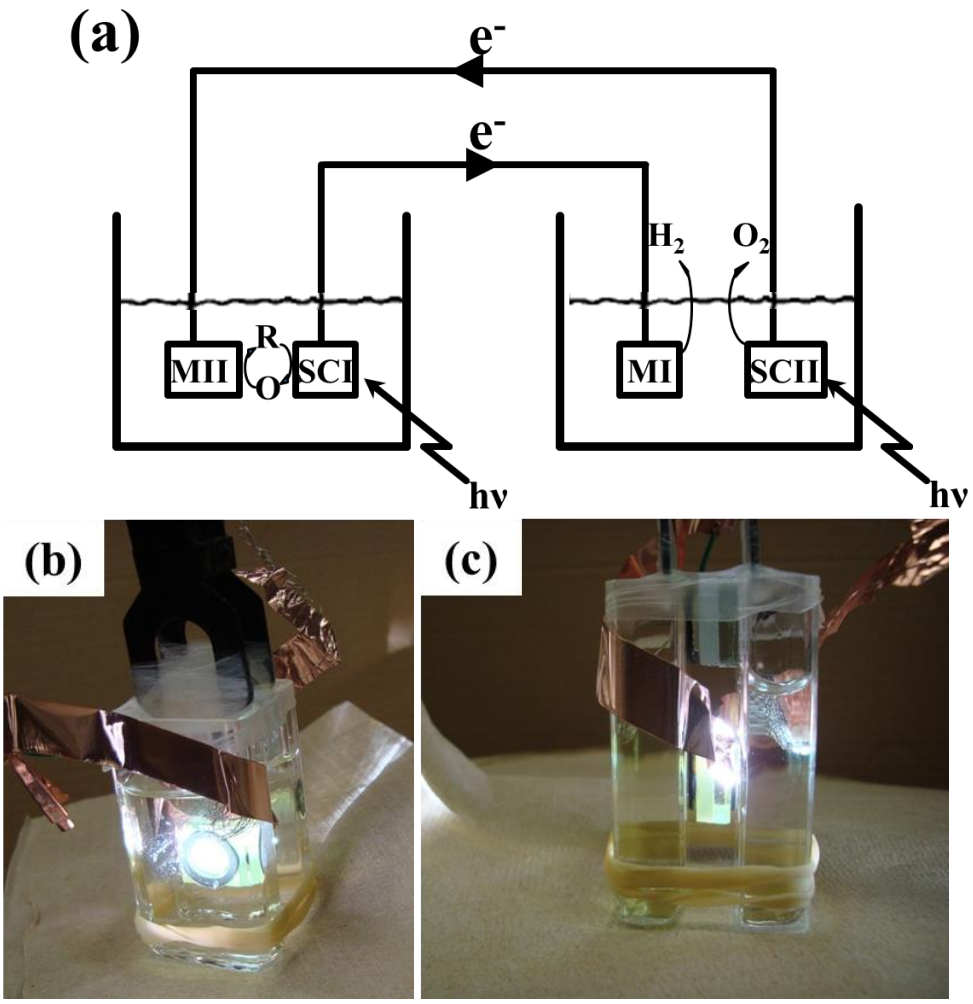

Figure 5.3. (a) Schematic diagram of a dual n-type semiconductor (SCI: semiconductor I, SCII: semiconductor II) system. Two metal electrodes (MI: metal I, MII: metal II) are used with redox couple (R/O). (b) and (c) are upper-front and side views of the Z-scheme device. Two Pt-W/Mo-$BiVO_4$ electrodes are placed between two glass cells and two Pt electrodes are in 25 mM / 25 mM I^-/IO_3^- and 0.1 M Na_2SO_4 solution (pH 7, 0.2 M sodium phosphate buffered). Electrodes are wired as described in (a).

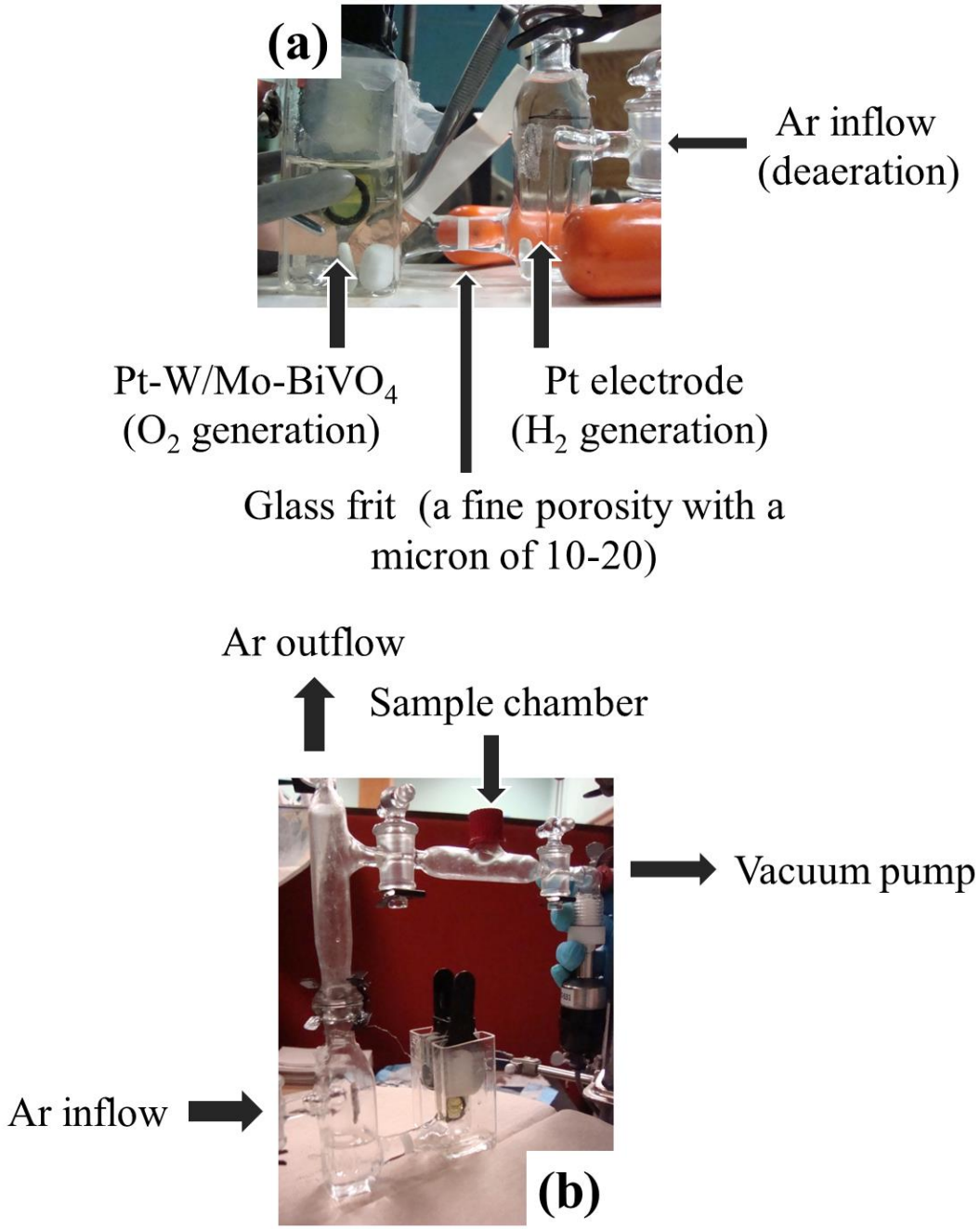

Figure 5.4. Home-built glass cell for gas chromatography-mass spectroscopy

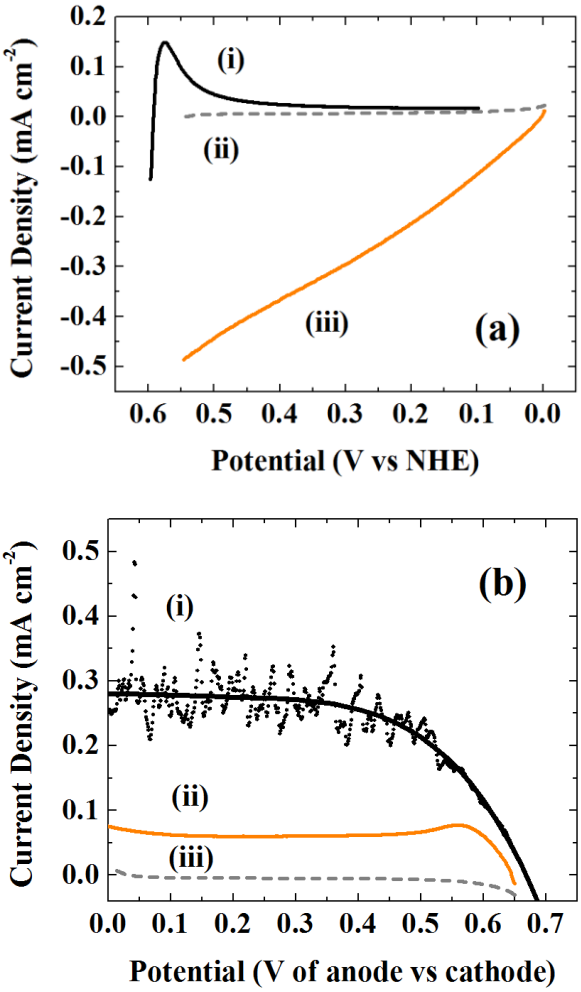

Figure 5.5. (a) Linear sweep voltammograms of IO_3^- reduction on Pt (scan from 0.6 to 0.1 V) (i) and I^- oxidation on Pt-W/Mo-$BiVO_4$ under dark (ii) and UV-visible irradiation (iii). (b) Linear sweep voltammograms in two electrode configuration using Pt and Pt-W/Mo-$BiVO_4$ for I^-/IO_3^- redox reactions. Scan rate was 20 mV s^{-1}. Photocurrent flows under UV-visible irradiation with magnetic stirring (i) without stirring (ii) and in the dark (iii). The measurements were conducted in 25 mM NaI and 25 mM $NaIO_3$ aqueous solution (pH 8.5). Light intensity was about 400 mW cm^{-2}.

Photocurrent from the Pt-W/Mo-$BiVO_4$ electrode for the oxidation of I^- or I_2 (I_2 can be an intermediate, e.g. from reaction of I^- with IO_3^-) to IO_3^- starts at about 0 V (shown in Figure 5.5(a, iii)). The onset potential of photooxidation agrees with the observed flat-band potential for the OER at a similar pH in Figure 5.2(a). The reduction current from the I^-/IO_3^- redox couple starts to flow at about 0.6 V on the Pt electrode, which is more positive than the onset potential of photooxidation on Pt-W/Mo-$BiVO_4$. Thus, the reduction and oxidation reactions of the I^-/IO_3^- redox couple can happen spontaneously under irradiation because the thermodynamic redox potential of I^-/IO_3^- is located within the conduction/valence band positions of Pt-W/Mo-$BiVO_4$. As the photogenerated electron/hole pairs are produced on Pt-W/Mo-$BiVO_4$, the electron in the conduction band is delivered to the Pt electrode at a potential sufficiently negative to reduce IO_3^- while the hole in the valence band of the metal oxide electrode has a potential positive enough to oxidize I^- to IO_3^-.

Figure 5.5(b) shows the current-potential behavior under UV-visible irradiation in a two electrode configuration using Pt-W/Mo-$BiVO_4$ and Pt electrodes with the I^-/IO_3^- redox couple in aqueous solution. The two electrode cell generates about 0.7 V open circuit potential (OCP) when no current flows and it produces about 0.3 mA cm^{-2} of photocurrent with magnetic stirring or 0.1 mA cm^{-2} without stirring of the solution when the two electrodes were short-circuited. Stirring causes an increase in the current because mass transport by diffusion is limited by the low solubility of IO_3^- or I_2.

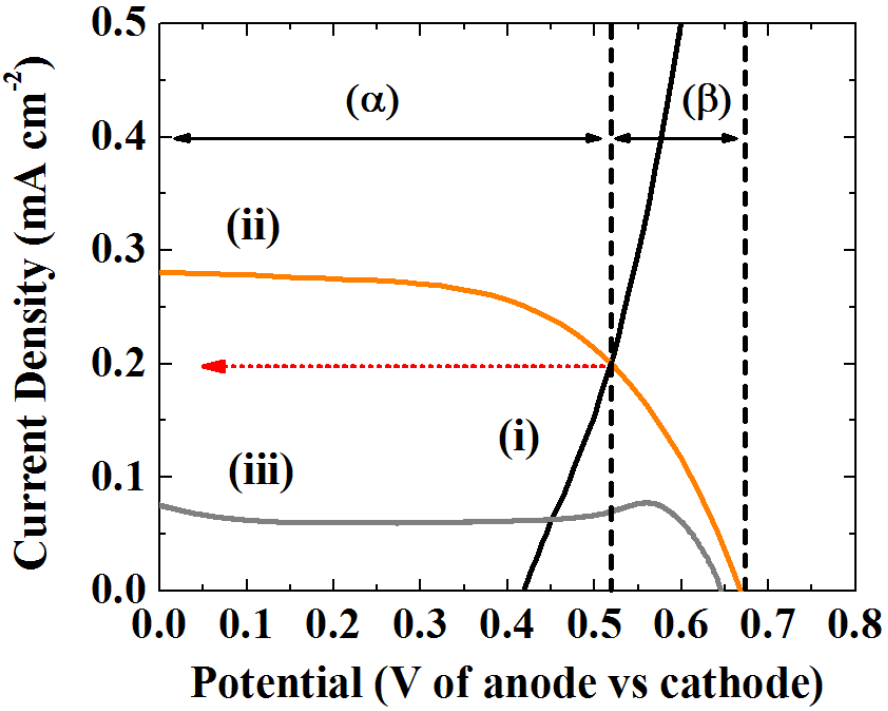

Figure 5.6. Overlapped linear sweep voltammograms of water splitting at Pt-W/Mo-$BiVO_4$ (i) and I^-/IO_3^- redox reactions with magnetic stirring (ii) and without stirring (iii) under UV-visible irradiation with an intensity of about 400 mW cm^{-2}. Data was taken from Figure 5.2(b) and Figure 5.5(b). In the plot, the current density for water splitting in the Z-scheme is estimated as 0.2 mA cm^{-2} (red arrow) under strong UV-visible irradiation with stirring for I^-/IO_3^- solution. This indicates about 0.5 V (α) of the generated potential from I^-/IO_3^- (from 0.7 V OCP) supplements the needed potential for proton reduction on Pt with the remaining 0.2 V (β) driving the I^-/IO_3^- reaction in the galvanic cell.

In Figure 5.6, the current-potential behavior for water splitting (i) and the redox reactions (ii and iii) in the two-electrode configuration are shown. When the four electrodes are connected as shown in Figure 5.3(a), the same current flows through all of the electrodes. Therefore, the crossing point of lines i (black) and ii (yellow) indicates the operating current of the Z-scheme device. In other words, an equivalent number of electrons must be used for H^+ and IO_3^- reduction on MI and MII, respectively, and the same number of holes must be used for I^- oxidation on SCI and the OER on SCII at the same time. Under this condition, the estimated current density for the water splitting system as described here is 0.2 mA cm^{-2} (red arrow).

We have shown how two semiconductors of the same material can be combined to fabricate a Z-scheme device for the photolysis of water. Its configuration and electrical contacts between the electrodes are as shown in Figure 5.3(a). Photographic images of front-top and side views of the Z-scheme device are shown in Figure 5.3(b) and 5.3(c). As described above, the device consists of two separate solution reactors: one with $NaI/NaIO_3$ (25 mM/25 mM) redox couple and the other contains a neutral aqueous solution for H_2 and O_2 generation. SCI/MI and SCII/MII were connected by conductive copper tape. For current measurements during the photolysis of water, SCI (or SCII) was used as the working electrode while MI (or MII) was used as the reference and counter electrode for chronoamperometry. The short-circuited condition (zero potential difference between counter/reference lead on MII and working electrode lead on SCII) was employed for the current measurement with no external resistance.

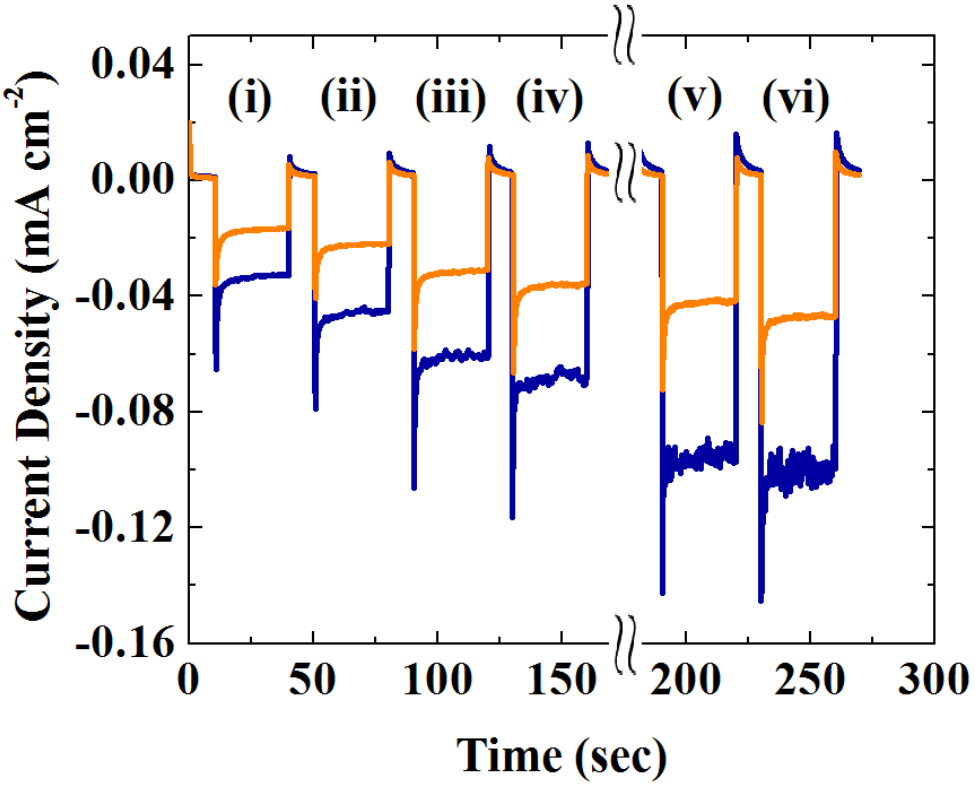

Figure 5.7. Water splitting current only using photon energy under different irradiation intensities for (i) 120, (ii) 180, (iii) 270, (iV) 310, (V) 360, and (Vi) 410 mW cm^{-2} of UV-visible (blue) and visible (yellow) illumination. Two sets of Pt-W/Mo-$BiVO_4$ and Pt electrodes were used in 0.1 M Na_2SO_4 (pH 7, 0.2 M sodium phosphate buffered) and 25 mM I^-/ 25 mM IO_3^- solution.

Figure 5.7 shows the current density for water photolysis resulting from the Z-scheme device using dual Pt-W/Mo-$BiVO_4$ semiconductors. The photocurrent generated from the photon energy is strongly dependent on the illumination intensity and the water splitting photocurrent increases as the intensity increased. The current density of the water photolysis increases from 0.04 mA cm^{-2} to 0.1 mA cm^{-2} as the intensity of the UV-visible irradiation increased from 100 mW cm^{-2} to 400 mW cm^{-2} with magnetic stirring of the I^-/IO_3^- redox solution. Also, Figure 5.7 indicates Pt-W/Mo-$BiVO_4$ utilizes visible irradiation as is expected from the size of the band-gap of Pt-W/Mo-$BiVO_4$, i.e., 2.4 eV. The measured current density for water splitting varied from 0.1 to 0.3 mA cm^{-2} (see also Figure 5.8(c)) under similar irradiation conditions (intensity of 400 mW cm^{-2}), which is within the scale of estimated current density from the analysis in Figure 5.6.

In Figure 5.8, gas bubbles generated on the Pt electrode (H_2) and the Pt-W/Mo-$BiVO_4$ electrode (O_2) were observed and this indicates that the photolysis of water was achieved without externally provided potential. In Figure 5.8(a), development of bubbles on both the Pt-W/Mo-$BiVO_4$ and Pt electrodes are shown as the illumination continued for 20 mins. Several small H_2 bubbles produced on the Pt electrode were also clearly observed and released from the electrode into the headspace in Figure 5.8(b). The photocurrent flow was stable for 6 h (inset, Figure 5.9), which indicates that the material and redox couple (I^-/IO_3^-) are chemically stable at least for this time period.

GC-MS was used to confirm H_2 generation from the Z-scheme water splitting. The home-built PEC cell for the GC-MS measurements was prepared as shown in Figure 5.4. To prevent O_2 reduction that is generated on Pt-W/Mo-$BiVO_4$ and can impede the

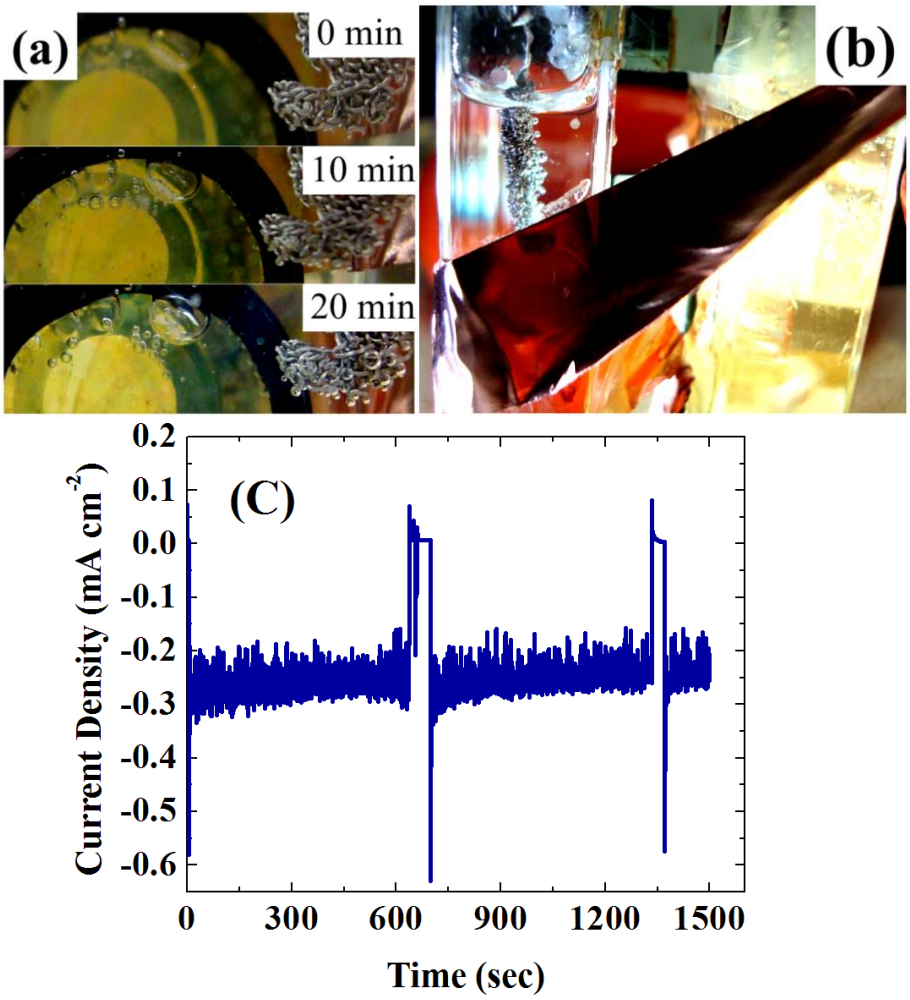

Figure 5.8. (a) Photographic images of bubbles generated on Pt (hydrogen) and Pt-W/Mo-$BiVO_4$ (oxygen) under irradiation and without externally applied potentials. Time shown in the images indicates the duration of irradiation. Large bubbles on the Pt-W/Mo-$BiVO_4$ at 0 min is Ar from the deaeration process before the experiments. (b) Side view during the water splitting experiments. Small bubbles are seen on Pt electrode in neutral aqueous solution. (c) Current density for water splitting under irradiation for 25 min. To take the images shown in (a), irradiation was blocked at about 600 s and 1300 s. UV-visible illumination intensity was about 400 mW cm^{-2}.

proton reduction on Pt, the two electrodes were separated by a glass frit with fine pores in the size range of 10 to 20 μm. However, the glass frit increased the solution resistance to about 600 ~ 700 Ω between the two electrodes and induced a potential drop. The potential loss from the solution resistance would be a few tens of mV with the current flow of hundreds of μA. The potential loss is non-negligible considering the overpotential for water splitting of the current device is less than 200 mV. The current flow in the GC-MS cell was thus less than 0.04 mA cm^{-2} because of the high solution resistance (inset, Figure 5.9) which is about half of that observed in Figure 5.6. The intensity of the UV-visible irradiation was about 300 mW cm^{-2}. To mitigate the potential drop and still have proper electrode separation, better device engineering is required to reduce the additional potential loss created by the solution resistance and this should be addressed in further studies. However, the current efficiency for H_2 generation from the measured amount of coulombs is about 90 % (calculations are shown in Figure 5.9). The result indicates that most of the photocurrent measured was from the photolysis of water and it is not originating from other reactions such as material decomposition or O_2 reduction reactions.

H_2 generation in the Z-scheme was also confirmed by the electrochemical detection of hydrogen using a membrane electrode assembly. Membrane electrodes consisting of two Pt/C (40 wt %) electrodes were prepared on Nafion membrane as described above (Figure 5.10(a)). One side of the membrane electrode faces the headspace of the electrochemical cell where Ar gas (and produced H_2) flows and the other side of the electrode faces air. The two electrodes in this mini-fuel cell were

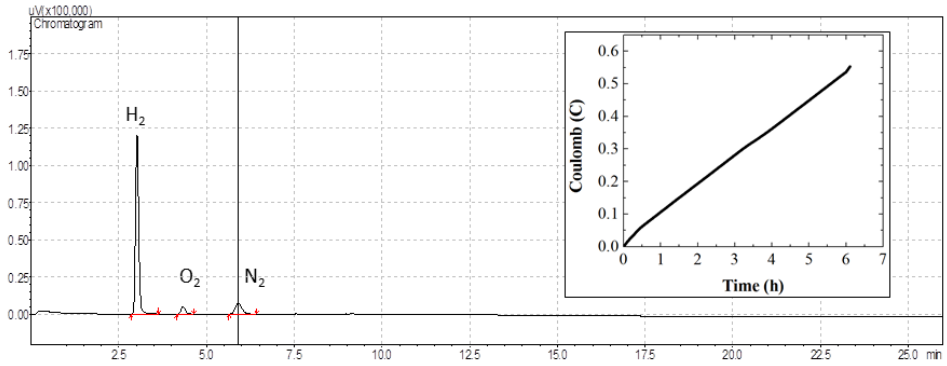

Peak#	Ret.Time	Area	Height	Conc.	Units	Compound
1	3.016	747472.7	120073.4	2953.72093	ppm	H_2
2	4.325	44153.3	5034.9	1601.86132	ppm	O_2
3	5.904	99367.6	7260.6	4214.20354	ppm	N_2

Figure 5.9. Gas chromatography-mass spectroscopy data

Calculations on GC-MS H_2 generation

- Volume of head space (gas) : 19 mL
- Volume of water : 18 mL
- Henry's constant for H_2 in water : k = 1282 [atm L /mol]

$$p = kC$$

where p is partial pressure and C the concentration.

- Electric charge flow: 0.55 C
- Number of moles of H_2 for 0.55 C : 0.55 [C] / 96485 [C/mol] / 2 = $2.85 * 10^{-6}$ [mol]

Volume : $2.85 * 10^{-6}$ [mol] * 22.4 [L/mol] * 1000 [mL/L] = 0.0638 mL

- Assume no gas bubbles in solution and simple Henry's law
- Define p as concentration in gas (also partial pressure or mole fraction) and c as concentration in solution

$$p = kc$$

$$2.85 * 10^{-6} \text{ [mol]} = (p/1282) \text{ [mol/L]} * 0.018 \text{ [L]} + p * 0.019 \text{ [L]} / 22.4 \text{ [L/mol]}$$

$$p = 3.30 * 10^{-3} = 3300 \text{ ppm}$$

- Experimental value : 2953 ppm

$$2953 / 3300 * 100 = 89.48 \text{ [\%]}$$

- 89 % of generated electric charge is detected as a hydrogen gas by gas chromatography.

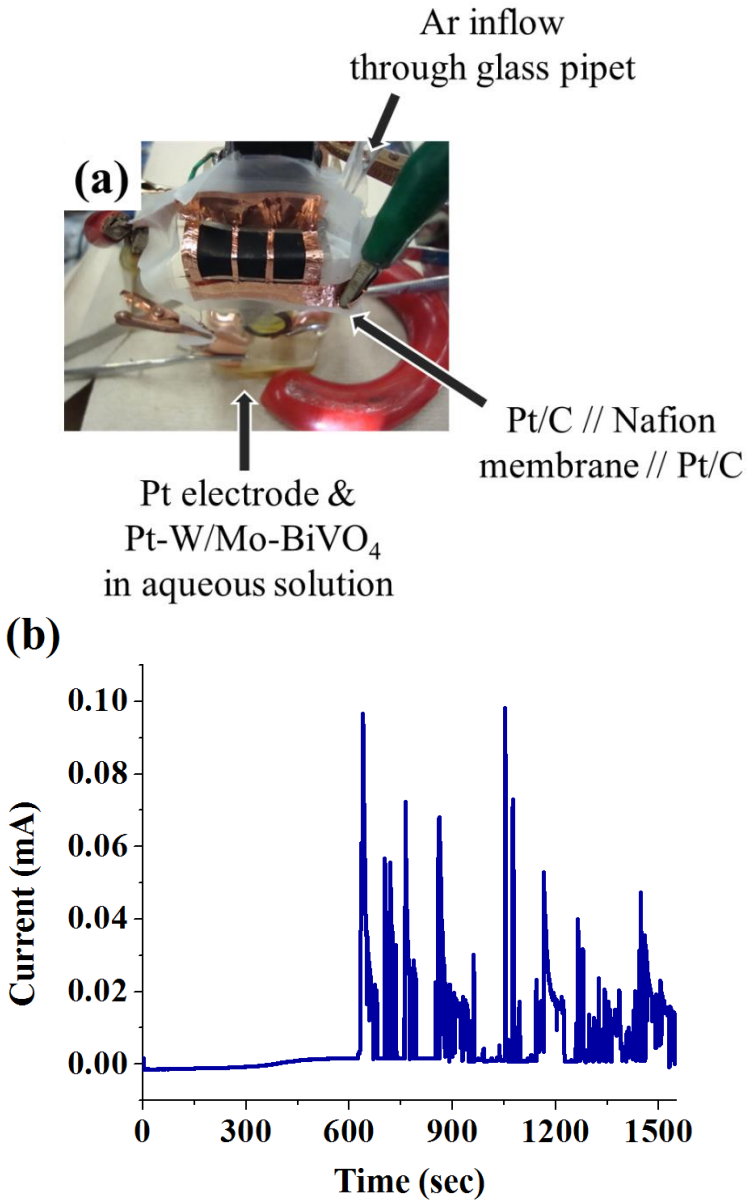

Figure 5.10. H_2 detection using membrane electrode assembly.

short-circuited and the current was monitored using a potentiostat. The membrane electrode toward the solution was used as the reference and the counter electrode and the electrode facing the air was set as the working electrode. Then, when H_2 bubbles are generated and released from the solution during water photolysis, the H_2 gas reacts on the membrane electrode to generate two protons (H_2 oxidation) on one side of membrane electrode. As the proton transfers to the other side of the membrane electrode, O_2 reduction occurs to generate water molecules with the transferred protons. Then, the current flowing through the external circuit proves the generation of H_2 from the water splitting. After about 10 min of irradiation, current was detected on the membrane electrode confirming H_2 generation in the cell (Figure 5.10(b)). The experiment simply simulates the reactions of proton exchange membrane fuel cells and shows the use of converted chemical energy from solar energy. It also confirmed H_2 production from water splitting in the Z-scheme along with the GC-MS measurements.

The Z-scheme device described above using two Pt-W/Mo-$BiVO_4$ electrodes demonstrates the use of two photons with the same semiconductor to boost the potential for water splitting, but it does not utilize the solar radiation with wavelengths longer than 500 nm because of the band gap of W/Mo-$BiVO_4$. $Zn_xCd_{1-x}S_ySe_{1-y}$ forms smaller band gap chalcogenide semiconductors that were investigated by maximizing the photocurrent of Zn-Cd-S-Se compositions by rapid synthesis and screening.[27] To harvest the photon energy with wavelengths longer than 500 nm, $Zn_{0.2}Cd_{0.8}Se$ chalcogenide band-gap of about 1.8 eV was prepared as reported previously.[27]

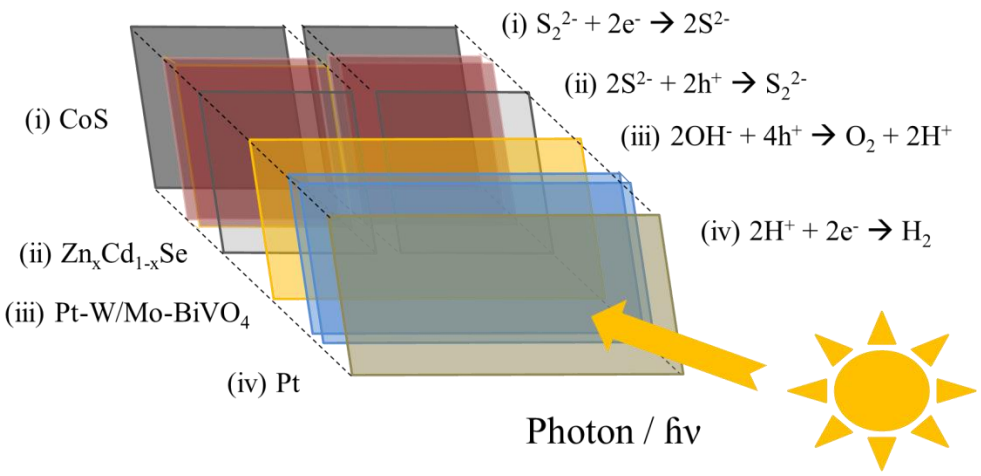

Figure 5.11. Schematic diagram shows Z-scheme using $Zn_{0.2}Cd_{0.8}Se$ and Pt-W/Mo-$BiVO_4$ as two absorber materials. Chemical reactions on electrodes are shown with corresponding roman numerals for each electrode.

The small band gap $Zn_{0.2}Cd_{0.8}Se$ photoanode can be used as described in Figure 5.11 to absorb that portion of the incident light transmitted through the Pt-W/Mo-$BiVO_4$. Briefly, $Zn_{0.2}Cd_{0.8}Se$ deposited on transparent conductive glass (FTO) oxidizes sulfides and the counter reaction (polysulfide reduction) on a CoS electrocatalyst completes the redox reactions.[39] LSVs of reduction on CoS and oxidation on $Zn_{0.2}Cd_{0.8}Se$ (and for comparison CdSe) are shown in Figure 5.12(a). For the study on the sulfide / polysulfide reaction, a Ag wire was used as a quasi-reference electrode (Ag/Ag_2S) instead of Ag/AgCl because of the instability of porous Vycor glass in a basic solution. However, the potentials reported here are quoted vs. the normal hydrogen electrode.

$$Ag_2S + 2e^- \rightarrow 2\ Ag + S^{2-} \qquad (E^0 = -0.69\ V\ vs.\ NHE) \qquad (5\text{-}5)$$

The reduction and oxidation reactions of polysulfide on CoS are facile enough to obtain a few mA cm^{-2} with only 0.1 V overpotential as shown in Figure 5.12(a-black). $Zn_{0.2}Cd_{0.8}Se$ and CdSe utilize photon energy under irradiation and sulfide oxidation current starts to flow from the potential of -1.1 V for CdSe and from -1.4 V for $Zn_{0.2}Cd_{0.8}Se$. Again, the negative shift of onset potential from -0.7 V (CoS) to -1.1 V (CdSe) shows the utilization of radiation energy by the photoanode. In addition, by adding Zn into CdSe, i.e., $Zn_{0.2}Cd_{0.8}Se$, the onset potential of sulfide oxidation shifts to an even more negative value of -1.4 V and the potential shift by Zn doping into CdSe agrees with our previous report on $Zn_xCd_{1-x}S_ySe_{1-y}$.[27] The data presented in Figure 5.12(a) are from one of the best performing samples for both CdSe and $Zn_{0.2}Cd_{0.8}Se$ based on the onset potential and the photocurrent at -0.6 V. The current and potential differ somewhat from sample to sample and the film preparation method and the

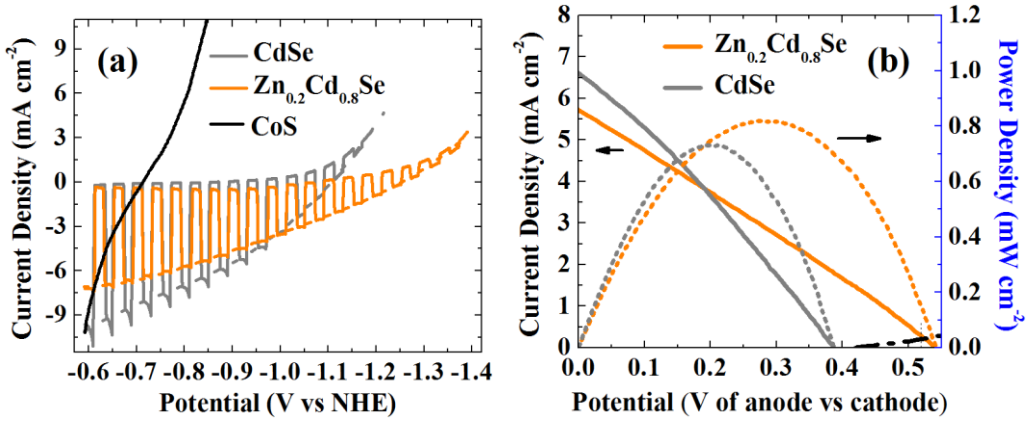

Figure 5.12. (a) Linear sweep voltammograms of a Pt electrode for polysulfide reduction and that for sulfide oxidation on $Zn_{0.2}Cd_{0.8}Se$ (yellow) and CdSe (gray) under chopped UV-visible irradiation. The measurements were conducted in 1 M Na_2S, 1M S, and 1M KOH aqueous solutions. Light intensity was about 120 mW cm^{-2}. (b) Calculated linear sweep voltammograms (solid line) for two electrode configuration, i.e., $Zn_{0.2}Cd_{0.8}Se$ (yellow) or CdSe (gray) with CoS electrode, from the data shown in (a). Power density of the cell (dotted line) is also calculated from the linear sweep voltammograms. Black dotted line barely seen at the right bottom of (b) shows the current and potential relationship for photolysis of water using Pt-W/Mo-$BiVO_4$ and Pt in two electrode configuration.

selenization process significantly affects the performance. However, $Zn_{0.2}Cd_{0.8}Se$ usually shows a more negative onset potential and smaller oxidation current than CdSe.

From the LSVs of $Zn_{0.2}Cd_{0.8}Se$ (or CdSe) with CoS, the performance of the PEC galvanic device in a two electrode configuration and its I E behavior can be drawn as shown in Figure 5.12(b). The open circuit potential, i.e., maximum potential produced from the galvanic device, is the potential difference between the photoanode and the cathode without current flow and it is calculated as 0.6 V and 0.4 V for $Zn_{0.2}Cd_{0.8}Se$-CoS and CdSe-CoS couples, respectively. The short-circuit current density, i.e., maximum current density that can be obtained from the galvanic cell, is the current density when the $Zn_{0.2}Cd_{0.8}Se$ (or CdSe) has the same electrochemical potential as CoS in Figure 5.12(a). As expected from the LSVs, the $Zn_{0.2}Cd_{0.8}Se$-CoS couple shows higher open circuit potential than the CdSe-CoS couple, and vice versa for the short circuit current density. Then, from the LSVs calculated in Figure 5.12(b), the current for photolysis of water in Z-scheme can be estimated as discussed in Figure 5.6.

The black dotted line in Figure 5.13(b) and 5.13(c) shows the current and potential relationship for water splitting using Pt-W/Mo-$BiVO_4$ and Pt in a neutral solution. As discussed in Figure 5.6, the crossing point of the LSVs for the galvanic redox reactions and the water splitting reactions shows the operating current of the Z-scheme device. The water splitting current is estimated to be as small as 0.1 mA cm^{-2} when a single cell of $Zn_{0.2}Cd_{0.8}Se$-CoS is used and no current flow is estimated when the CdSe-CoS couple is used with the S^{2-}/S_n^{2-} redox reactions (crossing point of gray line and

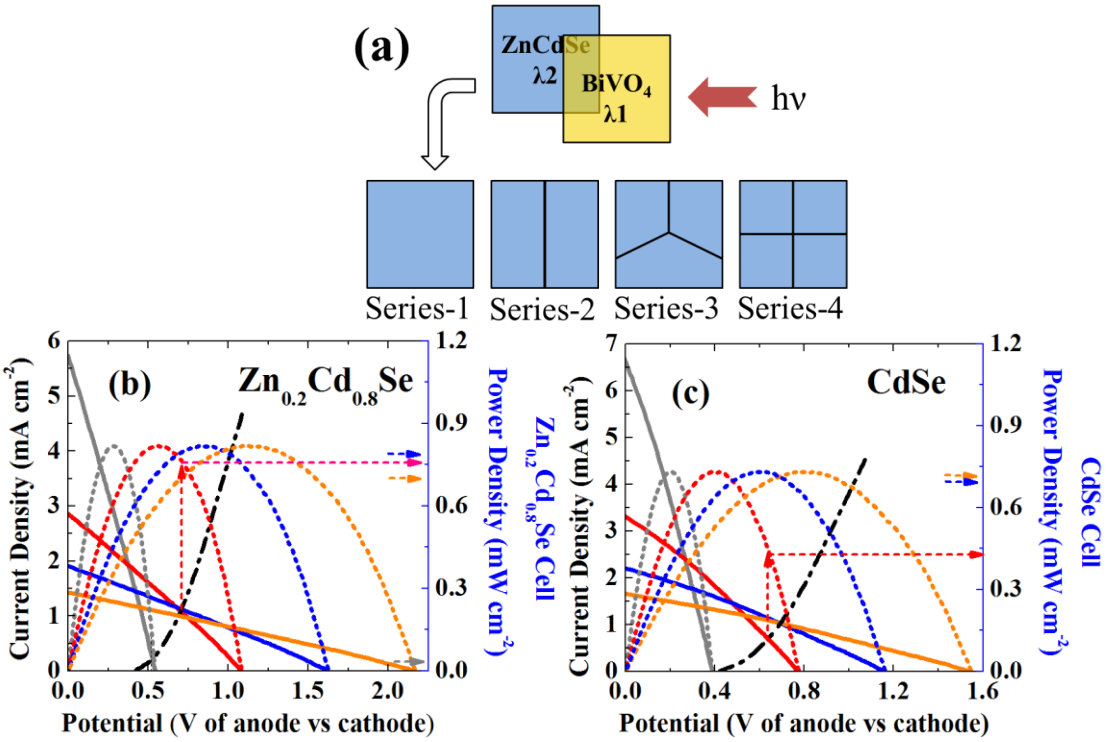

Figure 5.13. (a) Possible electrode configurations for singly-, doubly-, triply-, and quadruply-separated and connected cells in series with a constant area. (b) and (c) show linear sweep voltammograms (solid lines) and power density curves (dotted lines) for the supposed singly- (gray), doubly- (red), triply- (blue), and quadruply- (yellow) connected cells for $Zn_{0.2}Cd_{0.8}Se$ / CoS (b) and CdSe / CoS (c) thin film electrodes. Black dotted line in (b) and (c) shows the current density and potential relationship for water photolysis using Pt-W/Mo-$BiVO_4$ and Pt electrodes under UV-visible irradiation. Arrows shown on the right y-axis of (b) and (c) indicate the estimated power density for water splitting under UV-visible irradiation in Z-scheme. Data for the calculations are taken from the measurements shown in Figure 5.12(a).

black line in Figure 5.13(b) and 5.13(c)). Although the maximum power density generated from the S^{2-}/S_n^{2-} redox cell is about 1 mW cm^{-2} with $Zn_{0.2}Cd_{0.8}Se$ and CdSe photoanodes, the power produced by the redox cell cannot be efficiently used for water splitting. This is because the potential produced from the galvanic cell is not large enough for both the H_2 and O_2 evolution; only 0.5 V is produced from the $Zn_{0.2}Cd_{0.8}Se$-CoS couple and 0.4 V from the CdSe-CoS combination.

The available potential from the biasing $Zn_{0.2}Cd_{0.8}Se$-CoS cell can be increased by using several of these. When a single electrode with a constant area is divided into a number of smaller electrodes and they are connected in series as shown in Figure 5.13(a), the potential generated from the series cell can be larger; however this sacrifices some of the short circuit current density (calculated LSVs as shown Figure 5.13(b) and 5.13(c)). The maximum power density produced from this series cell at a given light intensity is constant because the total areas of the electrodes are the same. Again, the estimated current density for water photolysis can be obtained from the crossing point of the LSVs for water splitting using Pt-W/Mo-$BiVO_4$ (black line in Figure 5.13(b) and (c)) and of S^{2-}/S_n^{2-} redox reactions on $Zn_{0.2}Cd_{0.8}Se$ and CdSe redox cells. The arrows on the right y-axis in Figure 5.13(b) and 5.13(c) indicate the power densities at the operating conditions for water splitting with different cell configurations. Figure 5.14 also summarizes the analysis described above, which shows that two series connections of $Zn_{0.2}Cd_{0.8}Se$ cells can achieve a maximum water splitting photocurrent of about 1 mA cm^{-2} from the system used here.

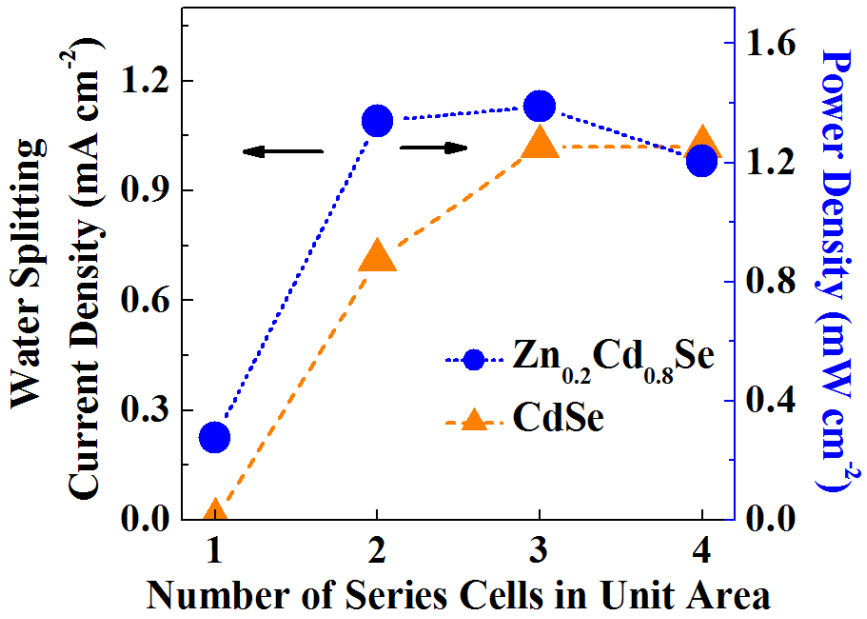

Figure 5.14. Summary of analysis discussed in Figure 5.13 for water splitting using $Zn_{0.2}Cd_{0.8}Se$ (or CdSe) and Pt-W/Mo-$BiVO_4$ photoanodes in a Z-scheme. The calculated current density for photolysis of water (left axis) and corresponding power density at operating condition from polysulfide cells (right axis) are shown for different numbers of series connected $Zn_{0.2}Cd_{0.8}Se$-CoS thin film electrodes cells.

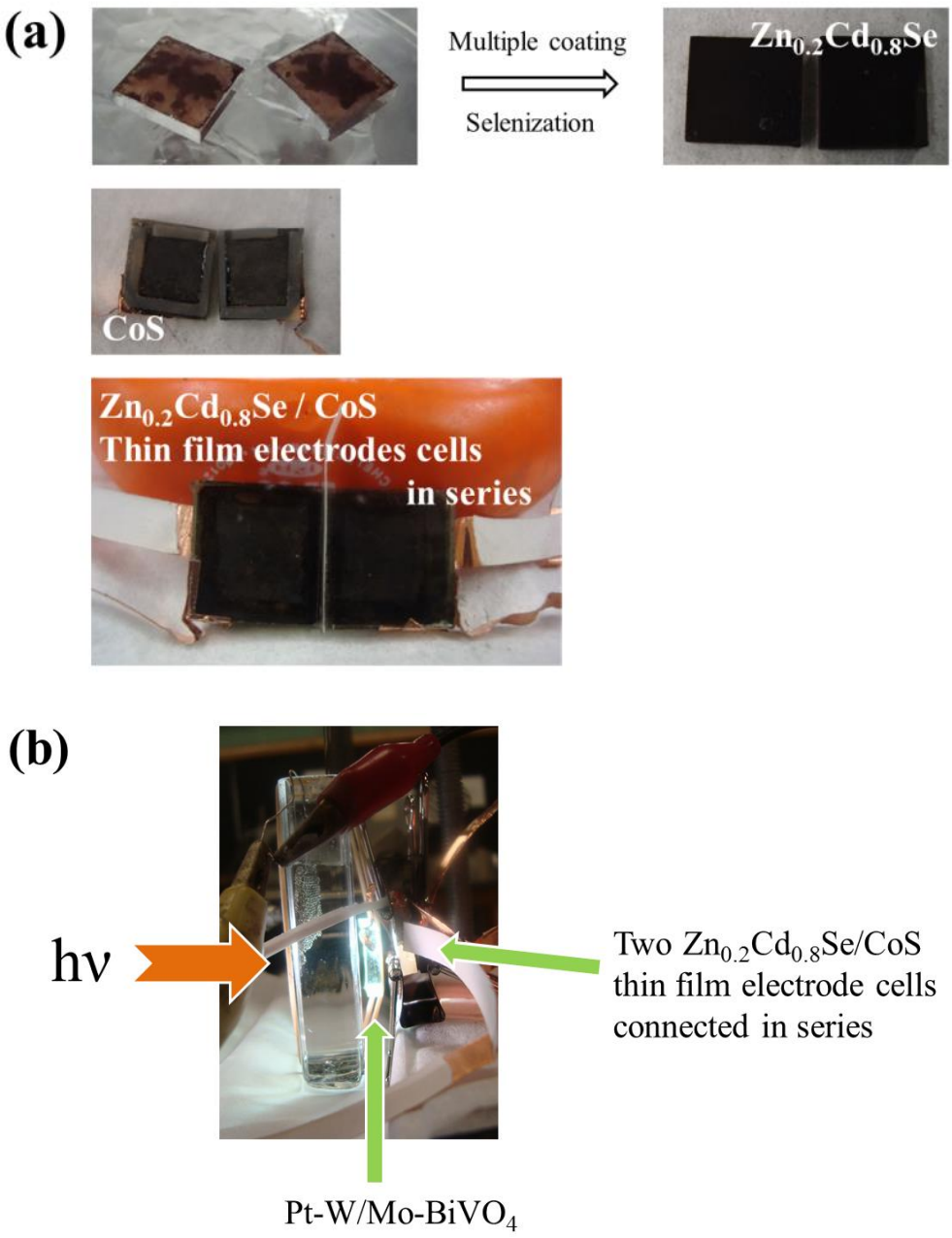

Figure 5.15. Photographs of $Zn_{0.2}Cd_{0.8}Se$ / CoS thin film electrodes cells.

Based on the analysis discussed in Figures 5.13 and 5.14, a PEC device consisting of two pairs of $Zn_{0.2}Cd_{0.8}Se$ photoanodes and CoS cathode was prepared (Figure 5.15). 1M Na_2S / 1 M S in 1 M KOH aqueous solution was used as the redox mediator for the $Zn_{0.2}Cd_{0.8}Se$ and CoS PEC galvanic cells. To minimize both the light absorption by the yellow redox solution and the solution resistance between the two electrodes, the spacing between $Zn_{0.2}Cd_{0.8}Se$ and CoS electrodes was decreased by placing a thin film rubber spacer (Latex, SLR-020-E, Small Parts, Amazon, Seattle, WA) with a thickness of 500 μm between them. After sealing the thin film cell using silicone resin (IS808, GE Silicones, Waterford, NY), the cell was allowed to cure overnight at room temperature. Then, both of the prepared cells were placed behind the Pt-W/Mo-$BiVO_4$ electrode as shown in Figure 5.15(b) for chronoamperometry measurements under irradiation.

Chronoamperometry in Figure 5.16(a) shows the results of the Z-scheme device utilizing Pt-W/Mo-$BiVO_4$ and the dual split $Zn_{0.2}Cd_{0.8}Se$ photoanode cells. Again, bubble generation of H_2 on Pt and O_2 on Pt-W/Mo-$BiVO_4$ was observed by water splitting (Figure 5.16(b)). The photocurrent flowing through the system was about 0.4 mA cm^{-2} under 400 mW cm^{-2} UV-visible irradiation. However, the power density generated by $Zn_{0.2}Cd_{0.8}Se$ and CoS galvanic cells reported in Figure 5.13(b) is only about 1 mW cm^{-2} which limits the maximum conversion efficiency for water splitting to less than 1 % with an irradiated photon energy of 120 mW cm^{-2}. The absolute photocurrent or conversion efficiency from photon energy to chemical energy of H_2 evolution is small and far from the best reported efficiencies utilizing buried junction photovoltaic cells (12.4 % using p-GaAs/p-$GaInP_2$, or 4.7 % using triple-junction a-Ge:Si.)[40, 41]

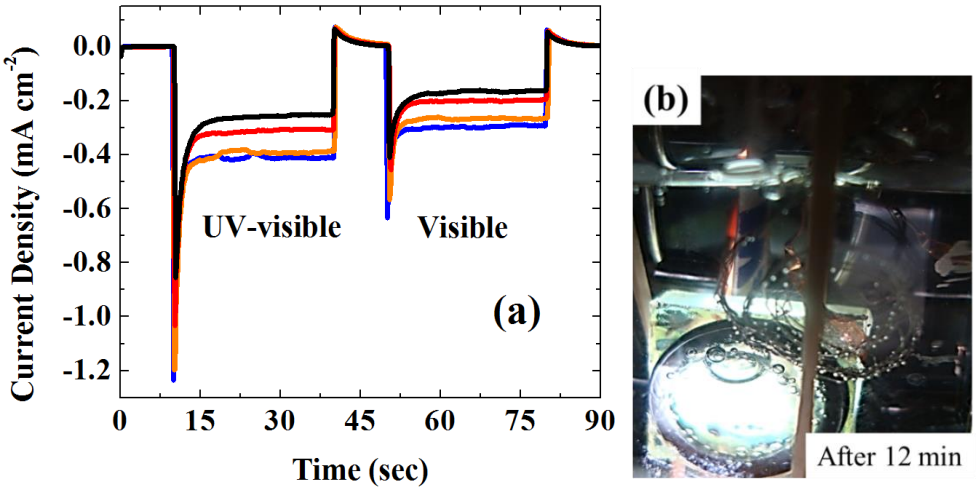

Figure 5.16. (a) Water photolysis current flow in a Z-scheme using $Zn_{0.2}Cd_{0.8}Se$ and Pt-W/Mo-$BiVO_4$ as two photoanodes under UV-visible and visible irradiation. Light intensity measurements based on full Xe-lamp output was 120 (black), 200 (red), 300 (yellow), and 440 mW cm^{-2} (blue). Detailed device configuration is as shown in Figure 5.15. (b) Photographic images taken after 12 min of irradiation (440 mW cm^{-2}, UV-visible) without any connection to external equipment. Hydrogen generated on Pt wire and oxygen bubbles on yellow Pt-W/Mo-$BiVO_4$ are observed.

Moreover, the overpotential of the overall water splitting reaction is still greatly limited by the OER reaction on the Pt-W/Mo-$BiVO_4$ electrode (as shown by the shape of LSVs in Figure 5.2(a) and 5.2(b)). Therefore, although the enhancement of the photocatalytic activity of the photoanodes has successfully been demonstrated for Pt-W/Mo-$BiVO_4$ and $Zn_{0.2}Cd_{0.8}Se$ through the previous studies, the development of highly active photocatalysts is still a limiting factor in practical water photolysis. In addition to material development, engineering the optimization of electrode configurations and cell design is necessary to utilize the converted photon energy efficiently in the device. However, the results shown here suggest that water photolysis can be achieved using inexpensive metal oxide photoanodes, i.e., Pt-W/Mo-$BiVO_4$, coupled with other small band-gap semiconductors, i.e., $Zn_{0.2}Cd_{0.8}Se$.

As shown in Figure 5.2(a), the Pt-W/Mo-$BiVO_4$ semiconductor is able to utilize the photon energy of the light to evolve oxygen at potentials below the thermodynamically predicted one for the OER. In a neutral aqueous solution (pH 7), the thermodynamic electrode potential (E^0) for the OER is 0.82 V for reaction (5-6) and 1.61 V for reaction (5-7);[38]

$$O_2 + 4H^+ + 4e^- \rightleftarrows 2H_2O \qquad (E^0 = 0.82 \text{ V vs. NHE at pH 7}) \qquad (5\text{-}6)$$

$$OH\bullet + e^- \rightleftarrows OH^- \qquad (E^0 = 1.61 \text{ V vs. NHE at pH 7}) \qquad (5\text{-}7)$$

The oxidation of hydroxide ion to hydroxyl radical (eqn. (5-7)) may be more relevant than reaction (6), when a single photogenerated hole transfer initiates the OER from water and roughly includes the kinetic overpotential to drive the OER. This is

because reaction (5-7) is a one-electron transfer reaction (as opposed to the four-electron transfer of reaction (5-6)) involving a single species, hydroxide ion. When compared to reaction (5-7), the maximum electrochemical energy gained by the photoanode, i.e., Pt-W/Mo-$BiVO_4$, from the absorbed photon is about 1.6 eV, which is the difference between the thermodynamic potential of hydroxide oxidation (1.61 V) and flat-band potential of the photoanode (ca. 0 V), where the observed onset potential is used as the flat-band potential. The flat-band potential of W/Mo-$BiVO_4$ has also been measured as about -0.4 V at pH 7 from capacitance measurements (Mott-Schottky (M-S) plot), which is more negative than the observed onset potential for the OER in Figure 5.2(a).[26] The observed onset potential of the photocurrent can be apparently shifted to more positive than the flat-band potential obtained from the M-S plot because of (i) the kinetic overpotential for the sluggish OER (i.e. loss of photogenerated holes by recombination rather than transfer to water; (ii) uncertainty in capacitance measurements in M-S plots;[42] or (iii) small, (i.e., not clearly observable) current flowing from the flat-band potential determined by the M-S plot to the observed onset potential in LSV. Here, the observed onset potential of the photocurrent is used as the flat-band position of the photoanode to simplify the discussion in this work.

Consequently, the obtainable electrochemical energy during OER (E_{SCII}) by Pt-W/Mo-$BiVO_4$ (semiconductor II or SCII in Figure 5.3(a)) per single electron from the absorbed photon energy from reaction (5-7) and the flat-band potential of Pt-W/Mo-$BiVO_4$ is

$$E_{SCII} = E_{HO^-/HO} - E_{flat\text{-}band} = 1.61 - 0.0 \approx 1.6 \text{ eV} \quad (5\text{-}8)$$

However, the total photon energy absorbed by the photoanode is determined from its band gap energy, which is 2.4 eV for W/Mo-$BiVO_4$. In this reaction, 800 mV is considered as the electromotive force (EMF) to transfer a hole from the valence band of Pt-W/Mo-$BiVO_4$ to the hydroxide in solution as shown in reaction (5-7).

$$E_{EMF} = E_{vb} - E_{HO-/HO} = 2.\ 4 - 1.6 = 0.8\ eV \quad (5\text{-}9)$$

where E_{vb} is the valence band position of W/Mo-$BiVO_4$.

Also, in Figure 5.6(b), the OCP of the second W/Mo-$BiVO_4$/ I^-/IO_3^- cell is 0.7 eV, which represents the maximum electrical energy obtained from the absorbed photon, i.e., the difference between the flat-band position of Pt-W/Mo-$BiVO_4$ and thermodynamic potential of the redox couple in the solution. When the onset potential of the photocurrent (about 0V) is adopted as the flat-band potential of Pt-W/Mo-$BiVO_4$ as discussed above, the maximum converted energy from the absorbed photon by Pt-W/Mo-$BiVO_4$ with I^-/IO_3^- redox couple (E_{SCI}) is

$$E_{SCI} = E_{I-/IO3-} - E_{flat\text{-}band} \approx 0.6 - 0.0 \approx 0.6\ eV \quad (5\text{-}10)$$

where $E_{I-/IO3-}$ is that of reaction (5-2) (or (5-3)), and the obtained OCP is close to the E_{SCI}. A larger potential could be obtained if a redox couple with a more positive E^o would be available.

In summary, the total electrochemical energy (E_{total}) that is converted from the two absorbed photons in the Z-scheme is the sum of that by SCI and SCII (equation (5-8) and (5-10)).

$$E_{total} = E_{SCI} + E_{SCII} \approx 0.6 + 1.6 \approx 2.2\ V \quad (5\text{-}11)$$

If E_{total} is larger than the energy required for the photolysis of water (E_{H2O}), water splitting thorough the Z-scheme occurs and H_2 and O_2 gases are produced.

$$E_{total} = E_{SCI} + E_{SCII} > E_{H2O} \quad (5\text{-}12)$$

Equation (5-12) is a necessary condition to complete the Z-scheme photolysis of water. In addition, E_{total} should equal the sum of the thermodynamic energy of water splitting (E_{H2O}), the electrochemical driving energy ($\eta_{H2/O2}$) needed to overcome the activation barrier of H_2 and O_2 generation, and the energy required to drive redox reactions on SCI and MII (η_{redox}) at a given current density as well as the sum of resistive drops in solution ($\eta_r = iR$).

$$E_{total} = E_{H2O} + \eta_{H2/O2} + \eta_r \quad (5\text{-}13)$$

$\eta_{H2/O2}$ and η_r of water splitting and redox reactions can be calculated from the electrochemical analysis as shown in Figure 5.6. From the generated 0.7 V from the I^-/IO_3^- redox reactions, 0.5 V (α) was used as to augment the potential for HER and OER on MI and SCII. Because the minimum potential to begin the photolysis of water on MI and irradiated SCII is about 0.4 V (the onset potential of the black line shown in Figure 5.6) only about 0.1 V from the augmented 0.5 V is available as the electrochemical overpotential ($\eta_{H2/O2}$) to raise the current for water splitting reactions. For I^-/IO_3^- redox reactions, about 0.2 V (β, η_{redox}) is used to drive the current on MII and SCI. Then, E_{H2O} calculated from equation (5-11) and (5-13) is

$$E_{H2O} = E_{total} - \eta_{H2/O2} - \eta_{redox} \approx 2.2 - 0.1 - 0.2 \approx 1.9 \text{ V} \quad (5\text{-}14)$$

The obtained E_{H2O}, which is a thermodynamic energy required to realize the water splitting, is larger than the chemical energy stored in the generated H_2 and O_2. When

hydroxyl radicals created by hydroxide oxidation (reaction (5-7)) react to evolve O_2 molecules, there is an additional energy loss due to the reaction of hydroxyl radicals to hydrogen peroxides and further of hydrogen peroxide to the oxygen and water molecules. In other words, from equation (5-12), the actual energy needed to realize the water splitting is larger than the often-quoted value of the water splitting, i.e., 1.23 V.

Hanna and Nozik considered the performance of pairs of semiconductors in a similar arrangement as described here and proposed that a pair of photoanodes with band gaps of 1.9 eV and 2.5 eV, could achieve a theoretical solar-to-chemical energy conversion for water splitting of about 10 % .[43] In the discussion of Hanna and Nozik, the theoretical conversion efficiency is largely determined by the band-gap size of the photoanodes, the obtainable radiant energy of the solar spectrum and electrochemical overpotentials for water splitting. However, equation (5-8) and (5-10) imply that both the flat-band position and the size of the band-gaps for the photoanodes are important to determine the thermodynamic energy that is obtainable from the radiant energy. As the position of the flat-band shifts more positive, the amount of the potential gained from the radiation energy at the photoanode decreases. This results in less favorable conditions to realize the water splitting. Consequently, one should consider not only the band-gap size of photoanodes, but also the position of band-edges, the maximum obtainable energy from water oxidation, and the redox couple in order to realize water splitting in a Z-scheme system. However, note that the amount of energy gained from the water oxidation is subtle in equation (5-8), because it is an electrochemically unpoised system having no redox couple in the solution; so the Fermi level of solution phase is not clearly

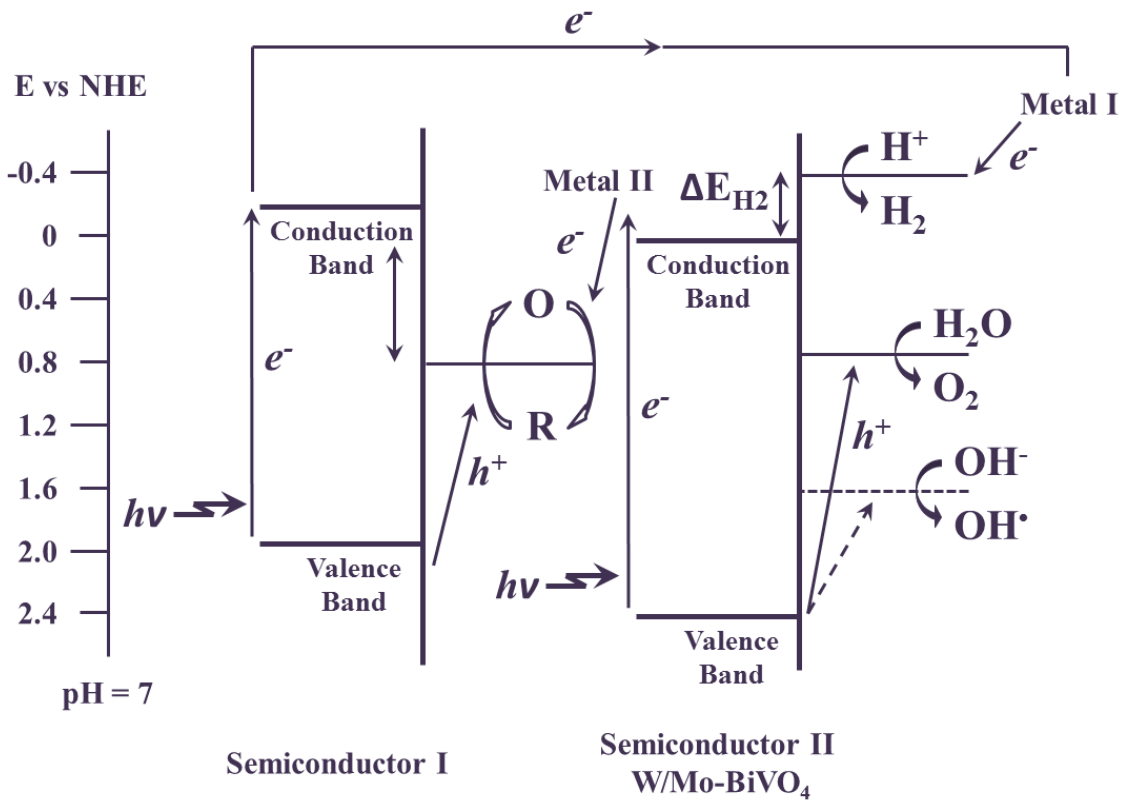

Figure 5.17. Schematic representations of the electron transport chain and redox potentials of Z-scheme device for the unbiased photolysis of water.

determined. Here, equation (5-8) with $E_{OH-/OH}$ shows the maximum obtainable thermodynamic energy from the OER as discussed above.

In Figure 5.17, the position of band-edges of W/Mo-$BiVO_4$ and the redox potentials of the HER and OER are shown. As discussed in connection with Figure 5.2(b), the additional potential that must be applied between the Pt-W/Mo-$BiVO_4$ and the Pt electrodes to initiate water splitting is at least the difference between the conduction band position of Pt-W/Mo-$BiVO_4$ and thermodynamic potential of HER (ΔE_{H2}). Thus, another PEC cell with the redox mediator was used to supply the additional potential in a Z-scheme. The total potential needed in a PEC system is the sum of the thermodynamic energy of water splitting (E_{H2O})plus an electrochemical driving energy ($\eta_{H2/O2}$) needed to overcome the activation barrier of H_2 and O_2 generation, and the energy required to drive redox reactions on SCI and MII (η_{redox}) at a given current density plus the sum of resistive drops in solution ($\eta_r = iR$), totaling about 2 V.

5.4 Conclusions

The photocatalytic activity of $BiVO_4$ has been improved by metal doping and surface treatment, e.g., W/Mo doping and deposition of electrocatalyst on the photoanode. The resulting Pt-W/Mo-$BiVO_4$ shows at least a 20 fold improvement in photoactivity compared to that of untreated $BiVO_4$ for the OER. Using the developed photoanode, PEC water splitting has been demonstrated without external bias. In the device for the photolysis of water, two n-type semiconductors, i.e., Pt-W/Mo-$BiVO_4$ and $Zn_{0.2}Cd_{0.8}Se$, coupled with electrocatalyst electrodes, i.e., Pt and CoS, were used to

complete the dual n-type semiconductor (or Z-scheme) water splitting devices. The Z-scheme configuration consists of two separate electrochemical cells: one with a redox reaction that generates a photopotential and the other for the H_2 and O_2 generation. Two different redox systems were studied. One is the I^-/IO_3^- redox couple for the dual Pt-W/Mo-$BiVO_4$-Pt system, and the other is the S^{2-}/S_n^{2-} redox couple for the $Zn_{0.2}Cd_{0.8}Se$ - CoS system. The work herein also exploited the factors that can maximize the utilization of the generated energy from photoanodes for the water splitting. However, less than 1 % of irradiated photon energy has been utilized for H_2 generation reactions and the development of more active photoanode material is still a key roadblock to the fabrication of a practical solar-fuel system.

5.5 References

[1] Bard, A. J. *Science* **1980**, *207*, 139-144.

[2] Nozik, A. J. *Ann. Rev. Phys. Chem.* **1978**, *29*, 189-222.

[3] Bard, A. J.; Fox, M. A. *Acc. Chem. Res.* **1995**, *28*, 141-145.

[4] United States Department of Energy, a National Vision of America's Transition to a Hydrogen Economy To 2030 and Beyond, February, **2002**.

[5] Fujishima, A.; Honda, K. *Nature* **1972**, *238*, 37-38.

[6] Youngblood, W. J.; Lee, S.-H. A.; Maeda, K.; Mallouk, T. E. *Acc. Chem. Res.* **2009**, *42*, 1966-1973.

[7] Li, L.; Duan, L.; Xu, Y.; Gorlov, M.; Hagfeldt, A.; Sun, L. *Chem. Commun.* **2010**, *46*, 7307-7309.

[8] Brimblecombe, R.; Koo, A.; Dismukes, G. C.; Swiegers, G. F.; Spiccia, L. *J. Am. Chem. Soc.* **2010**, *132*, 2892-2894.

[9] Walter, M. G.; Warren, E. L.; McKone, J. R.; Boettcher, S. W.; Mi, Q.; Santori, E. A.; Lewis, N. S. *Chem. Rev.* **2010**, *110*, 6446-6473.

[10] Boettcher, S. W.; Warren, E. L.; Putnam, M. C.; Santori, E. A.; Turner-Evans, D.; Kelzenberg, M. D.; Walter, M. G.; McKone, J. R.; Brunschwig, B. S.; Atwater, H. A.; Lewis, N. S. *J. Am. Chem. Soc.* **2011**, *133*, 1216-1219.

[11] Rocheleau, R. E.; Miller, E. L.; Misra, A. *Energy & Fuels* **1998**, *12*, 3-10.

[12] Sivula, K.; Le Formal, F.; Gratzel, M. *ChemSusChem* **2011**, *4*, 432-449.

[13] Cervera-March, S.; Smotkin, E. S.; Bard, A. J.; Campion, A.; Fox, M. A.; Mallouk, T.; Webber, S. E.; White, J. M. *J. Electrochem. Soc.* **1988**, *135*, 567-573.

[14] Smotkin, E.; Bard, A. J.; Campion, A.; Fox, M. A.; Mallouk, T.; Webber, S. E.; White, J. M. *J. Phys. Chem*. **1986**, *90*, 4604-4607.

[15] Smotkin, E. S.; Cervera-March, S.; Bard, A. J.; Campion, A.; Fox, M. A.; Mallouk, T.; Webber, S. E.; White, J. M. *J. Phys. Chem.* **1987**, *91*, 6-8.

[16] Bard, A. J. *J. Photochem.* **1979**, *10*, 59-75.

[17] Maeda, K.; Higashi, M.; Lu, D.; Abe, R.; Domen, K. *J. Am. Chem. Soc.* **2010**, *132*, 5858-5868.

[18] Katz, J. E.; Gingrich, T. R.; Santori, E. A.; Lewis, N. S. *Energy Environ. Sci.* **2009**, *2*, 103-112.

[19] Woodhouse, M.; Herman, G. S.; Parkinson, B. A. *Chem. Mater.* **2005**, *17*, 4318-4324.

[20] Jang, J. S.; Lee, J.; Ye, H.; Fan, F.-R. F.; Bard, A. J. *J. Phys. Chem. C.* **2009**, *113*, 6719-6724.

[21] He, J.; Parkinson, B. A. *ACS Comb. Sci.* **2011**, *13*, 399-404.

[22] Jang, J. S.; Yoon, K. Y.; Xiao, X.; Fan, F.-R. F.; Bard, A. J. *Chem. Mater.* **2009**, *21*, 4803-4810.

[23] Baeck, S. H.; Jaramillo, T. F.; Brandli, C.; McFarland, E. W. *J. Comb. Chem.* **2002**, *4*, 563-568.

[24] Liu, W.; Ye, H.; Bard, A. J. *J. Phys. Chem. C* **2010**, *114*, 1201-1207.

[25] Ye, H.; Lee, J.; Jang, J. S.; Bard, A. J. *J. Phys. Chem. C* **2010**, *114*, 13322-13328.

[26] Park, H. S.; Kweon, K. E.; Ye, H.; Paek, E.; Hwang, G. S.; Bard, A. J. *J. Phys. Chem. C* **2011**, *115*, 17870-17879.

[27] Liu, G.; Liu, C.; Bard, A. J. *J. Phys. Chem. C* **2010**, *114*, 20997-21002.

[28] Liu, G.; Bard, A. J. *J. Phys. Chem. C* **2010**, *114*, 17509-17513.

[29] Riha, S. C.; Parkinson, B. A.; Prieto, A. L. *J. Am. Chem. Soc.* **2011**, *133*, 15272-15275.

[30] Kudo, A.; Omori, K.; Kato, H. *J. Am. Chem. Soc.* **1999**, *121*, 11459-11467.

[31] Seabold, J. A.; Choi, K.-S. *J. Am. Chem. Soc.* **2012**, *134*, 2186-2192.

[32] Zhong, D. K.; Choi, S.; Gamelin, D. R. *J. Am. Chem. Soc.* **2011**, *133*, 18370-18377.

[33] Bridge, P. J.; Pryce, M. W. *Mineralog. Mag.* **1974**, *39*, 847-849.

[34] Sayama, K.; Nomura, A.; Arai, T.; Sugita, T.; Abe, R.; Yanagida, M.; Oi, T.; Iwasaki, Y.; Abe, Y.; Sugihara, H. *J. Phys. Chem. B* **2006**, *110*, 11352-11360.

[35] Y, He.; Park, H. S.; Bard, A. J. *J. Phys. Chem. C* **2011**, *115*, 12464-12470.

[36] Kim, M.-G.; Kanatzidis, M. G.; Facchetti, A.; Marks, T. J. *Nat. Mater.* **2011**, *10*, 382-388.

[37] Abe, R.; Sayama, K.; Sugihara, H. *J. Phys. Chem. B* **2005**, *109*, 16052-16061.

[38] Bard, A. J.; Faulkner, L. R. *Electrochemical Methods Fundamentals and Application*, 2nd ed.; John Wiley & Sons: New York, **2001**.

[39] Lessner, P. M.; McLarnon, F. R.; Winnick, J.; Cairns, E. J. *J. Electrochem. Soc.* **1993**, *140*, 1847-1849.

[40] Khaselev, O.; Turner, J. A. *Science* **1998**, *280*, 425-427.

[41] Reece, S. Y.; Hamel, J. A.; Sung, K.; Jarvi, T. D.; Esswein, A. J.; Pijpers, J. J.; Nocera, D. G. *Science* **2011**, *334*, 645-648.

[42] Cardon, F.; Gomes, W. P. *J. Phys. D: Appl. Phys.* **1978**, *11*, L63-L67.

[43] Hanna, M. C.; Nozik, A. J. *J. Appl. Phys.* **2006**, *100*, 074510.

Outlook

Scanning electrochemical microscopy (SECM) was used to discovery and to improve photocatalysts for their photoelectrochemical performance. Metal doping of the metal oxide photoelectrocatalyst, e.g. adding Mo to W-doped $BiVO_4$, dramatically increases its activity for water oxidation. The developed photoelectrocatalyst, W/Mo-$BiVO_4$, shows a photocurrent for water oxidation that is more than 10 times higher than undoped $BiVO_4$. The rapid screening method by SECM has been shown to be a tool to develop an active photocatalyst such as W/Mo-doped $BiVO_4$. SECM has also been used to study photogenerated surface OH• during water oxidation at W/Mo-$BiVO_4$. The OH• produced under strong irradiation at the W/Mo-$BiVO_4$ surface were interrogated using an $IrCl_6^{2-/3-}$ redox couple as the titrant of the radicals. Quantitative measurements showed that only a few percent of the absorbed photons contribute to the production of adsorbed OH• at W/Mo-$BiVO_4$. The improved carrier diffusion length, carrier mobilities and reduced recombination rate by the addition W/Mo dopants into $BiVO_4$ were studied by digital simulations. As results of the addition of metal dopants, the electron/hole diffusion length increased from 2.8/1.1 nm ($BiVO_4$) to 16/9.3 nm (W/Mo-$BiVO_4$). Using the developed photoanode, PEC water splitting has been demonstrated without external bias. In the device for the photolysis of water, two n-type semiconductors coupled with electrocatalyst electrodes, were used to complete the dual n-type semiconductor (or Z-scheme) water splitting devices. The Z-scheme configuration consists of two separate electrochemical cells: one with a redox reaction that generates a

photopotential and the other for the H_2 and O_2 generation. However, less than 1 % of irradiated photon energy has been utilized for H_2 generation reactions and the development of more active photoanode material is still a key roadblock to the fabrication of a practical solar-fuel system.

Appendix A. Publication list derived from photoelectrochemistry work

Chapter 2

Hyun S. Park, Kyoung Eun Kwon, Heechang Ye, Eunsu Paek, Gyeong S. Hwang, Allen J. Bard, "Factors in the Metal Doping of $BiVO_4$ for Improved Photoelectrocatalytic Activity as Studied by Scanning Electrochemical Microscopy (SECM) and First-Principles Density-Functional Calculation", *J. Phys. Chem. C*, (115) 17870-17879 (2011).

Chapter 3

Hyun S. Park, Kevin C. Leonard, Allen J. Bard, "Interrogation of the Water Oxidation Intermediate radicals at Metal Oxide Semiconductor (W/Mo-$BiVO_4$) by Scanning Electrochemical Microscopy (SCEM)", *In preparation, expected submission in January 2013.*

Yanqing Cong*, Hyun S. Park*, Shijun Wang, Hoang X. Dang, Fu-Ren F. Fan, C. Buddie Mullins, Allen J. Bard, "Synthesis of Ta_3N_5 Nanotube Arrays Modified with Electrocatalysts for Photoelectrochemical Water Oxidation", *J. Phys. Chem. C*, (116) *14541-14550* (2012). (*These authors contributed equally to this work.)

Chapter 4

Hyun S. Park, Hyung-Wook Ha, Rodney S. Ruoff, Allen J. Bard, "Photoelectrochemical behavior and Finite Elements Analysis of Reduced Graphene Oxide and $BiVO_4$ Composite Electrodes for Water Oxidation", *In preparation, expected submission in January 2013.*

Chapter 5

Hyun S. Park, Heung Chan Lee, Kevin C. Leonard, Guanjie Liu, Allen J. Bard, "Unbiased Photoelectrochemical Water Splitting in Z-scheme Device Using W/Mo-$BiVO_4$ and $Zn_xCd_{1-x}Se$", *In preparation, expected submission in January*

2013.

Other works

Hoang X. Dang, Nathan T. Hahn, Hyun S. Park, Allen J. Bard, C. Buddie Mullins, "Nanostructured Ta_3N_5 Films as Visible-Light Active Photoanodes for Water Oxidation", *J. Phys. Chem. C,* (116) 19225-19232 (2012).

Kevin Leonard, Hyun S. Park, Heung Chan Lee, Shijun Wang, Allen J. Bard, "Rapid Screening Methods in the Discovery and Investigation of New Photocatalyst Compositions," in Photoelectrochemical Water Splitting: Issues and Perspectives; H-J. Lewerenz and L. M. Peter, Eds.; Royal Society of Chemistry: Cambridge, UK, *expected publication in 2013*; Chapter 7.

Yanqing Cong, Hyun S. Park, Hoang X. Dang, Fu-Ren F. Fan, Allen J. Bard, C. Buddie Mullins, "Tantalum Cobalt Nitride Photocatalysts for Water Oxidation under Visible Light", *Chem. Mater.,* 24 (3) 579-586 (2012).

Heechang Ye, Hyun S. Park, Allen J. Bard, "Study of electrocatalysts for photoelectrochemical water oxidation on W-doped $BiVO_4$ photocatalysts by scanning electrochemical microscopy (SECM)", *J. Phys. Chem. C*, (115) 12464-12470 (2011).

Heechang Ye, Hyun S. Park, Vahid A. Akhavan, Brian W. Goodfellow, Matthew G. Panthani, Brian A. Korgel, Allen J. Bard, "Photoelectrochemical characterization of $CuInSe_2$ and $Cu(In_{1-x}Ga_x)Se_2$ thin films for solar cells", *J. Phys. Chem. C*, (115) 234-240 (2011).

Appendix B. Simulation reports generated by COMSOL Multiphysics

B.1 SECM calculations (Chapter 3)

1. Global Definitions

1.1. Parameters 1

Parameters		
Name	Expression	Description
FAR	96485	Faraday's constant
n	1	number of electrons
alpha	0.5	transfer coefficient
f	38.92	F/RT
E0	0.2	Standard potential
D	2e-9	diffusion coefficient
k0	1e-1	standard rate constant
E	0.2	

1.2. Variables

1.2.1. Variables 2a

Geometric entity level: Entire model

Name	Expression	Description
Ir	mod1.intop1(intcpl_source_Ir)	
Is	mod1.intop2(intcpl_source_Is)	

2. Model 1 (mod1)

2.1. DEFINITIONS

2.1.1. Variables

Variables 1

Geometric entity level: Boundary

Selection: Boundary 2

Name	Expression	Description
Es	E+flc1hs(-80+t,0.1)*(Eoxi-E)-flc1hs(-150+t,0.1)*(Eoxi-E)	
kaS	k0*exp((1-alpha)*n*f*(Es-E0))	
kcS	k0*exp(-alpha*n*f*(Es-E0))	
Eoxi	0.5	

Variables 2

Geometric entity level: Boundary

Selection: Boundary 4

Name	Expression	Description
E1	0	

kaR	k0*exp((1-alpha)*n*f*(E3-E0))	
kcR	k0*exp(-alpha*n*f*(E3-E0))	
E2	0.5	
E3	0	

Variables 1a

Geometric entity level: Boundary

Selection: Boundary 4

Name	Expression	Description
intcpl_source_Ir	-n*2*pi*r*FAR*D*FcOz	

Variables 3

Geometric entity level: Boundary

Selection: Boundary 2

Name	Expression	Description
intcpl_source_Is	n*2*pi*r*FAR*D*FcOz	

2.2. GEOMETRY 1

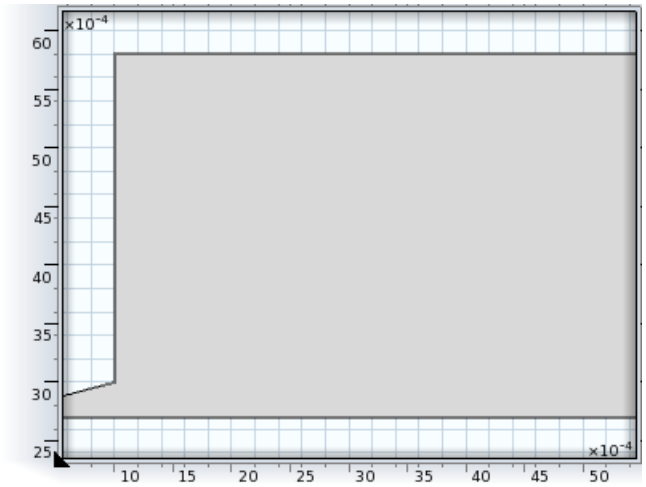

Geometry

Geometry statistics	
Property	Value
Space dimension	2
Number of domains	1
Number of boundaries	10

2.2.1. Composite Object 1 (CO1)

Settings	
Name	Value
Filename	$FILENAME$_geom1_CO1.mphbin

2.3. TRANSPORT OF DILUTED SPECIES (CHDI)

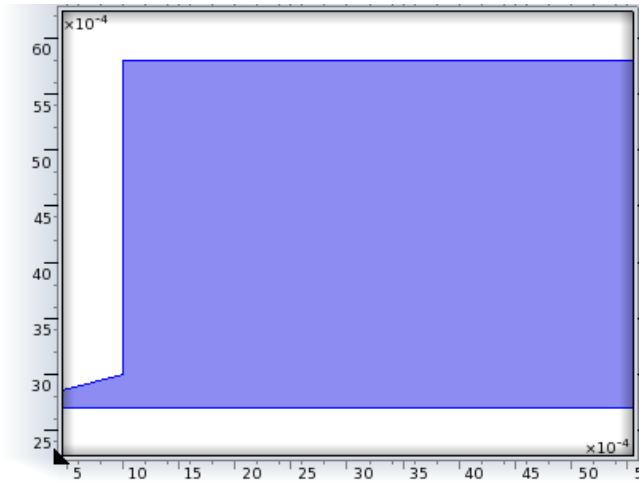

Transport of Diluted Species

Settings	
Description	Value
Concentration	Quadratic
Convection	0
Streamline diffusion	0
Crosswind diffusion	0

2.3.1. Diffusion

Settings

Settings	
Description	Value
Diffusion coefficient	{{D, 0, 0}, {0, D, 0}, {0, 0, D}}
Diffusion coefficient	{{D, 0, 0}, {0, D, 0}, {0, 0, D}}

Selection

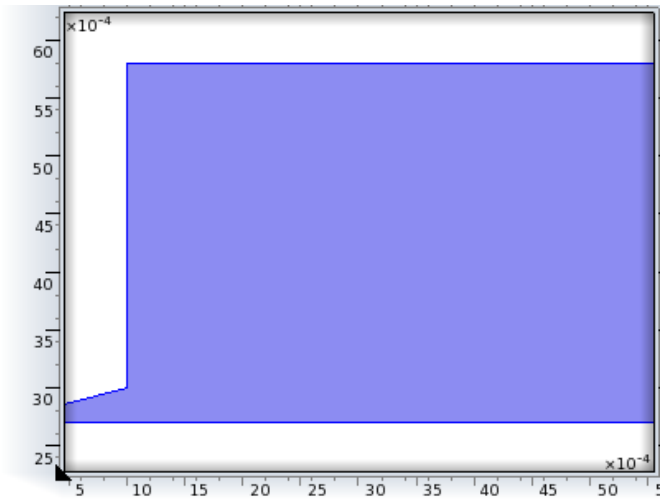

Diffusion

Variables

Name	Expression	Unit	Description	Selection
chdi.Drr_FcO	D	m^2/s	Diffusion coefficient, rr component	Domain 1
chdi.Dphir_FcO	0	m^2/s	Diffusion coefficient, phir component	Domain 1
chdi.Dzr_FcO	0	m^2/s	Diffusion coefficient, zr component	Domain 1
chdi.Drphi_FcO	0	m^2/s	Diffusion coefficient, rphi component	Domain 1
chdi.Dphiphi_FcO	D	m^2/s	Diffusion coefficient, phiphi component	Domain 1
chdi.Dzphi_FcO	0	m^2/s	Diffusion coefficient, zphi component	Domain 1
chdi.Drz_FcO	0	m^2/s	Diffusion coefficient, rz component	Domain 1
chdi.Dphiz_FcO	0	m^2/s	Diffusion coefficient, phiz component	Domain 1
chdi.Dzz_FcO	D	m^2/s	Diffusion coefficient, zz component	Domain 1
chdi.Dav_FcO	0.5*(chdi.Drr_FcO+chdi.Dzz_FcO)	m^2/s	Average diffusion coefficient	Domain 1
chdi.tfluxr_FcO	-chdi.Drr_FcO*FcOr-chdi.Drz_FcO*FcOz	mol/(m^2*s)	Total flux, r component	Domain 1
chdi.tfluxphi_FcO	-chdi.Dphir_FcO*FcOr-chdi.Dphiz_FcO*FcOz	mol/(m^2*s)	Total flux, phi component	Domain 1
chdi.tfluxz_FcO	-chdi.Dzr_FcO*FcOr-chdi.Dzz_FcO*FcOz	mol/(m^2*s)	Total flux, z component	Domain 1
chdi.dfluxr_FcO	-chdi.Drr_FcO*FcOr-chdi.Drz_FcO*FcOz	mol/(m^2*s)	Diffusive flux, r component	Domain 1
chdi.dfluxphi_FcO	-chdi.Dphir_FcO*FcOr-chdi.Dphiz_FcO*FcOz	mol/(m^2*s)	Diffusive flux, phi component	Domain 1
chdi.dfluxz_FcO	-chdi.Dzr_FcO*FcOr-chdi.Dzz_FcO*FcOz	mol/(m^2*s)	Diffusive flux, z component	Domain 1
chdi.gradr_FcO	FcOr	mol/m^4	Concentration gradient, r component	Domain 1
chdi.gradphi_FcO	0	mol/m^4	Concentration gradient, phi component	Domain 1
chdi.gradz_FcO	FcOz	mol/m^4	Concentration gradient, z component	Domain 1
chdi.ntflux_FcO	chdi.nr*chdi.tfluxr_FcO+chdi.nphi*chdi.tfluxphi_FcO+chdi.nz*chdi.tfluxz_FcO	mol/(m^2*s)	Normal total flux	Boundaries 1-10

chdi.ndflux_FcO	chdi.nr*chdi.dfluxr_FcO+chdi.nphi*chdi.dfluxphi_FcO+chdi.nz*chdi.dfluxz_FcO	mol/(m^2*s)	Normal diffusive flux	Boundaries 1-10
chdi.dfluxMag_FcO	sqrt(chdi.dfluxr_FcO^2+chdi.dfluxphi_FcO^2+chdi.dfluxz_FcO^2)	mol/(m^2*s)	Diffusive flux magnitude	Domain 1
chdi.tfluxMag_FcO	sqrt(chdi.tfluxr_FcO^2+chdi.tfluxphi_FcO^2+chdi.tfluxz_FcO^2)	mol/(m^2*s)	Total flux magnitude	Domain 1
chdi.Drr_FcR	D	m^2/s	Diffusion coefficient, rr component	Domain 1
chdi.Dphir_FcR	0	m^2/s	Diffusion coefficient, phir component	Domain 1
chdi.Dzr_FcR	0	m^2/s	Diffusion coefficient, zr component	Domain 1
chdi.Drphi_FcR	0	m^2/s	Diffusion coefficient, rphi component	Domain 1
chdi.Dphiphi_FcR	D	m^2/s	Diffusion coefficient, phiphi component	Domain 1
chdi.Dzphi_FcR	0	m^2/s	Diffusion coefficient, zphi component	Domain 1
chdi.Drz_FcR	0	m^2/s	Diffusion coefficient, rz component	Domain 1
chdi.Dphiz_FcR	0	m^2/s	Diffusion coefficient, phiz component	Domain 1
chdi.Dzz_FcR	D	m^2/s	Diffusion coefficient, zz component	Domain 1
chdi.Dav_FcR	0.5*(chdi.Drr_FcR+chdi.Dzz_FcR)	m^2/s	Average diffusion coefficient	Domain 1
chdi.tfluxr_FcR	-chdi.Drr_FcR*FcRr-chdi.Drz_FcR*FcRz	mol/(m^2*s)	Total flux, r component	Domain 1
chdi.tfluxphi_FcR	-chdi.Dphir_FcR*FcRr-chdi.Dphiz_FcR*FcRz	mol/(m^2*s)	Total flux, phi component	Domain 1
chdi.tfluxz_FcR	-chdi.Dzr_FcR*FcRr-chdi.Dzz_FcR*FcRz	mol/(m^2*s)	Total flux, z component	Domain 1
chdi.dfluxr_FcR	-chdi.Drr_FcR*FcRr-chdi.Drz_FcR*FcRz	mol/(m^2*s)	Diffusive flux, r component	Domain 1
chdi.dfluxphi_FcR	-chdi.Dphir_FcR*FcRr-chdi.Dphiz_FcR*FcRz	mol/(m^2*s)	Diffusive flux, phi component	Domain 1
chdi.dfluxz_FcR	-chdi.Dzr_FcR*FcRr-chdi.Dzz_FcR*FcRz	mol/(m^2*s)	Diffusive flux, z component	Domain 1
chdi.gradr_FcR	FcRr	mol/m^4	Concentration gradient, r component	Domain 1
chdi.gradphi_FcR	0	mol/m^4	Concentration gradient, phi component	Domain 1

chdi.gradz_FcR	FcRz	mol/m^4	Concentration gradient, z component	Domain 1
chdi.ntflux_FcR	chdi.nr*chdi.tfluxr_FcR+chdi.nphi*chdi.tfluxphi_FcR+chdi.nz*chdi.tfluxz_FcR	mol/(m^2*s)	Normal total flux	Boundaries 1-10
chdi.ndflux_FcR	chdi.nr*chdi.dfluxr_FcR+chdi.nphi*chdi.dfluxphi_FcR+chdi.nz*chdi.dfluxz_FcR	mol/(m^2*s)	Normal diffusive flux	Boundaries 1-10
chdi.dfluxMag_FcR	sqrt(chdi.dfluxr_FcR^2+chdi.dfluxphi_FcR^2+chdi.dfluxz_FcR^2)	mol/(m^2*s)	Diffusive flux magnitude	Domain 1
chdi.tfluxMag_FcR	sqrt(chdi.tfluxr_FcR^2+chdi.tfluxphi_FcR^2+chdi.tfluxz_FcR^2)	mol/(m^2*s)	Total flux magnitude	Domain 1

Shape functions

Name	Shape function	Unit	Description	Shape frame	Selection
FcO	Lagrange	mol/m^3	Concentration	Spatial	Domain 1
FcR	Lagrange	mol/m^3	Concentration	Spatial	Domain 1

Weak expressions

Weak expression	Integration frame	Selection
2*(-FcOt*test(FcO)-(chdi.Drr_FcO*FcOr+chdi.Drz_FcO*FcOz)*test(FcOr)-(chdi.Dzr_FcO*FcOr+chdi.Dzz_FcO*FcOz)*test(FcOz))*pi*r	Spatial	Domain 1
2*(-FcRt*test(FcR)-(chdi.Drr_FcR*FcRr+chdi.Drz_FcR*FcRz)*test(FcRr)-(chdi.Dzr_FcR*FcRr+chdi.Dzz_FcR*FcRz))*pi*r	Spatial	Domain 1

2.3.2. Axial Symmetry 1

Selection

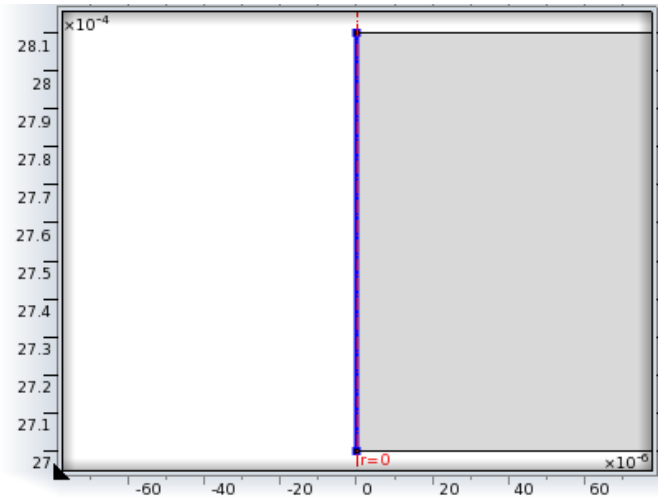

Axial Symmetry 1

2.3.3. No Flux 1

Selection

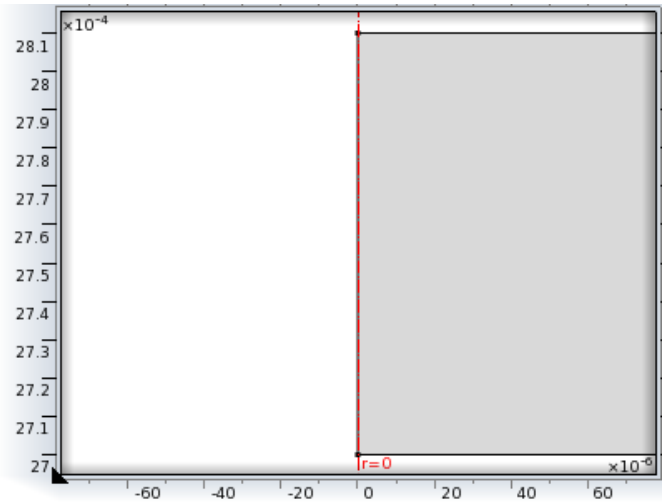

No Flux 1

2.3.4. Initial Values 1

Settings

Settings	
Description	Value
Concentration	4.3

Selection

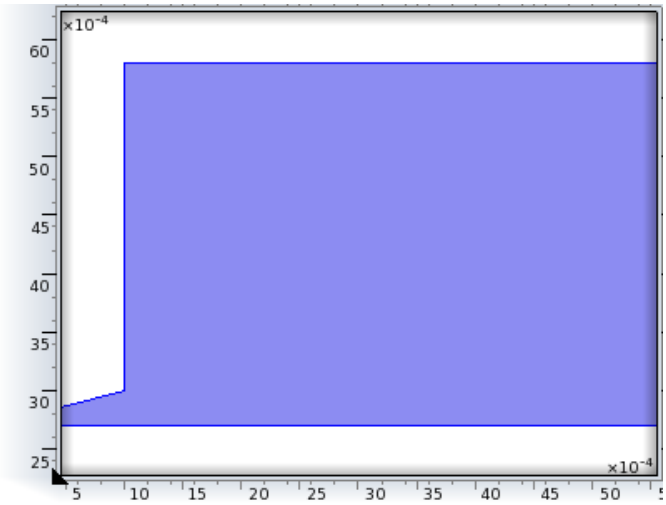

Initial Values 1

2.3.5. No Flux 2

Settings

Settings	
Description	Value
Apply for all species	Apply for...
Species FcO	1
Species FcR	1

Selection

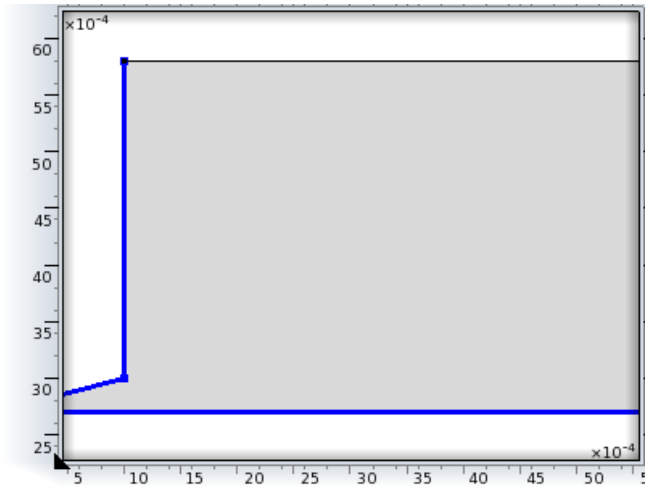

No Flux 2

2.3.6. Concentration 1

Settings

Settings	
Description	Value
Concentration	{0, 1}
Species FcO	1
Species FcR	1

Selection

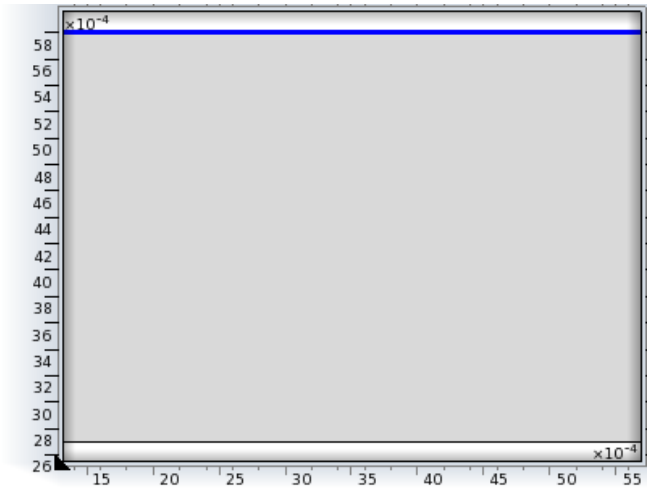

Concentration 1

Variables

Name	Expression	Unit	Description	Selection
chdi.c0_FcO	0	mol/m^3	Concentration	Boundaries 9-10
chdi.c0_FcR	1	mol/m^3	Concentration	Boundaries 9-10

Constraints

Constraint	Constraint force	Shape function	Selection

-FcO+chdi.c0_FcO	test(-FcO+chdi.c0_FcO)	Lagrange	Boundaries 9-10
-FcR+chdi.c0_FcR	test(-FcR+chdi.c0_FcR)	Lagrange	Boundaries 9-10

2.3.7. Flux 1

Settings

Settings	
Description	Value
Species FcO	1
Species FcR	1
Inward flux	{kaS*FcR-kcS*FcO, -kaS*FcR+kcS*FcO}

Selection

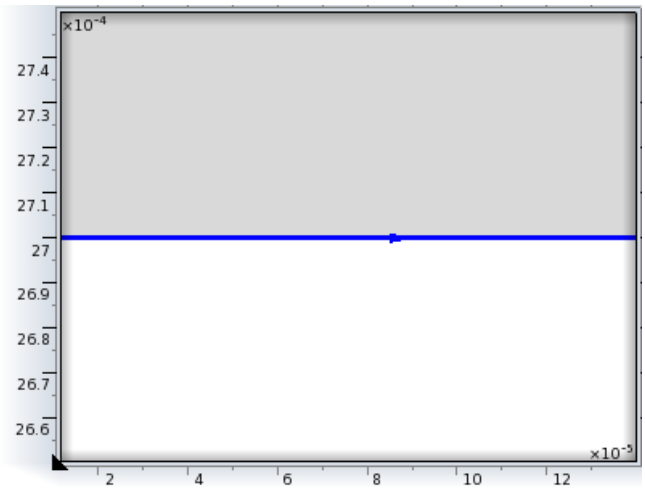

Flux 1

Variables

Name	Expression	Unit	Description	Selection
chdi.cb_FcO	0	mol/m^3	Bulk concentration	Boundary 2
chdi.kc_FcO	0	m/s	Mass transfer coefficient	Boundary 2
chdi.cb_FcR	0	mol/m^3	Bulk concentration	Boundary 2
chdi.kc_FcR	0	m/s	Mass transfer coefficient	Boundary 2

Weak expressions

Weak expression	Integration frame	Selection
2*(kaS*FcR-kcS*FcO)*test(FcO)*pi*r	Spatial	Boundary 2
2*(-kaS*FcR+kcS*FcO)*test(FcR)*pi*r	Spatial	Boundary 2
2*chdi.kc_FcO*(chdi.cb_FcO-FcO)*test(FcO)*pi*r	Spatial	Boundary 2
2*chdi.kc_FcR*(chdi.cb_FcR-FcR)*test(FcR)*pi*r	Spatial	Boundary 2

2.3.8. Flux 2

Settings

Settings	
Description	Value
Species FcO	1
Species FcR	1
Inward flux	{kaR*FcR-kcR*FcO, -kaR*FcR+kcR*FcO}

Selection

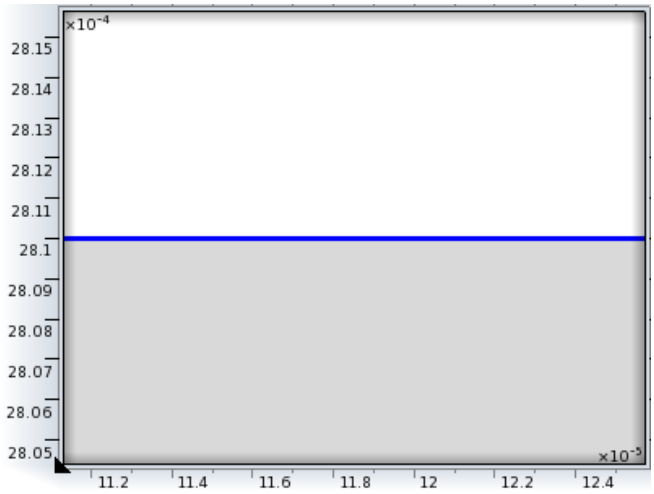

Flux 2

Variables

Name	Expression	Unit	Description	Selection
chdi.cb_FcO	0	mol/m^3	Bulk concentration	Boundary 4
chdi.kc_FcO	0	m/s	Mass transfer coefficient	Boundary 4
chdi.cb_FcR	0	mol/m^3	Bulk concentration	Boundary 4
chdi.kc_FcR	0	m/s	Mass transfer coefficient	Boundary 4

Weak expressions

Weak expression	Integration frame	Selection
2*(kaR*FcR-kcR*FcO)*test(FcO)*pi*r	Spatial	Boundary 4
2*(-kaR*FcR+kcR*FcO)*test(FcR)*pi*r	Spatial	Boundary 4
2*chdi.kc_FcO*(chdi.cb_FcO-FcO)*test(FcO)*pi*r	Spatial	Boundary 4
2*chdi.kc_FcR*(chdi.cb_FcR-FcR)*test(FcR)*pi*r	Spatial	Boundary 4

2.4. MESHES

2.4.1. Mesh 1

Mesh statistics	
Property	Value
Minimum element quality	0.696
Average element quality	0.9656
Triangular elements	18717
Edge elements	1405
Vertex elements	10

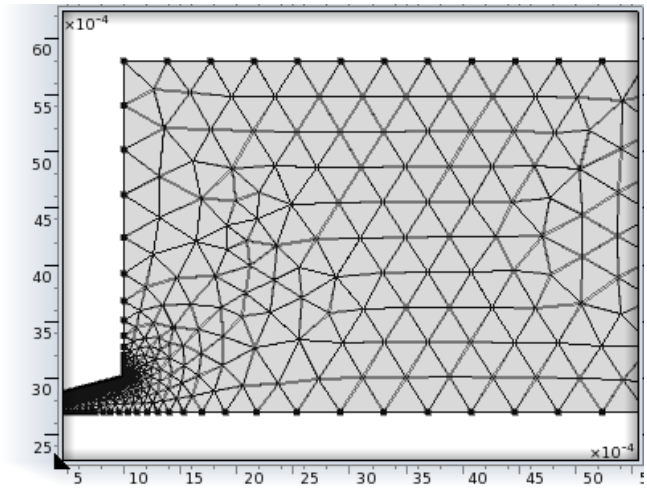

Mesh 1

Size (size)

Settings	
Name	Value
Maximum element size	4.02E-4
Minimum element size	1.8E-6
Resolution of curvature	0.3
Maximum element growth rate	1.3

Mesh Object (obj)

Settings	
Name	Value
Filename	$FILENAME$_mesh1_obj.mphbin

2.4.2. Mesh 2

Mesh statistics	
Property	Value
Minimum element quality	0.0
Average element quality	0.0

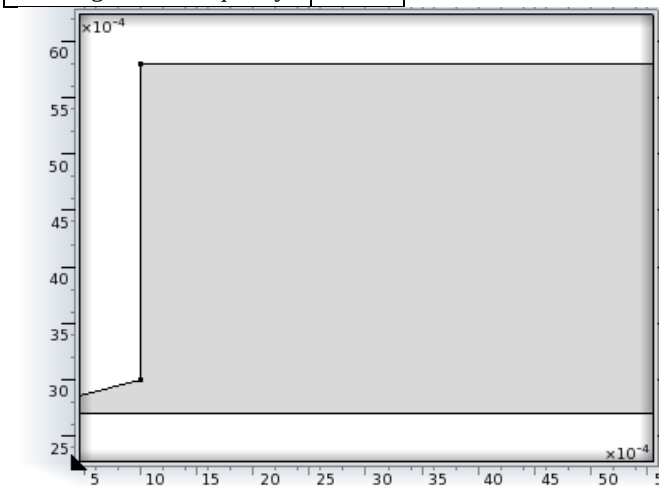

Mesh 2

Size (size)

Settings	
Name	Value
Maximum element size	4.02E-4
Minimum element size	1.8E-6
Resolution of curvature	0.3
Maximum element growth rate	1.3

Size 1 (size1)

Settings	
Name	Value
Maximum element size	5e-7
Minimum element size	1.8E-6
Minimum element size	off
Resolution of curvature	0.3
Resolution of curvature	off
Resolution of narrow regions	off
Maximum element growth rate	1.3
Maximum element growth rate	off
Custom element size	Custom

Size 2 (size2)

Settings	
Name	Value
Maximum element size	1e-6
Minimum element size	1.8E-6
Minimum element size	off
Resolution of curvature	0.3
Resolution of curvature	off
Resolution of narrow regions	off
Maximum element growth rate	1.3
Maximum element growth rate	off
Custom element size	Custom

3. Study 1

3.1. TIME DEPENDENT

Times: range(0,0.2,200)

Mesh selection	
Geometry	Mesh
Geometry 1 (geom1)	mesh1

Physics selection	
Physics interface	Discretization
Transport of Diluted Species (chdi)	physics

4. Results

4.1. 2D PLOT GROUP 1

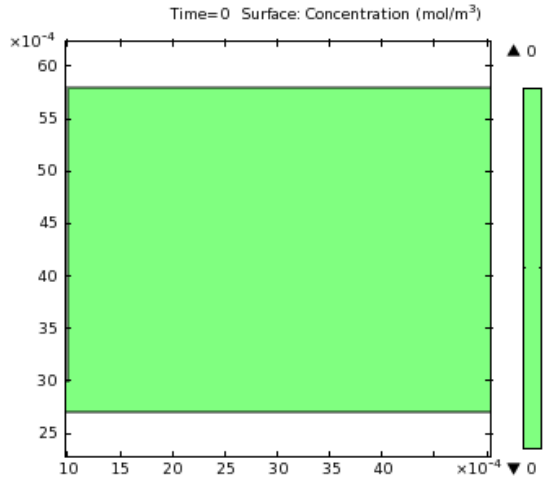

Time=0 Surface: Concentration (mol/m^3)

4.2. CONCENTRATION (CHDI)

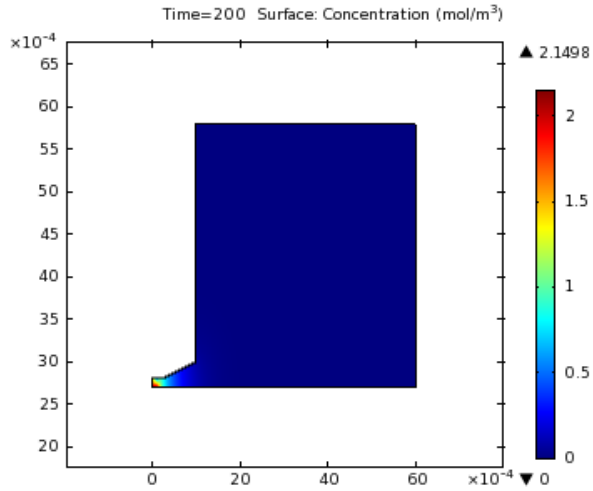

Time=200 Surface: Concentration (mol/m^3)

4.3. CONCENTRATION, 3D (CHDI)

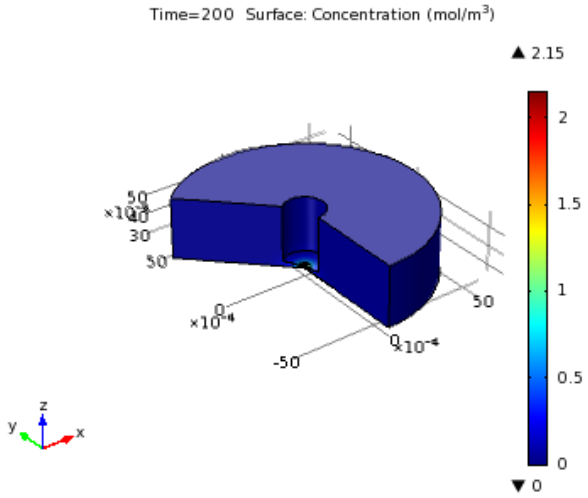

Time=200 Surface: Concentration (mol/m^3)

B.2 Semiconductor calculations (Chapter 4)

1. Global Definitions

1.1. PARAMETERS 1

Parameters		
Name	Expression	Description
q	1.602e-19 [C]	elementary charge
T	300[K]	temperature
k	1.38e-23 [J/K]	Boltzmann's constant
epsilonr	68	relative permittivity
epsilon0	8.854e-12[F/m]	vaccum permittivity
X_si	4.5[V]	electron affinity of Si
X_metal	6 [V]	work function of metal
Eg_si	2.4 [V]	band gap of Si
Vt	k*T/q	thermal velocity
Vg	0 [V]	gate voltage
Dn	Vt*mun	electron diffusivity
Dp	Vt*mup	hole diffusivity
ni	Ns*exp(-Eg_si/(2*Vt))	intrinsic doping density
Depth	1[um]	total depth of the semiconductor
Abs	2e4[1/cm]	absorption coefficient
Da	1e-5[cm^2/s]	diffusion coefficient
Db	2e-5[cm^2/s]	diffusion coefficient
Cabulk	1e-4[mol/cm^3]*NA	bulk concentration of A
NA	6.02e23[1/mol]	Avogardo number
Cbbulk	1.3e-6[mol/cm^3]*NA	bulk concentrtion of B
Ns	1e18[1/cm^3]	available states at room temperature
I0	8e16[1/cm^2/s]	initial light intensity
mup	100[cm^2/V/s]	hole mobility
mun	300[cm^2/V/s]	electron mobility
taun	3.3e-13[s]	life time of electron carrier
taup	3.3e-13[s]	life time of hole carrier
Ndoping	8e19[1/cm^3]	substrate doping
kf	12e-17[cm^3/s]	standard heterogeneous rate constant
kb	4e-20[cm^3/s]	standard heterogeneous rate constant
SurRec	1e-4[cm^4/s]	surface recombination kinetic conctant
Front	1	Front or back illumination
Back	0	Front or back illumination
sw	0	

1.2. VARIABLES

1.2.1. Variables 1

Geometric entity level: Entire model

Name	Expression	Description
Vd	0.0+sw*0.020[V/s]	gate potential
Switch	((sw-(floor(sw/(2.0*Interval))*(2.0*Interval)))>Interval)*1.0+((sw-(floor(sw/(2.0*Interval))*(2.0*Interval)))<Interval)*0.0	
Interval	1.0[s]	

2. Model 1 (mod1)
2.1. DEFINITIONS
2.1.1. Variables
Variables 2
Geometric entity level: Entire model

Name	Expression	Description
n0	ni*exp((psi_init+X_si+0.5*Eg_si+Vd)/Vt)	electron concentration in thermal equilibrium
p0	ni*exp(-(psi_init+X_si+0.5*Eg_si+Vd)/Vt)	hole concentration in thermal equilibrium
RSRH	(cn*cp-ni^2)/(taun*(cp+ni)+taup*(cn+ni))	Shockley-Reed-Hall recombination term
temp	abs(Ndoping)/2+sqrt(Ndoping^2/4+ni^2)	
n_init	temp	
p_init	ni^2/n_init	
psi_0	Vt*(-log(p_init/ni)*(Ndoping<0)+log(n_init/ni)*(Ndoping>=0))-X_si-0.5*Eg_si	initial guess for phi_init
I	I0*exp(-Abs*x)*Abs*Front+I0*exp(-Abs*(Depth-x))*Abs*Back	

Variables 3
Geometric entity level: Boundary
Selection: Boundary 2

Name	Expression	Description
DiodeCurrent	(cd.ntflux_cn-cd2.ntflux_cp)/NA	
Current	q*(-cd7.ntflux_DCa+cd8.ntflux_DCb)	
Surface	(cd2.ntflux_cp-cd.ntflux_cn)*q	

Variables 4
Geometric entity level: Boundary
Selection: Boundary 3

Name	Expression	Description
Electrode	(cd2.ntflux_cp-cd.ntflux_cn)*q/10	

Variables 1a
Geometric entity level: Domain
Selection: Domain 2

Name	Expression	Description
intcpl_source_Intensity	I	
Bound	genext1(extrcpl_source_Bound)	

Variables 2a
Geometric entity level: Boundary
Selection: Boundary 3

Name	Expression	Description
Intensity	intop1(intcpl_source_Intensity)	

Variables 3a
Geometric entity level: Boundary
Selection: Boundary 2

Name	Expression	Description
extrcpl_source_Bound	cp	

2.2. GEOMETRY 1

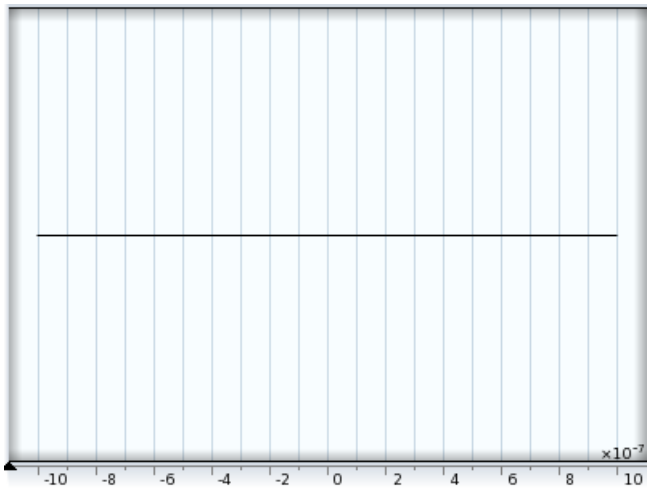

Geometry

Geometry statistics	
Property	Value
Space dimension	1
Number of domains	2
Number of boundaries	3

2.2.1. Composite Object 1 (I1)

Settings	
Name	Value
Filename	$FILENAME$_geom1_I1.mphbin

2.2.2. Composite Object 2 (I2)

Settings	
Name	Value
Filename	$FILENAME$_geom1_I2.mphbin

2.3. POISSON'S EQUATION (POEQ)

Poisson's Equation

2.3.1. Poisson's Equation 1

Settings

Settings	
Description	Value
Source term	q*(p0-n0+Ndoping)
Diffusion coefficient	epsilon0*epsilonr

Selection

Poisson's Equation 1

Shape functions

Name	Shape function	Unit	Description	Shape frame	Selection
psi_init	Lagrange		Dependent variable psi_init	Spatial	Domain 2

2.3.2. Zero Flux 1

Selection

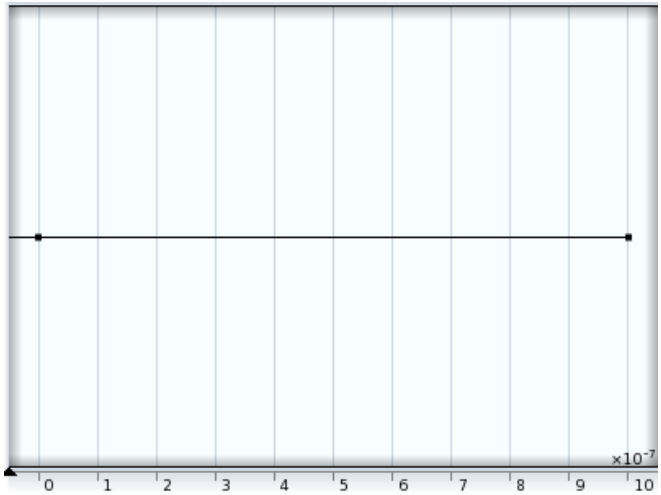

Zero Flux 1

2.3.3. Initial Values 1

Settings

Settings	
Description	Value
Initial value for psi_init	psi_0

Selection

Initial Values 1

2.3.4. Dirichlet Boundary Condition 1

Settings

Settings	
Description	Value
Value on boundary	psi_0

Selection

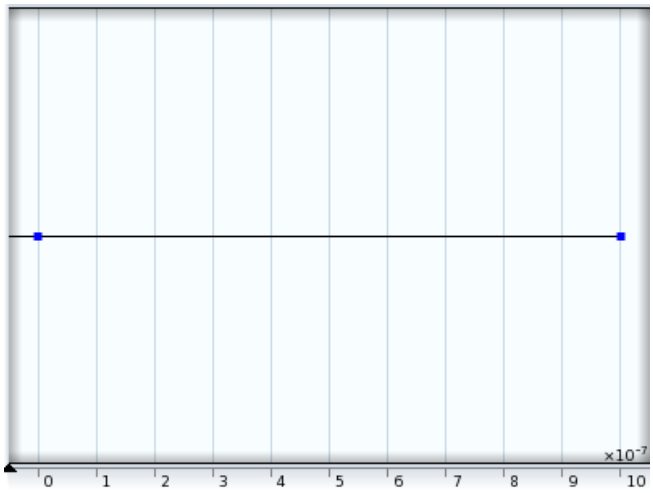

Dirichlet Boundary Condition 1

Constraints

Constraint	Constraint force	Shape function	Selection
psi_0-psi_init	-test(psi_init)	Lagrange	Boundaries 2-3

2.4. POISSON'S EQUATION 2 (POEQ2)

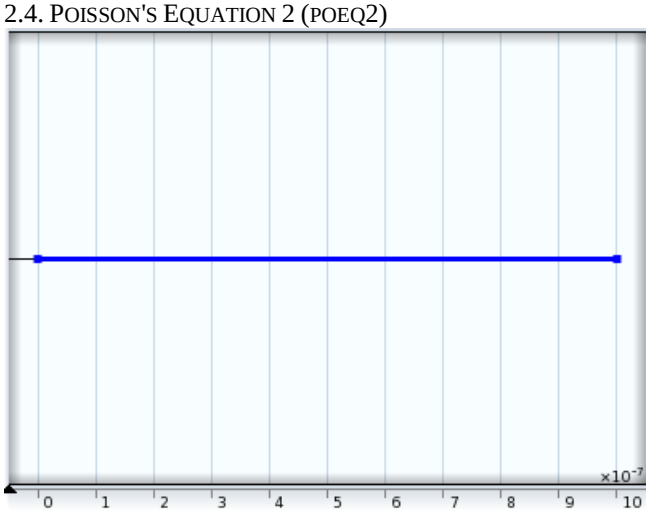

Poisson's Equation 2

2.4.1. Poisson's Equation 1

Settings

Settings	
Description	Value
Source term	q*(cp-cn+Ndoping)
Diffusion coefficient	epsilon0*epsilonr

Selection

Poisson's Equation 1

Shape functions

Name	Shape function	Unit	Description	Shape frame	Selection
psi	Lagrange		Dependent variable psi	Spatial	Domain 2

2.4.2. Zero Flux 1

Selection

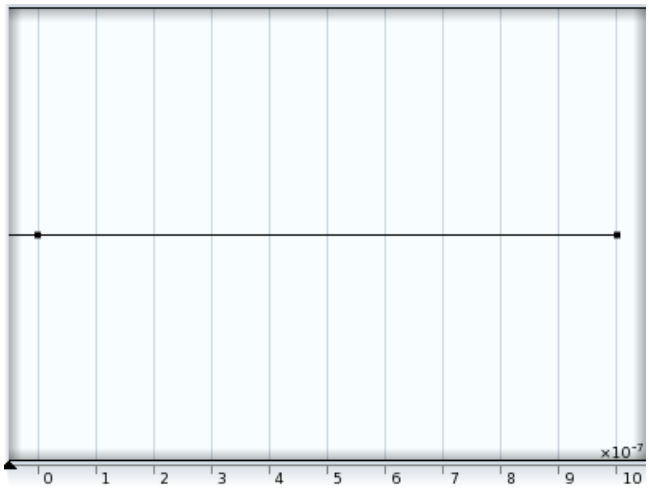

Zero Flux 1

2.4.3. Initial Values 1

Settings

Settings	
Description	Value
Initial value for psi	psi_init

Selection

Initial Values 1

2.4.4. Dirichlet Boundary Condition 1

Settings

Settings	
Description	Value
Value on boundary	psi_0-Vd

Selection

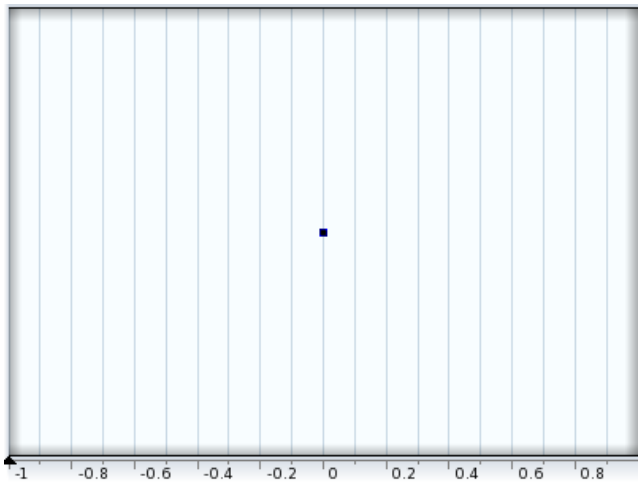

Dirichlet Boundary Condition 1

Constraints

Constraint	Constraint force	Shape function	Selection
psi_0-Vd-psi	-test(psi)	Lagrange	Boundary 2

2.4.5. Dirichlet Boundary Condition 2

Settings

Settings	
Description	Value
Value on boundary	psi_0

Selection

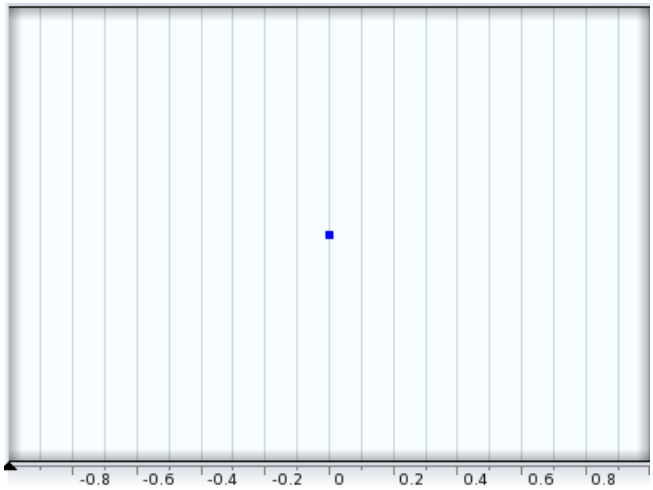

Dirichlet Boundary Condition 2

Constraints

Constraint	Constraint force	Shape function	Selection
psi_0-psi	-test(psi)	Lagrange	Boundary 3

2.5. TRANSPORT OF DILUTED SPECIES (CD)

Transport of Diluted Species

Settings	
Description	Value
Concentration	Quadratic
Convective term	Conservative form
Streamline diffusion	0
Crosswind diffusion	0
Show equation assuming	std1/stat

2.5.1. Convection and Diffusion 1

Settings

Settings	
Description	Value
Velocity field	{mun*psix, 0, 0}
Diffusion coefficient	{{Dn, 0, 0}, {0, Dn, 0}, {0, 0, Dn}}

Selection

Convection and Diffusion 1

Variables

Name	Expression	Unit	Description	Selection
cd.Dxx_cn	Dn	m^2/s	Diffusion coefficient, xx component	Domain 2
cd.Dyx_cn	0	m^2/s	Diffusion coefficient, yx component	Domain 2
cd.Dzx_cn	0	m^2/s	Diffusion coefficient, zx component	Domain 2
cd.Dxy_cn	0	m^2/s	Diffusion coefficient, xy component	Domain 2
cd.Dyy_cn	Dn	m^2/s	Diffusion coefficient, yy component	Domain 2
cd.Dzy_cn	0	m^2/s	Diffusion coefficient, zy component	Domain 2
cd.Dxz_cn	0	m^2/s	Diffusion coefficient, xz component	Domain 2
cd.Dyz_cn	0	m^2/s	Diffusion coefficient, yz component	Domain 2
cd.Dzz_cn	Dn	m^2/s	Diffusion coefficient, zz component	Domain 2
cd.Dav_cn	cd.Dxx_cn	m^2/s	Average diffusion coefficient	Domain 2
cd.tfluxx_cn	-cd.Dxx_cn*cnx+cd.cfluxx_cn	mol/(m^2*s)	Total flux, x component	Domain 2
cd.tfluxy_cn	-cd.Dyx_cn*cnx+cd.cfluxy_cn	mol/(m^2*s)	Total flux, y component	Domain 2
cd.tfluxz_cn	-cd.Dzx_cn*cnx+cd.cfluxz_cn	mol/(m^2*s)	Total flux, z component	Domain 2
cd.dfluxx_cn	-cd.Dxx_cn*cnx	mol/(m^2*s)	Diffusive flux, x component	Domain 2
cd.dfluxy_cn	-cd.Dyx_cn*cnx	mol/(m^2*s)	Diffusive flux, y component	Domain 2
cd.dfluxz_cn	-cd.Dzx_cn*cnx	mol/(m^2*s)	Diffusive flux, z component	Domain 2
cd.gradx_cn	cnx	mol/m^4	Concentration gradient, x component	Domain 2
cd.grady_cn	0	mol/m^4	Concentration gradient, y component	Domain 2
cd.gradz_cn	0	mol/m^4	Concentration gradient, z component	Domain 2
cd.ntflux_cn	cd.nx*cd.tfluxx_cn+cd.ny*cd.tfluxy_cn+cd.nz*cd.tfluxz_cn	mol/(m^2*s)	Normal total flux	Boundaries 2-3
cd.ndflux_cn	cd.nx*cd.dfluxx_cn+cd.ny*cd.dfluxy_cn+cd.nz*cd.dfluxz_cn	mol/(m^2*s)	Normal diffusive flux	Boundaries 2-3
cd.dfluxMag_cn	sqrt(cd.dfluxx_cn^2+cd.dfluxy_cn^2+cd.dfluxz_cn^2)	mol/(m^2*s)	Diffusive flux magnitude	Domain 2
cd.tfluxMag_cn	sqrt(cd.tfluxx_cn^2+cd.tfluxy_cn^2+cd.tfluxz_cn^2)	mol/(m^2*s)	Total flux magnitude	Domain 2
cd.u	u1	m/s	Velocity field, x component	Domain 2
cd.v	u2	m/s	Velocity field, y component	Domain 2
cd.w	u3	m/s	Velocity field, z component	Domain 2

cd.cfluxx_cn	cn*u1	mol/(m^2*s)	Convective flux, x component	Domain 2
cd.cfluxy_cn	cn*u2	mol/(m^2*s)	Convective flux, y component	Domain 2
cd.cfluxz_cn	cn*u3	mol/(m^2*s)	Convective flux, z component	Domain 2
cd.cfluxMag_cn	sqrt(cd.cfluxx_cn^2+cd.cfluxy_cn^2+cd.cfluxz_cn^2)	mol/(m^2*s)	Convective flux magnitude	Domain 2
cd.ncflux_cn	cd.nx*cd.cfluxx_cn+cd.ny*cd.cfluxy_cn+cd.nz*cd.cfluxz_cn	mol/(m^2*s)	Normal convective flux	Boundaries 2-3
cd.cbf_cn	0	mol/(m^2*s)	Convective boundary flux	Boundaries 2-3

Shape functions

Name	Shape function	Unit	Description	Shape frame	Selection
cn	Lagrange	mol/m^3	Concentration	Spatial	Domain 2

Weak expressions

Weak expression	Integration frame	Selection
-cnt*test(cn)-cd.Dxx_cn*cnx*test(cnx)	Spatial	Domain 2
cn*cd.u*test(cnx)	Spatial	Domain 2
cd.cbf_cn	Spatial	Boundaries 2-3

2.5.2. No Flux 1

Selection

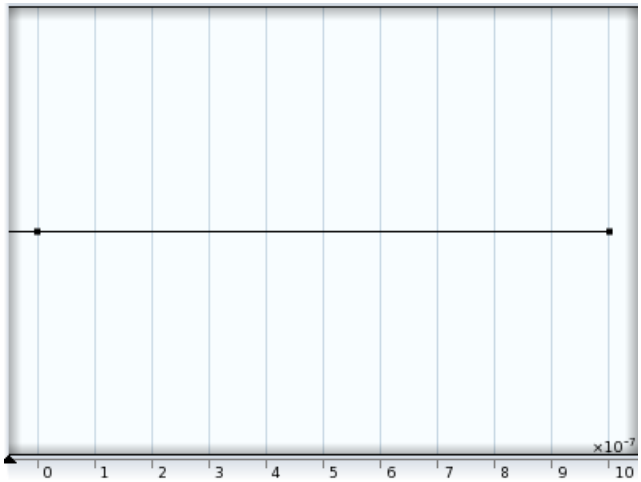

No Flux 1

2.5.3. Initial Values 1

Settings

Settings	
Description	Value
Concentration	n_init

Selection

Initial Values 1

2.5.4. Reactions 1

Settings

Settings	
Description	Value
Total rate expression	-RSRH+Switch*I

Selection

Reactions 1

Variables

Name	Expression	Unit	Description	Selection
cd.R_cn	-RSRH+Switch*I	mol/(m^3*s)	Total rate expression	Domain 2

Weak expressions

Weak expression	Integration frame	Selection
(-RSRH+Switch*I)*test(cn)	Spatial	Domain 2

2.5.5. Concentration 1

Settings

Settings	
Description	Value
Concentration	n_init

Species cn	1

Selection

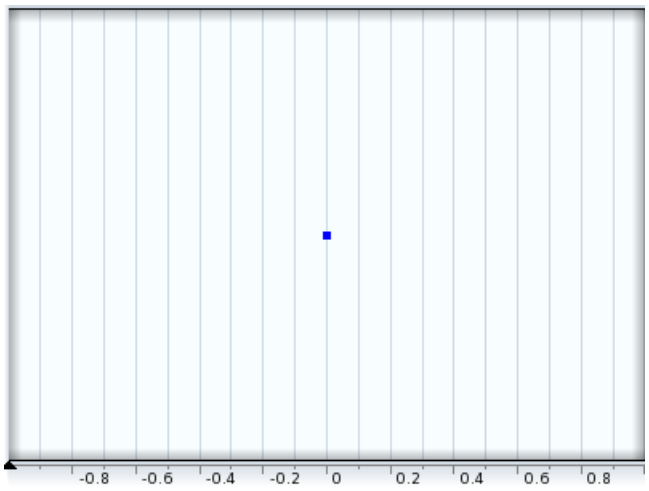

Concentration 1

Variables

Name	Expression	Unit	Description	Selection
cd.c0_cn	n_init	mol/m^3	Concentration	Boundary 3

Constraints

Constraint	Constraint force	Shape function	Selection
-cn+cd.c0_cn	test(-cn+cd.c0_cn)	Lagrange	Boundary 3

2.5.6. Flux 1

Settings

Settings	
Description	Value
Species cn	1
Inward flux	-kb*cn*DCb-SurRec*cn*cp

Selection

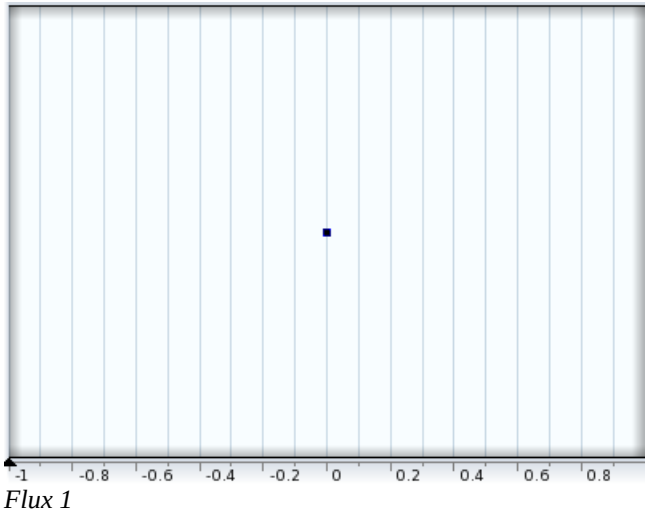

Flux 1

Weak expressions

Weak expression	Integration frame	Selection
cn*(-kb*DCb-SurRec*cp)*test(cn)	Spatial	Boundary 2

2.6. TRANSPORT OF DILUTED SPECIES 2 (CD2)

Transport of Diluted Species 2

Settings	
Description	Value
Concentration	Quadratic
Convective term	Conservative form
Streamline diffusion	0
Crosswind diffusion	0
Show equation assuming	std1/stat

2.6.1. Convection and Diffusion 1

Settings

Settings	
Description	Value
Velocity field	{-mup*psix, 0, 0}
Diffusion coefficient	{{Dp, 0, 0}, {0, Dp, 0}, {0, 0, Dp}}

Selection

Convection and Diffusion 1

Variables

Name	Expression	Unit	Description	Selection
cd2.Dxx_cp	Dp	m^2/s	Diffusion coefficient,	Domain 2

			xx component	
cd2.Dyx_cp	0	m^2/s	Diffusion coefficient, yx component	Domain 2
cd2.Dzx_cp	0	m^2/s	Diffusion coefficient, zx component	Domain 2
cd2.Dxy_cp	0	m^2/s	Diffusion coefficient, xy component	Domain 2
cd2.Dyy_cp	Dp	m^2/s	Diffusion coefficient, yy component	Domain 2
cd2.Dzy_cp	0	m^2/s	Diffusion coefficient, zy component	Domain 2
cd2.Dxz_cp	0	m^2/s	Diffusion coefficient, xz component	Domain 2
cd2.Dyz_cp	0	m^2/s	Diffusion coefficient, yz component	Domain 2
cd2.Dzz_cp	Dp	m^2/s	Diffusion coefficient, zz component	Domain 2
cd2.Dav_cp	cd2.Dxx_cp	m^2/s	Average diffusion coefficient	Domain 2
cd2.tfluxx_cp	-cd2.Dxx_cp*cpx+cd2.cfluxx_cp	mol/(m^2*s)	Total flux, x component	Domain 2
cd2.tfluxy_cp	-cd2.Dyx_cp*cpx+cd2.cfluxy_cp	mol/(m^2*s)	Total flux, y component	Domain 2
cd2.tfluxz_cp	-cd2.Dzx_cp*cpx+cd2.cfluxz_cp	mol/(m^2*s)	Total flux, z component	Domain 2
cd2.dfluxx_cp	-cd2.Dxx_cp*cpx	mol/(m^2*s)	Diffusive flux, x component	Domain 2
cd2.dfluxy_cp	-cd2.Dyx_cp*cpx	mol/(m^2*s)	Diffusive flux, y component	Domain 2
cd2.dfluxz_cp	-cd2.Dzx_cp*cpx	mol/(m^2*s)	Diffusive flux, z component	Domain 2
cd2.gradx_cp	cpx	mol/m^4	Concentration gradient, x component	Domain 2
cd2.grady_cp	0	mol/m^4	Concentration gradient, y component	Domain 2
cd2.gradz_cp	0	mol/m^4	Concentration gradient, z component	Domain 2
cd2.ntflux_cp	cd2.nx*cd2.tfluxx_cp+cd2.ny*cd2.tfluxy_cp+cd2.nz*cd2.tfluxz_cp	mol/(m^2*s)	Normal total flux	Boundaries 2-3
cd2.ndflux_cp	cd2.nx*cd2.dfluxx_cp+cd2.ny*cd2.dfluxy_cp+cd2.nz*cd2.dfluxz_cp	mol/(m^2*s)	Normal diffusive flux	Boundaries 2-3
cd2.dfluxMag_cp	sqrt(cd2.dfluxx_cp^2+cd2.dfluxy_cp^2+cd2.dfluxz_cp^2)	mol/(m^2*s)	Diffusive flux magnitude	Domain 2
cd2.tfluxMag_cp	sqrt(cd2.tfluxx_cp^2+cd2.tfluxy_cp^2+cd2.tfluxz_cp^2)	mol/(m^2*s)	Total flux magnitude	Domain 2
cd2.u	u1	m/s	Velocity field, x component	Domain 2
cd2.v	u2	m/s	Velocity field, y component	Domain 2
cd2.w	u3	m/s	Velocity field, z component	Domain 2
cd2.cfluxx_cp	cp*u1	mol/(m^2*s)	Convective flux, x component	Domain 2
cd2.cfluxy_cp	cp*u2	mol/(m^2*s)	Convective flux, y	Domain 2

			component	
cd2.cfluxz_cp	cp*u3	mol/(m^2*s)	Convective flux, z component	Domain 2
cd2.cfluxMag_cp	sqrt(cd2.cfluxx_cp^2+cd2.cfluxy_cp^2+cd2.cfluxz_cp^2)	mol/(m^2*s)	Convective flux magnitude	Domain 2
cd2.ncflux_cp	cd2.nx*cd2.cfluxx_cp+cd2.ny*cd2.cfluxy_cp+cd2.nz*cd2.cfluxz_cp	mol/(m^2*s)	Normal convective flux	Boundaries 2-3
cd2.cbf_cp	0	mol/(m^2*s)	Convective boundary flux	Boundaries 2-3

Shape functions

Name	Shape function	Unit	Description	Shape frame	Selection
cp	Lagrange	mol/m^3	Concentration	Spatial	Domain 2

Weak expressions

Weak expression	Integration frame	Selection
-cpt*test(cp)-cd2.Dxx_cp*cpx*test(cpx)	Spatial	Domain 2
cp*cd2.u*test(cpx)	Spatial	Domain 2
cd2.cbf_cp	Spatial	Boundaries 2-3

2.6.2. No Flux 1

Selection

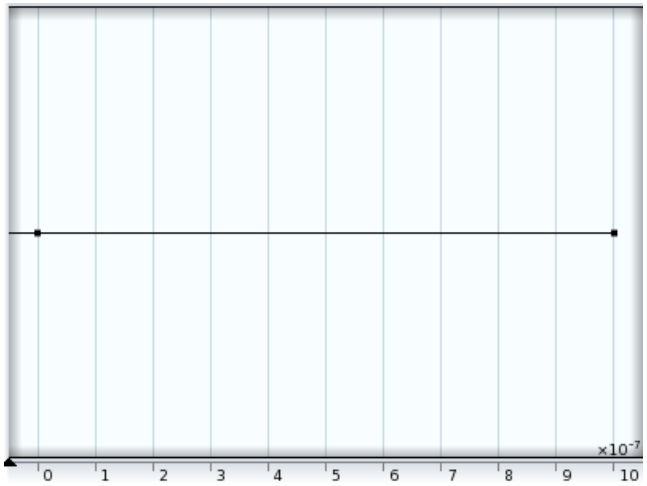

No Flux 1

2.6.3. Initial Values 1

Settings

Settings	
Description	Value
Concentration	p_init

Selection

Initial Values 1

2.6.4. Reactions 1

Settings

Settings	
Description	Value
Total rate expression	-RSRH+I*Switch

Selection

Reactions 1

Variables

Name	Expression	Unit	Description	Selection
cd2.R_cp	-RSRH+I*Switch	mol/(m^3*s)	Total rate expression	Domain 2

Weak expressions

Weak expression	Integration frame	Selection
(-RSRH+I*Switch)*test(cp)	Spatial	Domain 2

2.6.5. Concentration 1

Settings

Settings	
Description	Value
Concentration	p_init

Species cp	1

Selection

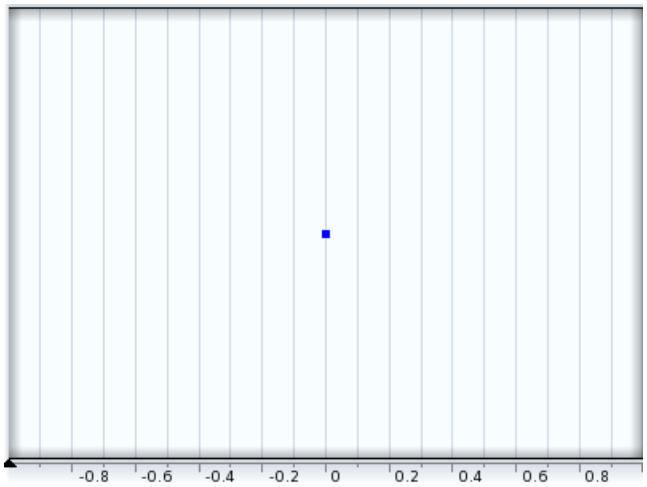

Concentration 1

Variables

Name	Expression	Unit	Description	Selection
cd2.c0_cp	p_init	mol/m^3	Concentration	Boundary 3

Constraints

Constraint	Constraint force	Shape function	Selection
-cp+cd2.c0_cp	test(-cp+cd2.c0_cp)	Lagrange	Boundary 3

2.6.6. Flux 1

Settings

Settings	
Description	Value
Species cp	1
Inward flux	-kf*DCa*cp-SurRec*cn*cp

Selection

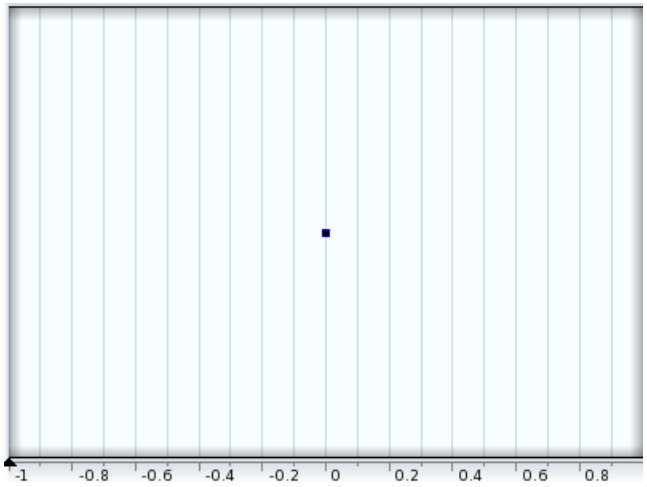

Flux 1

Weak expressions

Weak expression	Integration frame	Selection
cp*(-kf*DCa-SurRec*cn)*test(cp)	Spatial	Boundary 2

2.7. Transport of Diluted Species 7 (cd7)

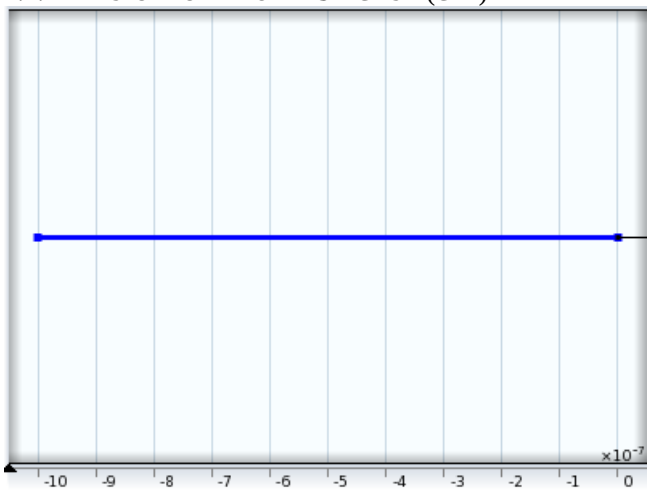

Transport of Diluted Species 7

Settings	
Description	Value
Concentration	Quadratic
Convective term	Conservative form
Streamline diffusion	0
Crosswind diffusion	0
Show equation assuming	std1/stat

2.7.1. Convection and Diffusion 1

Settings

Settings	
Description	Value
Diffusion coefficient	{{Da, 0, 0}, {0, Da, 0}, {0, 0, Da}}

Selection

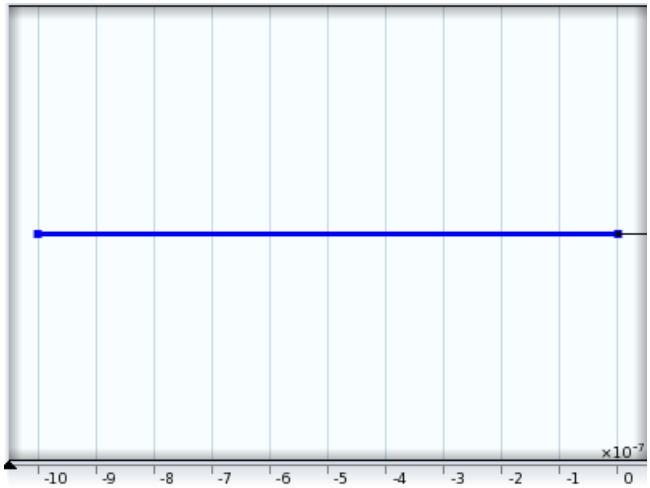

Convection and Diffusion 1

Variables

Name	Expression	Unit	Description	Selection
cd7.Dxx_DCa	Da	m^2/s	Diffusion coefficient, xx	Domain 1

			component	
cd7.Dyx_DCa	0	m^2/s	Diffusion coefficient, yx component	Domain 1
cd7.Dzx_DCa	0	m^2/s	Diffusion coefficient, zx component	Domain 1
cd7.Dxy_DCa	0	m^2/s	Diffusion coefficient, xy component	Domain 1
cd7.Dyy_DCa	Da	m^2/s	Diffusion coefficient, yy component	Domain 1
cd7.Dzy_DCa	0	m^2/s	Diffusion coefficient, zy component	Domain 1
cd7.Dxz_DCa	0	m^2/s	Diffusion coefficient, xz component	Domain 1
cd7.Dyz_DCa	0	m^2/s	Diffusion coefficient, yz component	Domain 1
cd7.Dzz_DCa	Da	m^2/s	Diffusion coefficient, zz component	Domain 1
cd7.Dav_DCa	cd7.Dxx_DCa	m^2/s	Average diffusion coefficient	Domain 1
cd7.tfluxx_DCa	-cd7.Dxx_DCa*DCax+cd7.cfluxx_DCa	mol/(m^2*s)	Total flux, x component	Domain 1
cd7.tfluxy_DCa	-cd7.Dyx_DCa*DCax+cd7.cfluxy_DCa	mol/(m^2*s)	Total flux, y component	Domain 1
cd7.tfluxz_DCa	-cd7.Dzx_DCa*DCax+cd7.cfluxz_DCa	mol/(m^2*s)	Total flux, z component	Domain 1
cd7.dfluxx_DCa	-cd7.Dxx_DCa*DCax	mol/(m^2*s)	Diffusive flux, x component	Domain 1
cd7.dfluxy_DCa	-cd7.Dyx_DCa*DCax	mol/(m^2*s)	Diffusive flux, y component	Domain 1
cd7.dfluxz_DCa	-cd7.Dzx_DCa*DCax	mol/(m^2*s)	Diffusive flux, z component	Domain 1
cd7.gradx_DCa	DCax	mol/m^4	Concentration gradient, x component	Domain 1
cd7.grady_DCa	0	mol/m^4	Concentration gradient, y component	Domain 1
cd7.gradz_DCa	0	mol/m^4	Concentration gradient, z component	Domain 1
cd7.ntflux_DCa	cd7.nx*cd7.tfluxx_DCa+cd7.ny*cd7.tfluxy_DCa+cd7.nz*cd7.tfluxz_DCa	mol/(m^2*s)	Normal total flux	Boundaries 1-2

cd7.ndflux_DCa	cd7.nx*cd7.dfluxx_DCa+cd7.ny*cd7.dfluxy_DCa+cd7.nz*cd7.dfluxz_DCa	mol/(m^2*s)	Normal diffusive flux	Boundaries 1-2
cd7.dfluxMag_DCa	sqrt(cd7.dfluxx_DCa^2+cd7.dfluxy_DCa^2+cd7.dfluxz_DCa^2)	mol/(m^2*s)	Diffusive flux magnitude	Domain 1
cd7.tfluxMag_DCa	sqrt(cd7.tfluxx_DCa^2+cd7.tfluxy_DCa^2+cd7.tfluxz_DCa^2)	mol/(m^2*s)	Total flux magnitude	Domain 1
cd7.u	u1	m/s	Velocity field, x component	Domain 1
cd7.v	u2	m/s	Velocity field, y component	Domain 1
cd7.w	u3	m/s	Velocity field, z component	Domain 1
cd7.cfluxx_DCa	DCa*u1	mol/(m^2*s)	Convective flux, x component	Domain 1
cd7.cfluxy_DCa	DCa*u2	mol/(m^2*s)	Convective flux, y component	Domain 1
cd7.cfluxz_DCa	DCa*u3	mol/(m^2*s)	Convective flux, z component	Domain 1
cd7.cfluxMag_DCa	sqrt(cd7.cfluxx_DCa^2+cd7.cfluxy_DCa^2+cd7.cfluxz_DCa^2)	mol/(m^2*s)	Convective flux magnitude	Domain 1
cd7.ncflux_DCa	cd7.nx*cd7.cfluxx_DCa+cd7.ny*cd7.cfluxy_DCa+cd7.nz*cd7.cfluxz_DCa	mol/(m^2*s)	Normal convective flux	Boundaries 1-2
cd7.cbf_DCa	0	mol/(m^2*s)	Convective boundary flux	Boundaries 1-2

Shape functions

Name	Shape function	Unit	Description	Shape frame	Selection
DCa	Lagrange	mol/m^3	Concentration	Spatial	Domain 1

Weak expressions

Weak expression	Integration frame	Selection
-DCat*test(DCa)-cd7.Dxx_DCa*DCax*test(DCax)	Spatial	Domain 1
DCa*cd7.u*test(DCax)	Spatial	Domain 1
cd7.cbf_DCa	Spatial	Boundaries 1-2

2.7.2. No Flux 1

Selection

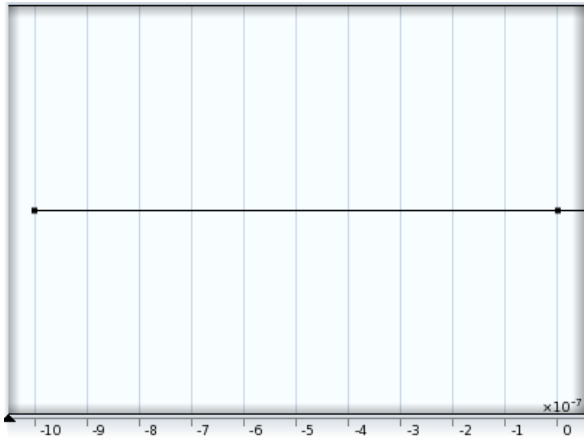

No Flux 1

2.7.3. Initial Values 1

Settings

Settings	
Description	Value
Concentration	Cabulk

Selection

Initial Values 1

2.7.4. Concentration 1

Settings

Settings	
Description	Value
Concentration	Cabulk
Species DCa	1

Selection

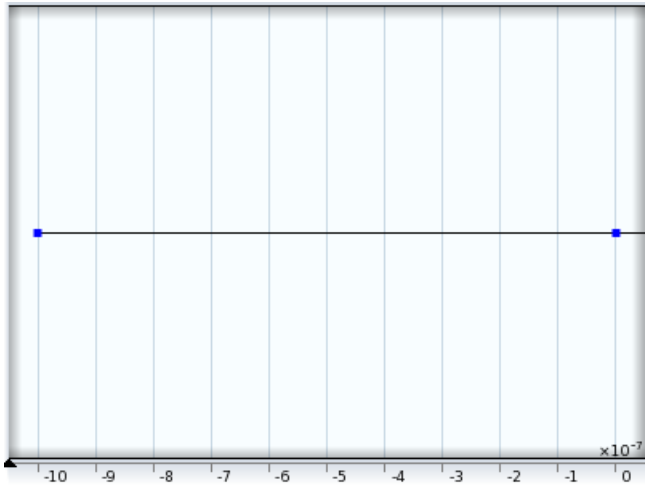

Concentration 1

Variables

Name	Expression	Unit	Description	Selection
cd7.c0_DCa	Cabulk	mol/m^3	Concentration	Boundaries 1-2

Constraints

Constraint	Constraint force	Shape function	Selection
-DCa+cd7.c0_DCa	test(-DCa+cd7.c0_DCa)	Lagrange	Boundaries 1-2

2.8. Transport of Diluted Species 8 (cd8)

Transport of Diluted Species 8

Settings	
Description	Value
Concentration	Quadratic
Convective term	Conservative form
Streamline diffusion	0
Crosswind diffusion	0
Show equation assuming	std1/stat

2.8.1. Convection and Diffusion 1

Settings

Settings	
Description	Value
Diffusion coefficient	{{Db, 0, 0}, {0, Db, 0}, {0, 0, Db}}

Selection

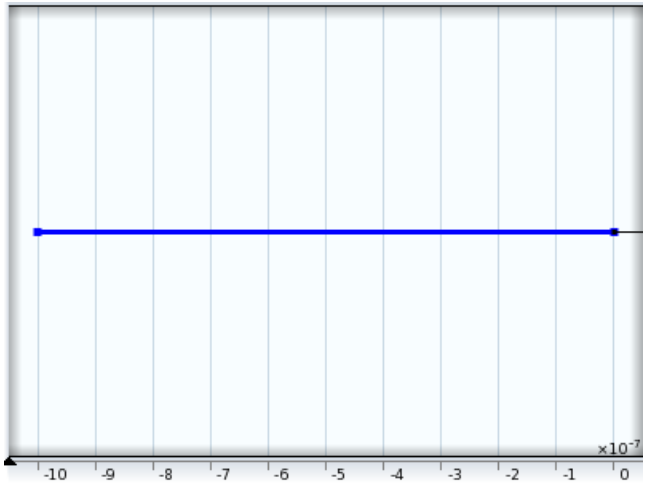

Convection and Diffusion 1

Variables

Name	Expression	Unit	Description	Selection
cd8.Dxx_DCb	Db	m^2/s	Diffusion coefficient, xx component	Domain 1
cd8.Dyx_DCb	0	m^2/s	Diffusion coefficient, yx component	Domain 1
cd8.Dzx_DCb	0	m^2/s	Diffusion coefficient, zx component	Domain 1
cd8.Dxy_DCb	0	m^2/s	Diffusion coefficient, xy component	Domain 1
cd8.Dyy_DCb	Db	m^2/s	Diffusion coefficient, yy component	Domain 1
cd8.Dzy_DCb	0	m^2/s	Diffusion coefficient, zy component	Domain 1
cd8.Dxz_DCb	0	m^2/s	Diffusion coefficient, xz component	Domain 1
cd8.Dyz_DCb	0	m^2/s	Diffusion coefficient, yz component	Domain 1
cd8.Dzz_DCb	Db	m^2/s	Diffusion coefficient, zz component	Domain 1
cd8.Dav_DCb	cd8.Dxx_DCb	m^2/s	Average diffusion coefficient	Domain 1
cd8.tfluxx_DCb	-cd8.Dxx_DCb*DCbx+cd8.cfluxx_DCb	mol/(m^2*s)	Total flux, x component	Domain 1
cd8.tfluxy_DCb	-cd8.Dyx_DCb*DCbx+cd8.cfluxy_DCb	mol/(m^2*s)	Total flux, y component	Domain 1
cd8.tfluxz_DCb	-cd8.Dzx_DCb*DCbx+cd8.cfluxz_DCb	mol/(m^2*s)	Total flux, z component	Domain 1
cd8.dfluxx_DCb	-cd8.Dxx_DCb*DCbx	mol/(m^2*s)	Diffusive flux, x component	Domain 1
cd8.dfluxy_DCb	-cd8.Dyx_DCb*DCbx	mol/(m^2*s)	Diffusive flux, y component	Domain 1
cd8.dfluxz_DCb	-cd8.Dzx_DCb*DCbx	mol/(m^2*s)	Diffusive flux, z component	Domain 1
cd8.gradx_DCb	DCbx	mol/m^4	Concentration gradient, x component	Domain 1
cd8.grady_DCb	0	mol/m^4	Concentration gradient, y component	Domain 1
cd8.gradz_DCb	0	mol/m^4	Concentration gradient, z component	Domain 1
cd8.ntflux_DCb	cd8.nx*cd8.tfluxx_DCb+cd8.ny*cd8.tfluxy_DCb+cd8.nz*cd8.tfluxz_DCb	mol/(m^2*s)	Normal total flux	Boundaries 1-2
cd8.ndflux_DCb	cd8.nx*cd8.dfluxx_DCb+cd8.ny*cd8.dfluxy_DCb+cd8.nz*cd8.dfluxz_DCb	mol/(m^2*s)	Normal diffusive flux	Boundaries 1-2
cd8.dfluxMag_DCb	sqrt(cd8.dfluxx_DCb^2+cd8.dfluxy_DCb^2+cd8.dfluxz_DCb^2)	mol/(m^2*s)	Diffusive flux magnitude	Domain 1
cd8.tfluxMag_DCb	sqrt(cd8.tfluxx_DCb^2+cd8.tfluxy_DCb^2+cd8.tfluxz_DCb^2)	mol/(m^2*s)	Total flux magnitude	Domain 1

cd8.u	u1	m/s	Velocity field, x component	Domain 1
cd8.v	u2	m/s	Velocity field, y component	Domain 1
cd8.w	u3	m/s	Velocity field, z component	Domain 1
cd8.cfluxx_DCb	DCb*u1	mol/(m^2*s)	Convective flux, x component	Domain 1
cd8.cfluxy_DCb	DCb*u2	mol/(m^2*s)	Convective flux, y component	Domain 1
cd8.cfluxz_DCb	DCb*u3	mol/(m^2*s)	Convective flux, z component	Domain 1
cd8.cfluxMag_DCb	sqrt(cd8.cfluxx_DCb^2+cd8.cfluxy_DCb^2+cd8.cfluxz_DCb^2)	mol/(m^2*s)	Convective flux magnitude	Domain 1
cd8.ncflux_DCb	cd8.nx*cd8.cfluxx_DCb+cd8.ny*cd8.cfluxy_DCb+cd8.nz*cd8.cfluxz_DCb	mol/(m^2*s)	Normal convective flux	Boundaries 1-2
cd8.cbf_DCb	0	mol/(m^2*s)	Convective boundary flux	Boundaries 1-2

Shape functions

Name	Shape function	Unit	Description	Shape frame	Selection
DCb	Lagrange	mol/m^3	Concentration	Spatial	Domain 1

Weak expressions

Weak expression	Integration frame	Selection
-DCbt*test(DCb)-cd8.Dxx_DCb*DCbx*test(DCbx)	Spatial	Domain 1
DCb*cd8.u*test(DCbx)	Spatial	Domain 1
cd8.cbf_DCb	Spatial	Boundaries 1-2

2.8.2. No Flux 1

Selection

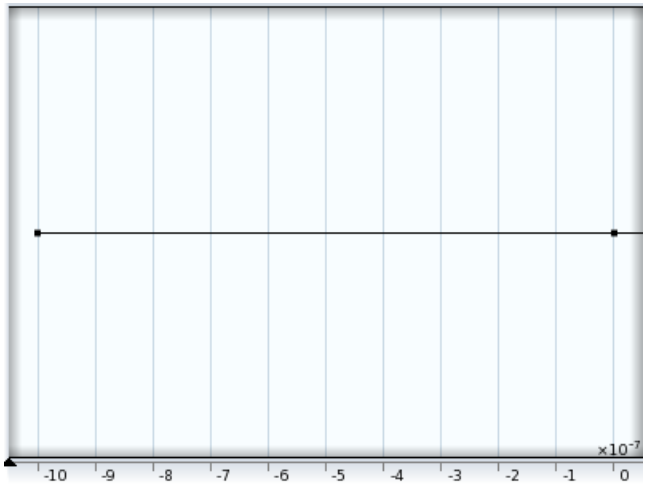

No Flux 1

2.8.3. Initial Values 1

Settings

Settings	
Description	Value
Concentration	Cbbulk

Selection

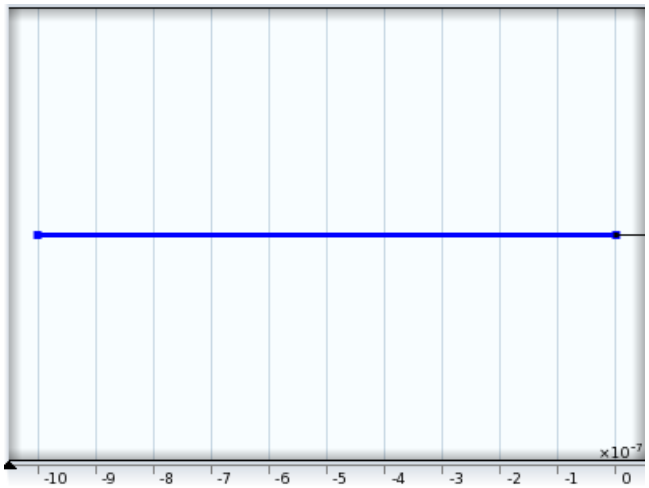

Initial Values 1

2.8.4. Concentration 1

Settings

Settings	
Description	Value
Concentration	Cbbulk
Species DCb	1

Selection

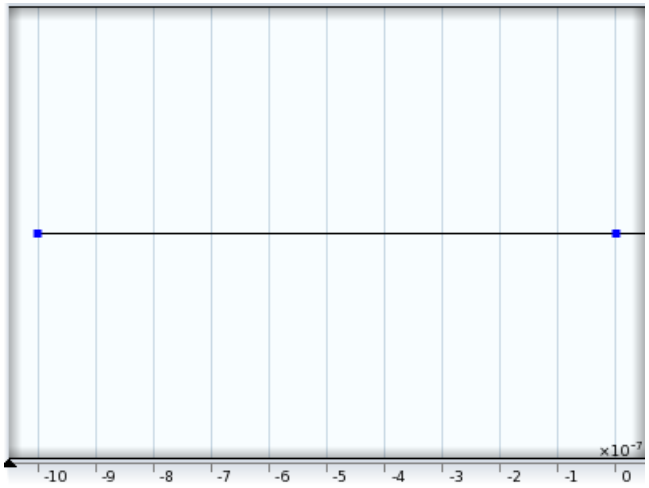

Concentration 1

Variables

Name	Expression	Unit	Description	Selection
cd8.c0_DCb	Cbbulk	mol/m^3	Concentration	Boundaries 1-2

Constraints

Constraint	Constraint force	Shape function	Selection
-DCb+cd8.c0_DCb	test(-DCb+cd8.c0_DCb)	Lagrange	Boundaries 1-2

2.9. MESHES

2.9.1. Mesh 1

Mesh statistics

Property	Value
Minimum element quality	1.0
Average element quality	1.0
Edge elements	3359
Vertex elements	3

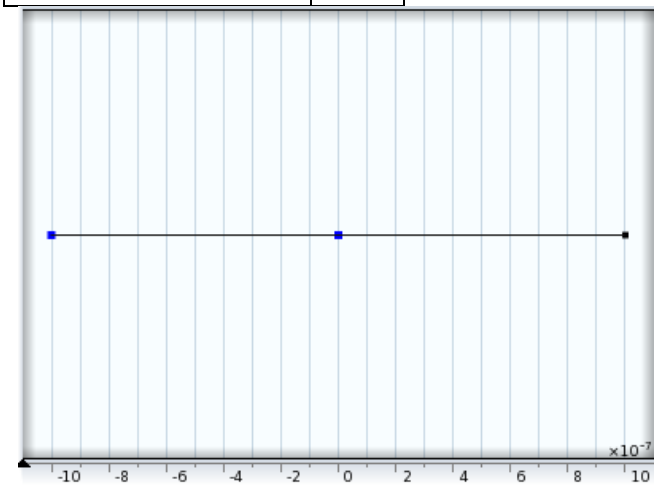

Mesh 1

Size (size)

Settings	
Name	Value
Maximum element size	2.0E-10
Minimum element size	4.0E-11
Resolution of curvature	0.2
Predefined size	Extremely fine
Custom element size	Custom

Mesh Object (obj)

Settings	
Name	Value
Filename	$FILENAME$_mesh1_obj.mphbin

Refine 1 (ref1)

Settings	
Name	Value
Number of refinements	1

2.9.2. Mesh 2

Mesh statistics	
Property	Value
Minimum element quality	0.0
Average element quality	0.0

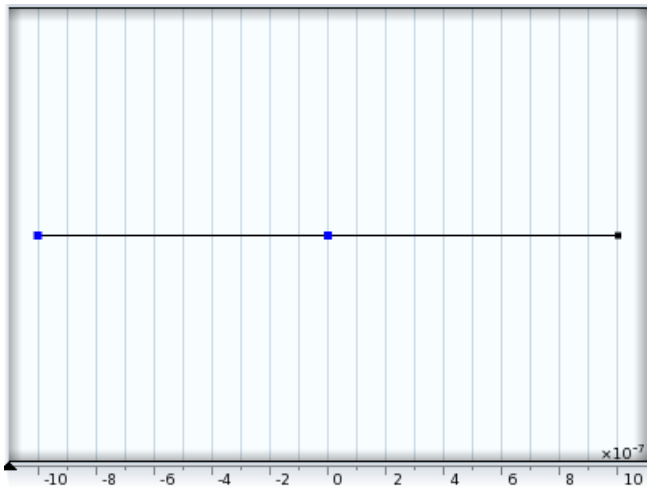

Mesh 2

Size (size)

Settings	
Name	Value
Maximum element size	1.3333E-7
Minimum element size	6.0E-10
Resolution of curvature	0.3
Maximum element growth rate	1.3
Custom element size	Custom

Size 1 (size1)

Settings	
Name	Value
Maximum element size	1e-12
Minimum element size	6.0E-10
Minimum element size	off
Resolution of curvature	0.3
Resolution of curvature	off
Resolution of narrow regions	off
Maximum element growth rate	1.3
Maximum element growth rate	off
Custom element size	Custom

Size 2 (size2)

Settings	
Name	Value
Maximum element size	1e-7
Minimum element size	6.0E-10
Minimum element size	off
Resolution of curvature	0.3
Resolution of curvature	off
Resolution of narrow regions	off
Maximum element growth rate	1.3
Maximum element growth rate	off
Custom element size	Custom

Size 3 (size3)

Settings

Name	Value
Maximum element size	1e-12
Minimum element size	6.0E-10
Minimum element size	off
Resolution of curvature	0.3
Resolution of curvature	off
Resolution of narrow regions	off
Maximum element growth rate	1.3
Maximum element growth rate	off
Custom element size	Custom

3. Study 1

3.1. PARAMETRIC SWEEP

Parameter name: sw

Parameters: range(10,0.05,50)

3.2. STATIONARY

Mesh selection	
Geometry	Mesh
Geometry 1 (geom1)	mesh1

Physics selection	
Physics interface	Discretization
Poisson's Equation (poeq)	physics
Poisson's Equation 2 (poeq2)	physics
Transport of Diluted Species (cd)	physics
Transport of Diluted Species 2 (cd2)	physics
Transport of Diluted Species 7 (cd7)	physics
Transport of Diluted Species 8 (cd8)	physics

4. Results

4.1. DERIVED VALUES

4.1.1. Point Evaluation 1

Selection	
Geometric entity level	Boundary
Selection	Boundary 3

Settings	
Name	Value
Data set	Solution 1
Expression	Electrode
Unit	A*mol/m^2

4.2. 1D PLOT GROUP 37

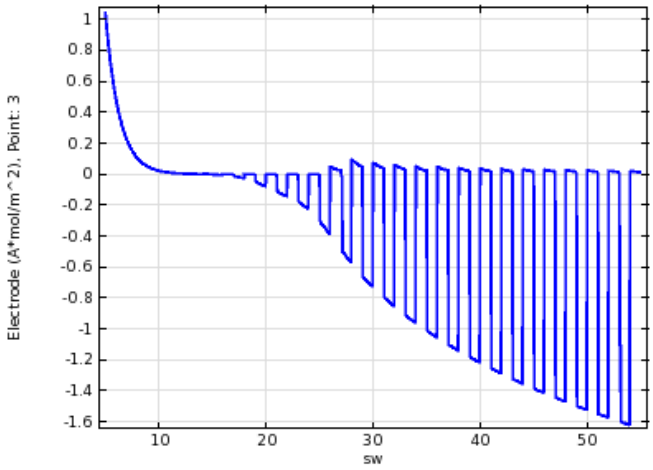

References

Chapter 1

Bard, A. J. *Science* **1980,** *207,* 139-144.

Brattain, W. H.; Garrett, C. G. B. *Bell Syst. Tech. J.* **1955,** 34, 129-176.

Nozik, A. J. *Ann. Rev. Phys. Chem.* **1978,** *29,* 189-222.

Fujishima, A.; Honda, K. *Nature,* **1972,** *238,* 37-38.

Bard, A. J.; Fox, M. A. *Acc. Chem. Res.* **1995,** *28,* 141-145.

Kudo, A.; Omori, K.; Kato, H. *J. Am. Chem. Soc.* **1999,** *121,* 11459-11467.

Oshikiri, M.; Mauro, B. *J. Phys. Chem. B* **2006,** *110,* 9188-9194.

Bard, A. J.; Faulkner, L. R. *Electrochemical Methods: Fundamentals and Applications; Wiley: New York,* **2001**; Chapter 18, pp 736-768.

Bard, A. J. *J. Photochem.* **1979,** *10,* 59-75.

Youngblood, W. J.; Lee, S.-H. A.; Maeda, K.; Mallouk, T. E. *Acc. Chem. Res.* **2009**, *42*, 1966-1973.

Li, L.; Duan, L.; Xu, Y.; Gorlov, M.; Hagfeldt, A.; Sun, L. *Chem. Commun.* **2010**, *46,* 7307-7309.

Brimblecombe, R.; Koo, A.; Dismukes, G. C.; Swiegers, G. F.; Spiccia, L. *J. Am. Chem. Soc.* **2010**, *132*, 2892-2894.

Walter, M. G.; Warren, E. L.; McKone, J. R.; Boettcher, S. W.; Mi, Q.; Santori, E. A.; Lewis, N. S. *Chem. Rev.* **2010**, *110,* 6446-6473.

Boettcher, S. W.; Warren, E. L.; Putnam, M. C.; Santori, E. A.; Turner-Evans, D.; Kelzenberg, M. D.; Walter, M. G.; McKone, J. R.; Brunschwig, B. S.; Atwater, H. A.; Lewis, N. S. *J. Am. Chem. Soc.* **2011**, *133*, 1216-1219.

Rocheleau, R. E.; Miller, E. L.; Misra, A. *Energy & Fuels* **1998**, *12*, 3-10.

Sivula, K.; Le Formal, F.; Gratzel, M. *ChemSusChem* **2011**, *4*, 432-449.

Cervera-March, S.; Smotkin, E. S.; Bard, A. J.; Campion, A.; Fox, M. A.; Mallouk, T.; Webber, S. E.; White, J. M. *J. Electrochem. Soc.* **1988**, *135*, 567-573.

Smotkin, E.; Bard, A. J.; Campion, A.; Fox, M. A.; Mallouk, T.; Webber, S. E.; White, J. M. *J. Phys. Chem*. **1986**, *90*, 4604-4607.

Smotkin, E. S.; Cervera-March, S.; Bard, A. J.; Campion, A.; Fox, M. A.; Mallouk, T.; Webber, S. E.; White, J. M. *J. Phys. Chem.* **1987**, *91*, 6-8.

Maeda, K.; Higashi, M.; Lu, D.; Abe, R.; Domen, K. *J. Am. Chem. Soc.* **2010**, *132*, 5858-5868.

Bard, A. J.; Fan, F.-R.; Kwak, J.; Lev, O. *Anal. Chem.* **1989,** *61*, 132-138.

Kwak, J.; Bard, A. J. *Anal. Chem.* **1989,** *61*, 1221-1227.

Sanchez-Sanchez, C. M.; Rodriguez-Lopez, J.; Bard, A. J. *Anal. Chem.* **2008,** *80*, 3254-3260.

Bertoncello, P. *Energy Environ. Sci.* **2010,** *3*, 1620-1633.

Shah, B. C.; Hillier, A. C. *J. Electrochem. Soc.* **2000,** *147*, 3043-3048.

Horrocks, B. R.; Mirkin, M. V.; Bard, A. J. *J. Phys. Chem.* **1994,** *98*, 9106-9114.

Mandler, D.; Bard, A. J. *J. Electrochem. Soc.* **1990,** *137*, 2468-2472.

Cong, Y.; Park, H. S.; Wang, S.; Dang, H. X.; Fan, F.-R. F.; Mullins, B.; Bard, A. J. *J. Phys. Chem. C* **2012,** *116*, 14541-14550.

Fernandez, J. L.; Walsh, D. A.; Bard, A. J. *J. Am. Chem. Soc.* **2005,** *127*, 357-365.

Kylberg, W.; Wain, A. J.; Castro, F. A. *J. Phys. Chem. C* **2012,** *116*, 17384-17392.

Ye, H.; Park, H. S.; Bard, A. J. *J. Phys. Chem. C* **2011,** *115*, 12464-12470.

Lee, J.; Ye, H.; Pan, S.; Bard, A. J. *Anal. Chem*, **2008,** *80*, 7445-7450.

Katz, J. E.; Gingrich, T. R.; Santori, E. A.; Lewis, N. S. *Energy Environ. Sci.* **2009**, *2*, 103-112.

Woodhouse, M.; Herman, G. S.; Parkinson, B. A. *Chem. Mater.* **2005**, *17*, 4318-4324.

Jang, J. S.; Lee, J.; Ye, H.; Fan, F.-R. F.; Bard, A. J. *J. Phys. Chem. C.* **2009**, *113*, 6719-6724.

He, J.; Parkinson, B. A. *ACS Comb. Sci.* **2011**, *13*, 399-404.

Jang, J. S.; Yoon, K. Y.; Xiao, X.; Fan, F.-R. F.; Bard, A. J. *Chem. Mater.* **2009**, *21*, 4803-4810.

Baeck, S. H.; Jaramillo, T. F.; Brandli, C.; McFarland, E. W. *J. Comb. Chem.* **2002**, *4*, 563-568.

Liu, W.; Ye, H.; Bard, A. J. *J. Phys. Chem. C* **2010**, *114*, 1201-1207.

Ye, H.; Lee, J.; Jang, J. S.; Bard, A. J. *J. Phys. Chem. C* **2010**, *114*, 13322-13328.

Park, H. S.; Kweon, K. E.; Ye, H.; Paek, E.; Hwang, G. S.; Bard, A. J. *J. Phys. Chem. C* **2011**, *115*, 17870-17879.

Liu, G.; Liu, C.; Bard, A. J. *J. Phys. Chem. C* **2010**, *114*, 20997-21002.

Liu, G.; Bard, A. J. *J. Phys. Chem. C* **2010**, *114*, 17509-17513.

Riha, S. C.; Parkinson, B. A.; Prieto, A. L. *J. Am. Chem. Soc.* **2011**, *133*, 15272-15275.

Mirkin, M. V.; Nogala, W.; Velmurugan, J.; Wang, Y. *Phys. Chem. Chem. Phys.* **2011,** *13*, 21196-21212.

Zaera, F. *Chem. Rev.* **2012,** *112*, 2920-2986.

Snowden, M. E.; Guell, A. G.; Lai, S. C. S.; McKelvey, K.; Ebejer, N.; O'Connell, M. A.; Colburn, A. W.; Unwin, P. R. *Anal. Chem.* **2012,** *84*, 2483-2491.

Lee, C.; Kwak, J.; Bard, A. J. *Proc. Natl. Acad. Sci. USA* **1990,** *87*, 1740-1743.

Patten, H. V.; Lai, S. C. S.; Macpherson, J. V.; Unwin, P. R. *Anal. Chem.* **2012,** *84*, 5427-5432.

Grisotto, F.; Ghorbal, A.; Goyer, C.; Charlier, J.; Palacin, S. *Chem. Mater.* **2011,** *23*, 1396-1405.

Bard, A. J.; Faulkner, L. R. *Electrochemical Methods: Fundamentals and Applications; Wiley: New York*, **2001**; Chapter 5, pp 168-176.

Bard, A. J.; Faulkner, L. R. *Electrochemical Methods: Fundamentals and Applications; Wiley: New York*, **2001**; Chapter 16, pp 669-675.

Bard, A. J.; Mirkins, M. V.; Unwin, P. R.; Wipf, D. O. *J. Phys. Chem.* **1992,** *96*, 1861-1868.

Eckhard, K.; Chen, X.; Turcu, F.; Schuhmann, W. *Phys. Chem. Chem. Phys.* **2006,** 8, 5359-5365.

Chapter 2

Woodhouse, M.; Parkinson, B. A. *Chem. Soc. Rev.* **2009,** 38, 197-210.

Baeck, S. H.; Jaramillo, T. F.; Brandli, C.; McFarland, E. W. *J. Comb. Chem.* **2002,** 4, 563-568.

Lee, J.; Ye, H.; Pan, S.; Bard, A. J. *Anal. Chem.* **2008**, *80*, 7445-7450.

Jang, J. S.; Lee, J.; Ye, H.; Fan, F.-R. F.; Bard, A. J. *J. Phys. Chem. C* **2009**, *113*, 6719-6724.

Jang, J. S.; Yoon, K. Y.; Xiao, X.; Fan, F.-R. F.; Bard, A. J. *Chem. Mater.* **2009**, *21*, 4803-4810.

Liu, W.; Ye, H.; Bard, A. J. *J. Phys. Chem. C* **2010**, *114*, 1201-1207.

Ye, H.; Lee, J.; Jang, J. S.; Bard, A. J. *J. Phys. Chem. C* **2010**, *114*, 13322-13328.

Liu, G.; Liu, C.; Bard, A. J. *J. Phys. Chem. C* **2010**, *114*, 20997-21002.

Fujishima, A.; Honda, K. *Nature* **1972**, *238*, 37-38.

Bard, A. J. *J. Am. Chem. Soc.* **2010**, *132*, 7559-7567.

Yao, W.; Ye, J. *J. Phys. Chem. B* **2006**, *110*, 11188-11195.

Sleight, A. W.; Aykan, K.; Rogers, D. B. *J. Solid State Chem.* **1975**, *13*, 231-236.

Tokunaga, S.; Kato, H.; Kudo, A. *Chem. Mater.* **2001**, *13*, 4624-4628.

Sayama, K.; Nomura, A.; Arai, T.; Sugita, T.; Abe, R.; Yanagida, M.; Oi, T.; Iwasaki, Y.; Abe, Y.; Sugihara, H. *J. Phys. Chem. B* **2006**, *110*, 11352-11360.

Walsh, A.; Yan, Y.; Huda, M. N.; Al-Jassim, M. M.; Wei, S.-H. *Chem. Mater.* **2009**, *21*, 547-551.

Myung, N.; Ham S.; Choi S.; Chae Y.; Kim, W.-G.; Jeon, Y. J.; Paeng, K.-J.; Chanmanee, W.; de Tacconi, N. R.; Rajeshwar K. *J. Phys. Chem. C* **2011,** 115, 7793-7800.

Van de Krol, R.; Liang Y.; Schoonman J. *J. Mater. Chem.* **2008,** 18, 2311-2320.

Kudo, A.; Omori, K.; Kato, H. *J. Am. Chem. Soc*. **1999**, *121*, 11459.

Sayama, K.; Nomura, A.; Arai,T.; Sugita, T.; Abe, R.;Yanagida, M.; Oi, T.; Iwasaki, Y.; Abe, Y.; Sugihara, H. *J. Phys. Chem. B* **2006,** *110*, 11352-11360.

Ferrari, M.; Lutterotti, L. *J. Appl. Phys.* **1994**, *76*, 7246-7255.

Bard, A. J.; Faulkner, L. R. *Electrochemical Methods Fundamentals and Application*, 2nd ed.; John Wiley & Sons: New York, **2001**, pp 746-752.

Cardon, F.; Gomes, W. P. *J. Phys. D: Appl. Phys.* **1978**, *11*, L63-L67.

Corbel, G.; Laligant, Y.; Goutenoire, F.; Suard, E.; Lacorre, P. *Chem. Mater.* **2005**, *17*, 4678-4684.

Chapter 3

Barber, J. *Chem. Soc. Rev.* **2009,** *38*, 185-196.

Nakamura, R.; Okamura, T.; Ohashi, N.; Imanishi, A.; Nakato, Y. *J. Am. Chem. Soc.* **2005,** *127*, 12975-12983.

Subbaraman, R.; Tripkovic, D.; Chang, K.-C.; Strmcnik, D.; Paulikas, A. P.; Hirunsit, P.; Chan, M.; Greeley, J.; Stamenkovic, V.; Markovic, N. M. *Nature Mater.* **2012**, *11*, 550-557.

Zong, R.; Thummel, R. P. *J. Am. Chem. Soc.* **2005,** *127*, 12802-12803.

Clausen, J.; Junge, W. *Nature* **2004,** *430*, 480-483.

Jaeger, C. D.; Bard, A. J. *J. Phys. Chem.* **1979**, *83*, 3146-3152.

Ahmed, A. Y.; Kandiel, T. A.; Oekermann, T.; Bahnemann, D. *J. Phys. Chem. Lett.* **2011,** *2*, 2461-2465.

Schwarz, P. F.; Turro, N. J.; Bossmann, S. H.; Braun, A. M.; Wahab, A.-M. A. A.; Durr, H. *J. Phys. Chem. B* **1997,** *101,* 7127-7134.

Izumi, I.; Fan, Fan, F.-R. F.; Bard, A. J. *J. Phys. Chem.* **1981,** *85,* 218-223.

Nakamura, R.; Nakato, Y. *J. Am. Chem. Soc.* **2004,** *126,* 1290-1298.

Micic, O. I.; Zhang, Y.; Cromack, K. R.; Trifunac, A. D.; Thurnauer, M. C. *J. Phys. Chem.* **1993,** *97,* 7277-7283.

Park, S. H.; Roy, A.; Beaupre, S.; Cho, S.; Coates, N.; Moon, J. S.; Moses, D.; Leclerc, M.; Lee, K.; Heeger, A. J. *Nature Photon.* **2009,** *3,* 297-303.

Nozik, A. J. *Inorg. Chem.* **2005,** *44,* 6893-6899.

Nosaka, Y.; Fox, M. A. *J. Phys. Chem.* **1986,** *90,* 6521-6522.

Ishibashi, K.; Fujishima, A.; Watanabe, T.; Hashimoto, K. *J. Phys. Chem. B* **2000,** *104,* 4934-4938.

Nosaka, Y.; Komori, S.; Yawata, K.; Hirakawa, T.; Nosaka, A. Y. *Phys. Chem. Chem. Phys.* **2003,** *5,* 4731-4735.

Ohko, Y.; Hashimoto, K.; Fujishima, A. *J. Phys. Chem. A* **1997,** *101,* 8057-8062.

Sun, P.; Laforge, F. O.; Mirkin, M. V. *Phys. Chem. Chem. Phys.* **2007**, *9,* 802-823.

Tanaka, K.; White, J. M. *J. Phys. Chem.* **1982,** *86,* 4708-4714.

Primet, M.; Pichat, P.; Mathieu, M.-V. *J. Phys. Chem.* **1971,** *75,* 1216-1220.

Lawless, D.; Serpone, N.; Meisel, D. *J. Phys. Chem.* **1991,** *95,* 5166-5170.

Ohikiri, M.; Boero, M. *J. Phys. Chem. B.* **2006,** *110,* 9188-9194.

Shankar, K.; Basham, J. I.; Allam, N. K.; Varghese, O. K.; Mor, G. K.; Feng, X.; Paulose, M.; Seabold, J. A.; Choi, K.-S.; Grimes, C. A. *J. Phys. Chem. C* **2009,** *113,* 6327-6359.

Ulanski, P.; Von Sonntag, C. *J. Chem. Soc., Perkin Trans.* **1999,** *2,* 165-168.

Zhong, D. K.; Choi, S.; Gamelin, D. R. *J. Am. Chem. Soc.* **2011**, *133,* 18370-18377.

Spray, R. L.; McDonald, K. J.; Choi, K.-S. *J. Phys. Chem. C* **2011**, *115,* 3497-3506.

Jo, W. J.; Jang, J.-W.; Kong, K.-J.; Kang, H. J.; Kim, J. Y.; Jun, H.; Parmar, K. P. S.; Lee J. S. *Angew. Chem. Int. Ed.* **2012,** *51,* 1-6.

Hong, S. J.; Lee, S.; Jang, J. S.; Lee, J. S. *Energy Environ. Sci.* **2011,** *4,* 1781-1787.

Su, J.; Guo, L.; Bao, N.; Grimes, C. A. *Nano Lett.* **2011,** *11,* 1928-1933.

Saito, R.; Maiseki, Y.; Sayama, K. *Chem. Commun.* **2012,** *48,* 3833-3835.

Liang, Y.; Tsubota, T.; Mooij, L. P. A.; Van de Krol, R. *J. Phys. Chem. C* **2011,** *115,* 17594-17598.

Lee, Y.; Amemiya, S.; Bard, A. J. *Anal. Chem.* **2001**, *73,* 2261-2267.

Ferrell, R. T.; Himmelblau, D. M. *J. Chem. Eng. Data*, **1967,** *12,* 111-115.

Minguzzi, A.; Fan, F.-R. F.; Vertova, A.; Rondininia, S.; Bard, A. J. *Chem. Sci.*, **2012**, *3,* 217-229.

Park, H. S.; Kweon, K. E.; Ye, H.; Paek, E.; Hwang, G. S.; Bard, A. J. *J. Phys. Chem. C,* **2011,** *115,* 17870-17879.

Chapter 4

Alexander B. D.; Kulesza P. J.; Rutkowska I.; Solarska R.; Augustynski J. *J. Mater. Chem.* **2008,** 18, 2298-2303.

Cesar I.; Kay A.; Martinez J. A. G.; Gratzel M. *J. Am. Chem. Soc.* **2006,** 128, 4582-4583.

Cole B.; Marsen B.; Miller E.; Yan Y.; To B.; Jones K.; Al-Jassim M. *J. Phys. Chem. C* **2008,** 112, 5213-5220.

Ye H.; Lee, J.; Jang, J. S.; Bard, A. J. *J. Phys. Chem. C* **2010**, *114*, 13322-13328.

Park H. S.; Kweon K. E.; Ye H.; Paek E.; Hwang G. S.; Bard A. J. *J. Phys. Chem. C* **2011**, *115*, 17870-17879.

Glasscock J. A.; Barnes P. R. F.; Plumb I. C.; Savvides N. *J. Phys. Chem. C.* **2007,** 111, 16477-16488.

Kennedy J. H.; Frese Jr. K. W. *J. Electrochem. Soc.* **1978,** 125, 709-714.

Butler M. A. *J. Appl. Phys.* **1977,** 48, 1914-1920.

Lin Y.; Liu X.; Sheehan S.; Wang D. *J. Am. Chem. Soc.* **2009,** 131, 2772-2773.

Banerjee S.; Mohapatra S. K.; Misra M. *J. Phys. Chem. C* **2011**, 115, 12643-12649.

Liu R.; Lin Y.; Chou L.-Y.; Sheehan S. W.; He W.; Zhang F.; Hou H. J. M.; Wang D. *Angew. Chem. Int. Ed.* **2011,** 50, 499-502.

Lin Y.; Zhou S.; Sheehan S. W.; Wang D. *J. Am. Chem. Soc.* **2011,** 133, 2398-2401.

Mohapatra S. K.; Raja K. S.; Mahajan V. K.; Misra M. *J. Phys. Chem. C* **2008,** 112, 11007-11012.

Ng Y. H.; Linghtcap I. V.; Goodwin K.; Matsumura M.; Kamat P. V. *J. Phys. Chem. Lett.* **2010**, 1, 2222-2227.

Williams, G.; Seger B.; Kamat P. V. *Acs Nano* **2008**, 2, 1487-1491.

Ng Y. H.; Iwase A.; Kudo A.; Amal R. *J. Phys. Chem. Lett.* **2010**, 1, 2607-2612.

Fleetwood D. M.; Winokur P. S.; Reber Jr. R. A.; Meisenheimer T. L.; Schwank J. R.; Shaneyfelt M. R.; Riewe L. C. *J. Appl. Phys.* **1993,** 73, 5058-5074.

Brodie B. C. *Philos. Trans. R. Soc. London*, **1859**, 149, 249-259.

Dreyer D. R.; Park S.; Bielawski C. W.; Ruoff R. S. *Chem. Soc. Rev.* **2010**, 39, 228-240.

Loh K. P.; Bao Q.; Eda G.; Chhowalla M. *Nat. Chem.* **2010,** 2, 1015-1024.

Potts J. R.; Dreyer D. R.; Bielawski C. W.; Ruoff R. S. *Polymer* **2011,** 52, 5-25.

Lee D. H.; Kim J. E.; Han T. H.; Hwang J. W.; Jeon S.; Choi S.-Y.; Hong S. H.; Lee W. J.; Ruoff R. S.; Kim S. O. *Adv. Mater.* **2010,** 22, 1247-1252.

Stoller M. D.; Park S.; Zhu Y.; An J.; Ruoff R. S. *Nano Lett.* **2008**, *8*, 3498-3502.

Laser, D.; Bard, A. J. *J. Electrochem. Soc.* **1976,** *123*, 1828-1832.

Orazem, M. E.; Newman, J. *J. Elctrochem. Soc.* **1984,** *131*, 2574-2582.

Anz, S. J.; Lewis, N. S. *J. Phys. Chem. B* **1999,** *103*, 3908-3915.

Hummers W. S.; Offeman R. E. *J. Am. Chem. Soc.* **1958**, *80*, 1339.

Kraeutler B.; Bard A. J. *J. Am. Chem. Soc.* **1978**, *100*, 4317-4318.

Foley, J. M.; Price, M. J.; Feldblyum, J. I.; Maldonado, S. *Energy Environ. Sci.* **2012,** *5*, 5203-5220.

Tokunaga S.; Kato H.; Kudo A. *Chem Mater.* **2001**, *13*, 4624-4628.

Yang D.; Velamakanni A.; Bozoklu G.; Park S.; Stoller M.; Piner R. D.; Stankovich S.; Jung I.; Field D. A.; Ventrice Jr. C. A.; Ruoff R. S. *Carbon* **2009**, *47*, 145-152.

Ye H.; Park H. S.; Bard A. J. *J. Phys. Chem. C.* **2011**, *115*, 12464-12470.

Wheeler, D. A.; Wang, G.; Ling, Y.; Li, Y.; Zhang, J. Z. *Energy Environ. Sci.* **2012**, *5*, 6682-6702.

Leng, W. H.; Barnes, P. R. F.; Juozapavicius, M.; O'Regan, B. C.; Durrant, J. R. *J. Phys. Chem. Lett.* **2010**, *1*, 967-972.

Chapter 5

Bard, A. J. *Science* **1980**, *207*, 139-144.

Nozik, A. J. *Ann. Rev. Phys. Chem.* **1978**, *29*, 189-222.

Bard, A. J.; Fox, M. A. *Acc. Chem. Res.* **1995**, *28*, 141-145.

United States Department of Energy, a National Vision of America's Transition to a Hydrogen Economy To 2030 and Beyond, February, **2002**.

Fujishima, A.; Honda, K. *Nature* **1972**, *238*, 37-38.

Youngblood, W. J.; Lee, S.-H. A.; Maeda, K.; Mallouk, T. E. *Acc. Chem. Res.* **2009**, *42*, 1966-1973.

Li, L.; Duan, L.; Xu, Y.; Gorlov, M.; Hagfeldt, A.; Sun, L. *Chem. Commun.* **2010**, *46*, 7307-7309.

Brimblecombe, R.; Koo, A.; Dismukes, G. C.; Swiegers, G. F.; Spiccia, L. *J. Am. Chem. Soc.* **2010**, *132*, 2892-2894.

Walter, M. G.; Warren, E. L.; McKone, J. R.; Boettcher, S. W.; Mi, Q.; Santori, E. A.; Lewis, N. S. *Chem. Rev.* **2010**, *110*, 6446-6473.

Boettcher, S. W.; Warren, E. L.; Putnam, M. C.; Santori, E. A.; Turner-Evans, D.; Kelzenberg, M. D.; Walter, M. G.; McKone, J. R.; Brunschwig, B. S.; Atwater, H. A.; Lewis, N. S. *J. Am. Chem. Soc.* **2011**, *133*, 1216-1219.

Rocheleau, R. E.; Miller, E. L.; Misra, A. *Energy & Fuels* **1998**, *12*, 3-10.

Sivula, K.; Le Formal, F.; Gratzel, M. *ChemSusChem* **2011**, *4*, 432-449.

Cervera-March, S.; Smotkin, E. S.; Bard, A. J.; Campion, A.; Fox, M. A.; Mallouk, T.; Webber, S. E.; White, J. M. *J. Electrochem. Soc.* **1988**, *135*, 567-573.

Smotkin, E.; Bard, A. J.; Campion, A.; Fox, M. A.; Mallouk, T.; Webber, S. E.; White, J. M. *J. Phys. Chem.* **1986**, *90*, 4604-4607.

Smotkin, E. S.; Cervera-March, S.; Bard, A. J.; Campion, A.; Fox, M. A.; Mallouk, T.; Webber, S. E.; White, J. M. *J. Phys. Chem.* **1987**, *91*, 6-8.

Bard, A. J. *J. Photochem.* **1979**, *10*, 59-75.

Maeda, K.; Higashi, M.; Lu, D.; Abe, R.; Domen, K. *J. Am. Chem. Soc.* **2010**, *132*, 5858-5868.

Katz, J. E.; Gingrich, T. R.; Santori, E. A.; Lewis, N. S. *Energy Environ. Sci.* **2009**, *2*, 103-112.

Woodhouse, M.; Herman, G. S.; Parkinson, B. A. *Chem. Mater.* **2005**, *17*, 4318-4324.

Jang, J. S.; Lee, J.; Ye, H.; Fan, F.-R. F.; Bard, A. J. *J. Phys. Chem. C.* **2009**, *113*, 6719-6724.

He, J.; Parkinson, B. A. *ACS Comb. Sci.* **2011**, *13*, 399-404.

Jang, J. S.; Yoon, K. Y.; Xiao, X.; Fan, F.-R. F.; Bard, A. J. *Chem. Mater.* **2009**, *21*, 4803-4810.

Baeck, S. H.; Jaramillo, T. F.; Brandli, C.; McFarland, E. W. *J. Comb. Chem.* **2002**, *4*, 563-568.

Liu, W.; Ye, H.; Bard, A. J. *J. Phys. Chem. C* **2010**, *114*, 1201-1207.

Ye, H.; Lee, J.; Jang, J. S.; Bard, A. J. *J. Phys. Chem. C* **2010**, *114*, 13322-13328.

Park, H. S.; Kweon, K. E.; Ye, H.; Paek, E.; Hwang, G. S.; Bard, A. J. *J. Phys. Chem. C* **2011**, *115*, 17870-17879.

Liu, G.; Liu, C.; Bard, A. J. *J. Phys. Chem. C* **2010**, *114*, 20997-21002.

Liu, G.; Bard, A. J. *J. Phys. Chem. C* **2010**, *114*, 17509-17513.

Riha, S. C.; Parkinson, B. A.; Prieto, A. L. *J. Am. Chem. Soc.* **2011**, *133*, 15272-15275.

Kudo, A.; Omori, K.; Kato, H. *J. Am. Chem. Soc.* **1999**, *121*, 11459-11467.

Seabold, J. A.; Choi, K.-S. *J. Am. Chem. Soc.* **2012**, *134*, 2186-2192.

Zhong, D. K.; Choi, S.; Gamelin, D. R. *J. Am. Chem. Soc.* **2011**, *133*, 18370-18377.

Bridge, P. J.; Pryce, M. W. *Mineralog. Mag.* **1974**, *39*, 847-849.

Sayama, K.; Nomura, A.; Arai, T.; Sugita, T.; Abe, R.; Yanagida, M.; Oi, T.; Iwasaki, Y.; Abe, Y.; Sugihara, H. *J. Phys. Chem. B* **2006**, *110*, 11352-11360.

Y, He.; Park, H. S.; Bard, A. J. *J. Phys. Chem. C* **2011**, *115*, 12464-12470.

Kim, M.-G.; Kanatzidis, M. G.; Facchetti, A.; Marks, T. J. *Nat. Mater.* **2011**, *10*, 382-388.

Abe, R.; Sayama, K.; Sugihara, H. *J. Phys. Chem. B* **2005**, *109*, 16052-16061.

Bard, A. J.; Faulkner, L. R. *Electrochemical Methods Fundamentals and Application*, 2nd ed.; John Wiley & Sons: New York, **2001**.

Lessner, P. M.; McLarnon, F. R.; Winnick, J.; Cairns, E. J. *J. Electrochem. Soc.* **1993**, *140*, 1847-1849.

Khaselev, O.; Turner, J. A. *Science* **1998**, *280*, 425-427.

Reece, S. Y.; Hamel, J. A.; Sung, K.; Jarvi, T. D.; Esswein, A. J.; Pijpers, J. J.; Nocera, D. G. *Science* **2011**, *334*, 645-648.

Cardon, F.; Gomes, W. P. *J. Phys. D: Appl. Phys.* **1978**, *11*, L63-L67.

Hanna, M. C.; Nozik, A. J. *J. Appl. Phys.* **2006**, *100*, 074510